APPLIED COMPUTATIONAL ELECTROMAGNETICS SOCIETY JOURNAL

January 2022
Vol. 37 No. 1
ISSN 1054-4887

The ACES Journal is abstracted in INSPEC, in Engineering Index, DTIC, Science Citation Index Expanded, the Research Alert, and to Current Contents/Engineering, Computing & Technology.

The illustrations on the front cover have been obtained from the research groups at the Department of Electrical Engineering, The University of Mississippi

Published, sold and distributed by: River Publishers, Alsbjergvej 10, 9260 Gistrup, Denmark

JANUARY 2022 REVIEWERS

Galip Orkun Arican
Behrokh Beiranvand
Amerigo Capria
Vedula Chakravarthy
John F. Dawson
Tijana Dimitrijevic
Ibrahim Elshafiey
J.C. Hernandez
Yong Mao Huang
Shian Hwu
Tianqi Jiao
Hussein Thary Khamess
Rajesh Kumar
K. Kumarasamy
Runa Kumari
Haotian Li
Yan Li
Yongwei Li
Tu-Lu Liang
Ding-Bing Lin
Shengyuan Luo
Lin Meiyan
Asmaa Majeed
Satyanarayan Murthy
Sima Noghanian
Leszek Nowosielski
Mahdi Oliaei
Amalendu Patnaik
Kannadhasan S.
Natarajamani S.
Grzegorz Tytko
Marsellas Waller
Jianbao Wang
Ke Xu
Abubakar Yakubu
Erdem Yazgan
Xiaoyan Zhang

THE APPLIED COMPUTATIONAL ELECTROMAGNETICS SOCIETY JOURNAL

Vol. 37 No. 1 January 2022

TABLE OF CONTENTS

An Adaptive and Highly Accurate FDTD Mesh Generation Technique for Objects with Complex Edge Structures

Chunhui Mou[1] **and Juan Chen**[1,2]

[1]School of Information and Communications Engineering
Xi'an Jiaotong University, Xi'an 710049, China
mouchunhui@163.com

[2]Shenzhen Research School
Xi'an Jiaotong University, Shenzhen 518057, China
chen.juan.0201@mail.xjtu.edu.cn

Abstract – In this paper, a triangular facets based, highly accurate, and adaptive finite-difference time-domain (FDTD) mesh generation technique is presented. There are two innovations in the implementation of this technique. One is adaptive mesh lines placement method. The mesh lines are automatically set to be dense where the object has fine structure and sparse where the object has rough structure based on the incremental placement of the triangular mesh vertices. The other is ray column tracing method. Ray columns in the normal direction of the coordinate plane are employed to intersect the surface facets to make the mesh generation results highly accurate. The generating FDTD results of the numerical examples show that the proposed technique can well-restore objects with complex edge structures. The simulation results are in good agreement with the theoretical results.

Index Terms – Adaptive, FDTD, mesh generation, ray column tracing.

I. INTRODUCTION

The finite-difference time-domain (FDTD) algorithm is implemented by calculating the electric and magnetic fields on each Yee cell [1-3]. The Yee cells, whose sizes and related material parameters are simultaneously employed in the iterative formulas of the FDTD algorithm, must be established before FDTD simulation. Unlike unstructured meshes [4, 5], which can be easily obtained by computer-aided design (CAD) or some open source programs, there are relatively few ways to obtain the structured cuboid meshes. Therefore, the transformation from unstructured meshes to structured meshes has attracted much attention [6-13].

Since the ray tracing method (RTM) was proposed by Sun in 1993 [6], it has been widely used in mesh generation for FDTD simulation. The RTMs proposed before mainly casted single ray to intersect the surface facets for each two-dimensional (2D) grid on the projection plane. This kind of processing may lead to missing mapping at the edge of the target. In practice, edge structure of a target may have a great influence on its overall electromagnetic performance [14-16]. For example, slot design at the edge of patch antennas can not only realize miniaturization but also reduce antenna radar cross section (RCS). In addition, the biologically inspired antennas usually have complex edge structures. Therefore, the precision of edge mesh conversion needs to be considered.

For complex objects, if a uniform mesh generation method (UMGM) is employed, there will be a problem of large number of mesh cells, compared with employing a non-uniform mesh generation method (NUMGM). The increase in the number of mesh cells caused by using the UMGM than the NUMGM then can result in problems such as high memory consumption and long simulation time. Therefore, in contrast to the UMGM, the NUMGM is more suitable for complex objects mesh generation. A key step in NUMGM is to place proper mesh lines [[12], 17-20]. In reference [12], a non-uniform mesh lines placement method is presented for multi-object scenarios. An NUMGM for overlapping objects was proposed by Kanai in reference [17]. The NUMGMs proposed before were implemented based on the condition that the bounding box of each object was known. In other words, they solved a complex problem by breaking it down into a group of individual objects. The non-uniform mesh lines were placed by setting reasonable grid sizes in the overlapping part and the adjacent part of the objects. However, in the field of electromagnetism, some electromagnetic devices, such as multi-frequency antenna, broad band frequency selective surface (FSS), are too complex to be easily and quickly separated into several independent objects. Therefore,

Submitted On: October 14, 2021
Accepted On: February 14, 2022

https://doi.org/10.13052/2022.ACES.J.370101

an adaptive mesh lines placement method based on the incremental placement of the triangular mesh vertices is proposed in this paper. Obviously, the choice of triangulation in the preparation of the triangulated mesh is critical to the performance of the proposed NUMGM. We choose Altair FEKO v2019.1 [21] to get the triangular meshes. Since FEKO is a mature commercial electromagnetic simulation software and has been globally used in high-frequency electromagnetic simulation for over 20 years, the triangular mesh generation results of it are reliable.

In this paper, an adaptive FDTD mesh generation technique is proposed. This technique presents high accuracy in FDTD mesh generation, especially at the edge part of the target. Two key methods are employed to achieve this capability. One is ray column tracing method (RCTM), and the other is adaptive mesh lines placement method. Numerical examples are given and discretized. The simulation and theoretical results show that the proposed mesh generation technique can properly restore the target with fine structure, especially at the edge part.

II. RAY COLUMN TRACING METHOD

For RTM, generally, a single ray perpendicular to a grid on the coordinate plane is employed to intersect the plane where the triangular facet is located [6]. The triangular facets mentioned in this section are obtained by .STL files exported from CAD software. The specific operation is to build a model in CAD and save it as. STL format. As shown in Figure 1, the shaded part without slash lines are the Yee cells transformed by RTM, while the shaded part with slash lines are the Yee cells of missing marks.

In this paper, RCTM is proposed. For each grid on the coordinate plane, multiple rays in the normal direction are selected to intersect the facets in one tracing process. Taking one triangular facet as an example, the RCTM is described in detail as follows.

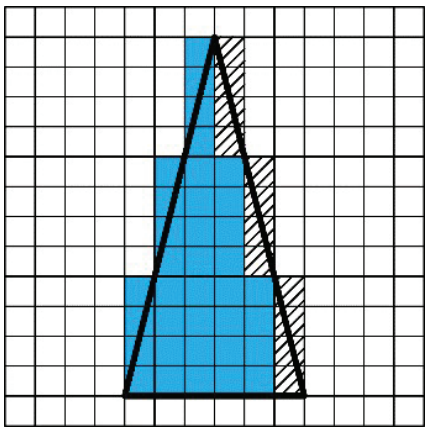

Fig. 1. The transformed Yee cells of the 2D triangle by RTM.

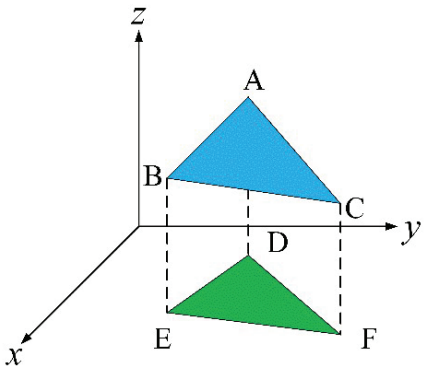

Fig. 2. Triangular facet *ABC* and its projection *DEF*.

First, project the triangular facet *ABC*. onto *XOY* plane and denote its projection as *DEF*, as shown in Figure 2.

Second, find out the maximum and minimum values of triangle *DEF* in the x-direction and confirm the starting and ending mesh numbers in the x-direction accordingly. Denote the starting number as x_s and the ending number as x_e. Taking the grids numbered i in the x-direction as examples, calculate the intersection points of their two adjacent grid lines and the three sides of triangle *DEF*. Determine the maximum and minimum y values of these intersection points and mark the grids between them as shown in Figure 3(a). In this way, the triangle *DEF* is discretized as shown in Figure 3(b).

Third, for the grids inside triangle *DEF*, obtain the intersections of the rays perpendicular to the four nodes of each grid and triangle *ABC*, respectively. For the grids at the edge of triangle *DEF*, figure out the intersection points of their adjacent grid lines and the three sides of triangle *DEF* first and then obtain the intersections of the rays perpendicular to these points and triangle *ABC* severally. The three-dimensional (3D) RCTM is shown in Figure 4.

Take a hexagonal star ring as an example to illustrate the validity of the proposed RCTM in edge mesh generation. The hexagonal star ring is shown in Figure 5(a), and its triangulation is shown in Figure 5(b).

Figures 6 and 7 show the resulting Yee cells of the hexagonal star ring obtained by RTM and RCTM, respectively. The mesh size in Figure 6 is 5 mm, and the mesh size in Figure 7 is 2 mm.

It can be seen from Figure 6 that, when the mesh size is 5 mm, there are obvious missing marks in the discretization result obtained by RTM. Although the Yee cells transformed by RCTM are not completely

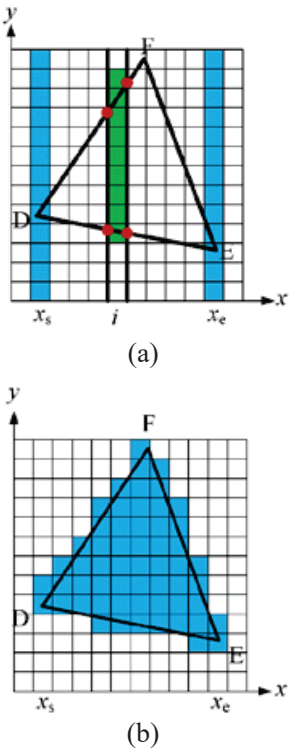

Fig. 3. 2D ray column tracing method. (a) The discretization result of grids numbered i in the x-direction and (b) the discretization result of the triangle *DEF*.

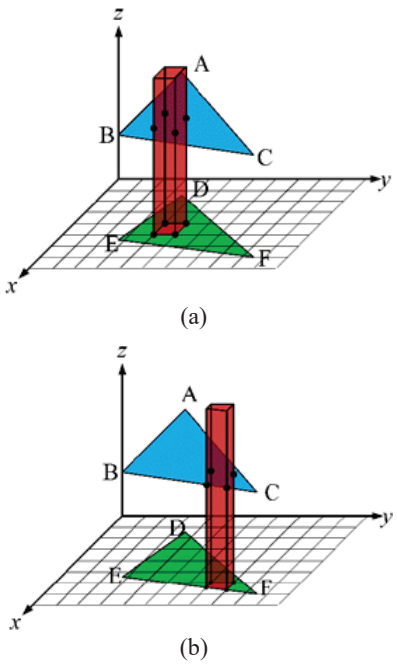

Fig. 4. 3D ray column tracing method: (a) grids inside *DEF* and (b) grids at the edge of *DEF*.

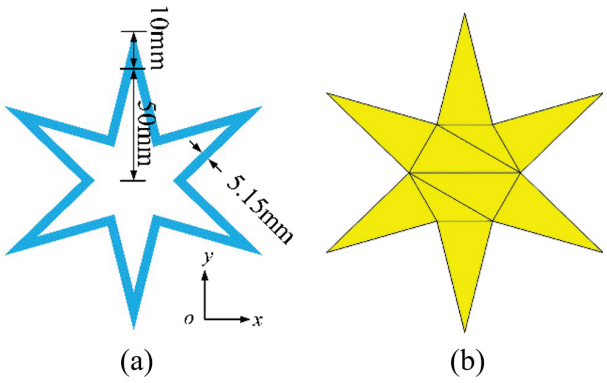

Fig. 5. The structure and triangulation of the hexagonal star ring: (a) the structure and (b) the triangulation.

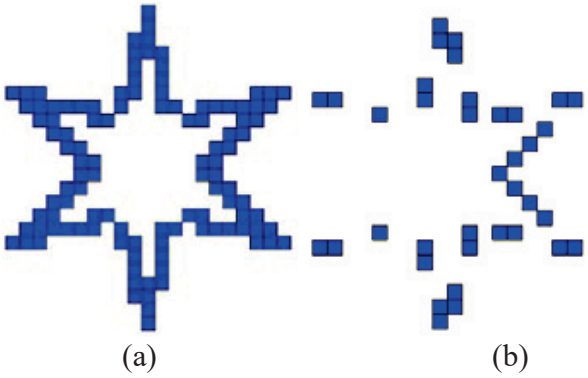

Fig. 6. The discretization results of the hexagonal star ring when the grid size is 5 mm: (a) by RCTM and (b) by RTM.

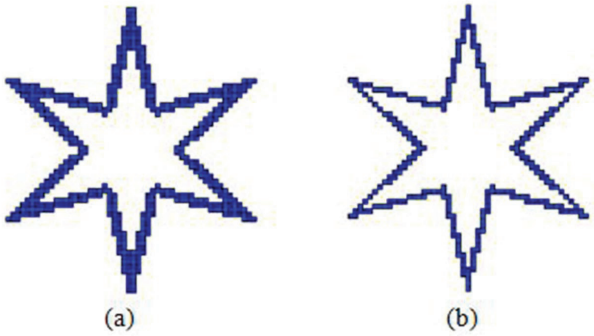

Fig. 7. The discretization results of the hexagonal star ring when the grid size is 2 mm: (a) by RCTM and (b) by RTM.

appropriate to the original structure, the accuracy of RCTM is obviously improved compared with that of RTM. When the mesh size is 2 mm, as shown in Figure 7, both RCTM and RTM perform better. However, the

transformation result of RCTM is closer to the original shape and size of the target than that of RTM.

III. ADAPTIVE MESH LINES PLACEMENT METHOD

In the process of structured cuboid mesh generation, the first step is to create efficient structured mesh lines, which must satisfy the numerical dispersion requirement of the FDTD method and can be adapted to geometric models. These mesh lines can provide spatial coordinate information for subsequent material mapping. Taking an object with fine structure into account, if it is discretized by uniform mesh, there will be a problem of huge mesh quantity. This problem can be solved by using non-uniform meshes. In this paper, an adaptive mesh lines placement method is proposed, which can set mesh lines automatically according to the mechanical structure and the electromagnetic characteristics of the target.

In the implementation of the adaptive mesh lines placement method, the object is modeled and meshed by FEKO software. The mesh generation results are saved as .STL file. Since FEKO is a powerful 3D full wave electromagnetic simulation software, we can use its triangulation results as the basis of the NUMGM proposed in this paper. The adaptive mesh lines placement method is illustrated as follows.

(1) Determine the minimum wavelength, denoted as $\lambda_{\min}$, in terms of frequency and material property. Constrained by the typical rule of FDTD spatial discretization, the maximum mesh size, $d_{\max}$, of the entire computing space should satisfy $d_{\max} =\leq \lambda_{\min}/10$.

(2) Calculate the side lengths of each triangular facet and find out the minimum side length $l_{\min}$. Set the minimum interval of the entire computing space to be $d_{\min} = l_{\min}/2$.

(3) Project each triangular facet onto three principal coordinate planes, respectively. Find out the maximum and minimum coordinates along three axes and calculate the differences between them severally, as shown in Figure 8. Denote these differences as $\Delta x, \Delta y$, and Δz.

(4) Sort all the $\Delta x, \Delta y$, and Δz from the smallest one to largest one and insert the starting and ending coordinates of them on the corresponding axes, respectively. Let us take the x-axis treatment as an example. If Δx is equal to zero, this means that the triangular facet is perpendicular to the XOZ plane. At this point, the Δx needs to be adjusted to a suitable value to represent the thickness of the vertical plane. If Δx is greater than zero and less than $d_{\min}$, change the value of Δx to $d_{\min}$ to ensure that the minimum mesh size of the entire space is $d_{\min}$. Take a cylinder as an example to explain how we decide where to put the mesh lines when Δx is less than $d_{\min}$. The cylinder and its triangulation are shown in Figure 9. When we project the triangular facets onto the XOY plane, we will find that the intervals determined by the vertices of the triangular facets are smaller than $d_{\min}$. At this point, we should change Δx to $d_{\min}$.

(5) Finally, for the intervals greater than $d_{\max}$ on the coordinate axes, divide them equally with the value of d. Taking an internal whose length is L as an example, let the integer $N = \text{ceil}(L/d_{\max})$, then $d = L/N$.

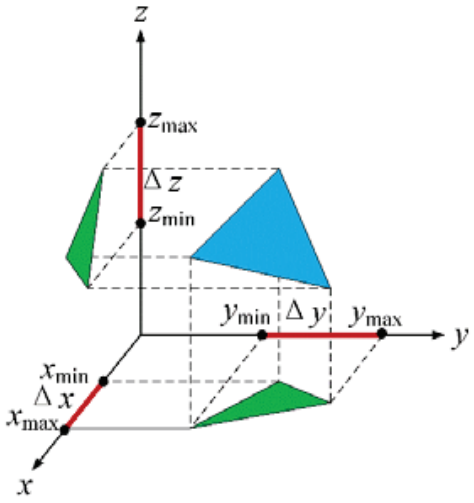

Fig. 8. The projections of the facet on three coordinate planes.

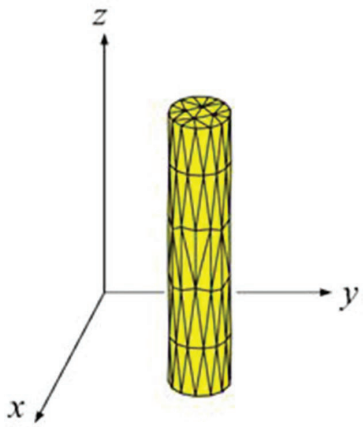

Fig. 9. The cylinder and its triangulation.

Figures 10(a) and (b) show the overall and local structures of a parabolic antenna. The parabolic antenna

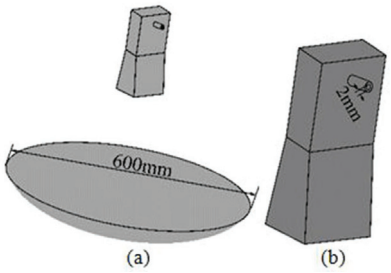

Fig. 10. The structure of the parabolic antenna: (a) the overall structure and (b) the structure of the horn antenna.

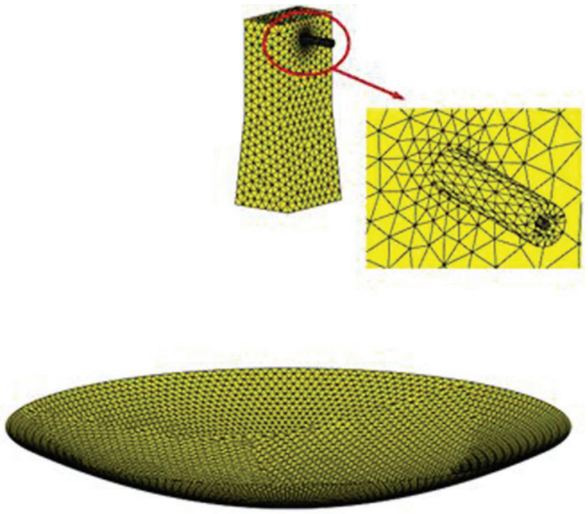

Fig. 11. The triangulation of the parabolic antenna.

is fed by a horn antenna and it works at the center frequency of 2.45 GHz. As shown in Figures 10(a) and (b), the maximum size of the antenna is the diameter of the parabola, which is 600 mm, and the minimum size of the antenna is the diameter of the coaxial probe inner conductor, which is 2 mm. The ratio of the maximum size to the minimum size is 300.

Figure 11 shows the triangulation of the parabolic antenna obtained from FEKO 2019.1. FEKO software has its own mesh function. When we build a model in FEKO and set it to the working frequency, the software will automatically generate the appropriate triangular meshes.

Table 1: The total mesh numbers of the parabolic antenna generated by UMGM and NUMGM

	UMGM	NUMGM
Mesh number	529205	102776

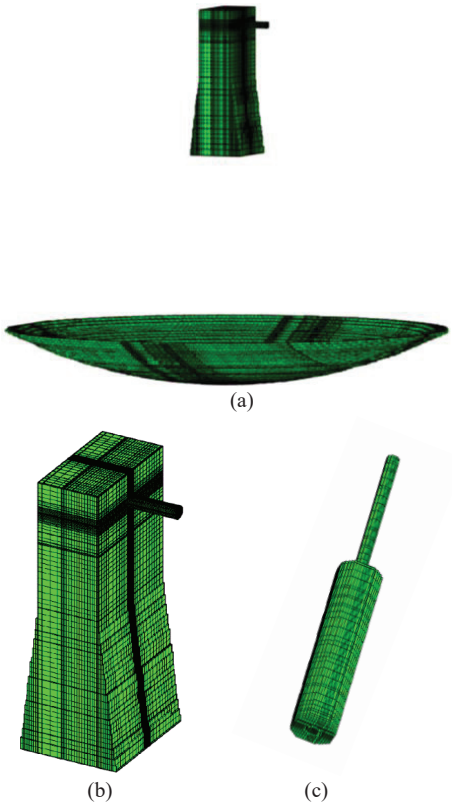

Fig. 12. The discretization results of the parabolic antenna: (a) the overall discretization result, (b) the discretization result of the horn antenna, and (c) the discretization result of the coaxial probe.

Figure 12 shows the discretization results of the parabolic antenna, the horn antenna, and the coaxial probe. The maximum mesh size is 6.1 mm, and the minimum mesh size is 0.5 mm. It can be seen from Figure 12 that the adaptive mesh lines placement method proposed in this paper can set dense meshes in the fine part and sparse meshes in the other part. The discretization results are in good agreement with the antenna model.

Table 1 shows the total mesh numbers of the parabolic antenna obtained by UMGM and NUMGM. The mesh size of the UMGM is 0.5 mm. The maximum and minimum mesh sizes of the NUMGM are 6.1 and 0.5 mm. We can see from Table 1 that the number of mesh cells of the target using NUMGM is about 1/5 of that using UMGM.

IV. NUMERICAL EXAMPLES AND SIMULATION RESULTS

Numerical examples are given to illustrate the efficiency of the adaptive mesh generation technique proposed in this paper. The first example is a metal sphere, and the second example is a band-stop FSS. The

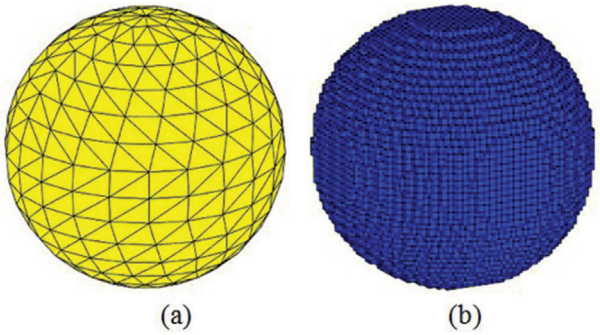

Fig. 13. The structure and Yee cells of the sphere: (a) the structure and triangulation of the sphere and (b) the Yee cells distribution of the sphere.

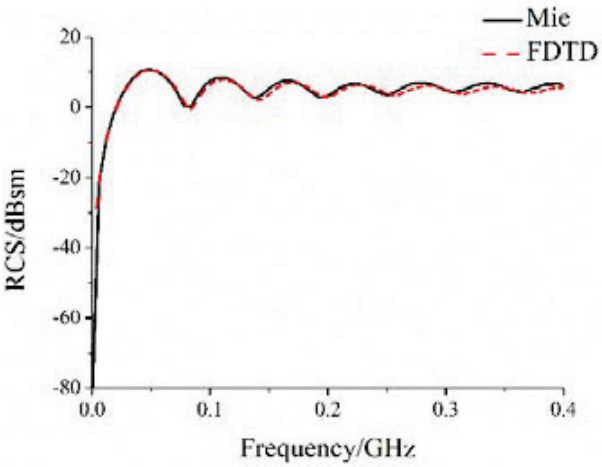

Fig. 14. The RCS of the metal sphere.

structures and the generating FDTD grids of the numerical examples are represented, respectively. We also give some simulation results of the numerical examples by performing the novel mesh generation technique.

A. Metal sphere

Figure 13 shows the structure and the resulting FDTD meshes of a metal sphere. The radius of the sphere is 1 m, and the mesh size is 0.025 m. The RCS of the metal sphere simulated by the FDTD method is shown in Figure 14. As comparison, we also give the Mie series result of the sphere's RCS [22]. It can be seen from Figure 14 that the simulated result is in good agreement with the theoretical result.

B. Band-stop FSS

A band-stop FSS is shown in Figure 15(a), and its triangulation is shown in Figure 15(b). In order to realize the miniaturization and broad band-stop characteristics, a relatively complex structure was employed in the

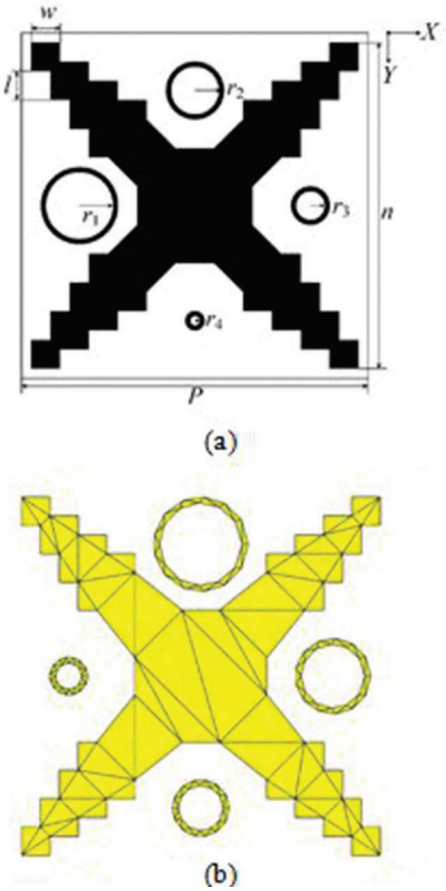

Fig. 15. The structure and triangulation of the FSS. (a) The structure. (b) The triangulation.

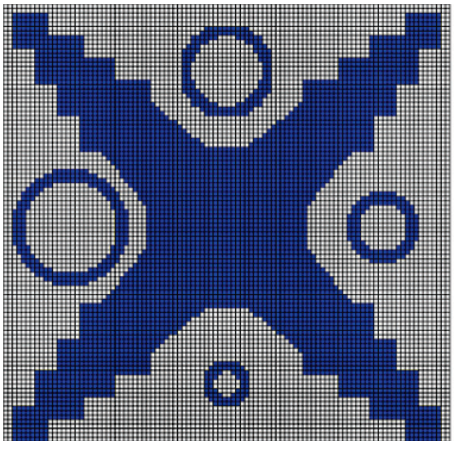

Fig. 16. The discretization result of the FSS.

design of this FSS, especially in the design of the edge part.

As shown in Figure 15(a), the parameters of the patch is $n = 19$ mm, $w = 1.5$ mm, and $l = 1$ mm.

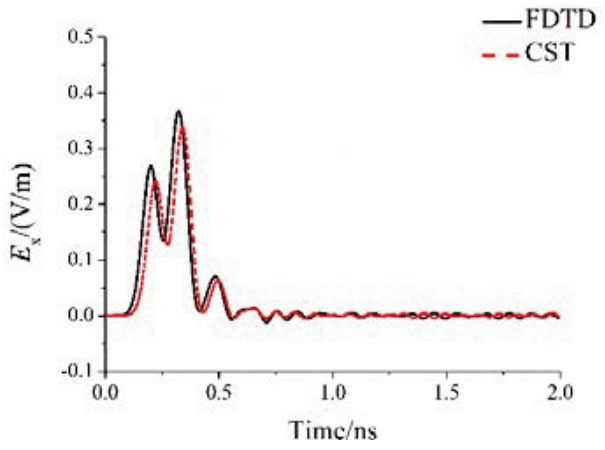

Fig. 17. The E_x of the point which is 1-mm backward of the FSS.

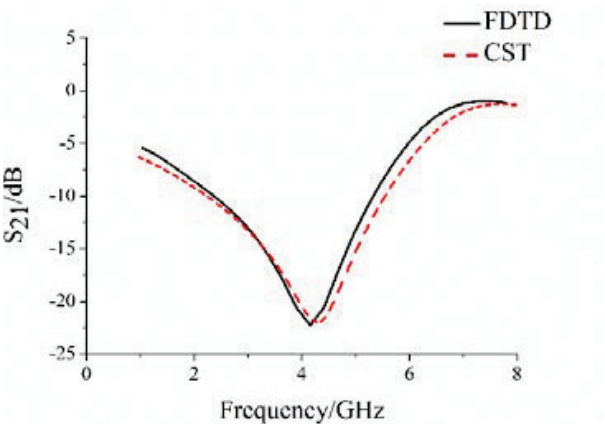

Fig. 18. The S_{21} of the FSS obtained by FDTD method and CST Studio Suite simulation.

The radii of the four rings are $r_1 = 2.5$ mm, $r_2 = 2$ mm, $r_3 = 1.5$ mm, and $r_4 = 1$ mm, respectively. The width of each ring is 0.2 mm. The length of the substrate is $P = 20$ mm and the thickness of the substrate is $h = 3.2$ mm.

The FDTD meshes of the band-stop FSS generated by RCTM are shown in Figure 16. The mesh size is 0.2 mm. It can be seen from Figure 16 that the FSS is well-restored in the FDTD grid.

The transient E_x values at a point which is 1 mm backward of the FSS is shown in Figure 17. We can see that the FDTD result is in good agreement with the result obtained by CST Studio Suite 2020 [23]. CST Studio Suite is a high-performance 3D EM analysis software package for designing, analyzing, and optimizing electromagnetic components and systems.

Figure 18 shows the S_{21} curves of the FSS obtained by FDTD method and CST Studio Suite, respectively. The calculated S_{21} shows reasonable agreement with the CST Studio Suite one, which represents that the mesh generation technique proposed in this paper has the ability to deal with the target with complex edge structure.

V. CONCLUSION

Based on the triangular facets obtained by the .STL file of the object, an adaptive mesh generation technique is proposed for 3D FDTD simulation in this paper. First, RCTM is introduced. As opposed to RTM, for each grid on the coordinate plane, the RCTM employs multiple rays in the normal direction to intersect the triangular facets. The implementation of RCTM makes the mesh generation technique have high accuracy in edge structure mesh transformation. Second, according to the vertex coordinates of the triangular facets, adaptive mesh lines placement method is illustrated. For an object with fine structure, the mesh lines placement method can automatically set dense meshes in fine structure and sparse meshes in rough structure. A metal sphere and a band-stop FSS are given as numerical examples. Simulated and theoretical results show that the proposed mesh generation technique is flexible and accurate.

ACKNOWLEDGMENT

This work was supported by the National Key Research and Development Program of China under Grant 2020YFA0709800, by the Technology Program of Shenzhen under Grant JCYJ20180508 152233431, and by the National Natural Science Foundations of China under Grant 61971340.

REFERENCES

[1] K. S. Yee, "Numerical solution of initial boundary value problems involving Maxwell's equations in isotropic media," *IEEE Trans. Antennas Propagat.*, vol. AP-14, pp. 302–307, 1966.

[2] A. Taflove and S. C. Hagness, Computational Electrodynamics: The Finite-Difference Time-Domain Method, Artech House, Boston, MA, 2005.

[3] A. G. Taflove, A. Oskooi, and S. G. Johnson, Advances in FDTD Computational Electrodynamics: Photonics and Nanotechnology, Artech House, Boston, MA, 2013.

[4] P. Li, J. J. Li, M. Tang, Y. J. Zhang, S. Xu, and H. Bagci, "A novel subdomain 2D/Q-2D finite element method for power/ground plate-pair analysis," *IEEE Trans. Electromagnetic Compatibility*, vol. 62, no. 5, pp. 2217–2226, Oct. 2020.

[5] P. Li, J. J. Li, Y. J. Zhang, S. Xu, and H. Bagci, "An efficient mode based domain decomposition hybrid 2D/Q-2D finite-element time-domain method for power/ground plate-pair analysis," *IEEE Trans. Microwave Theory and Techniques*, vol. 66, no. 10, pp. 4357–4366, Oct. 2018.

[6] W. Sun, C. A. Balanis, M. P. Purchine, and G. Barber, "Three dimensional automatic FDTD mesh generation on a PC," Proceedings of IEEE Antennas and Propagation Society International Symposium, Ann Arbor, MI, pp. 30–33, 1993.

[7] Y. Srisukh, J. Nehrbass, F. L. Teixeira, J. F. Lee, and R. Lee, "An approach for automatic grid generation in three-dimensional FDTD simulations of complex geometries," *IEEE Antennas Propag. Mag.*, vol. 44, no. 4, pp. 75–80, Aug. 2002.

[8] J. T. MacGillivray, "Trillion cell CAD-based cartesian mesh generator for the finite-difference time-domain method on a single-processor 4-GB workstation," *IEEE Trans. Antennas Propagat.*, vol. 56, no. 8, pp. 2187–2190, Aug. 2008.

[9] T. Ishida, S. Takahashi, and K. Nakahashi, "Efficient and robust cartesian mesh generation for building-cube method," *Journal of Computational Science and Technology*, vol. 2, no. 4, pp. 435-446, 2008.

[10] G. Waldschmidt, A. Taflove, "Three-dimensional CAD-based mesh generator for the Dey-Mittra conformal FDTD algorithm," *IEEE Trans. Antennas Propagat.*, vol. 52, no. 7, pp. 1658–1664, July 2004.

[11] L. X. Yang, D. B. Ge, J. Bai, and S. T. Zhang, "A novel FDTD modeling technique based on triangle mesh-units of an object," *Journal of Xidian University*, vol. 34, no. 2, pp. 298–302, Apr. 2007.

[12] M. K. Berens, I. D. Flintoft, and J. F. Dawson, "Structured mesh generation: Open-source automatic nonuniform mesh generation for FDTD simulation," *IEEE Antennas and Propagation Magazine*, vol. 58, iss. 3, pp. 45–55, June 2016.

[13] X. C. Bo, X. B. Jin, J. F. Zhang, and T. J. Cui, "Study of corner singularity in conformal structured mesh generation for the finite-difference time-domain method based on ray tracing," *IEEE Transactions on Microwave Theory and Techniques*, vol. 67, no. 1, pp. 57–69, Jan. 2019.

[14] W. Jiang, Y. Liu, S.-X. Gong, and T. Hong, "Application of bionics in antenna radar cross section reduction," *IEEE Antennas and Wireless Propagation Letters*, vol. 8, pp. 275–1278, 2009.

[15] B. Biswas, R. Ghatak, and D. R. Poddar, "A fern fractal leaf inspired wideband antipodal vivaldi antenna for microwave imaging system," *IEEE Trans. Antennas Propagat.*, vol. 65, no. 11, pp. 6126–6129, Nov. 2017.

[16] G. N. Zhou, B. H. Sun, and Q. Y. Liang, "Triband dual-polarized shared-aperture antenna for 2G/3G/4G/5G base station applications," *IEEE Trans. Antennas Propagat.*, vol. 69, no. 1, pp. 97–108, Jan. 2021.

[17] Y. Kanai and K. Sato, "Automatic mesh generation for 3D electromagnetic field analysis by FDTD method," *IEEE Trans. Magn.*, vol. 34, no. 5, pp. 3383–3386, Sept. 1998.

[18] M. W. Yang, and Y. C. Chen, "AutoMesh: an automatically adjustable, non-uniform, orthogonal FDTD mesh generator," *IEEE Antennas and Propagation Magazine*, vol. 41, no. 2, pp. 13–19, April 1999.

[19] H. S. Kim, I. S. Ihm, and K. Choi, "Generation of non-uniform meshes for finite-difference time-domain simulations," *Journal of Electrical Engineering and Technology*, vol. 6, no. 1, pp. 128–132, Jan. 2011.

[20] H. A. Fernanades, "Development of software for antenna analysis and design using FDTD," M.S. dissertation, Instituto Superior Técnico, University of Lisbon, LIS, Portugal, 2007.

[21] Altair Feko. (2019). [Online]. Available: https://www.altair.com/feko.

[22] J. M. Jin, Theory and Computation of Electromagnetic Fields, John Wiley & Sons Inc., Hoboken, NJ, 2010.

[23] CST STUDIO SUITE. (2020). [Online]. Available: https://www.3ds.com/products-services/simulia/products/cst-studio-suite/.

[24] Javier Moreno, María J. Algar, Iván González, and Felipe Cátedra, "Design and evaluation of the multilevel mesh generation mode for computational electromagnetics," *Applied Computational Electromagnetic Society (ACES) Journal*, vol. 30, no. 6, pp. 578–588, June 2015.

[25] M. Bai, B. Liang, and H. Ma, "An efficient FDTD algorithm to analyze skewed periodic structures impinged by obliquely incident wave," *Applied Computational Electromagnetic Society (ACES) Journal*, vol. 30, no. 10, pp. 1068–1073, Oct. 2015.

Chunhui Mou was born in Yantai, China, in 1988. She received the B.S. and M.S. degrees in electromagnetics from Xidian University, Xi'an, China, in 2012 and 2015, respectively. She is currently working toward the Ph.D. degree with Xi'an Jiaotong University, Xi'an, China. Her research interests include the fast FDTD method, multi-physical field calculation, and FDTD mesh generation method.

Juan Chen was born in Chongqing, China, in 1981. She received the Ph.D. degree in electromagnetic field and microwave techniques from Xi'an Jiaotong University, Xi'an, China, in 2008. From April 2016 to March 2017, she was a Visiting Researcher with the Department of Electrical and Computer Engineering, Duke University, Durham, NC, USA, under the financial support from the China Scholarship Council. She currently serves as a Professor with Xi'an Jiaotong University. Her research interests include the numerical electromagnetic methods, advanced antenna designs, and graphene theory and application.

Newton-ADE-FDTD Method for Oblique Incident Magnetized Time-varying Plasma

Hui Liu[1,2], Li-Xia Yang*[1,2], Wei Chen[1], and Yong Bo[1]

[1]School of Electronic Information Engineering Anhui University, Hefei 230601, China

[2]Anhui Province Key Laboratory of Target Recognition and Feature Extraction, Lu'an 237000, China
(Corresponding author: lixiayang@yeah.net)

***Abstract* –** In this paper, the Newtonian equation of motion describing the movement of electrons when electromagnetic waves propagate in a magnetized plasma is combined with the traditional auxiliary differential equation finite difference time domain (ADE-FDTD) method. The FDTD iterative formulas of transverse magnetic (TM) wave and transverse electric (TE) wave of the electromagnetic wave obliquely incident on the magnetized time-varying plasma plate are derived. The biggest difference between this method and the ordinary ADE-FDTD algorithm is the addition of the logarithmic derivative of the time-varying plasma electron density to calculate the current density, which is called the Newton-ADE-FDTD method. Through Example 1, the reflection coefficient of electromagnetic wave incident on the magnetization time-varying plasma plate was calculated, and the correctness of the improved algorithm was verified. At the same time, the Newton-ADE-FDTD algorithm is used to calculate the reflection coefficient of electromagnetic waves incident on the magnetized plasma-dielectric photonic crystal. The results show that different incident angles have a greater impact on the reflection coefficients of left-handed circularly polarized wave (LCP) and right-handed circularly polarized wave (RCP).

***Keywords* –** Magnetized plasma, finite difference time domain (FDTD), electromagnetic wave, oblique incidence.

I. INTRODUCTION

The finite difference time domain (FDTD) [1–3] plays an important role in computational electromagnetics. FDTD can be used for modeling dispersive media, such as soil modeling in ground penetrating radar [4, 5]. At present, many researchers apply FDTD method to deal with the propagation of electromagnetic waves in plasma [6–9]. For example, literature [10] uses FDTD method to deal with the propagation of electromagnetic waves in cold plasma.

When the plasma medium is in a constant magnetic field, it will exhibit electrical anisotropy, which is called magnetized plasma [11–14]. The constant direction of the magnetic field and the phase direction of the electromagnetic wave can be any angle. The theory of magnetic plasma can be used to study the propagation of plane waves of arbitrary polarization in magnetized plasma. In an anisotropic magnetic plasma medium, the polarization state of electromagnetic waves will constantly change. When the phase propagation direction is the direction of the constant magnetic field, two polarized waves will be excited in the magnetic plasma medium, namely the left-handed circularly polarized waves (LCP) and the right-handed circularly polarized waves (RCP).

In recent decades, researchers have proposed a variety of FDTD methods for processing magnetized plasma media. Among them, the current density convolution finite difference time domain (JEC-FDTD) method proposed by Chen in 1998 [15] has been used to deal with complex plasma, dispersion media including magnetized plasma. The auxiliary differential equation finite difference time domain method (ADE-FDTD) [16] directly performs difference iteration by setting the ADE, which improves the calculation efficiency, and its accuracy is the same as that of the JEC-FDTD method. In addition, there are many methods to deal with the electromagnetic problem of plasma dispersion medium, including piecewise linear recursive convolution finite difference time domain (PLRC-FDTD) [17], moving operator finite difference time domain (SO-FDTD) [18–20], Runge-Kutta exponential finite difference time domain (PKETD-FDTD), and so on.

In some cases, the electron density of the time-varying magnetization plasma is not fixed but changes with time. When electromagnetic waves pass through the plasma, the time-varying characteristics of the plasma should be considered. The electron density movement of the electromagnetic wave propagating in the magnetization time-varying plasma can be described by the Newtonian equation of motion. Therefore, in this

Submitted On: October 19, 2021
Accepted On: January 28, 2022

https://doi.org/10.13052/2022.ACES.J.370102

article, when the electromagnetic wave is incident on the magnetized time-varying plasma plate obliquely, the basic Newtonian equation of motion is combined with the ADE-FDTD algorithm to derive the Newton-ADE-FDTD iterative formula for transverse electric (TE) wave and transverse magnetic (TM) wave. The reflection coefficients of TE wave and TM wave were calculated, respectively, and compared with the analytical solution and the traditional ADE-FDTD algorithm, which verified the effectiveness of the algorithm. At the same time, the reflection coefficients of electromagnetic waves at 0°, 30°, 45°, and 60° incident on the magnetized plasma dielectric photonic crystal are calculated.

II. METHOD

Newton's equation of motion describing electron motion when electromagnetic wave propagates in magnetized plasma can be expressed as

$$me\frac{d\mathbf{u}_e}{dt} = -e\mathbf{E} - mev\mathbf{u}_e + e\mathbf{u}_e \times \mathbf{B}, \tag{1}$$

where $\mathbf{u}_e$ is electron velocity, e is electron charge, $\mathbf{E}$ is electric field intensity, me is electron mass, v is plasma collision frequency, and $\mathbf{B}$ is magnetic induction intensity.

The electron density of plasma sometimes exhibits time-varying properties. Current density $\mathbf{J}$ in magnetized time-varying plasma can be expressed as

$$\mathbf{J} = -eNe(t)\mathbf{u}_e, \tag{2}$$

where $Ne(t)$ is the time-varying plasma electron density. According to Equation (2), $\mathbf{u}_e$ can be expressed as

$$\mathbf{u}_e = -\frac{\mathbf{J}}{eNe(t)}. \tag{3}$$

The electron cyclotron frequency of magnetized plasma is

$$\omega_b = \frac{e\mathbf{B}}{me}. \tag{4}$$

Magnetic induction intensity can be expressed as

$$\mathbf{B} = \frac{\omega_b me}{e}. \tag{5}$$

Substitute Equation (3) and (5) into Equation (1); then

$$-me\frac{d\left(\frac{\mathbf{J}}{eNe(t)}\right)}{dt} = -e\mathbf{E} + \frac{mev\mathbf{J}}{eNe(t)} - \frac{\mathbf{J}}{Ne(t)} \times \frac{\omega_b me}{e}. \tag{6}$$

The updating equation of current density is obtained by sorting out Equation (6)

$$\frac{\partial \mathbf{J}}{\partial t} = \left(\frac{1}{Ne(t)}\frac{\partial Ne(t)}{\partial t} - v\right)\mathbf{J} + \varepsilon_0\omega_p^2(t)\mathbf{E} + \omega_b \times \mathbf{J}. \tag{7}$$

Definition $L(t)$ is the derivative of plasma electron density, namely

$$L(t) = \ln(Ne(t)). \tag{8}$$

$$\frac{1}{Ne(t)}\frac{\partial Ne(t)}{\partial t} = \frac{\partial \ln(Ne(t))}{\partial t} = \frac{L^{n+1} - L^n}{\Delta t}. \tag{9}$$

Combined with Equation (9), the updating Equation (7) of current density can be written as

$$\frac{\partial \mathbf{J}}{\partial t} = \left(\frac{L^{n+1} - L^n}{\Delta t} - v\right)\mathbf{J} + \varepsilon_0\omega_p^2(t)\mathbf{E} + \omega_b \times \mathbf{J}, \tag{10}$$

where ε_0 is the vacuum permittivity, and $\omega_p(t)$ is the time-varying plasma frequency, which can be expressed as

$$\omega_p(t) = \sqrt{\frac{e^2 Ne(t)}{\varepsilon_0 me}}. \tag{11}$$

It can be seen from Equation (10) that after combining Newton's motion equation, the derivative of logarithm of electron density of time-varying plasma is added in the calculation of current density. The equation is applied to ADE-FDTD algorithm of electromagnetic wave incident on magnetized time-varying plasma plate below, and the Newton-ADE-FDTD iterative formula can be obtained.

A. Newton-ADE-FDTD iteration of TE wave

When the incident wave is TE wave, it is known from literature [21] that the one-dimensional Maxwell correction equation in the magnetized time-varying plasma with oblique incident electromagnetic wave is

$$\frac{\partial \mathbf{E}}{\partial z} = u_0\frac{\partial \mathbf{H}}{\partial t}. \tag{12}$$

$$\frac{\partial \mathbf{E}}{\partial t} = \frac{1}{\varepsilon_0 \cos^2\theta}\left(\frac{\partial \mathbf{H}}{\partial z} - \mathbf{J}\right). \tag{13}$$

$$\frac{d\mathbf{J}}{dt} + v\mathbf{J} = \varepsilon_0\omega_p^2\mathbf{E} + \omega_b \times \mathbf{J}, \tag{14}$$

where $\mathbf{u}_0$ is the permeability in vacuum and θ is the oblique incidence angle of electromagnetic waves,

$$\mathbf{E} = \begin{bmatrix} E_x \\ E_y \end{bmatrix},\ \mathbf{H} = \begin{bmatrix} H_y \\ H_x \end{bmatrix},\ \mathbf{J} = \begin{bmatrix} J_x \\ J_y \end{bmatrix}.$$

Formula (14) is replaced by the iterative formula (10) of current density obtained after simultaneous Newton equations of motion. The governing equation of electromagnetic wave propagation in magnetized time-varying plasma can be expressed as Formulae (10), (12), and (13). ADE-FDTD is used for difference discretization; then

$$\begin{bmatrix} H_y^{n+1/2}\left(k+\frac{1}{2}\right) \\ H_x^{n+1/2}\left(k+\frac{1}{2}\right) \end{bmatrix} = \begin{bmatrix} H_y^{n-1/2}\left(k+\frac{1}{2}\right) \\ H_x^{n-1/2}\left(k+\frac{1}{2}\right) \end{bmatrix} - \frac{\Delta t}{u_0\Delta z} \bullet \begin{bmatrix} E_x^n(k+1) - E_x^n(k) \\ -\left(E_y^n(k+1) - E_y^n(k)\right) \end{bmatrix}. \tag{15}$$

$$J_x^{n+1}(k)=\frac{1}{1-0.5\Delta t\left(\frac{L^{n+1}(k+1/2)-L^n(k+1/2)}{\Delta t}-v\right)}\bullet \left[J_x^n(k)\bullet\left(1+0.5\Delta t\left(\frac{L^{n+1}(k+1/2)}{-L^n(k+1/2)}{\Delta t}-v\right)\right)+\frac{\Delta t e^2}{me}\bullet\left(\frac{Ne^{n+1}(k+1/2)+Ne^n(k+1/2)}{2}\right)\bullet\left(\frac{E_x^{n+1}(k+1/2)+E_x^n(k+1/2)}{2}\right)-\omega_b\Delta t\bullet\left(\frac{J_y^{n+1}(k+1/2)+J_y^n(k+1/2)}{2}\right)\right]. \quad (16)$$

$$J_y^{n+1}(k)=\frac{1}{1-0.5\Delta t\left(\frac{L^{n+1}(k+1/2)-L^n(k+1/2)}{\Delta t}-v\right)}\bullet \left[J_y^n(k)\bullet\left(1+0.5\Delta t\left(\frac{L^{n+1}(k+1/2)}{-L^n(k+1/2)}{\Delta t}-v\right)\right)+\frac{\Delta t e^2}{me}\bullet\left(\frac{Ne^{n+1}(k+1/2)+Ne^n(k+1/2)}{2}\right)\bullet\left(\frac{E_y^{n+1}(k+1/2)+E_y^n(k+1/2)}{2}\right)+\omega_b\Delta t\bullet\left(\frac{J_x^{n+1}(k+1/2)+J_x^n(k+1/2)}{2}\right)\right]. \quad (17)$$

$$E_x^{n+1}(k)=\frac{1}{1+\frac{(\Delta t)^2e^2}{4\varepsilon_0(\cos\theta)^2me}\frac{1}{1-0.5\Delta t(\frac{L^{n+1}\left(k+\frac12\right)-L^n\left(k+\frac12\right)}{\Delta t}-v)}\frac{1}{(\frac{Ne^{n+1}\left(k+\frac12\right)+Ne^n\left(k+\frac12\right)}{2})}\left[\left(1-\frac{(\Delta t)^2e^2}{4\varepsilon_0(\cos\theta)^2me}\bullet\frac{1}{1-0.5\Delta t(\frac{L^{n+1}\left(k+\frac12\right)-L^n\left(k+\frac12\right)}{\Delta t}-v)}(\frac{Ne^{n+1}\left(k+\frac12\right)+Ne^n\left(k+\frac12\right)}{2})\right)\bullet E_x^n(k)+\frac{\Delta t}{\varepsilon_0(\cos\theta)^2}(-\frac{H_y^{n+1/2}\left(k+\frac12\right)-H_y^{n+1/2}\left(k-\frac12\right)}{\Delta z})-\frac{\Delta t}{2\varepsilon_0(\cos\theta)^2}\bullet\frac{1}{1-0.5\Delta t(\frac{L^{n+1}\left(k+\frac12\right)-L^n\left(k+\frac12\right)}{\Delta t}-v)}1+0.5\Delta t\bullet(\frac{L^{n+1}\left(k+\frac12\right)-L^n\left(k+\frac12\right)}{\Delta t}-v)+1\right)$$

$$J_x^n(k)+\frac{\omega_b(\Delta t)^2}{2\varepsilon_0(\cos\theta)^2}\bullet\frac{1}{1-0.5\Delta t(\frac{L^{n+1}\left(k+\frac12\right)-L^n\left(k+\frac12\right)}{\Delta t}-v)}\left(\frac{J_y^{n+1}\left(k+\frac12\right)+J_y^n\left(k+\frac12\right)}{2}\right)\Bigg]. \quad (18)$$

$$E_y^{n+1}(k)=\frac{1}{1+\frac{(\Delta t)^2e^2}{4\varepsilon_0(\cos\theta)^2me}\frac{1}{1-0.5\Delta t(\frac{L^{n+1}\left(k+\frac12\right)-L^n\left(k+\frac12\right)}{\Delta t}-v)}\frac{1}{(\frac{Ne^{n+1}\left(k+\frac12\right)+Ne^n\left(k+\frac12\right)}{2})}\left[\left(1-\frac{(\Delta t)^2e^2}{4\varepsilon_0(\cos\theta)^2me}\bullet\frac{1}{1-0.5\Delta t(\frac{L^{n+1}\left(k+\frac12\right)-L^n\left(k+\frac12\right)}{\Delta t}-v)}(\frac{Ne^{n+1}\left(k+\frac12\right)+Ne^n\left(k+\frac12\right)}{2})\right)\bullet E_y^n(k)-\frac{\Delta t}{\varepsilon_0(\cos\theta)^2}(\frac{H_x^{n+1/2}\left(k+\frac12\right)-H_x^{n+1/2}\left(k-\frac12\right)}{\Delta z})-\frac{\Delta t}{2\varepsilon_0(\cos\theta)^2}\bullet\frac{1}{1-0.5\Delta t(\frac{L^{n+1}\left(k+\frac12\right)-L^n\left(k+\frac12\right)}{\Delta t}-v)}\left(1+0.5\Delta t\bullet(\frac{L^{n+1}\left(k+\frac12\right)-L^n\left(k+\frac12\right)}{\Delta t}-v)+1\right)J_y^n(k)-\frac{\omega_b(\Delta t)^2}{2\varepsilon_0(\cos\theta)^2}\bullet\frac{1}{1-0.5\Delta t(\frac{L^{n+1}\left(k+\frac12\right)-L^n\left(k+\frac12\right)}{\Delta t}-v)}\left(\frac{J_x^{n+1}\left(k+\frac12\right)+J_x^n\left(k+\frac12\right)}{2}\right)\Bigg]. \quad (19)$$

Equation (15)−(19) are FDTD iterative expressions of TE wave of electromagnetic wave incident obscenely to magnetized time-varying plasma plate.

B. Newton-ADE-FDTD iteration of TM wave

When the incident wave is TM wave, it is known from literature [21] that the one-dimensional Maxwell correction equation in the magnetized time-varying plasma with oblique incident electromagnetic wave is

$$\frac{\partial \mathbf{H}}{\partial z}=-\varepsilon_0\varepsilon_{nr}\frac{\partial \mathbf{E}}{\partial t}. \quad (20)$$

$$\frac{\partial \mathbf{E}}{\partial z}=-\left(1-\frac{\sin^2\theta}{\varepsilon_{nr}}\right)u_0\frac{\partial \mathbf{H}}{\partial t}. \quad (21)$$

$$\frac{\partial \mathbf{J}}{\partial t}=-v\mathbf{J}+\varepsilon_0\omega_p^2(t)\mathbf{E}+\omega_b\times\mathbf{J}. \quad (22)$$

Formula (22) is replaced by the iterative formula (10) of current density obtained after the simultaneous Newton equation of motion. Then the one-dimensional Maxwell correction equation in the magnetized time-varying plasma with oblique incident electromagnetic wave can be written as

$$\frac{\partial \mathbf{H}}{\partial z} = -\varepsilon_0 \varepsilon_{nr} \frac{\partial \mathbf{E}}{\partial t}. \tag{23}$$

$$\frac{\partial \mathbf{E}}{\partial z} = -\left(1 - \frac{\sin^2\theta}{\varepsilon_{nr}}\right) u_0 \frac{\partial \mathbf{H}}{\partial t}. \tag{24}$$

$$\frac{\partial \mathbf{J}}{\partial t} = \left(\frac{1}{Ne(t)} \frac{\partial Ne(t)}{\partial t} - v\right)\mathbf{J} + \varepsilon_0 \omega_p^2(t)\mathbf{E} + \omega_b \times \mathbf{J}, \tag{25}$$

where ε_{nr} is the relative permittivity of the n layer, and $\boldsymbol{\sigma}(w)$ is the conductivity

$$\varepsilon_{nr} = 1 + \frac{\boldsymbol{\sigma}(w)}{jw\varepsilon_0}. \tag{26}$$

$$\boldsymbol{\sigma}(w) = \varepsilon_0 \frac{\omega_p^2}{jw + v}. \tag{27}$$

Substitute Equation (26) into Equation (23); then

$$\frac{\partial \mathbf{H}}{\partial z} = -\varepsilon_0 \frac{\partial \mathbf{E}}{\partial t} - \mathbf{J}. \tag{28}$$

Make $\boldsymbol{\xi}$ for

$$\boldsymbol{\xi} = \left(\frac{\varepsilon_{nr} - \sin^2\theta}{\varepsilon_{nr}}\right)\mathbf{H}. \tag{29}$$

Substituting Equation (26) into the above equation, then

$$\frac{\partial \xi}{\partial t} = \cos^2\theta \frac{\partial \mathbf{H}}{\partial t} + \frac{1}{\varepsilon_0}\left[\boldsymbol{\sigma}(t) * \mathbf{H}(t) - \boldsymbol{\sigma}(t) * \boldsymbol{\xi}(t)\right]. \tag{30}$$

At this point, let

$$\boldsymbol{\psi}(t) = \boldsymbol{\sigma}(t) * \mathbf{H}(t). \tag{31}$$

$$\boldsymbol{\chi}(t) = \boldsymbol{\sigma}(t) * \boldsymbol{\xi}(t). \tag{32}$$

Among them, $\mathbf{E} = \begin{bmatrix} E_x \\ E_y \end{bmatrix}$,$\mathbf{H} = \begin{bmatrix} H_y \\ H_x \end{bmatrix}$, $\mathbf{J} = \begin{bmatrix} J_x \\ J_y \end{bmatrix}$, $\boldsymbol{\xi} = \begin{bmatrix} \xi_y \\ \xi_x \end{bmatrix}$.

Meanwhile, the method in [21] is used to process the above formula, and the FDTD discrete formula of the magnetic field part is

$$\begin{bmatrix} \xi_y^{n+1/2}\left(k+\frac{1}{2}\right) \\ \xi_x^{n+1/2}\left(k+\frac{1}{2}\right) \end{bmatrix} = \begin{bmatrix} \xi_y^{n\text{-}1/2}\left(k+\frac{1}{2}\right) \\ \xi_x^{n\text{-}1/2}\left(k+\frac{1}{2}\right) \end{bmatrix} - \\ - \frac{\Delta t}{u_0 \Delta z}\begin{bmatrix} E_x^n(k+1) - E_x^n(k) \\ -\left(E_y^n(k+1) - E_y^n(k)\right) \end{bmatrix}. \tag{33}$$

$$\begin{bmatrix} H_y^{n+1/2}\left(k+\frac{1}{2}\right) \\ H_x^{n+1/2}\left(k+\frac{1}{2}\right) \end{bmatrix} = \begin{bmatrix} H_y^{n\text{-}1/2}\left(k+\frac{1}{2}\right) \\ H_x^{n\text{-}1/2}\left(k+\frac{1}{2}\right) \end{bmatrix} + \frac{1}{\cos^2\theta} \\ \begin{bmatrix} \xi_y^{n+1/2}\left(k+\frac{1}{2}\right) - \xi_y^{n\text{-}1/2}\left(k+\frac{1}{2}\right) \\ \xi_x^{n+1/2}\left(k+\frac{1}{2}\right) - \xi_x^{n\text{-}1/2}\left(k+\frac{1}{2}\right) \end{bmatrix} \\ - \frac{\Delta t \omega_p^2}{\cos^2\theta}\begin{bmatrix} \chi_y^n\left(k+\frac{1}{2}\right) - \psi_y^n\left(k+\frac{1}{2}\right) \\ \chi_x^n\left(k+\frac{1}{2}\right) - \psi_x^n\left(k+\frac{1}{2}\right) \end{bmatrix}. \tag{34}$$

$$\begin{bmatrix} \chi_y^{n+1/2}\left(k+\frac{1}{2}\right) \\ \chi_x^{n+1/2}\left(k+\frac{1}{2}\right) \end{bmatrix} = e^{-v\Delta t}\begin{bmatrix} \cos\omega_b\Delta t & -\sin\omega_b\Delta t \\ \sin\omega_b\Delta t & \cos\omega_b\Delta t \end{bmatrix} \\ \begin{bmatrix} \chi_y^{n\text{-}1/2}\left(k+\frac{1}{2}\right) \\ \chi_x^{n\text{-}1/2}\left(k+\frac{1}{2}\right) \end{bmatrix} + \Delta t e^{-v\Delta t/2} \\ \begin{bmatrix} \cos\frac{\omega_b\Delta t}{2} & -\sin\frac{\omega_b\Delta t}{2} \\ \sin\frac{\omega_b\Delta t}{2} & \cos\frac{\omega_b\Delta t}{2} \end{bmatrix}\begin{bmatrix} \xi_y^{n\text{-}1/2}\left(k+\frac{1}{2}\right) \\ \xi_x^{n\text{-}1/2}\left(k+\frac{1}{2}\right) \end{bmatrix}. \tag{35}$$

$$\begin{bmatrix} \psi_y^{n+1/2}\left(k+\frac{1}{2}\right) \\ \psi_x^{n+1/2}\left(k+\frac{1}{2}\right) \end{bmatrix} = e^{-v\Delta t}\begin{bmatrix} \cos\omega_b\Delta t & -\sin\omega_b\Delta t \\ \sin\omega_b\Delta t & \cos\omega_b\Delta t \end{bmatrix} \\ \begin{bmatrix} \psi_y^{n\text{-}1/2}\left(k+\frac{1}{2}\right) \\ \psi_x^{n\text{-}1/2}\left(k+\frac{1}{2}\right) \end{bmatrix} + \Delta t e^{-v\Delta t/2} \\ \begin{bmatrix} \cos\frac{\omega_b\Delta t}{2} & -\sin\frac{\omega_b\Delta t}{2} \\ \sin\frac{\omega_b\Delta t}{2} & \cos\frac{\omega_b\Delta t}{2} \end{bmatrix}\begin{bmatrix} H_y^{n\text{-}1/2}\left(k+\frac{1}{2}\right) \\ H_x^{n\text{-}1/2}\left(k+\frac{1}{2}\right) \end{bmatrix}. \tag{36}$$

ADE-FDTD method was used to discretize the current density, and the following results were obtained:

ADE-FDTD method was used to discretize the current density, and the following results were obtained:

$$J_x^{n+1}(k) = \frac{1}{1-0.5\Delta t\left(\frac{L^{n+1}(k+1/2)-L^n(k+1/2)}{\Delta t} - v\right)}\left[J_x^n(k) \bullet (1+ \right. \\ 0.5\Delta t\left(\frac{L^{n+1}(k+1/2)-L^n(k+1/2)}{\Delta t} - v\right)\Big) + \frac{\Delta t e^2}{me} \bullet \\ \left(\frac{Ne^{n+1}(k+1/2)+Ne^n(k+1/2)}{2}\right)\left(\frac{E_x^{n+1}(k+1/2)+E_x^n(k+1/2)}{2}\right) \\ \left. - \omega_b\Delta t\left(\frac{J_y^{n+1}(k+1/2)+J_y^n(k+1/2)}{2}\right)\right]. \tag{37}$$

$$J_y^{n+1}(k) = \frac{1}{1-0.5\Delta t\left(\frac{L^{n+1}(k+1/2)-L^n(k+1/2)}{\Delta t} - v\right)}\left[J_y^n(k) \bullet (1+ \right. \\ 0.5\Delta t\left(\frac{L^{n+1}(k+1/2)-L^n(k+1/2)}{\Delta t} - v\right)\Big) + \frac{\Delta t e^2}{me} \bullet \\ \left(\frac{Ne^{n+1}(k+1/2)+Ne^n(k+1/2)}{2}\right)\left(\frac{E_y^{n+1}(k+1/2)+E_y^n(k+1/2)}{2}\right) \\ \left. + \omega_b\Delta t\left(\frac{J_x^{n+1}(k+1/2)+J_x^n(k+1/2)}{2}\right)\right]. \tag{38}$$

$$\begin{bmatrix} E_x^{n+1}(k) \\ E_y^{n+1}(k) \end{bmatrix} = \begin{bmatrix} E_x^n(k) \\ E_y^n(k) \end{bmatrix} - \frac{\Delta t}{\varepsilon_0 \Delta z} \\ \begin{bmatrix} H_y^{n+1/2}\left(k+\frac{1}{2}\right) - H_y^{n+1/2}\left(k-\frac{1}{2}\right) \\ -\left(H_x^{n+1/2}\left(k+\frac{1}{2}\right) - H_x^{n+1/2}\left(k-\frac{1}{2}\right)\right) \end{bmatrix} \\ - \frac{\Delta t}{\varepsilon_0}\begin{bmatrix} J_x^{n+1/2}(k) \\ J_y^{n+1/2}(k) \end{bmatrix}. \tag{39}$$

Equation (33)−(39) are FDTD iterative expressions of TM wave of electromagnetic wave incident diagonally to magnetized time-varying plasma plate.

III. NUMERICAL RESULTS

A. Example 1

In order to verify the correctness of the algorithm in this paper, an improved algorithm is used to calculate the reflection coefficient of TE wave and TM wave incident on the magnetization time-varying plasma layer at a certain angle. The incident angles are 0°, 30°, 45°, and 60°, respectively, and the thickness of magnetized time-varying plasma plate is d =1.5 cm. In this example, the number of spatial grids is 800, the plasma occupies 200 grids, the spatial step dx = 75 $\times$ 10^{-6} m, the time step dt =1.25 $\times$ 10^{-13} s, and the modified Mur absorption boundary is adopted at both ends.

The incident wave adopts Gaussian pulse, and the expression is

$$f(t) = \exp\left(-\frac{4\pi(t-\mathrm{t}_1)^2}{\tau^2}\right) \tag{40}$$

wherein pulsewidth τ is 150 time steps, $t_1 = 0.8 \times \tau$.

Collision frequency of magnetized time-varying plasma v = 20 GHz, plasma electron cyclotron frequency w_b = 100 GHz, and its electron density changes exponentially as follows:

$$Ne(t) = \begin{cases} Ne\mathrm{max} & (t < t_0) \\ Ne\mathrm{max} \times \exp(-\frac{t-t_0}{k}) & (t \geq t_0) \end{cases}. \tag{41}$$

In the above formula, Nemax is the maximum electron density, and the value is 5 $\times$ $10^{18}\mathrm{m}^{-3}$; t_0 is the time when the electron density decreases from the maximum value; k is the variable that controls the rate of change with time. In this example, t_0 = 200 $\times$ dt.

The reflection coefficients of RCP wave and LCP wave of TE wave and TM wave are calculated by using Example 1 and compared with the analytical solution and the traditional ADE-FDTD algorithm, and the correctness of the algorithm is verified.

Figure 1 shows the reflection coefficients of RCP wave when TE waves are incident on the magnetized plasma plate at 0°, 30°, 45°, and 60°. Compare the results obtained by the Newton-ADE-FDTD algorithm with the traditional ADE-FDTD algorithm and analytical solution. It can be seen that the calculation of the reflection coefficient of the RCP wave when the TE wave is obliquely incident on the magnetized plasma plate is consistent with the analytical solution, and the accuracy is basically consistent with the traditional ADE-FDTD algorithm. Verify the correctness of the algorithm.

Figure 2 shows the reflection coefficient of the LCP wave when the TE wave is incident on the magnetized plasma plate at 0°, 30°, 45°, and 60°. It can be seen that the algorithm is consistent with the analytical solution when calculating the reflection coefficient of the LCP wave incident on the magnetized plasma plate, and the accuracy is basically the same as that of the traditional ADE-FDTD algorithm, that is, the correctness of the algorithm is verified. In summary, it can be seen that the Newton-ADE-FDTD algorithm is correct and effective in calculating the reflection coefficient of the varying plasma plate when the magnetization of the obliquely incident TE wave is magnetized.

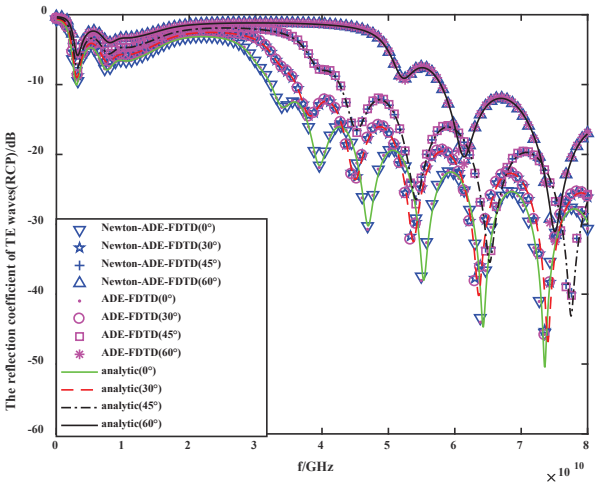

Fig. 1. TE wave reflection coefficient (RCP).

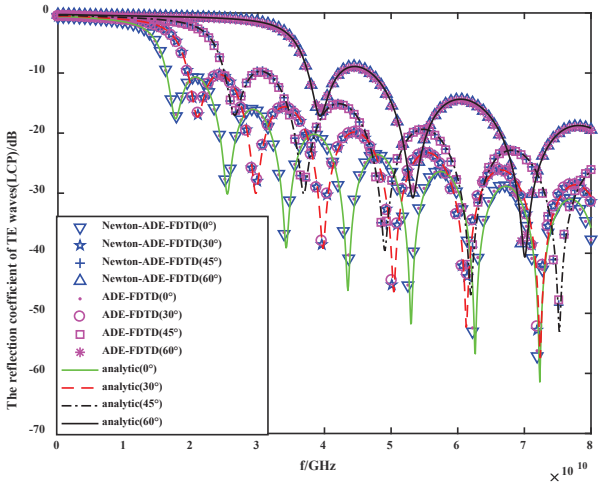

Fig. 2. TE wave reflection coefficient (LCP).

Figure 3 shows the reflection coefficient of the RCP wave when the TM wave is incident on the magnetized plasma plate at 0°, 30°, 45°, and 60°. It can be seen that when the TM wave is obliquely incident on the magnetized plasma plate, the calculation of the reflection coefficient of the RCP wave is consistent with the analytical solution, and the accuracy is basically the same as that of the traditional ADE-FDTD algorithm. Verify the correctness of the algorithm.

Figure 4 shows the reflection coefficient of the LCP wave when the TM wave is incident on the magnetized

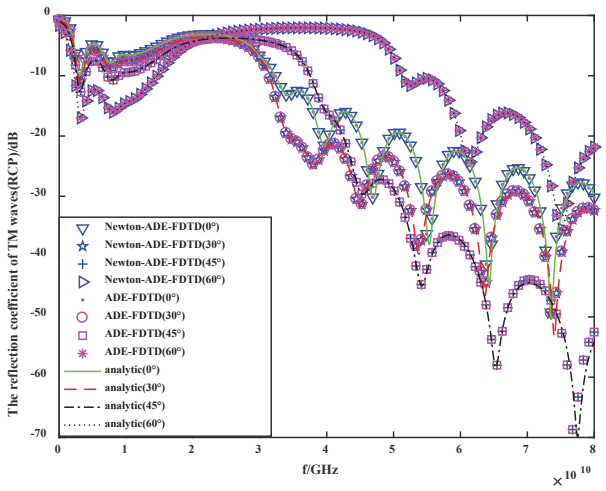

Fig. 3. TM wave reflection coefficient (RCP).

plasma plate at 0°, 30°, 45°, and 60°. It can be seen that the algorithm is consistent with the analytical solution when calculating the reflection coefficient of the LCP wave incident on the magnetized plasma plate, and the accuracy is basically the same as that of the traditional ADE-FDTD algorithm, which verifies the correctness of the algorithm. In summary, it can be seen that the Newton-ADE-FDTD algorithm is correct and effective in calculating the reflection coefficient when the TM wave is incident on the magnetization time-varying plasma plate obliquely.

B. Example 2

The Newton-ADE-FDTD algorithm is used to calculate the electromagnetic wave incident to magnetized plasma-dielectric photonic crystal. The magne-

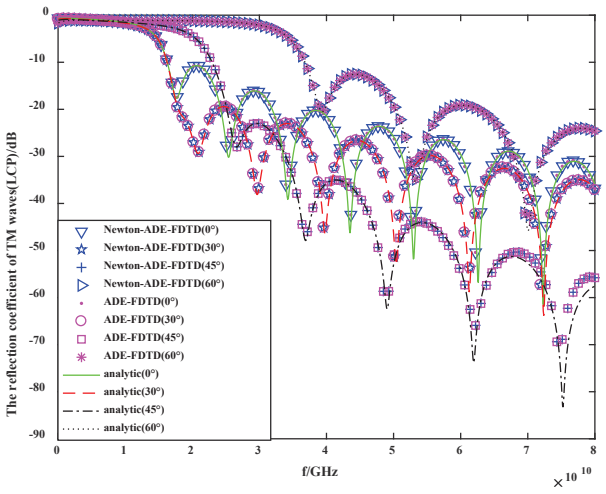

Fig. 4. TM wave reflection coefficient (LCP).

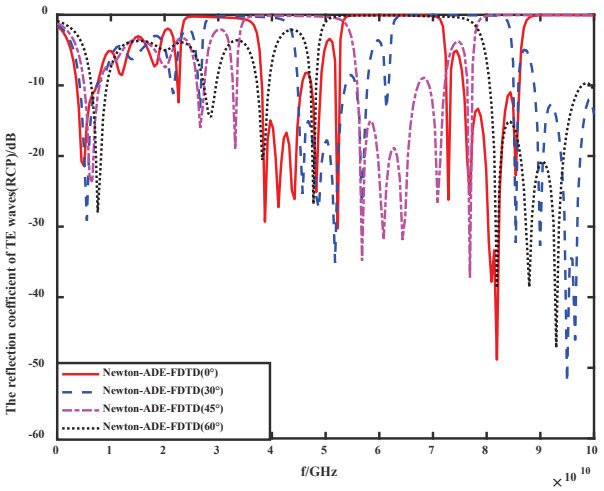

Fig. 5. Reflection coefficient of TE wave in plasma photonic crystal with oblique incident electromagnetic wave (RCP).

tized plasma plate has six layers, the dielectric constant of the dielectric plate is 6, and the number of layers is 5. The magnetized plasma and the dielectric plate are connected alternately to form plasma-dielectric photonic crystals. In this example, the spatial step dx = 75 × 10^{-6} m, the time step dt = 1.25 × 10^{-13} s, and the modified Mur absorption boundary is adopted at both ends. The incident wave parameters are consistent with Example 1, which is a Gaussian pulse, and the expression is shown in Equation (40). Collision frequency of magnetized time-varying plasma $v = 20\,\mathrm{GHz}$, plasma electron cyclotron frequency $\omega_b = 100\,\mathrm{GHz}$, and its electron density changes sinusoidal, as shown in the following ormula:

$$Ne(t) = Ne\mathrm{avg}\left(1 + \Delta_{Ne}\left(\sin\left(2\pi f_0 t\right)\right)\right). \qquad (42)$$

Neavg is the average electron density, with a value of 3 × 10^{18};Δ_{Ne} is the change amplitude of electron density, with a value of 0.3; f_0 is the change rate of electron density, with a value of 80 MHz.

The incident angles of the electromagnetic wave are 0°, 30°, 45°, and 60°. Then the reflection coefficients of the dextrally polarized wave and the left-handed polarized wave of TE wave and TM wave are calculated, respectively. The result is shown in the figure below.

Figures 5 and 6, respectively, for TE wave oblique incidence to the plasma dielectric photonic crystal board RCP and LCP reflection coefficient, can be seen from the diagram, whether it is right-hand or left-hand polarization wave, along with the oblique incident electromagnetic wave to the increase of the angle of the photonic crystals, the band gap of the reflection coefficient corresponding to the right, and the band gap bandwidth has been increased.

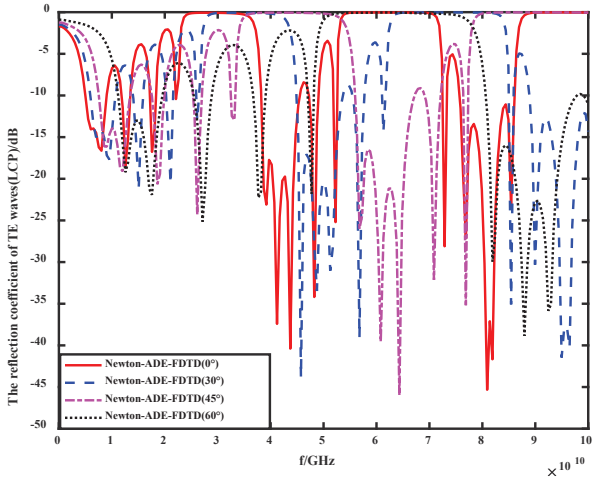

Fig. 6. Reflection coefficient of TE wave in plasma photonic crystal with oblique incident electromagnetic wave (LCP).

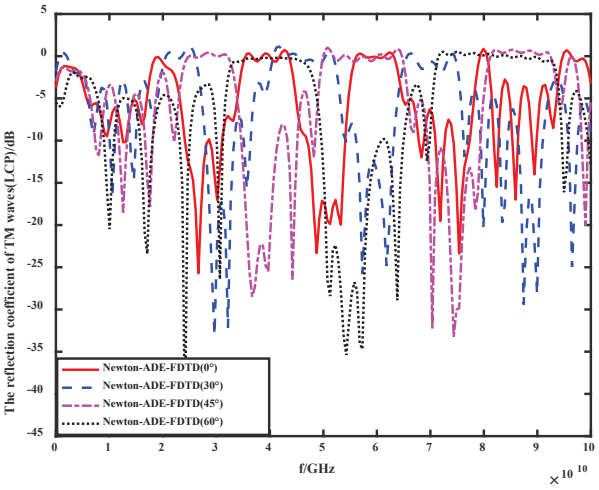

Fig. 8. Reflection coefficient of TM wave in plasma photonic crystal with oblique incident electromagnetic wave (LCP).

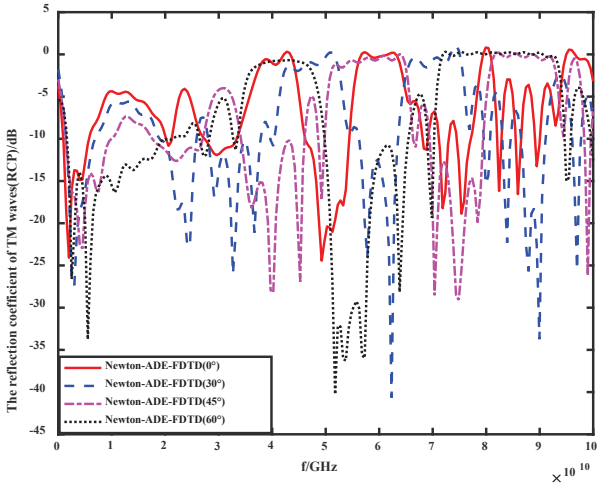

Fig. 7. Reflection coefficient of TM wave in plasma photonic crystal with oblique incident electromagnetic wave (RCP).

Figures 7 and 8, respectively, show the reflection coefficients of RCP and LCP waves of TM wave incident at an oblique angle of plasma dielectric photonic crystal plate. It can be seen from the figure that with the increase of the angle of electromagnetic wave incident at an oblique angle of photonic crystal, the reflection coefficient of band gap moves to the right and the band gap bandwidth increases, which is consistent with the conclusion of TE wave.

IV. CONCLUSION

In this paper, the basic Newtonian equation of motion is combined with the ADE-FDTD algorithm to derive the Newton-ADE-FDTD iterative formula for the TE wave and TM wave of the magnetized time-varying plasma plate with electromagnetic waves incident at a certain angle and calculate the TE wave. The reflection coefficient of TM wave is compared with the analytical solution and the traditional ADE-FDTD algorithm. Verify the effectiveness of the algorithm. Compared with the traditional ADE-FDTD method, the formula of the improved algorithm is simple to derive, and the current density updating equation of magnetized time-varying plasma is derived completely according to the basic Newtonian equation of motion. For the current density updating equation of the traditional ADE-FDTD algorithm, the current density updating equation of Newton-ADE-FDTD algorithm is more detailed. At the same time, the algorithm is used to calculate the reflection coefficient of electromagnetic waves incident on the magnetized plasma dielectric photonic crystal at 0°, 30°, 45°, and 60°. It is found that when the incident angle increases, the band gap will move to the right, and the band gap bandwidth will increase accordingly.

ACKNOWLEDGMENT

This work was supported by the Natural Science Foundation of China under Grant 62071003, Grant 41874174, Grant 61901004, and Grant U21A20457, the Natural Science Foundation of Anhui Province under Grant 2008085MF186, the University Synergy Innovation of Program of Anhui Province under Grant GXXT-2020-050, the Key Basic Research Projects of the State Administration of Science, Technology and Industry for National Defense, and the Collaborative Innovation Program of Universities in Anhui Province under Grant GXXT-2021-028.

REFERENCES

[1] K. Yee, "Numerical solution of initial boundary value problems involving Maxwell's equations in isotropic media," *IEEE Trans. Antennas Propagat.*, vol. 14, no. 3, pp. 302-307, 1966.

[2] Kunz and R. Luebbers, The Finite Diference Time Domain Method for Electromagnetics, CRC, Boca Raton, FL, 1993.

[3] A. Taflove and S. Hagness, Computational Electrodynamics: The Finite-Difference Time-Domain Method, 2nd ed., Artech House, Boston, MA, 2000.

[4] F. Teixeira, W. Chew, M. Straka, M. Oristaglio, and T. Wang, "Finite-difference time-domain simulation of ground penetrating radar on dispersive, inhomogenous, and conductive soils," *IEEE Trans. Geosci. Remote Sensing*, vol. 36, pp. 1928-1937, Nov. 1998.

[5] L. H. Song, X. P. Li, and Y. M. Liu, "Effect of time-varying plasma sheath on hypersonic vehicle-borne Radar target detection," *IEEE Sensors Journal.*, vol. 21, no. 15, pp. 16880-16893, Aug. 2021.

[6] J. Li, L.-X. Guo, Y.-C. Jiao, and R. Wang, "Composite scattering of a plasma-coated target above dispersive sea surface by the ADE-FDTD method," *IEEE Geoscience and Remote Sensing Letters*, vol. 10, no. 1, pp. 4-8, 2013.

[7] S. Liu, S. Liu, and S. Liu, "Finite-difference timedomain algorithm for plasma based on trapezoidarecursive convolution technique," Journal of Infrared, Millimeter, and Terahertz Waves, 2010.

[8] Z. Y. Wang, L. X. Guo, and J. T. Li, "Analysis of echo characteristics of spatially inhomogeneous and time-varying plasma sheath," *IEEE Transactions on Plasma Science.*, vol. 49, no. 6, pp. 1804-1811, Jun. 2021.

[9] J. Chen, J. Tan, X. M. Yu, and H. Y. Shi, "Using WCS-FDTD method to study the plasma frequency selective surface," *IEEE Access.*, vol. 7, pp. 152473-152477, 2019.

[10] M. Pourbagher and S. Sohafi, "A three dimensional FDTD algorithm for wave propagation in cold plasma media using forth-order schemes," *Applied Computational Electromagnetic Society (ACES) Journal*, vol. 28, No. 12, pp. 1153-1161, Dec. 2013.

[11] J. Cho, M. S. Park, and K. Y. Jung, "Perfectly matched layer for accurate FDTD for anisotropic magnetized plasma," *Journal of Electromagnetic Engineering And Science.*, vol. 20, no. 4, pp. 277-284, Oct. 2020.

[12] L. J. Xu, and N. C. Yuan, "FDTD formulations for scattering from 3-D anisotropic magnetized plasma objects," *IEEE Antennas and Wireless Propagation Letters.*, vol. 5, pp. 335-338, 2006.

[13] L. J. Xu, and N. C. Yuan, "JEC-FDTD for 2-D conducting cylinder coated by anisotropic magnetized plasma," *IEEE Antennas and Wireless Propagation Letters.*, vol. 15, no. 12, pp. 892-894, Dec. 2005.

[14] Z. H. Qian, and R. S. Chen, "FDTD analysis of magnetized plasma with arbitrary magnetic declination," *International Journal of Infrared and Millimeter Waves.*, vol. 28, no. 2, pp. 157-167, Feb. 2007.

[15] Q. Chen, M. Katsurai, and P. H. Aoyagi, "An FDTD formulation for dispersive media using a current density," *IEEE Trans. Antennas Propagat.*, vol. 46, pp. 1739–1745, 1998.

[16] M. Okoniewski, M. Mrozowski, and M. Stuchly, "Simple treatment of multi-term dispersion in FDTD," *IEEE Microw. Guided Wave Lett.*, vol. 7, no. 5, pp. 121–123, May 1997.

[17] D. F. Kelley and R. J. Luebbers, "Piecewise linear recursive convolution for dispersive media using FDTD," *IEEE Trans. Antennas Propagat.*, vol. 44, pp. 792–797, 1996.

[18] F. Wang, D. B. Ge, and B. Wei, "SO-FDTD analysis of EM scattering of magnetized ferrite," *Acta Physice Sinice.*, vol. 58, pp. 6356–6362, 2009.

[19] Y. Q. Zhang, and D. B. Ge, "An improved shift operator finite-difference time-domain method based on digital signal processing technique for general dispersive medium," *Acta Physice Sinice.*, vol. 58, pp. 8243–8248, 2009.

[20] H. W. Yang, and Y. Liu, "SO-FDTD analysis on the stealth effect of magnetized plasma with Epstein distribution," *Optik.*, vol. 124, pp. 2037–2040, 2013.

[21] L. X. Yang, S. W. Zheng, and W. D. Shi, etal, Finite difference time domain method for electromagnetic properties of plasma medium and its application. Science Press, 2015, in China.

Hui Liu was born in Bozhou City, Anhui Province, China, in 1998. She received the B.S. degree in electronic information engineering from Hefei Normal University, Hefei, China, in 2020. She is currently working toward the master's degree in electromagnetic field and microwave technology of electronic science and technology with the School of Electronic Information Engineering, Anhui University, Hefei, China.

Her current research interest is computational electromagnetism.

Li-Xia Yang was born in Ezhou, Hubei, China, in 1975. He received the B.S. degree in physics from Hubei University, Wuhan, China, in 1997, and the Ph.D. degree in radio physics from Xidian University, Xi'an, China, in 2007.

Since 2010, he has been an Associate Professor with the Communication Engineering Department, Jiangsu University, Zhenjiang, China. From 2010 to 2011, he was a Postdoctoral Research Fellow with the Electro Science Laboratory (ESL), The Ohio State University, Columbus, OH, USA. From 2015 to 2016, he was a Visiting Scholar with the Institute of Space Science, The University of Texas at Dallas, Dallas, TX, USA. From 2016 to 2019, he has been a Professor, a Ph.D. Supervisor, and the Chairman of the Communication Engineering Department, Jiangsu University. Since 2020, he has been a Distinguished Professor, a Ph.D. Supervisor, and the Vice Dean with the School of Electronic and Information Engineering, Anhui University, Hefei, China. His research interests include wireless communication technique, radio sciences, the computational electromagnetic, and the antenna theory and design in wireless communication systems. He is a member of the Editor Board of Radio Science Journal in China.

Wei Chen was born in Jiangsu Province, China, in 1987. He received the B.S. and M.S. degrees from Jiangsu University, Jiangsu, China, in 2010 and 2013, respectively, and the Ph.D. degree from Xidian University, Xi'an, China, in 2018.

He is currently a Lecturer with the School of Electronics and Information Engineering, Anhui University, Hefei, China. His current research interests include numerical methods in electromagnetic scattering from plasma and wave propagation in complex systems.

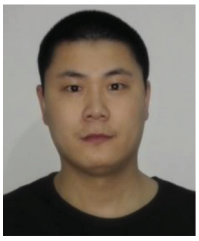

Yong Bo was born in Shandong Province, China, on November 11, 1989. He received the B.S. degree in Shandong University of Science and Technology, Qingdao, China, in 2012, and the Ph.D. degree from the Center for Information Geoscience, University of Electronic Science and Technology of China, Chengdu, China.

He is currently a Lecturer with the University of Anhui, Hefei, China. The main subjects of his interest include computational electromagnetic, wave propagation in plasmas, and low temperature plasma technology and application.

Spatial Processing Using High-Fidelity Models of Dual-Polarization Antenna Elements

John N. Spitzmiller and Sanyi Y. Choi

Integration and Production Program Directorate
Parsons, Huntsville, AL 35806, USA
john.spitzmiller@parsons.com, sanyi.choi@parsons.com

***Abstract* –** This paper generalizes a recent improvement to a traditional spatial-processing algorithm to optimally use body-mounted arrays of dual-polarization radio-frequency antenna elements rather than single-polarization antenna elements. The paper's generalized algorithm exploits high-fidelity far-field gain and polarization data, generated most practically by a computational electromagnetic solver (CES), to characterize the antenna array's individual dual-polarization elements. Using this characterization and that of the desired and undesired communication nodes' antennas, the generalized algorithm determines the array's optimal weights. The subsequent application of a CES to a practical scenario, in which an optimally weighted array of dual-polarization antenna elements is mounted on a representative body, demonstrates the generalized algorithm's exceptional spatial-processing performance.

***Index Terms* –** antenna arrays, beamforming, nullsteering, polarization matching, spatial filters, spatial processing.

I. INTRODUCTION

This paper generalizes a recent improvement [1] to a traditional algorithm for spatial processing (beamforming in the direction of a single desired communication node and nullsteering in the directions of potentially multiple undesired communication nodes). The recent algorithmic improvement optimally used an array of potentially diverse single-polarization radio-frequency (RF) antenna elements arbitrarily arranged on a body of arbitrary shape and material composition. This paper generalizes that improved algorithm to optimally use arrays of dual-polarization antenna elements. A dual-polarization antenna element has two ports, each of which corresponds to one of two nominally orthogonal polarizations in the direction of the element's maximum gain. For example, the two polarizations could be orthogonally linear (say, vertical and horizontal) or orthogonally circular (i.e., right-hand circular (RHC) and left-hand circular (LHC)). This paper assumes the antenna array functions exclusively in a receive mode. However, under the assumed principle of reciprocity [2], this paper's generalized spatial-processing algorithm applies equally to a transmitting antenna array.

Previous research in spatial processing with arrays of dual-polarization elements [3–10] has recognized this problem's extraordinary complexity in even relatively simple practical scenarios. For example, the electrical effects caused by surface waves on the body, mutual coupling between array elements, and spatial variations in element gain and polarization patterns are practically impossible to characterize without a full-wave computational electromagnetic solver (CES) solution or sophisticated measurements [3]. In response researchers have generally made three simplifying assumptions to facilitate their analyses and simulations. Firstly, most researchers assume the absence of any tangible body [3–6] on which the antenna array is mounted. This assumption precludes the study of surface-wave effects that are crucial to scenarios in which the body is physically between an emitter and the receiving antenna [11] or antenna array [1]. Although some researchers [7–10] assume a planar or cylindrical physical layout of the antenna elements, they still account for no explicit body in their analyses. Secondly, most researchers explicitly assume negligible mutual coupling between the array's elements [3–7, 9, 10]. Thirdly, most researchers assume the array's dual-polarization elements are ideal crossed-dipole (or electrically equivalent) elements which have perfectly orthogonally linear transmission and reception characteristics [4–7, 9, 10].

Since these effects are typically small, much meaningful research can be performed while ignoring them. However, the accurate characterization of a spatial-processing algorithm's performance in practical scenarios requires exceptional fidelity in all three typically simplified areas. For example, to achieve extremely deep nulls in a receive array's gain pattern, a spatial-processing algorithm must weight the element output signals so that their sum is nearly exactly zero. By maximally exploiting the high-fidelity data produced by

Submitted On: August 27, 2021
Accepted On: October 18, 2021

https://doi.org/10.13052/2022.ACES.J.370103

a CES, this paper's generalized algorithm accounts for the typically small yet non-negligible electrical effects of the presence of the body, mutual coupling between array elements, and element gain and polarization deviations from ideal behavior.

All traditional receive-mode spatial-processing algorithms [12–14] require knowledge of the array elements' locations in the receive array's coordinate system, the thermal-noise power-spectral density (PSD) at every array output port, the desired and undesired far-field emitters' apparent angular directions in the array's coordinate system, and all undesired emitters' spatial power densities at the array's location. This paper's generalized algorithm requires additional information. Specifically, the generalized algorithm requires quantitative knowledge (or, at least, estimates) of the desired and undesired emitters' antenna gains and polarization characteristics in the direction of the receive array. The algorithm also requires high-fidelity quantitative knowledge of the *transmitted* far-field vector electric field in the directions of all scenario emitters produced by each port of each array element, accounting for the structure of the corresponding element, the electromagnetic interactions with the other elements (i.e., mutual-coupling effects), and the electromagnetic interactions with the body. Only a CES or high-fidelity testing can practically provide such detailed data. Proper processing of this additional information produces the parameters needed to populate the recently developed, high-fidelity RF antenna models (both transmit and receive modes) [15, 16].

Using the populated antenna models, the generalized algorithm calculates a set of complex weights (effecting amplitude scalings and phase shifts) to apply to the output signals of the array elements' ports. The summation of these weighted signals optimizes some appropriate figure of merit (e.g., the signal-to-interference ratio (SIR) when the array operates in an RF-interference (RFI) environment). These signal modifications effectively produce an antenna pattern having high effective gain in the direction of the desired emitter and low effective gains in the directions of the undesired emitters. Note that effective gain is the total gain less the polarization-mismatch loss, which is ideally very low for the desired emitter and very high for all undesired emitters.

Section II reviews this problem's technical background. Section III generalizes the spatial-processing technique of [1] assuming dual-polarization antenna elements. Section IV presents high-fidelity digital-simulation results for an array of realistic dual-polarization antenna elements mounted on a representative body. Section V concludes the paper with a summary of key results and several suggestions for future work.

II. TECHNICAL BACKGROUND

This section reviews the technical background needed for the development of Section III's generalized algorithm. Subsection A provides the general scenario's physical description, including the locations of the receive-antenna elements, the single desired emitter, and the potentially multiple undesired emitters. Subsection B mathematically specifies the desired and undesired emitters' transmitted signals. Subsections C, D, and E respectively characterize the receive-antenna array's elements, the desired emitter's antenna, and the undesired emitters' antennas. Subsection F derives the electric fields incident on the receive-antenna elements. Subsection G develops the array elements' output signals. Subsection H describes the receiver/spatial-processor model fed by the receive-antenna array's elements. Section I presents the problem statement.

A. Physical description of scenario

The diagram of Figure 1 notionally depicts the scenario of interest. A receive-antenna array mounted on a body of potentially complex shape and material composition attempts to receive an RF signal from a desired far-field emitter. Multiple spatially diverse undesired far-field RF emitters interfere with the desired signal's reception. Note that the body may be physically between one or more of the receive array's elements and one or more of the scenario's emitters.

Figure 2 shows the basic scenario geometry in which an array of M dual-polarization antenna elements arranged on a body receives signals from a single desired far-field emitter and N undesired far-field emitters. The

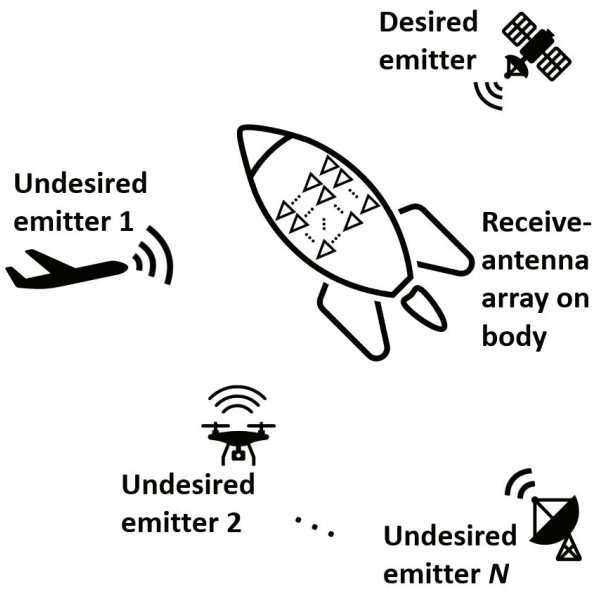

Fig. 1. Notional depiction of scenario.

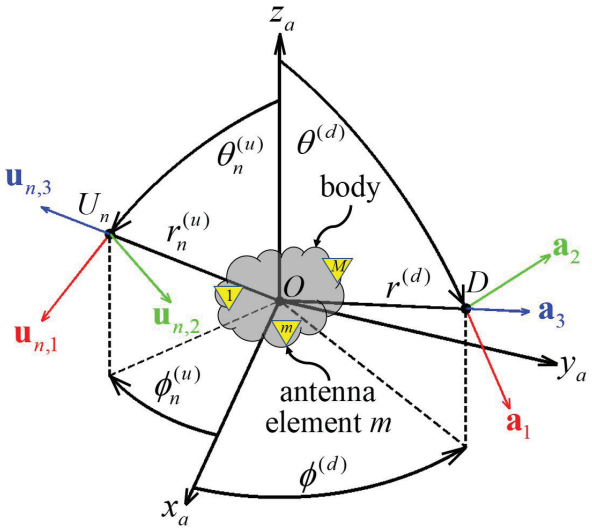

Fig. 2. Basic scenario geometry.

Cartesian coordinate system shown in Figure 2 has its origin at O, some convenient point near the physical center of the antenna array on the body. Figure 2 also shows a spherical coordinate system using the traditional quantities of the distance r ($r \geq 0$) and the two orthogonal angles $\theta (0 \leq \theta \leq \pi)$ and $\phi (0 \leq \phi < 2\pi)$ to specify an arbitrary point of interest.

The single desired emitter's antenna's phase center, located at D, has spherical coordinates $(r^{(d)}, \theta^{(d)}, \phi^{(d)})$ and Cartesian coordinates

$$\begin{bmatrix} x^{(d)} \\ y^{(d)} \\ z^{(d)} \end{bmatrix} = \begin{bmatrix} r^{(d)} s_{\theta^{(d)}} c_{\phi^{(d)}} \\ r^{(d)} s_{\theta^{(d)}} s_{\phi^{(d)}} \\ r^{(d)} c_{\theta^{(d)}} \end{bmatrix}, \tag{1}$$

where we use the shorthand notation

$$\begin{bmatrix} c_\rho & s_\rho \end{bmatrix} = \begin{bmatrix} \cos(\rho) & \sin(\rho) \end{bmatrix} \; \forall \rho \in \mathbb{R}. \tag{2}$$

The nth undesired emitter's antenna's phase center, located at U_n, has spherical coordinates $(r_n^{(u)}, \theta_n^{(u)}, \phi_n^{(u)})$ and Cartesian coordinates

$$\begin{bmatrix} x_n^{(u)} \\ y_n^{(u)} \\ z_n^{(u)} \end{bmatrix} = \begin{bmatrix} r_n^{(u)} s_{\theta_n^{(u)}} c_{\phi_n^{(u)}} \\ r_n^{(u)} s_{\theta_n^{(u)}} s_{\phi_n^{(u)}} \\ r_n^{(u)} c_{\theta_n^{(u)}} \end{bmatrix}, \; n \in \{1, \cdots, N\}. \tag{3}$$

The phase center of the mth element's pth port has Cartesian coordinates $(x_{m,p}{}^{(a)}, y_{m,p}{}^{(a)}, z_{m,p}{}^{(a)})$.

As shown in Figure 2, we define three orthogonal unit vectors associated with the antenna array and the desired emitter. Firstly, unit vector

$$\mathbf{a}_3 = \begin{bmatrix} s_{\theta^{(d)}} c_{\phi^{(d)}} & s_{\theta^{(d)}} s_{\phi^{(d)}} & c_{\theta^{(d)}} \end{bmatrix}^T, \tag{4}$$

with T denoting simple (unconjugated) transposition, points along the ray from O to D (i.e., in the direction of increasing distance from O at D). Secondly, unit vector

$$\mathbf{a}_1 = \begin{bmatrix} c_{\phi^{(d)}} c_{\theta^{(d)}} & s_{\phi^{(d)}} c_{\theta^{(d)}} & -s_{\theta^{(d)}} \end{bmatrix}^T, \tag{5}$$

points in the direction of the antenna array's increasing θ at D. Thirdly, unit vector

$$\mathbf{a}_2 = \begin{bmatrix} -s_{\phi^{(d)}} & c_{\phi^{(d)}} & 0 \end{bmatrix}^T, \tag{6}$$

points in the direction of the antenna array's increasing ϕ at D. Unit vectors $\mathbf{a}_1$ and $\mathbf{a}_2$ are parallel to all planes normal to the line passing through O and D. Thus, for any point on this line, the plane defined by these unit vectors contains the polarization ellipse of a plane electromagnetic (EM) wave propagating between D and O.

As shown in Figure 2, we define three orthogonal unit vectors associated with the antenna array and the nth undesired emitter. Firstly, unit vector

$$\mathbf{u}_{n,3} = \begin{bmatrix} s_{\theta_n^{(u)}} c_{\phi_n^{(u)}} & s_{\theta_n^{(u)}} s_{\phi_n^{(u)}} & c_{\theta_n^{(u)}} \end{bmatrix}^T, \tag{7}$$

points along the ray from O to U_n (i.e., in the direction of increasing distance from O at U_n). Secondly, unit vector

$$\mathbf{u}_{n,1} = \begin{bmatrix} c_{\phi_n^{(u)}} c_{\theta_n^{(u)}} & s_{\phi_n^{(u)}} c_{\theta_n^{(u)}} & -s_{\theta_n^{(u)}} \end{bmatrix}^T, \tag{8}$$

points in the direction of the antenna array's increasing θ at U_n. Thirdly, unit vector

$$\mathbf{u}_{n,2} = \begin{bmatrix} -s_{\phi_n^{(u)}} & c_{\phi_n^{(u)}} & 0 \end{bmatrix}^T, \tag{9}$$

points in the direction of the antenna array's increasing ϕ at U_n. Unit vectors $\mathbf{u}_{n,1}$ and $\mathbf{u}_{n,2}$ are parallel to all planes normal to the line passing through O and U_n. Thus, for any point on this line, the plane defined by these unit vectors contains the polarization ellipse of a plane EM wave propagating between U_n and O.

As shown in Figure 3, unit vector

$$\mathbf{p}_3 = -\mathbf{a}_3, \tag{10}$$

points along the ray from D to O. We define the orientation of the desired emitter's local spherical coordinate

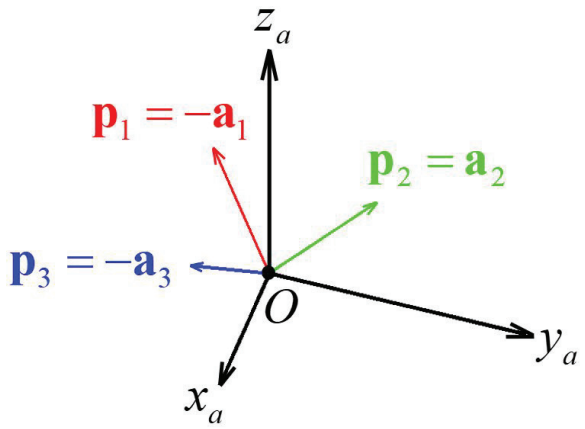

Fig. 3. Unit vectors associated with the desired emitter.

system, having origin at D, to satisfy two requirements. Firstly, unit vector

$$\mathbf{p}_1 = -\mathbf{a}_1, \tag{11}$$

points in the direction of the desired emitter's increasing θ at O. Secondly, unit vector

$$\mathbf{p}_2 = \mathbf{a}_2, \tag{12}$$

points in the direction of the desired emitter's increasing ϕ at O. Unit vectors $\mathbf{p}_1$ and $\mathbf{p}_2$ define planes normal to the line passing through O and D. Thus, for any point on this line, the plane defined by these unit vectors contains the polarization ellipse of a plane EM wave propagating between D and O.

As shown in Figure 4, unit vector

$$\mathbf{q}_{n,3} = -\mathbf{u}_{n,3}, \tag{13}$$

points along the ray from U_n to O. We define the orientation of the nth undesired emitter's local spherical coordinate system, having origin at U_n, to satisfy two requirements. Firstly, unit vector

$$\mathbf{q}_{n,1} = -\mathbf{u}_{n,1}, \tag{14}$$

points in the direction of the nth undesired emitter's increasing θ at O. Secondly, unit vector

$$\mathbf{q}_{n,2} = \mathbf{u}_{n,2}, \tag{15}$$

points in the direction of the nth undesired emitter's increasing ϕ at O. Unit vectors $\mathbf{q}_{n,1}$ and $\mathbf{q}_{n,2}$ define planes normal to the line containing O and U_n. Thus, for any point on this line, the plane defined by these unit vectors contains the polarization ellipse of a plane EM wave propagating between U_n and O.

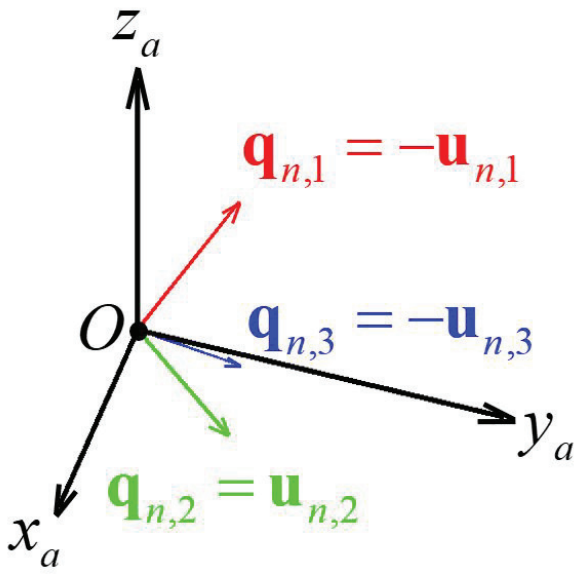

Fig. 4. Unit vectors associated with the nth undesired emitter.

B. Mathematical description of transmitted signals

The desired emitter's transmitter sends to its antenna the deterministic narrowband signal

$$x^{(d)}(t) = A^{(d)}(t)\cos\left[2\pi f_{RF}t + \gamma^{(d)}(t)\right], \tag{16}$$

where $A^{(d)}(t)$ and $\gamma^{(d)}(t)$ are the narrowband signal's slowly varying amplitude modulation and phase modulation, respectively, f_{RF} is the center RF in hertz, and t is time in seconds. Assuming the desired emitter's antenna has unit impedance, the desired emitter's time-averaged power is

$$P^{(d)} = \left[A^{(d)}\right]^2 \Big/ 2, \tag{17}$$

if we also assume $A^{(d)}(t)$ is a constant $A^{(d)}$.

The nth undesired emitter's transmitter sends to its antenna the zero-mean, wide-sense stationary (WSS) random narrowband signal

$$x_n^{(u)}(t) = x_{I,n}^{(u)}(t)\cos(2\pi f_{RF}t) - x_{Q,n}^{(u)}(t)\sin(2\pi f_{RF}t), \tag{18}$$

where ${x_{I,n}}^{(u)}(t)$ and ${x_{Q,n}}^{(u)}(t)$ are, respectively, the inphase (I) and quadrature (Q) components of ${x_n}^{(u)}(t)$. We assume the N undesired emitters' signals are mutually uncorrelated.

The nth undesired emitter's signal has double-sided PSD

$$S_n^{(u)}(f) = \frac{N_n^{(u)}}{2}\left[\Pi\left(\frac{f-f_{RF}}{B_n^{(u)}}\right) + \Pi\left(\frac{f+f_{RF}}{B_n^{(u)}}\right)\right], \tag{19}$$

where ${N_n}^{(u)}/2$ is the PSD's level in W/Hz, ${B_n}^{(u)}$ is the bandwidth in Hz, and

$$\Pi(x) = \begin{cases} 1, & |x| \le 1/2 \\ 0, & \text{otherwise} \end{cases}, \tag{20}$$

is the unit pulse function. The nth undesired emitter's I and Q components are independent, zero-mean, WSS random lowpass processes with double-sided PSD

$$S_{I,n}^{(u)}(f) = S_{Q,n}^{(u)}(f) = N_n^{(u)}\Pi\left(f/B_n^{(u)}\right). \tag{21}$$

C. Electrical description of antenna array

We assume complete quantitative knowledge of the practically planar vector electric field

$$\begin{aligned}&\mathbf{E}_{m,p}^{(a)}(t, r^{(a)}, \theta, \phi, f_{RF}) = \\ &\mathbf{v}_1(\theta,\phi)E_{m,p,1}^{(a)}(r^{(a)}, \theta, \phi, f_{RF}) \\ &\times\cos[2\pi f_{RF}t + \gamma_{m,p,1}^{(a)}(r^{(a)}, \theta, \phi, f_{RF})], \\ &+\mathbf{v}_2(\theta,\phi)E_{m,p,2}^{(a)}(r^{(a)}, \theta, \phi, f_{RF}) \\ &\times\cos[2\pi f_{RF}t + \gamma_{m,p,2}^{(a)}(r^{(a)}, \theta, \phi, f_{RF})]\end{aligned} \tag{22}$$

produced at known far-field slant range $r^{(a)}$ from O for every combination of θ and ϕ corresponding to a scenario emitter when monochromatic source signal

$$s_s(t) = A_s\cos(2\pi f_{RF}t + \gamma_s), \tag{23}$$

exclusively stimulates port p of array element m with all elements present on the body. In (22) direction-dependent unit vector $\mathbf{v}_i$, $i \in \{1,2\}$, can represent $\mathbf{a}_i$ or

$\mathbf{u}_{n,i}$ as appropriate. Equation (22) is the electric field produced at a point with spherical coordinates $(r^{(a)}, \theta, \phi)$ when element m is transmitting due to the stimulation by (23) of only its pth port while all other elements are physically present but electrically inactive. A CES is the most practical source of such high-fidelity data, but sophisticated testing might be capable of generating these data. Figure 5 shows the high-fidelity antenna model [15] corresponding to the pth port of the antenna array's mth element. The model has two sets of direction-dependent parameters. The first set comprises an apparent internal attenuation ${K_{m,p,1}}^{(a)}(\theta,\phi)$ and an apparent internal delay ${\tau_{m,p,1}}^{(a)}(\theta,\phi)$ associated with an antenna perfectly linearly polarized along $\mathbf{v}_1$. The second set comprises an apparent internal attenuation ${K_{m,p,2}}^{(a)}(\theta,\phi)$ and an apparent internal delay ${\tau_{m,p,2}}^{(a)}(\theta,\phi)$ associated with a collocated antenna perfectly linearly polarized along $\mathbf{v}_2$.

The model's apparent internal attenuations are

$$K_{m,p,i}^{(a)}(r^{(a)},\theta,\phi,f_{RF}) = \frac{\sqrt{2E_{m,p,i}^{(a)}(r^{(a)},\theta,\phi,f_{RF})}}{A_s}K^{(a)},\ i\in\{1,2\}, \tag{24}$$

where [16]

$$K^{(a)} = \lambda r^{(a)}/Z_0. \tag{25}$$

In (25) the EM wave's wavelength is

$$\lambda = c/f_{RF}, \tag{26}$$

where c is the speed of light (exactly 299,792,458 m/s in free space, the assumed propagation medium). Also, in (25) $Z_0 = 4\pi\times10^{-7}c \approx 376.7303\ \Omega$ is the intrinsic impedance of free space.

The model's apparent internal time delays are

$$\begin{aligned}\tau_{m,p,i}^{(a)}(\theta,\phi,f_{RF}) &\approx \frac{\gamma_s-\gamma_{m,p,i}^{(a)}(r^{(a)},\theta,\phi,f_{RF})}{2\pi f_{RF}}\\ &-r^{(a)}/c+k_{m,p,i}^{(a)}/f_{RF}\\ &+\left[s_\theta c_\phi x_{m,p}^{(a)}+s_\theta s_\phi y_{m,p}^{(a)}+c_\theta z_{m,p}^{(a)}\right]\Big/c,\ i\in\{1,2\},\end{aligned} \tag{27}$$

where ${k_{m,p,i}}^{(a)}$ is any integer satisfying

$$\begin{aligned}\gamma_{m,p,i}^{(a)}(r^{(a)},\theta,\phi,f_{RF}) &= \gamma_s+2\pi k_{m,p,i}^{(a)}\\ &-2\pi f_{RF}\left[r^{(a)}+s_\theta c_\phi x_{m,p}^{(a)}+s_\theta s_\phi y_{m,p}^{(a)}+c_\theta z_{m,p}^{(a)}\right]\Big/c\\ &-2\pi f_{RF}\tau_{m,p,i}^{(a)}(r^{(a)},\theta,\phi,f_{RF}).\end{aligned} \tag{28}$$

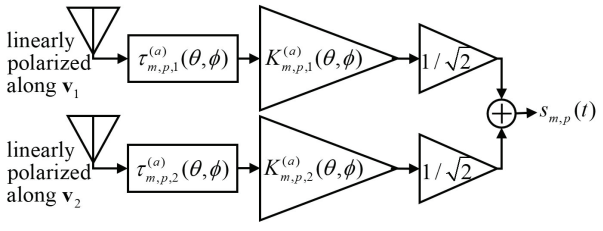

Fig. 5. Model for the pth port of the antenna array's mth element.

We intuitively choose each ${k_{m,p,i}}^{(a)}$ to make the corresponding ${\tau_{m,p,i}}^{(a)}$ positive but minimal. Note that (24) and (27) account for the presence of the body and the other antenna elements. In other words, for each of the array's $2M$ ports, this technique produces apparent internal attenuations and delays which generally differ—often significantly—from the apparent internal attenuations and delays obtained in the absence of the other antenna elements and the body.

D. Electrical description of desired emitter's antenna

We assume the desired emitter's transmit antenna has a known total gain of $G^{(d)}$ in the direction of O. We further assume the desired emitter's transmit antenna has a known polarization characterized by axial ratio $R^{(d)}$, tilt angle $\alpha^{(d)}$, and rotation sense $s^{(d)}$ in the direction of O. The phase difference $\delta^{(d)}$ between the untilted spatially orthogonal electric field components appearing in the far field is [16]

$$\delta^{(d)} = \begin{cases} -\pi/2, & s^{(d)} = R \\ \pi/2, & s^{(d)} = L \end{cases}. \tag{29}$$

Given these characteristics, we model the desired emitter's transmit antenna as shown in Figure 6, where [16]

$$K_1^{(d)} = \bar{K}_1^{(d)}K^{(d)}, \tag{30}$$

$$K_2^{(d)} = \bar{K}_2^{(d)}K^{(d)}, \tag{31}$$

$$\begin{aligned}\tau_1^{(d)} &= -\measuredangle\left[c_{\alpha^{(d)}} - s_{\alpha^{(d)}}e^{j\delta^{(d)}}/R^{(d)}\right]\Big/(2\pi f_{RF})\\ &\quad -r^{(d)}/c+k_1^{(d)}/f_{RF},\end{aligned} \tag{32}$$

and

$$\begin{aligned}\tau_2^{(d)} &= -\measuredangle\left[s_{\alpha^{(d)}} + c_{\alpha^{(d)}}e^{j\delta^{(d)}}/R^{(d)}\right]\Big/(2\pi f_{RF})\\ &\quad -r^{(d)}/c+k_2^{(d)}/f_{RF}.\end{aligned} \tag{33}$$

In (30) and (31), respectively,

$$\bar{K}_1^{(d)} = \frac{\frac{1}{r^{(d)}}\sqrt{\frac{Z_0G^{(d)}}{2\pi}}\left|c_{\alpha^{(d)}} - \frac{s_{\alpha^{(d)}}e^{j\delta^{(d)}}}{R^{(d)}}\right|}{\sqrt{\left|c_{\alpha^{(d)}} - \frac{s_{\alpha^{(d)}}e^{j\delta^{(d)}}}{R^{(d)}}\right|^2 + \left|s_{\alpha^{(d)}} + \frac{c_{\alpha^{(d)}}e^{j\delta^{(d)}}}{R^{(d)}}\right|^2}}, \tag{34}$$

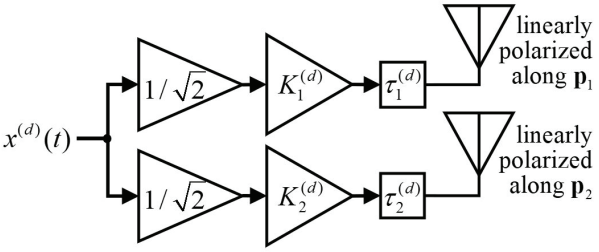

Fig. 6. Model for the desired emitter's transmit antenna.

and

$$\bar{K}_2^{(d)} = \frac{\frac{1}{r^{(d)}}\sqrt{\frac{Z_0 G^{(d)}}{2\pi}}\left|s_{\alpha^{(d)}} + \frac{c_{\alpha^{(d)}} e^{j\delta^{(d)}}}{R^{(d)}}\right|}{\sqrt{\left|c_{\alpha^{(d)}} - \frac{s_{\alpha^{(d)}} e^{j\delta^{(d)}}}{R^{(d)}}\right|^2 + \left|s_{\alpha^{(d)}} + \frac{c_{\alpha^{(d)}} e^{j\delta^{(d)}}}{R^{(d)}}\right|^2}}. \tag{35}$$

In both (30) and (31),

$$K^{(d)} = \frac{A_s^{(d)}\lambda}{2}\sqrt{\frac{G^{(d)}}{Z_0\pi\left[\left(E_1^{(d)}\right)^2 + \left(E_2^{(d)}\right)^2\right]}}, \tag{36}$$

where [16] $A_s{}^{(d)}$ is the amplitude in volts of the monochromatic source signal which results in the amplitudes $E_1{}^{(d)}$ and $E_2{}^{(d)}$ of the spatially orthogonal electric-field components appearing at O. In (32) and (33), positive integers $k_1{}^{(d)}$ and $k_2{}^{(d)}$ respectively satisfy

$$\begin{aligned} &\measuredangle\left[c_{\alpha^{(d)}} - s_{\alpha^{(d)}} e^{j\delta^{(d)}}/R^{(d)}\right] = \\ &-2\pi f_{RF}\tau_1^{(d)} - 2\pi f_{RF} r^{(d)}/c + 2\pi k_1^{(d)}, \end{aligned} \tag{37}$$

and

$$\begin{aligned} &\measuredangle\left[s_{\alpha^{(d)}} + c_{\alpha^{(d)}} e^{j\delta^{(d)}}/R^{(d)}\right] = \\ &-2\pi f_{RF}\tau_2^{(d)} - 2\pi f_{RF} r^{(d)}/c + 2\pi k_2^{(d)}. \end{aligned} \tag{38}$$

E. Electrical description of undesired emitters' antennas

We assume the nth undesired emitter's transmit antenna has a known total gain of $G_n{}^{(u)}$ in the direction of O. We further assume that, in the direction of O, the nth undesired emitter's transmit antenna has a polarization characterized by axial ratio $R_n{}^{(u)}$, tilt angle $\alpha_n{}^{(u)}$, and rotation sense $s_n{}^{(u)}$. The phase difference $\delta_n{}^{(u)}$ between the untilted spatially orthogonal electric-field components appearing in the far field is [16]

$$\delta_n^{(u)} = \begin{cases} -\pi/2, & s_n^{(u)} = R \\ \pi/2, & s_n^{(u)} = L \end{cases}. \tag{39}$$

Given these characteristics, we model the nth undesired emitter's transmit antenna as shown in Figure 7, where [16]

$$K_{n,1}^{(u)} = \bar{K}_{n,1}^{(u)} K_n^{(u)}, \tag{40}$$

$$K_{n,2}^{(u)} = \bar{K}_{n,2}^{(u)} K_n^{(u)}, \tag{41}$$

$$\begin{aligned} \tau_{n,1}^{(u)} = &-\measuredangle\left[c_{\alpha_n^{(u)}} - s_{\alpha_n^{(u)}} e^{j\delta_n^{(u)}}/R_n^{(u)}\right]\Big/(2\pi f_{RF}) \\ &-r_n^{(u)}/c + k_{n,1}^{(u)}/f_{RF}, \end{aligned} \tag{42}$$

and

$$\begin{aligned} \tau_{n,2}^{(u)} = &-\measuredangle\left[s_{\alpha_n^{(u)}} + c_{\alpha_n^{(u)}} e^{j\delta_n^{(u)}}/R_n^{(u)}\right]\Big/(2\pi f_{RF}) \\ &-r_n^{(u)}/c + k_{n,2}^{(u)}/f_{RF}. \end{aligned} \tag{43}$$

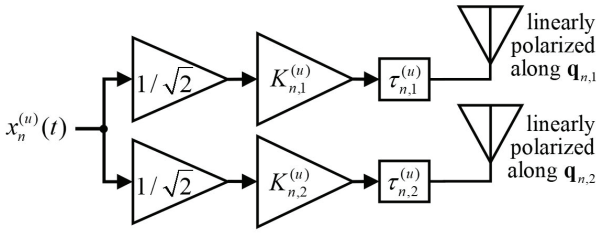

Fig. 7. Model for the nth undesired emitter's transmit antenna.

In (40) and (41), respectively,

$$\bar{K}_{n,1}^{(u)} = \frac{\frac{1}{r_n^{(u)}}\sqrt{\frac{Z_0 G_n^{(u)}}{2\pi}}\left|c_{\alpha_n^{(u)}} - \frac{s_{\alpha_n^{(u)}} e^{j\delta_n^{(u)}}}{R_n^{(u)}}\right|}{\sqrt{\left|c_{\alpha_n^{(u)}} - \frac{s_{\alpha_n^{(u)}} e^{j\delta_n^{(u)}}}{R_n^{(u)}}\right|^2 + \left|s_{\alpha_n^{(u)}} + \frac{c_{\alpha_n^{(u)}} e^{j\delta_n^{(u)}}}{R_n^{(u)}}\right|^2}}, \tag{44}$$

and

$$\bar{K}_{n,2}^{(u)} = \frac{\frac{1}{r_n^{(u)}}\sqrt{\frac{Z_0 G_n^{(u)}}{2\pi}}\left|s_{\alpha_n^{(u)}} + \frac{c_{\alpha_n^{(u)}} e^{j\delta_n^{(u)}}}{R_n^{(u)}}\right|}{\sqrt{\left|c_{\alpha_n^{(u)}} - \frac{s_{\alpha_n^{(u)}} e^{j\delta_n^{(u)}}}{R_n^{(u)}}\right|^2 + \left|s_{\alpha_n^{(u)}} + \frac{c_{\alpha_n^{(u)}} e^{j\delta_n^{(u)}}}{R_n^{(u)}}\right|^2}}. \tag{45}$$

In both (40) and (41),

$$K_n^{(u)} = \frac{A_{n,s}^{(u)}\lambda}{2}\sqrt{\frac{G_n^{(u)}}{\pi Z_0\left[\left(E_{n,1}^{(u)}\right)^2 + \left(E_{n,2}^{(u)}\right)^2\right]}} = \frac{\lambda r_n^{(u)}}{Z_0}, \tag{46}$$

where [16] $A_{n,s}{}^{(u)}$ is the amplitude in volts of the monochromatic source signal which results in the amplitudes $E_{n,1}{}^{(u)}$ and $E_{n,2}{}^{(u)}$ of the spatially orthogonal electric-field components appearing at O. In (42) and (43), positive integers $k_{n,1}{}^{(u)}$ and $k_{n,2}{}^{(u)}$ respectively satisfy

$$\begin{aligned} &\measuredangle\left[c_{\alpha_n^{(u)}} - s_{\alpha_n^{(u)}} e^{j\delta_n^{(u)}}/R_n^{(u)}\right] = \\ &-2\pi f_{RF}\tau_{n,1}^{(u)} - 2\pi f_{RF} r_n^{(u)}/c + 2\pi k_{n,1}^{(u)}, \end{aligned} \tag{47}$$

and

$$\begin{aligned} &\measuredangle\left[s_{\alpha_n^{(u)}} + c_{\alpha_n^{(u)}} e^{j\delta_n^{(u)}}/R_n^{(u)}\right] = \\ &-2\pi f_{RF}\tau_{n,2}^{(u)} - 2\pi f_{RF} r_n^{(u)}/c + 2\pi k_{n,2}^{(u)}. \end{aligned} \tag{48}$$

F. Electric fields incident on antenna array's elements

Since the desired emitter's transmitter sends (16) to its antenna, the desired emitter's antenna effectively produces at a point very near D on the line passing through

D and O the vector electric field [16]

$$\begin{aligned}&\mathbf{E}_D^{(d)}(t)\approx\\&\frac{K_1^{(d)}A^{(d)}(t)}{\sqrt{2}}\cos\left[2\pi f_{RF}(t-\tau_1^{(d)})+\gamma^{(d)}(t)\right]\mathbf{p}_1\\&+\frac{K_2^{(d)}A^{(d)}(t)}{\sqrt{2}}\cos\left[2\pi f_{RF}(t-\tau_2^{(d)})+\gamma^{(d)}(t)\right]\mathbf{p}_2.\end{aligned}\tag{49}$$

After propagating to the receive-antenna array's mth element's pth port's phase center, the desired emitter's transmitted electric field is

$$\begin{aligned}&\mathbf{E}_{m,p}^{(d)}(t)\approx-\bar{K}_1^{(d)}A^{(d)}(t-\tau^{(d)})/\sqrt{2}\\&\times\cos\left[2\pi f_{RF}(t-\tau_1^{(d)}-\tau_{m,p}^{d\to a})+\gamma^{(d)}(t-\tau^{(d)})\right]\mathbf{a}_1\\&+\bar{K}_2^{(d)}A^{(d)}(t-\tau^{(d)})/\sqrt{2}\\&\times\cos\left[2\pi f_{RF}(t-\tau_2^{(d)}-\tau_{m,p}^{d\to a})+\gamma^{(d)}(t-\tau^{(d)})\right]\mathbf{a}_2,\end{aligned}\tag{50}$$

where

$$\tau^{(d)}=r^{(d)}/c,\tag{51}$$

is the propagation delay from D to O and

$$\begin{aligned}&\tau_{m,p}^{(d\to a)}=r_{m,p}^{(d\to a)}/c\approx r^{(d)}/c\\&-\left[s_{\theta^{(d)}}c_{\phi^{(d)}}x_{m,p}^{(a)}+s_{\theta^{(d)}}s_{\phi^{(d)}}y_{m,p}^{(a)}+c_{\theta^{(d)}}z_{m,p}^{(a)}\right]\Big/c,\end{aligned}\tag{52}$$

is the propagation delay from D to the phase center of the receive-antenna array's mth element's pth port.

Since the nth undesired emitter's transmitter sends (18) to its antenna, the nth undesired emitter's antenna produces at a point very near U_n on the line passing through U_n and O the vector electric field [16]

$$\begin{aligned}&\mathbf{E}_{n\to U_n}^{(u)}(t)\approx K_{n,1}^{(u)}A_n^{(u)}(t)/\sqrt{2}\\&\times\cos\left[2\pi f_{RF}(t-\tau_{n,1}^{(u)})+\gamma_n^{(u)}(t)\right]\mathbf{q}_{n,1}\\&+K_{n,2}^{(u)}A_n^{(u)}(t)/\sqrt{2}\\&\times\cos\left[2\pi f_{RF}(t-\tau_{n,2}^{(u)})+\gamma_n^{(u)}(t)\right]\mathbf{q}_{n,2}.\end{aligned}\tag{53}$$

After propagating to the receive-antenna array's mth element's pth port's phase center, the nth undesired emitter's transmitted electric field is

$$\begin{aligned}&\mathbf{E}_{n\to m,p}^{(u)}(t)\approx-\mathbf{u}_{n,1}\bar{K}_{n,1}^{(u)}A_n^{(u)}(t-\tau_n^{(u)})/\sqrt{2}\\&\times\cos\left[2\pi f_{RF}(t-\tau_{n,1}^{(u)}-\tau_{n\to m,p}^{(u\to a)})+\gamma_n^{(u)}(t-\tau_n^{(u)})\right]\\&+\mathbf{u}_{n,2}\bar{K}_2^{(u,n)}A_n^{(u)}(t-\tau_n^{(u)})/\sqrt{2}\\&\times\cos\left[2\pi f_{RF}(t-\tau_{n,2}^{(u)}-\tau_{n\to m,p}^{(u\to a)})+\gamma_n^{(u)}(t-\tau_n^{(u)})\right],\end{aligned}\tag{54}$$

where

$$\tau_n^{(u)}=r_n^{(u)}/c,\tag{55}$$

is the propagation delay from U_n to O and

$$\begin{aligned}&\tau_{n\to m,p}^{(u\to a)}=r_{n\to m,p}^{(u\to a)}/c\approx r_n^{(u)}/c\\&-\frac{s_{\theta_n^{(u)}}c_{\phi_n^{(u)}}x_{m,p}^{(a)}+s_{\theta_n^{(u)}}s_{\phi_n^{(u)}}y_{m,p}^{(a)}+c_{\theta_n^{(u)}}z_{m,p}^{(a)}}{c},\end{aligned}\tag{56}$$

is the propagation delay from U_n to the phase center of the receive-antenna array's mth element's pth port.

G. Output signals of receive-antenna array's elements

We assume the ports of the receive-antenna array's elements respond linearly to incident EM waves. That is, each port's response to the incident EM waves from the desired and undesired emitters is the sum of that port's response to the individual incident EM waves. We further assume mutually independent thermal-noise signals corrupt the array's $2M$ outputs.

The response of the receive-antenna array's mth element's pth port to (50) is

$$\begin{aligned}&x_{m,p}^{(d)}(t)\approx-K_{m,p,1}^{(a)}(\theta^{(d)},\phi^{(d)})\bar{K}_1^{(d)}A^{(d)}(t-\tau^{(d)})/2\\&\times\cos\left\{2\pi f_{RF}\left[t-\tau_1^{(d)}-\tau_{m,p}^{(d\to a)}-\tau_{m,p,1}^{(a)}(\theta^{(d)},\phi^{(d)})\right]\right.\\&\left.+\gamma^{(d)}(t-\tau^{(d)})\right\}\\&+K_{m,p,2}^{(a)}(\theta^{(d)},\phi^{(d)})\bar{K}_2^{(d)}A^{(d)}(t-\tau^{(d)})/2\\&\times\cos\left\{2\pi f_{RF}\left[t-\tau_2^{(d)}-\tau_{m,p}^{(d\to a)}-\tau_{m,p,2}^{(a)}(\theta^{(d)},\phi^{(d)})\right]\right.\\&\left.+\gamma^{(d)}(t-\tau^{(d)})\right\}.\end{aligned}\tag{57}$$

The response of the receive-antenna array's mth element's pth port to (54) is

$$\begin{aligned}&x_{m,p}^{(u,n)}(t)\approx\\&-\left[K_{m,p,1}^{(a)}(\theta_n^{(u)},\phi_n^{(u)})\bar{K}_{n,1}^{(u)}/2\right]A_n^{(u)}(t-\tau_n^{(u)})\\&\times\cos\left\{2\pi f_{RF}\left[t-\tau_{n,1}^{(u)}-\tau_{n\to m,p}^{(u\to a)}-\tau_{m,p,1}^{(a)}(\theta_n^{(u)},\phi_n^{(u)})\right]\right.\\&\left.+\gamma_n^{(u)}(t-\tau_n^{(u)})\right\}\\&+\left[K_{m,p,2}^{(a)}(\theta_n^{(u)},\phi_n^{(u)})\bar{K}_{n,2}^{(u)}/2\right]A_n^{(u)}(t-\tau_n^{(u)})\\&\times\cos\left\{2\pi f_{RF}\left[t-\tau_{n,2}^{(u)}-\tau_{n\to m,p}^{(u\to a)}-\tau_{m,p,2}^{(a)}(\theta_n^{(u)},\phi_n^{(u)})\right]\right.\\&\left.+\gamma_n^{(u)}(t-\tau_n^{(u)})\right\}.\end{aligned}\tag{58}$$

WSS, Gaussian, zero-mean thermal-noise signal

$$\begin{aligned}x_{m,p}^{(tn)}(t)\;=\;&x_{I,m,p}^{(tn)}(t)\cos(2\pi f_{RF}t)\\&-x_{Q,m,p}^{(tn)}(t)\sin(2\pi f_{RF}t)\end{aligned},\tag{59}$$

additively corrupts the output of the pth port of the mth antenna-array element. In (59) ${x_{I,m,p}}^{(tn)}(t)$ and ${x_{Q,m,p}}^{(tn)}(t)$ are, respectively, the I and Q components of ${x_{m,p}}^{(tn)}(t)$. The thermal-noise signal has PSD

$$S_{m,p}^{(tn)}(f)=\frac{N_{m,p}^{(tn)}}{2}\left[\Pi\left(\frac{f-f_{RF}}{B_{m,p}^{(tn)}}\right)+\Pi\left(\frac{f+f_{RF}}{B_{m,p}^{(tn)}}\right)\right],\tag{60}$$

where ${N_{m,p}}^{(tn)}/2$ is the PSD's level in W/Hz and ${B_{m,p}}^{(tn)}$ is the RF bandwidth in Hz of the thermal noise of the pth port of the mth antenna-array element. The I and Q thermal-noise components of the pth port of the mth antenna-array element are independent, zero-mean, Gaussian, WSS random lowpass processes with PSD

$$S_{I,m,p}^{(tn)}(f)=S_{Q,m,p}^{(tn)}(f)=N_{m,p}^{(tn)}\Pi\left[f/B_{m,p}^{(tn)}\right].\tag{61}$$

H. Receiver/spatial-processor model

Figure 8 shows the $2M$ ports' output signals feeding the employed receiver/spatial-processor model. Phase-synchronized quadrature demodulators [17] linearly produce the complex envelopes of their respective inputs.

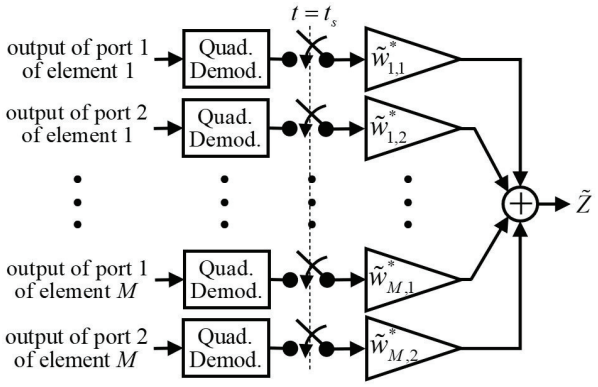

Fig. 8. Receiver/spatial-processor model.

Samplers then take time-coincident samples of these complex envelopes, and the weight-and-sum network produces a weighted sum of the $2M$ sampled values. The model of Figure 8 represents several practical systems. For example, this model represents a system which scales in amplitude and shifts in phase $2M$ RF signals prior to summing them to produce a single RF signal which then feeds, e.g., a global navigation satellite system (GNSS) receiver or a single GNSS-receiver channel (i.e., a channel corresponding to a specific GNSS satellite's unique pseudorandom-noise code).

The complex envelope of (57) is

$$\tilde{x}^{(d)}_{m,p}(t) \approx \tilde{d}_{m,p} A^{(d)}(t-\tau^{(d)}) e^{j\gamma^{(d)}(t-\tau^{(d)})}, \tag{62}$$

where

$$\begin{aligned}
\tilde{d}_{m,p} &= -K^{(a)}_{m,p,1}(\theta^{(d)},\phi^{(d)})\bar{K}^{(d)}_1 \Big/ 2 \\
&\times e^{-j2\pi f_{RF}[\tau^{(d)}_1 + \tau^{(d\to a)}_{m,p} + \tau^{(a)}_{m,p,1}(\theta^{(d)},\phi^{(d)})]} \\
&+ K^{(a)}_{m,p,2}(\theta^{(d)},\phi^{(d)})\bar{K}^{(d)}_2 \Big/ 2 \\
&\times e^{-j2\pi f_{RF}[\tau^{(d)}_2 + \tau^{(d\to a)}_{m,p} + \tau^{(a)}_{m,p,2}(\theta^{(d)},\phi^{(d)})]} \\
&= e^{-j2\pi f_{RF}\tau^{d\to a}_{m,p}} \\
&\times \left\{ -K^{(a)}_{m,p,1}(\theta^{(d)},\phi^{(d)})\bar{K}^{(d)}_1 \Big/ 2 \right. \\
&\times e^{-j2\pi f_{RF}\left[\tau^{(d)}_1 + \tau^{(a)}_{m,p,1}(\theta^{(d)},\phi^{(d)})\right]} \\
&+ K^{(a)}_{m,p,2}(\theta^{(d)},\phi^{(d)})\bar{K}^{(d)}_2 \Big/ 2 \\
&\left. \times\, e^{-j2\pi f_{RF}\left[\tau^{(d)}_2 + \tau^{(a)}_{m,p,2}(\theta^{(d)},\phi^{(d)})\right]} \right\} \\
&\approx e^{-j2\pi f_{RF}\left[\frac{r^{(d)} - s_{\theta^{(d)}} c_{\phi^{(d)}} x^{(a)}_{m,p} - s_{\theta^{(d)}} s_{\phi^{(d)}} y^{(a)}_{m,p} - c_{\theta^{(d)}} z^{(a)}_{m,p}}{c}\right]} \\
&\times \left\{ -K^{(a)}_{m,p,1}(\theta^{(d)},\phi^{(d)})\bar{K}^{(d)}_1 \Big/ 2 \right. \\
&\times e^{-j2\pi f_{RF}\left[\tau^{(d)}_1 + \tau^{(a)}_{m,p,1}(\theta^{(d)},\phi^{(d)})\right]} \\
&+ K^{(a)}_{m,p,2}(\theta^{(d)},\phi^{(d)})\bar{K}^{(d)}_2 \Big/ 2 \\
&\left. \times\, e^{-j2\pi f_{RF}\left[\tau^{(d)}_2 + \tau^{(a)}_{m,p,2}(\theta^{(d)},\phi^{(d)})\right]} \right\}.
\end{aligned} \tag{63}$$

For future convenience we define

$$\begin{aligned}
\tilde{g}_{m,p} &= e^{-j2\pi f_{RF}\left[\frac{-s_{\theta^{(d)}} c_{\phi^{(d)}} x^{(a)}_{m,p} - s_{\theta^{(d)}} s_{\phi^{(d)}} y^{(a)}_{m,p} - c_{\theta^{(d)}} z^{(a)}_{m,p}}{c}\right]} \\
&\times \left\{ -K^{(a)}_{m,p,1}(\theta^{(d)},\phi^{(d)})\bar{K}^{(d)}_1 \Big/ 2 \right. \\
&\times e^{-j2\pi f_{RF}\left[\tau^{(d)}_1 + \tau^{(a)}_{m,p,1}(\theta^{(d)},\phi^{(d)})\right]} \\
&+ K^{(a)}_{m,p,2}(\theta^{(d)},\phi^{(d)})\bar{K}^{(d)}_2 \Big/ 2 \\
&\left. \times\, e^{-j2\pi f_{RF}\left[\tau^{(d)}_2 + \tau^{(a)}_{m,p,2}(\theta^{(d)},\phi^{(d)})\right]} \right\} \\
&\Rightarrow \tilde{d}_{m,p} \approx e^{-j2\pi f_{RF} r^{(d)}/c} \tilde{g}_{m,p}.
\end{aligned} \tag{64}$$

The complex envelope of (58) is

$$\begin{aligned}
\tilde{x}^{(u,n)}_{m,p}(t) &\approx \tilde{u}_{n,m,p} A^{(u)}_n (t-\tau^{(u)}_n) e^{j\gamma^{(u)}_n (t-\tau^{(u)}_n)} \\
&= \tilde{u}_{n,m,p}\left[x^{(u)}_{I,n}(t-\tau^{(u)}_n) + j x^{(u)}_{Q,n}(t-\tau^{(u)}_n) \right],
\end{aligned} \tag{65}$$

where

$$\begin{aligned}
\tilde{u}_{n,m,p} &= -K^{(a)}_{m,p,1}(\theta^{(u)}_n,\phi^{(u)}_n)\bar{K}^{(u)}_{n,1}/2 \\
&\times e^{-j2\pi f_{RF}\left[\tau^{(u)}_{n,1} + \tau^{(u\to a)}_{n\to m,p} + \tau^{(a)}_{m,p,1}(\theta^{(u)}_n,\phi^{(u)}_n)\right]} \\
&+ K^{(a)}_{m,p,2}(\theta^{(u)}_n,\phi^{(u)}_n)\bar{K}^{(u)}_{n,2}/2 \\
&\times e^{-j2\pi f_{RF}\left[\tau^{(u)}_{n,2} + \tau^{(u\to a)}_{n\to m,p} + \tau^{(a)}_{m,p,2}(\theta^{(u)}_n,\phi^{(u)}_n)\right]} \\
&= e^{-j2\pi f_{RF}\tau^{(u\to a)}_{n\to m,p}} \left[-K^{(a)}_{m,p,1}(\theta^{(u)}_n,\phi^{(u)}_n)\bar{K}^{(u)}_{n,1}/2 \right. \\
&\times e^{-j2\pi f_{RF}\left[\tau^{(u)}_{n,1} + \tau^{(a)}_{m,p,1}(\theta^{(u)}_n,\phi^{(u)}_n)\right]} \\
&+ K^{(a)}_{m,p,2}(\theta^{(u)}_n,\phi^{(u)}_n)\bar{K}^{(u)}_{n,2}/2 \\
&\left. \times\, e^{-j2\pi f_{RF}\left[\tau^{(u)}_{n,2} + \tau^{(a)}_{m,p,2}(\theta^{(u)}_n,\phi^{(u)}_n)\right]} \right] \\
&\approx e^{-j2\pi f_{RF}\left[\frac{r^{(u)}_n - s_{\theta^{(u)}_n} c_{\phi^{(u)}_n} x^{(a)}_{m,p} - s_{\theta^{(u)}_n} s_{\phi^{(u)}_n} y^{(a)}_{m,p} - c_{\theta^{(u)}_n} z^{(a)}_{m,p}}{c}\right]} \\
&\times \left[-K^{(a)}_{m,p,1}(\theta^{(u)}_n,\phi^{(u)}_n)\bar{K}^{(u)}_{n,1}/2 \right. \\
&\times e^{-j2\pi f_{RF}\left[\tau^{(u)}_{n,1} + \tau^{(a)}_{m,p,1}(\theta^{(u)}_n,\phi^{(u)}_n)\right]} \\
&+ K^{(a)}_{m,p,2}(\theta^{(u)}_n,\phi^{(u)}_n)\bar{K}^{(u)}_{n,2}/2 \\
&\left. \times\, e^{-j2\pi f_{RF}\left[\tau^{(u)}_{n,2} + \tau^{(a)}_{m,p,2}(\theta^{(u)}_n,\phi^{(u)}_n)\right]} \right].
\end{aligned} \tag{66}$$

For future convenience we define

$$\begin{aligned}
\tilde{h}_{n,m,p} &= e^{-j2\pi f_{RF}\left[\frac{-s_{\theta^{(u)}_n} c_{\phi^{(u)}_n} x^{(a)}_{m,p} - s_{\theta^{(u)}_n} s_{\phi^{(u)}_n} y^{(a)}_{m,p} - c_{\theta^{(u)}_n} z^{(a)}_{m,p}}{c}\right]} \\
&\times \left[-K^{(a)}_{m,p,1}(\theta^{(u)}_n,\phi^{(u)}_n)\bar{K}^{(u)}_{n,1}/2 \right. \\
&\times e^{-j2\pi f_{RF}\left[\tau^{(u)}_{n,1} + \tau^{(a)}_{m,p,1}(\theta^{(u)}_n,\phi^{(u)}_n)\right]} \\
&+ K^{(a)}_{m,p,2}(\theta^{(u)}_n,\phi^{(u)}_n)\bar{K}^{(u)}_{n,2}/2 \\
&\left. \times\, e^{-j2\pi f_{RF}\left[\tau^{(u)}_{n,2} + \tau^{(a)}_{m,p,2}(\theta^{(u)}_n,\phi^{(u)}_n)\right]} \right] \\
&\Rightarrow \tilde{u}_{n,m,p} \approx e^{-j2\pi f_{RF} r^{(u)}_n/c} \tilde{h}_{n,m,p}.
\end{aligned} \tag{67}$$

The complex envelope of (59) is

$$\tilde{x}^{(tn)}_{m,p}(t) = x^{(tn)}_{I,m,p}(t) + j x^{(tn)}_{Q,m,p}(t). \tag{68}$$

The component of the sampled complex envelope of the mth element's pth port's output due to the desired emitter's signal is

$$\begin{aligned}\tilde{x}_{m,p}^{(d)}(t_s) &= \tilde{X}_{m,p}^{(d)} \\ &\approx \tilde{d}_{m,p} A^{(d)}(t_s - \tau^{(d)}) e^{j\gamma^{(d)}(t_s-\tau^{(d)})}.\end{aligned} \tag{69}$$

The component of the sampled complex envelope of the mth element's pth port's output due to the nth undesired emitter's signal is

$$\begin{aligned}\tilde{x}_{m,p}^{(u,n)}(t_s) &= \tilde{X}_{m,p}^{(u,n)} \\ &\approx \tilde{u}_{n,m,p}\left[x_{I,n}^{(u)}(t_s - \tau_n^{(u)}) + jx_{Q,n}^{(u)}(t_s - \tau_n^{(u)})\right].\end{aligned} \tag{70}$$

The component of the sampled complex envelope of the mth element's pth port's output due to thermal noise is

$$\begin{aligned}\tilde{x}_{m,p}^{(tn)}(t_s) &= \tilde{X}_{m,p}^{(tn)} \\ &= x_{I,m,p}^{(tn)}(t_s) + jx_{Q,m,p}^{(tn)}(t_s) = X_{I,m,p}^{(tn)} + jX_{Q,m,p}^{(tn)}.\end{aligned} \tag{71}$$

The receiver/spatial processor's final output is

$$\tilde{Z} = \sum_{p=1}^{2}\sum_{m=1}^{M} \tilde{w}_{m,p}^{*}\left[\tilde{X}_{m,p}^{(d)} + \sum_{n=1}^{N}\tilde{X}_{n,m,p}^{(u)} + \tilde{X}_{m,p}^{(tn)}\right]. \tag{72}$$

The component of the receiver/spatial processor's final output due to the desired emitter's signal is

$$\begin{aligned}\tilde{S} &= \sum_{p=1}^{2}\sum_{m=1}^{M} \tilde{w}_{m,p}^{*}\tilde{X}_{m,p}^{(d)} \\ &\approx A^{(d)}(t_s - \tau^{(d)}) e^{j\gamma^{(d)}(t_s-\tau^{(d)})} \sum_{p=1}^{2}\sum_{m=1}^{M} \tilde{w}_{m,p}^{*}\tilde{d}_{m,p}.\end{aligned} \tag{73}$$

The component of the receiver/spatial processor's final output due to the N undesired emitters' signals is

$$\begin{aligned}\tilde{U} &= \sum_{p=1}^{2}\sum_{m=1}^{M} \tilde{w}_{m,p}^{*}\sum_{n=1}^{N}\tilde{X}_{n,m,p}^{(u)} = \sum_{n=1}^{N}\sum_{p=1}^{2}\sum_{m=1}^{M} \tilde{w}_{m,p}^{*}\tilde{X}_{n,m,p}^{(u)} \\ &\approx \sum_{n=1}^{N}\left[x_{I,n}^{(u)}(t_s - \tau_n^{(u)}) + jx_{Q,n}^{(u)}(t_s - \tau_n^{(u)})\right] \\ &\times \sum_{p=1}^{2}\sum_{m=1}^{M} \tilde{w}_{m,p}^{*}\tilde{u}_{n,m,p}.\end{aligned} \tag{74}$$

The component of the receiver/spatial processor's final output due to the $2M$ thermal-noise signals is

$$\begin{aligned}\tilde{N} &= \sum_{p=1}^{2}\sum_{m=1}^{M} \tilde{w}_{m,p}^{*}\tilde{X}_{m,p}^{(tn)} \\ &= \sum_{p=1}^{2}\sum_{m=1}^{M} \tilde{w}_{m,p}^{*}\left[X_{I,m,p}^{(tn)} + jX_{Q,m,p}^{(tn)}\right].\end{aligned} \tag{75}$$

I. Problem statement

We define the SIR as [12]

$$SIR \triangleq \frac{\left|\tilde{S}\right|^2}{E\left[\left|\tilde{U} + \tilde{N}\right|^2\right]}, \tag{76}$$

where $E(\cdot)$ denotes expectation. We desire to maximize (76) by choosing

$$\mathbf{w} = \left[\begin{array}{cccc}\tilde{w}_{1,1} & \tilde{w}_{1,2} & \cdots & \tilde{w}_{M,1} \;\; \tilde{w}_{M,2}\end{array}\right]^T \tag{77}$$

subject to the traditional and practical constraint [12]

$$\mathbf{w}'\mathbf{w} = 1, \tag{78}$$

where the $'$ represents conjugated matrix transposition.

III. ALGORITHM GENERALIZATION

This section generalizes the spatial-processing algorithm of [1] to support arrays of dual-polarization antenna elements. The squared magnitude of (73) is

$$\begin{aligned}\left|\tilde{S}\right|^2 &\approx \left[A^{(d)}(t_s - \tau^{(d)})\right]^2 \left|\sum_{p=1}^{2}\sum_{m=1}^{M} \tilde{w}_{m,p}^{*}\tilde{d}_{m,p}\right|^2 \\ &\approx \left[A^{(d)}(t_s - \tau^{(d)})\right]^2 \left|\sum_{p=1}^{2}\sum_{m=1}^{M} \tilde{w}_{m,p}^{*} e^{-j2\pi f_{RF} r^{(d)}/c}\tilde{g}_{m,p}\right|^2 \\ &= \left[A^{(d)}(t_s - \tau^{(d)})\right]^2 \left|\sum_{p=1}^{2}\sum_{m=1}^{M} \tilde{w}_{m,p}^{*}\tilde{g}_{m,p}\right|^2.\end{aligned} \tag{79}$$

By defining a second complex vector

$$\mathbf{s} = \left[\begin{array}{cccc}\tilde{g}_{1,1} & \tilde{g}_{1,2} & \cdots & \tilde{g}_{M,1} \;\; \tilde{g}_{M,2}\end{array}\right]^T, \tag{80}$$

we can write (79) as

$$\left|\tilde{S}\right|^2 \approx \left[A^{(d)}(t_s - \tau^{(d)})\right]^2 \left|\mathbf{w}'\mathbf{s}\right|^2. \tag{81}$$

Since the $2M$ thermal-noise signals and the N undesired emitters' signals are zero mean and mutually uncorrelated,

$$\begin{aligned}E\left[\left|\tilde{U} + \tilde{N}\right|^2\right] &= E\left[\left(\tilde{U} + \tilde{N}\right)\left(\tilde{U} + \tilde{N}\right)^*\right] \\ &= E\left[\left|\tilde{U}\right|^2 + \tilde{U}\tilde{N}^* + \tilde{N}\tilde{U}^* + \left|\tilde{N}\right|^2\right] \\ &= E\left[\left|\tilde{U}\right|^2\right] + E\left[\left|\tilde{N}\right|^2\right],\end{aligned} \tag{82}$$

so

$$SIR = \left|\tilde{S}\right|^2 \Big/ \left\{E\left[\left|\tilde{U}\right|^2\right] + E\left[\left|\tilde{N}\right|^2\right]\right\}. \tag{83}$$

Now,

$$\begin{aligned}E\left[\left|\tilde{N}\right|^2\right] &= E\left[\left|\sum_{p=1}^{2}\sum_{m=1}^{M} \tilde{w}_{m,p}^{*}\left[X_{I,m,p}^{(tn)} + jX_{Q,m,p}^{(tn)}\right]\right|^2\right] \\ &= E\left\{\left[\sum_{p=1}^{2}\sum_{m=1}^{M} \tilde{w}_{m,p}^{*}\left[X_{I,m,p}^{(tn)} + jX_{Q,m,p}^{(tn)}\right]\right]\right. \\ &\times \left.\left[\sum_{p=1}^{2}\sum_{m=1}^{M} \tilde{w}_{m,p}\left[X_{I,m,p}^{(tn)} - jX_{Q,m,p}^{(tn)}\right]\right]\right\} \\ &= E\left\{\sum_{p=1}^{2}\sum_{q=1}^{2}\sum_{m=1}^{M}\sum_{l=1}^{M} \tilde{w}_{m,p}^{*}\left[X_{I,m,p}^{(tn)} + jX_{Q,m,p}^{(tn)}\right]\right. \\ &\times \left.\tilde{w}_{l,q}\left[X_{I,l,q}^{(tn)} - jX_{Q,l,q}^{(tn)}\right]\right\} \\ &= \sum_{p=1}^{2}\sum_{q=1}^{2}\sum_{m=1}^{M}\sum_{l=1}^{M} \tilde{w}_{m,p}^{*}\tilde{w}_{l,q}\left\{E\left[X_{I,m,p}^{(tn)}X_{I,l,q}^{(tn)}\right]\right. \\ &+ \left.E\left[X_{Q,m,p}^{(tn)}X_{Q,l,q}^{(tn)}\right]\right\} \\ &= \sum_{p=1}^{2}\sum_{q=1}^{2}\sum_{m=1}^{M}\sum_{l=1}^{M} \tilde{w}_{m,p}^{*}\tilde{w}_{l,q}\left\{2N_{m,p}^{(tn)}B_{m,p}^{(tn)}\delta_{m,l}\delta_{p,q}\right\} \\ &= 2\sum_{p=1}^{2}\sum_{q=1}^{2}\sum_{m=1}^{M} N_{m,p}^{(tn)}B_{m,p}^{(tn)}\tilde{w}_{m,p}^{*}\tilde{w}_{m,q}\delta_{p,q} \\ &= 2\sum_{p=1}^{2}\sum_{m=1}^{M} N_{m,p}^{(tn)}B_{m,p}^{(tn)}\left|\tilde{w}_{m,p}\right|^2,\end{aligned} \tag{84}$$

where $\delta_{m,l}$ represents the Kronecker delta function, having a value of unity if $m = l$ and zero otherwise. We next

write

$$
\begin{aligned}
&E\left[\left|\tilde{U}\right|^2\right] = E\left(\tilde{U}\tilde{U}^*\right)\\
&\approx E\left\{\left\{\sum_{n=1}^{N}\left[x_{I,n}^{(u)}(t_s-\tau_n^{(u)})+jx_{Q,n}^{(u)}(t_s-\tau_n^{(u)})\right]\right.\right.\\
&\times\left.\left(\sum_{p=1}^{2}\sum_{m=1}^{M}\tilde{w}_{m,p}^{*}\tilde{u}_{n,m,p}\right)\right\}\\
&\times\left\{\sum_{n=1}^{N}\left[x_{I,n}^{(u)}(t_s-\tau_n^{(u)})-jx_{Q,n}^{(u)}(t_s-\tau_n^{(u)})\right]\right.\\
&\times\left.\left.\left(\sum_{p=1}^{2}\sum_{m=1}^{M}\tilde{w}_{m,p}\tilde{u}_{n,m,p}^{*}\right)\right\}\right\}\\
&=E\left\{\sum_{n=1}^{N}\sum_{l=1}^{N}\left[x_{I,n}^{(u)}(t_s-\tau_n^{(u)})+jx_{Q,n}^{(u)}(t_s-\tau_n^{(u)})\right]\right.\\
&\times\left[x_{I,l}^{(u)}(t_s-\tau_l^{(u)})-jx_{Q,l}^{(u)}(t_s-\tau_l^{(u)})\right]\\
&\times\left.\left(\sum_{p=1}^{2}\sum_{m=1}^{M}\tilde{w}_{m,p}^{*}\tilde{u}_{n,m,p}\right)\left(\sum_{p=1}^{2}\sum_{m=1}^{M}\tilde{w}_{m,p}\tilde{u}_{l,m,p}^{*}\right)\right\}\\
&=\sum_{n=1}^{N}\sum_{l=1}^{N}E\left\{\left[x_{I,n}^{(u)}(t_s-\tau_n^{(u)})+jx_{Q,n}^{(u)}(t_s-\tau_n^{(u)})\right]\right.\\
&\times\left.\left[x_{I,l}^{(u)}(t_s-\tau_l^{(u)})-jx_{Q,l}^{(u)}(t_s-\tau_l^{(u)})\right]\right\}\\
&\times\left(\sum_{p=1}^{2}\sum_{m=1}^{M}\tilde{w}_{m,p}^{*}\tilde{u}_{n,m,p}\right)\left(\sum_{p=1}^{2}\sum_{m=1}^{M}\tilde{w}_{m,p}\tilde{u}_{l,m,p}^{*}\right).
\end{aligned}
\tag{85}
$$

Manipulation of the expectation in (85) produces

$$
\begin{aligned}
&E\left\{\left[x_{I,n}^{(u)}(t_s-\tau_n^{(u)})+jx_{Q,n}^{(u)}(t_s-\tau_n^{(u)})\right]\right.\\
&\times\left.\left[x_{I,l}^{(u)}(t_s-\tau_l^{(u)})-jx_{Q,l}^{(u)}(t_s-\tau_l^{(u)})\right]\right\}\\
&=E\left[x_{I,n}^{(u)}(t_s-\tau_n^{(u)})x_{I,l}^{(u)}(t_s-\tau_l^{(u)})\right]\\
&+E\left[x_{Q,n}^{(u)}(t_s-\tau_n^{(u)})x_{Q,l}^{(u)}(t_s-\tau_l^{(u)})\right]\\
&=2N_n^{(u)}B_n^{(u)}\delta_{n,l}.
\end{aligned}
\tag{86}
$$

Substituting (86) into (85) gives

$$
\begin{aligned}
&E\left[\left|\tilde{U}\right|^2\right]\approx\sum_{n=1}^{N}\sum_{l=1}^{N}\left[2N_n^{(u)}B_n^{(u)}\delta_{n,l}\right.\\
&\times\left.\left(\sum_{p=1}^{2}\sum_{m=1}^{M}\tilde{w}_{m,p}^{*}\tilde{u}_{n,m,p}\right)\left(\sum_{p=1}^{2}\sum_{m=1}^{M}\tilde{w}_{m,p}\tilde{u}_{l,m,p}^{*}\right)\right]\\
&=\sum_{n=1}^{N}2N_n^{(u)}B_n^{(u)}\left(\sum_{p=1}^{2}\sum_{m=1}^{M}\tilde{w}_{m,p}^{*}\tilde{u}_{n,m,p}\right)\\
&\times\left(\sum_{p=1}^{2}\sum_{m=1}^{M}\tilde{w}_{m,p}\tilde{u}_{n,m,p}^{*}\right)\\
&=\sum_{n=1}^{N}2N_n^{(u)}B_n^{(u)}\sum_{q=1}^{2}\sum_{k=1}^{M}\sum_{p=1}^{2}\sum_{m=1}^{M}\tilde{w}_{m,p}^{*}\tilde{u}_{n,m,p}\tilde{w}_{k,q}\tilde{u}_{n,k,q}^{*}\\
&=\sum_{q=1}^{2}\sum_{k=1}^{M}\sum_{p=1}^{2}\sum_{m=1}^{M}\tilde{w}_{m,p}^{*}\tilde{w}_{k,q}\\
&\times\sum_{n=1}^{N}2N_n^{(u)}B_n^{(u)}\tilde{u}_{n,m,p}\tilde{u}_{n,k,q}^{*}\\
&=\sum_{q=1}^{2}\sum_{k=1}^{M}\sum_{p=1}^{2}\sum_{m=1}^{M}\tilde{w}_{m,p}^{*}\tilde{w}_{k,q}\\
&\times\sum_{n=1}^{N}2N_n^{(u)}B_n^{(u)}\tilde{h}_{n,m,p}\tilde{h}_{n,k,q}^{*}.
\end{aligned}
\tag{87}
$$

For each n ($1\le n\le N$), we define a $2M\times 2M$ matrix

$$
\mathbf{Q}_n = 2N_n^{(u)}B_n^{(u)}\begin{bmatrix}\tilde{h}_{n,1,1}\\ \tilde{h}_{n,1,2}\\ \vdots\\ \tilde{h}_{n,M,1}\\ \tilde{h}_{n,M,2}\end{bmatrix}\begin{bmatrix}\tilde{h}_{n,1,1}^{*}\\ \tilde{h}_{n,1,2}^{*}\\ \vdots\\ \tilde{h}_{n,M,1}^{*}\\ \tilde{h}_{n,M,2}^{*}\end{bmatrix}^{T}. \tag{88}
$$

We can then write

$$
E\left[\left|\tilde{U}\right|^2\right] = \mathbf{w}'\left(\sum_{n=1}^{N}\mathbf{Q}_n\right)\mathbf{w}. \tag{89}
$$

Thus, substituting (81), (84), and (89) into (83) gives

$$
\begin{aligned}
SIR &\approx \frac{\left[A^{(d)}(t_s-\tau^{(d)})\right]^2|\mathbf{w}'\mathbf{s}|^2}{\sum_{n=1}^{N}\mathbf{w}'\mathbf{Q}_n\mathbf{w}+2\sum_{p=1}^{2}\sum_{m=1}^{M}N_{m,p}^{(tn)}B_{m,p}^{(tn)}\left|\tilde{w}_{m,p}\right|^2}\\
&=\left[A^{(d)}(t_s-\tau^{(d)})\right]^2|\mathbf{w}'\mathbf{s}|^2\Big/\left(\mathbf{w}'\mathbf{R}\mathbf{w}\right),
\end{aligned}
\tag{90}
$$

where

$$
\begin{aligned}
\mathbf{R} &= \textstyle\sum_{n=1}^{N}\mathbf{Q}_n+\operatorname{diag}\left[2N_{1,1}^{(tn)}B_{1,1}^{(tn)},\ 2N_{1,2}^{(tn)}B_{1,2}^{(tn)},\right.\\
&\left.\cdots,\ 2N_{M,1}^{(tn)}B_{M,1}^{(tn)},\ 2N_{M,2}^{(tn)}B_{M,2}^{(tn)}\right].
\end{aligned}
\tag{91}
$$

We maximize (90) by choosing

$$
\mathbf{w} = k_C\mathbf{R}^{-1}\mathbf{s}, \tag{92}
$$

where k_C is an arbitrary nonzero complex constant. Finally, we satisfy (78) with

$$
\begin{aligned}
&\mathbf{w}'\mathbf{w} = 1 = k_C^{*}\mathbf{s}'(\mathbf{R}^{-1})'k_C\mathbf{R}^{-1}\mathbf{s}\\
&=|k_C|^2\mathbf{s}'(\mathbf{R}^{-1})'\mathbf{R}^{-1}\mathbf{s}\Rightarrow|k_C| = 1\Big/\sqrt{\mathbf{s}'(\mathbf{R}^{-1})'\mathbf{R}^{-1}\mathbf{s}}.
\end{aligned}
\tag{93}
$$

Since any phase angle for k_C is acceptable, we choose for convenience

$$
k_C = 1\Big/\sqrt{\mathbf{s}'\left(\mathbf{R}^{-1}\right)'\mathbf{R}^{-1}\mathbf{s}}. \tag{94}
$$

IV. SIMULATION RESULTS

To demonstrate the generalized algorithm's performance, we reconsider the example scenario of [1]. Figure 9 shows a perfectly electrically conducting (PEC)

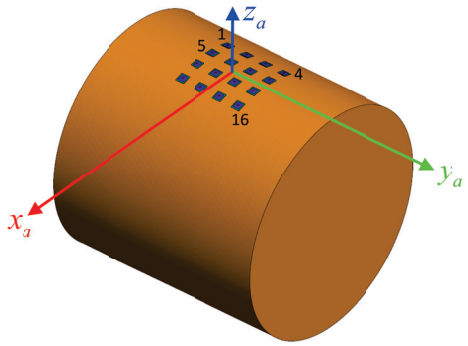

Fig. 9. Antenna array on cylindrical PEC body.

Table 1: Emitter parameters

Emitter	r (km)	θ(°)	ϕ (°)	Transmit Pow. (W)	G (dB)
Des.	100	35	50	don't care	
Undes. 1	100	35	140	0.1	20
Undes. 2	100	105	155	1	20
Undes. 3	100	165	105	2	20

cylindrical body with outer radius 0.5 m and length 1 m. We longitudinally center a 4×4 array of identical, dual-polarization patch (microstrip) antennas on the body's curved outer surface. We number these 16 array elements as shown in Figure 9. Using the procedure of [2], we design the array's probe-fed elements for operation at GPS L1 (f_{RF} = 1575.42 MHz). We longitudinally and circumferentially separate the elements by a half wavelength (9.52 cm). We assume the thermal-noise signal at the output of each port has a noise temperature of 576 K (representing a receive channel with a 4.75-dB standard noise figure [18]) and an RF bandwidth of 1 MHz. Table 1 lists the parameters of the scenario's desired and undesired emitters. All scenario emitters operate at GPS L1 and with perfect RHC polarization. All undesired emitters have 1-MHz RF noise bandwidths.

Figure 10's additional detail of element 11 includes the numbering (common to all 16 elements) of its two feed points (the physical points on the patch to which the ports are directly electrically connected by a probe feed). Each feed point corresponds to a nominally orthogonal linear polarization in the direction normal to the element's copper patch. In [1] we configured each element for single-port operation (thus needing only one complex weight) by applying the same signal to both feed points but with an additional 90° phase lag for feed point 2 with respect to feed point 1. This configuration achieved nominally RHC polarization in the direction normal to the element's patch.

For this paper's generalized algorithm, we assume the receiver/spatial-processor structure of Figure 8 and

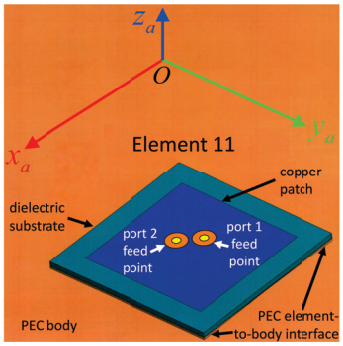

Fig. 10. Detail of antenna element 11.

Table 2: MoM solution and corresponding antenna-model parameters for $m = p = 1$ at $\theta = 35^\circ$ and $\phi = 50^\circ$

$\mathrm{Re}[\tilde{E}_1^{(a,1,1)}(\theta,\phi)]$	$-1.5550709 \times 10^{-5}$ V m^{-1}
$\mathrm{Im}[\tilde{E}_1^{(a,1,1)}(\theta,\phi)]$	$3.50444601 \times 10^{-6}$ V m^{-1}
$E_1^{(a,1,1)}(\theta,\phi)$	$1.59406930 \times 10^{-5}$ V m^{-1}
$\gamma_1^{(a,1,1)}(\theta,\phi)$	2.919939365 rad
$K_1^{(a,1,1)}(\theta,\phi)$	0.00113871745
$\tau_1^{(a,1,1)}(\theta,\phi)$	$1.89938530409 \times 10^{-10}$ s
$k_1^{(a,1,1)}$	525,505
$\mathrm{Re}[\tilde{E}_2^{(a,1,1)}(\theta,\phi)]$	$2.03270802 \times 10^{-5}$ V m^{-1}
$\mathrm{Im}[\tilde{E}_2^{(a,1,1)}(\theta,\phi)]$	$-6.2683354 \times 10^{-6}$ V m^{-1}
$E_2^{(a,1,1)}(\theta,\phi)$	$2.12716294 \times 10^{-5}$ V m^{-1}
$\gamma_2^{(a,1,1)}(\theta,\phi)$	–0.2991212046 rad
$K_2^{(a,1,1)}(\theta,\phi)$	0.0015195309
$\tau_2^{(a,1,1)}(\theta,\phi)$	$5.151403190 \times 10^{-10}$ s
$k_2^{(a,1,1)}$	525,505

Table 3: Complex weights

m	p	Value
1	1	0.077819763793407 – j0.029465368993892
	2	0.12459247349541 + j0.056703522041672
2	1	0.04516455849397 + j0.088872686331463
	2	–0.065219319424497 + j0.12102226092079
3	1	–0.084334092382453 + j0.05080185997583
	2	–0.080437225078455 – j0.03253844379338
4	1	–0.064700015503375 – j0.09520474257253
	2	–0.006716174970139 – j0.09855765370402
5	1	0.07240921216198 + j0.128209559888171
	2	–0.15646309053785 + j0.092759629157202
6	1	–0.1181600997625 + j0.0987977754199944
	2	–0.12530905300321 – j0.158594127589902
7	1	0.121564402276342 – j0.100967272857737
	2	0.129714464685709 – j0.137050242386695
8	1	0.086584951359559 – j0.138732803481413
	2	0.17288811461883 + j0.089184429403536
9	1	–0.14794676203213 + j0.222500477675839
	2	–0.18429998546202 – j0.104658615087023
10	1	–0.24105956227135 – j0.087952073329248
	2	0.09175938725054 – j0.211979313185187
11	1	0.036227149294823 – j0.253494967774504
	2	0.20696199056989 + j0.044332359948352
12	1	0.23987987902997 – j0.0066528888725053
	2	0.003340598877023 + j0.21313132797126
13	1	–0.15316226330551 – j0.026851522912361
	2	–0.036866990090258 – j0.13751921996212
14	1	0.0022933490913445 – j0.16987881222102
	2	0.15162145119333 – j0.0696164846633674
15	1	0.160637367698868 – j0.026138400102631
	2	0.056684020299592 + j0.15759987438645
16	1	0.040167786422328 + j0.17579356008101
	2	–0.13038580760452 + j0.081501570656114

seek the 32 complex weights to maximize (90). To this end we first populate the parameters of the desired and undesired emitters' antenna models of Figure 6 and Figure 7, respectively, using the technique of [16]. We then use a CES (FEKO's method-of-moments (MoM) solver) to calculate the far-field vector electric-field data for each port of each antenna element with that port enabled and the other 31 ports disabled. We collect the far-field vector electric-field data at a constant slant range of 100 km for $0^\circ \leq \theta \leq 180^\circ$ and $0^\circ \leq \phi < 360^\circ$ in 5° increments each. To populate the parameters of the model of Figure 5 for all 32 ports, we process the electric-field data according to (24)–(28), assuming the phase center is at the center of the corresponding element's copper patch. Table 2 shows FEKO's electric-field solution and the corresponding antenna-model parameters for the first element's first port for $\theta = 35^\circ$ and $\phi = 50^\circ$.

Table 3 lists the complex weights calculated with (92) and (94). To find the optimally weighted array's total and effective receive-gain patterns, we firstly exploit the principle of reciprocity by applying the calculated complex weights to the respective ports as source-signal amplitudes and phases. We then use FEKO's MoM solver to numerically calculate the total and effective (RHC-polarization, in this case) transmit-gain patterns.

The annotated plots of Figure 11 and Figure 12 respectively show the achieved total-gain and effective-gain patterns. Clearly, the resulting gain patterns favor the desired emitter's angular location with high total gain and nearly equal effective (i.e., RHC-polarization) gain, indicating very low polarization-mismatch loss due to an excellent match to the desired emitter's polarization. In sharp contrast, however, the resulting gain patterns disfavor the undesired emitters' angular locations with significantly lower total gains and strikingly lower RHC-polarization gains, indicating very high polarization-mismatch losses due to nearly perfect mismatches to the undesired emitters' polarization. That is, in the directions of the undesired emitters, the optimally weighted array's polarization states are nearly perfectly antipodal to the undesired emitters' RHC polarization states [19]. Also, as we intuitively expect, the spatial-processing algorithm's calculated weights result in the deepest effective null to counter the most powerful undesired emitter.

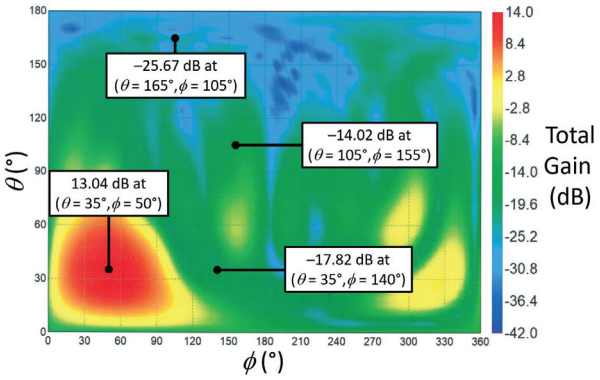

Fig. 11. Total-gain pattern of optimally weighted array.

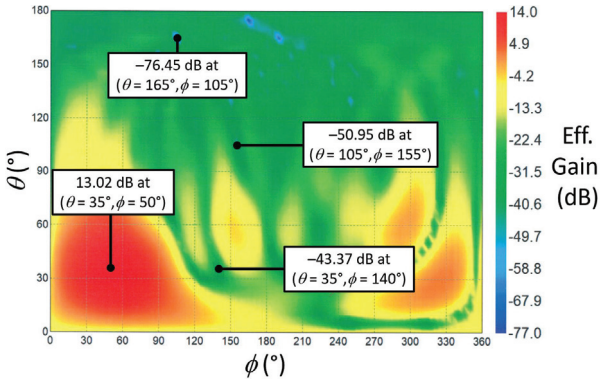

Fig. 12. Effective-gain pattern of optimally weighted array.

Table 4 lists the achieved antenna gain and polarization characteristics corresponding to the desired and undesired emitters' directions for three spatial-processing algorithms. Firstly, the traditional spatial-processing algorithm of [12] uses each individual element's (total) receive directivity (as calculated with FEKO's MoM solver) in the directions of all emitters due to the element itself, the cylindrical body, and the other elements. However, when calculating its sixteen complex weights, this first approach does not account for the apparent signal phase shifts (time delays) introduced within each individual element. Note that this first approach assumes each element is nominally RHC polarized (i.e., each element has a single port which drives both patch feed points with equal amplitude but with a 90° phase lag applied between the element's single port and its second feed point). Secondly, we repeat the results of the modern, improved algorithm of [1]. Like the traditional algorithm, the improved algorithm assumes single-port, nominally RHC-polarized elements. However, when calculating the sixteen complex weights, the improved algorithm does account for each individual element's apparent internal attenuations and phase shifts using the high-fidelity antenna model of [15]. Thirdly, we report the results of this paper's generalized algorithm in which we apply the thirty-two complex weights to their corresponding array ports (each connected directly to a patch feed point).

The results listed in Table 4 indicate the improved algorithm of [1] drastically outperforms the traditional

Table 4: Achieved antenna gain and polarization characteristics in emitter directions

	Traditional Algorithm	Improved Algorithm	Generalized Algorithm
Desired Emitter			
G	12.65 dB	12.78 dB	13.04 dB
G_{eff}	12.63 dB	12.76 dB	13.02 dB
L_{pmm}	0.02 dB	0.02 dB	0.02 dB
R	1.137	1.149	1.159
α	63.53°	63.87°	19.53°
s	R	R	R
Undesired Emitter 1			
G	–2.64 dB	–29.08 dB	–17.82 dB
G_{eff}	–2.72 dB	–43.24 dB	–43.37 dB
L_{pmm}	0.09 dB	14.16 dB	25.56 dB
R	1.329	1.500	1.112
α	175.84°	21.21°	74.61°
s	R	L	L
Undesired Emitter 2			
G	–15.54 dB	–25.83 dB	–14.02 dB
G_{eff}	–18.85 dB	–49.54 dB	–50.95 dB
L_{pmm}	3.30 dB	23.71 dB	39.94 dB
R	30.488	1.140	1.029
α	143.22°	85.97°	88.28°
s	L	L	L
Undesired Emitter 3			
G	–24.81 dB	–32.59 dB	–25.67 dB
G_{eff}	–30.32 dB	–65.61 dB	–76.45 dB
L_{pmm}	5.52 dB	33.02 dB	50.79 dB
R	4.333	1.046	1.006
α	30.03°	31.03°	118.56°
s	L	L	L

algorithm in nullsteering. Specifically, the improved algorithm yielded much lower effective gain (the most important figure of merit highlighted in yellow in Table 4) in each undesired emitter's direction. The improved algorithm also yielded modestly better beamforming as evidenced by its higher effective gain in the desired emitter's direction. The improved algorithm's performance advantage stems from complex weights calculated using high-fidelity quantitative data describing each element's apparent internal attenuations and delays which account for that element's inherent structure and the presence of the body and the other elements.

The results listed in Table 4 also indicate this paper's generalized algorithm yields even better nullsteering and beamforming than the improved algorithm. The generalized algorithm's performance advantage stems from the algorithm's high-fidelity calculation of complex weights for both ports of each dual-polarization element. Note that the generalized algorithm produced typically modest performance advantages over the improved algorithm as compared to the conspicuous performance advantages the improved algorithm demonstrated over the traditional algorithm. The only exception to this was the significantly lower effective gain in the direction of undesired emitter 3–the interference source producing the highest spatial power density at the receive array's location.

Interestingly, for this example scenario, the generalized spatial-processing algorithm achieved its lower effective gains via combinations of *higher* total gain and much higher polarization-mismatch loss as compared to the improved spatial-processing algorithm's results. Note that the generalized algorithm's performance improvements require more advanced antenna elements to transmit and/or receive two nominally orthogonal polarizations, additional CES computations to characterize the extra port models, more computations to obtain the optimal complex weights, and a more complex receiver/spatial processor to modify and combine the additional signals.

V. CONCLUSION

This paper generalized a recently improved spatial-processing algorithm for arrays of potentially diverse antenna elements arbitrarily arranged on a body of arbitrary shape and material composition. Whereas the improved algorithm applied exclusively to arrays of single-port elements, the generalized algorithm supports arrays of dual-polarization antenna elements. Unlike traditional spatial-processing algorithms, the generalized algorithm requires high-fidelity far-field gain and polarization data in the directions of the desired and undesired communication nodes for both ports of each array element. Only a CES or sophisticated testing can provide such data since each element's data must account for the presence of the body and the other antenna elements. The generalized algorithm also requires the total gain and polarization characteristics of each desired and undesired communication node's antenna in the direction of the antenna array. After appropriate processing this information populates the parameters of recently developed high-fidelity antenna models (both transmit and receive modes). The generalized algorithm uses the populated antenna models to obtain a highly detailed expression for SIR which is mathematically compatible with the traditional technique for calculating the optimal complex weights. In an illustrative practical example simulated with high fidelity via a CES, the generalized spatial-processing algorithm outperformed both the improved algorithm and the traditional algorithm.

This paper's investigation and development suggest several potential avenues for additional, related work. Firstly, space-time adaptive processing [12–14] may exhibit improved performance after a

straightforward integration of this paper's high-fidelity spatial-processing technique. Secondly, in Section IV the generalized algorithm achieved its exceptional performance using double-precision computations to calculate complex weights having about fifteen significant digits in both their real and imaginary parts. However, some practical (e.g., legacy) systems can only effect much coarser control of signal amplitude and phase. Thus, an investigation of the generalized algorithm's performance under such limitations could help assess the breadth of the algorithm's practical applicability. Thirdly, adapting this paper's algorithm to arrays comprising arbitrary combinations of single-polarization and dual-polarization elements represents a further yet straightforward generalization. Fourthly, one may adapt this paper's generalized algorithm to use antenna-element models with orthogonally circularly polarized components as described in [20, 21] rather than orthogonally linearly polarized components. Fifthly, the gain and polarization data describing the undesired emitters may not be available. In such cases we may still use the high-fidelity representation of (64) and (80), assuming the desired emitter's location and antenna properties are available. However, we must approximate (91) with sample-mean techniques [12]. A performance comparison of this suboptimal but practical technique with this paper's optimal but potentially impractical technique might characterize the degradation in results. Finally, Section IV's results suggest the generalized algorithm may rely on high polarization-mismatch losses (as opposed to low total gains) to achieve its exceptional effective null depths. Even a modest change in an undesired emitter's antenna polarization may yield significantly greater RFI penetration of the receiver/spatial processor. Some suitable algorithm modifications might produce lower total gains in the directions of the undesired emitters, perhaps at the expense of lower polarization-mismatch losses. Such a modified spatial-processing algorithm may increase the receive array's overall robustness to any variations in the undesired emitters' polarization states by making the algorithm less reliant on closely matching the array to polarization states antipodal to those of the undesired emitters.

REFERENCES

[1] J. Spitzmiller, "Improved spatial processing through high-fidelity antenna modeling," *IEEE/ION Position, Location, and Navigation Symposium*, Portland, OR, April 2020.

[2] W. Stutzman and G. Thiele, *Antenna Theory and Design, 3rd ed.*, John Wiley & Sons, Hoboken, 2013.

[3] C. Pang, P. Hoogeboom, F. Le Chevalier, H. Russchenberg, J. Dong, T. Wang, and X. Wang, "Dual-polarized planar phased array analysis for meteorological applications," *International Journal of Antennas and Propagation*, 2015.

[4] Z. Chen, T. Li, D. Peng, and K. Du, "Two-dimensional beampattern synthesis for polarized smart antenna array and its sparse array optimization," *International Journal of Antennas and Propagation*, 2020.

[5] R. Fante, "Principles of adaptive space-time-polarization cancellation of broadband interference," MITRE Corporation, 2004.

[6] H. Wang, L. Yang, Y. Yang, and H. Zhang, "Anti-jamming of Beidou navigation based on polarization sensitive array," *Int. Applied Comp. Electromagnetics Society (ACES) Symp.*, Suzhou, China, August 2017.

[7] I. D. Olin, "Polarization characteristics of coherent waves," Naval Research Laboratory publications, NRL/FR/5317-12-10,210, 2012.

[8] C. Liu, Z. Ding, and X. Liu, "Pattern synthesis for conformal arrays with dual polarized antenna elements," *7th Int. Congress on Image and Signal Proc.*, Dalian, China, pp. 968-973, October 2014.

[9] H. Li, T. Wang, and X. Huang, "Joint adaptive AoA and polarization estimation using hybrid dual-polarization antenna arrays," *IEEE Access*, vol. 7, 2019.

[10] M. Golbon-Haghighi, M. Mirmozafari, H. Saeidi-Manesh, and G. Zhang, "Design of a cylindrical crossed dipole phased array antenna for weather surveillance radars," *IEEE Open Journal of Antennas and Propagation*, vol. 2, pp. 402-411, 2021.

[11] E. McMilin, Y. Chen, D. De Lorenzo, D. Akos, T. Walter, T. Lee, and P. Enge, "Single antenna, dual use," *Inside GNSS*, September/October 2015, pp. 40-53, 2015.

[12] M. Budge, Jr. and S. German, *Basic Radar Analysis, 2nd ed.*, Artech House, Boston, 2020.

[13] J. Guerci, *Space-Time Adaptive Processing, 2nd ed.*, Artech House, Boston, 2015.

[14] M. Richards, *Fundamentals of Radar Signal Processing, 2nd ed.*, McGraw-Hill, New York, 2014.

[15] J. Spitzmiller, "Antenna model using ideal passive RF components," *IEEE SoutheastCon*, Raleigh, NC, March 2020.

[16] J. Spitzmiller, "Antenna model from total gain and polarization characteristics," *IEEE SoutheastCon*, Raleigh, NC, March 2020.

[17] I. Cumming and F. Wong, *Digital Processing of Synthetic Aperture Radar Data*, Artech House, Boston, 2005.

[18] P. Peebles, Jr., *Communication System Principles*, Addison-Wesley, Reading, 1976.

[19] J. Kraus, *Antennas, 2nd ed*., McGraw-Hill, New York, 1988.

[20] J. Spitzmiller, "Antenna model using ideal passive RF components and circularly polarized antenna elements," *IEEE SoutheastCon*, Atlanta, GA, March 2021.
[21] J. Spitzmiller, "Antenna model using circularly polarized elements from total gain and polarization characteristics," *IEEE SoutheastCon*, Atlanta, GA, March 2021.

John Spitzmiller has worked for Parsons (formerly Cobham Analytic Solutions and SPARTA, Inc.) in Huntsville, Alabama since 2006. He has served as Chief Engineer of Offensive Missile Programs since 2011. In this position he has worked on a wide variety of efforts involving analysis, modeling, simulation, and assessment of radar, RF-navigation, RF-telemetry, and electronic-warfare systems. Parsons named him a Fellow in 2018. From 1999 to 2006, he served as an electronics engineer in the Scientific and Technical Modeling and Simulation Branch of the Defense Intelligence Agency's Missile and Space Intelligence Center on Redstone Arsenal, Alabama. From 1995 to 1999, he worked in the Sensor Systems and Technologies Department at Dynetics, Inc. in Huntsville, Alabama. A 1994 Goldwater Scholar, he graduated summa cum laude with a B.S. in electrical engineering from the University of Missouri at Rolla in 1995. He subsequently earned an M.S.E. and Ph.D. in electrical engineering from the University of Alabama in Huntsville. His current research interests include advanced techniques for signal, image, and spatial processing and linear and nonlinear state estimation.

Sanyi Choi is a senior engineer at Parsons Government Services, where she has been employed since 2018. She is responsible for performing radar system analysis, modeling, and simulation. She has primarily supported the Defense Intelligence Agency/Missile and Space Intelligence Center (DIA/MSIC) with advanced signal processing methodologies and Synthetic Aperture Imaging. From 2010 to 2018 she was with Northrop Grumman Corp. in Huntsville, Alabama where she worked in Enhanced Command and Control Battle Management and Communications (EC2BMC) activities in support of the Missile Defense Agency (MDA) as a system engineer supporting on the development of advanced discrimination algorithm. She earned a B.S.E. and M.S.E. in electrical engineering from the University of Alabama in Huntsville.

Surrogate-Based Design Optimization of Multi-Band Antenna

Aysu Belen[1], Ozlem Tari[2], Peyman Mahouti[3], Mehmet A. Belen[4], and Alper Çalışkan[5]

[1]Department of Hybrid and Electric Vehicles Technology İskenderun Technical University, Hatay, Turkey
aysu.belen@iste.edu.tr

[2]Department of Mathematics and Computer Science İstanbul Arel University, İstanbul, Turkey
ozlemilgin@arel.edu.tr

[3]Department of Aviation Electrics and Electronics of Yıldız Technical University, Turkey
pmahouti@ytu.edu.tr

[4]Department of Electrical and Electronics İskenderun Technical University, Hatay, Turkey
mali.belen@iste.edu.tr

[5]Department of Electronics and Communication Yıldız Technical University, İstanbul, Turkey
alperc@yildiz.edu.tr

Abstract – In this work, design optimization process of a multi-band antenna via the use of artificial neural network (ANN) based surrogate model and meta-heuristic optimizers are studied. For this mean, first, by using Latin-Hyper cube sampling method, a data set based on 3D full wave electromagnetic (EM) simulator is generated to train an ANN-based model. By using the ANN-based surrogate model and a meta-heuristic optimizer invasive weed optimization (IWO), design optimization of a multi-band antenna for (1) 2.4–3.6 GHz for ISM, LTE, and 5G sub-frequencies, and (2) 9–10 GHz for X-band applications is aimed. The obtained results are compared with the measured and simulated results of 3D EM simulation tool. Results show that the proposed methodology provides a computationally efficient design optimization process for design optimization of multi-band antennas.

Index Terms – Artificial Neural Network (ANN), multi-band antenna, optimization, surrogate modeling.

I. INTRODUCTION

With the rapid improvement in wireless communication systems, many systems with different standards, global system for mobile communications (GSM), universal mobile telecommunications system (UMTS), wireless local area network (WLAN) [1], have been developed in the last decades. Since each of the mentioned systems may require to operate in different frequencies, instead of having multiple antenna designs, it is more convenient to have an antenna with broadband or multi-band characteristics [2–5].

Many works had been proposed for achieving designs with multi-band characteristics using 3D printed multi-layer antenna [6], stacked designs with novel meta-material [7], designs comprising two planar inverted F antenna (PIFA) elements integrated with two PIN diodes [8], alongside of unique designs such as star-shaped patch and their performance evaluations [9].

However, optimization of such designs is a challenging problem where increases in the complexity of design for achieving multi-band characteristics would also increase the simulation duration of these designs. Ultimately, this leads designers to choose between using a coarse model for the design optimization process at the expense of accuracy or using a fine model at the expense of having a computationally inefficient design optimization process [10].

One of the commonly used methods proposed for achieving mentioned design optimization problem is to employ data-driven surrogate models for design optimization. Surrogate-based models have many applications such as parameter tuning [11, 12], statistical analysis [13–15], and multi-objective design [16—18]. Although there are a series of techniques that can be used for surrogate-based modeling such as polynomial regression [19], Kriging interpolation [20], radial basis functions [21], support vector regression [22], and polynomial chaos expansion [23], one of the commonly used technique is artificial neural networks (ANNs) [10, 24].

Herein, to achieve a computationally efficient design optimization process for designing a multi-band antenna, ANN-based surrogate modeling of an antenna design is studied. First, a 3D electromagnetic (EM)

Submitted On: September 16, 2021
Accepted On: January 22, 2022

https://doi.org/10.13052/2022.ACES.J.370104

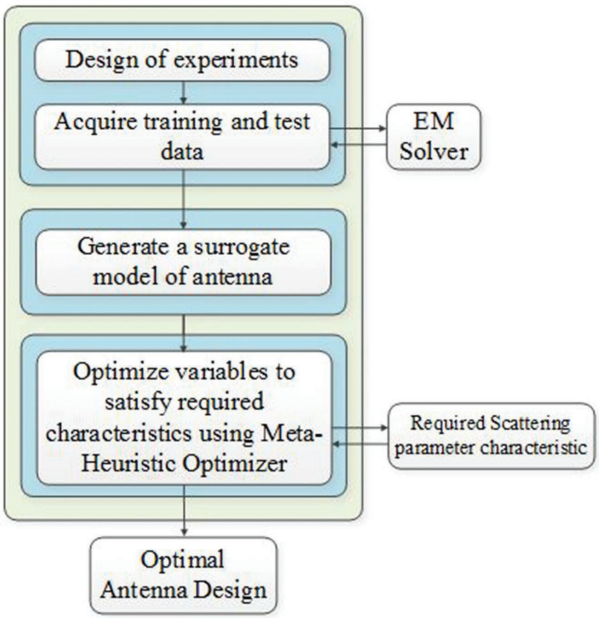

Fig. 1. Flow chart of the proposed design optimization process.

simulation-based data set of the antenna design has been generated using the 3D full-wave EM-simulator tool. Here, a novel regression ANN algorithm, modified multi-layer perceptron (M2LP) [25, 26] is used for creating the mapping between input and output of the data set. After that, by using M2LP, a surrogate model of the design has been generated. Finally, the surrogate model is used alongside of a meta-heuristic optimization algorithm to achieve the desired antenna design. The general procedures of the study are presented in Figure 1.

II. SURROGATE-BASED MODELING OF ANTENNA

A. Proposed multi-band antenna and its data set

In this work, a microstrip antenna (Figure 2) with an E-shaped defected ground structure is taken for study to achieve the requested multi-band characteristics [27]. The antenna consists of a rectangular radiator, a 50-Ω microstrip feed line, and a ground plane. An E-shaped defected ground structure had been placed in the ground layer to tune the resonance frequency of the design without increasing the overall size of the antenna.

In Table 1, the variable space of data set belonging to the proposed antenna design has been presented alongside of their upper and lower limitations. In order to reduce the total number of design variables, some of the design parameters are taken as constants. $S1 = 2 \times W1, S5 = S2 + 2 \times S6, W2 = 11.6$ (mm), and $L2 = 3$ (mm) for having a transmission line with 50-Ω for FR4 substrate, and $S3 = 0.5$ (mm). Furthermore, in order to have a computationally efficient modeling, the number of training samples should be low as much as possible. For this mean, instead of using traditional linear sampling which might end up making the required training samples size up to thousands, Latin-Hyper cube sampling (LHS) method is used for generating design samples from the ranges given in Table 1. By using LHS, a training data set with 500 samples and a test data set with 100 samples had been generated to be used for training the proposed surrogate model. The frequency range is 1–10 GHz with a step size of 0.1.

Table 1: Design variables and their variation limits

Variable	Min	Max
W1	15	25
L1	10	20
S2	5	15
S4	10	20
S6	2	8
S7	2	8

B. ANN-based surrogate model

In this sub-section, the generated data set is used for creating a surrogate model to create a mapping between the given input parameters in Table 1 and scattering parameters of the proposed antenna design. Herein, in order to compare the performance of the M2LP model, traditional counterpart and commonly used state-of-the-art regression algorithms in literature such as (1) multi-layer perceptron, (2) support vector regression machine [22], (3) gradient boosted tree [28], (4) Keras deep residual neural network regressor [29], and (5) Gaussian process regression [30] are taken into consideration. The performance of the mentioned methods is presented in Table 2. The given performance belongs to the k-fold validation results where $k = 5$. Furthermore, for checking the overfitting performance of the models, the holdout performance of the models evaluated using 100 sample test data sets are presented. The given values are calculated using relative mean error (RME) metric:

$$\text{RME} = \frac{1}{N}\sum_{i=1}^{N}\frac{|T_i - P_i|}{|T_i|}. \quad (1)$$

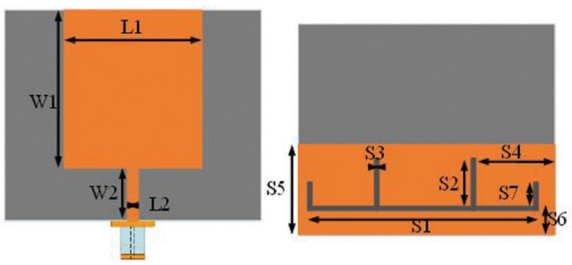

Fig. 2. Schematic of the proposed multi-band antenna.

Table 2: Performance results of surrogate models

Model	HP	*K*-fold/holdout
MLP	Two layers with 20 and 30 neurons	5.8%/6.8%
SVRM [22]	Epsilon SVR, Epsilon = 0.1, with radial basis kernel	7.1%/8.5%
Gradient boosted tree [28]	Learning rate of 0.02 6250 number of estimators and depth of 5	6.6%/7.5%
Keras deep residual neural network regressor [29]	Two layers: 512, 512 units	4.8%/5.3%
Gaussian process regression [30]	Kernel function "matern5/2," prediction method of block coordinate descent with block size of 1500	4.4%/5.2%
M2LP	Depth size of 2, initial neuron number of 32	3.9%/4.8%

Here, T_i is the ith sample targeted value, P_i is the ith sample predicted value, and N is the total number of tested samples over the given operation frequency.

As it can be seen from the table, the M2LP method achieves better k-fold and holdout performance compared to other counterpart algorithms where both of the metrics are less than 5%. Thus, the M2LP does not fall into overfitting while having a good validation error. Thus, from now on, M2LP will be used as the surrogate model of the antenna for the design optimization process.

III. STUDY CASE: DESIGN OPTIMIZATION USING ANN-BASED SURROGATE MODEL

Herein, for the determination of optimal design variables of the proposed multi-band antenna, a population-based meta-heuristic optimization algorithm, invasive weed optimization (IWO) [31], has been used (Figure 3). IWO is inspired from the behavior of weed colonies, in which the population members are in search of an optimal environment to live [31]. Some of the applications of IWO in design optimization of microwave antennas can be named as aperiodic planar thinned array antennas [32], the shape of non-planar electronically scanned arrays [33], directivity maximization of uniform linear array of half-wavelength dipoles [34], low-pass elliptic filter [35], reflector antenna [36], design of a compact step impedance transmission line low-pass filter [37], and design optimization of di-electric loaded horn

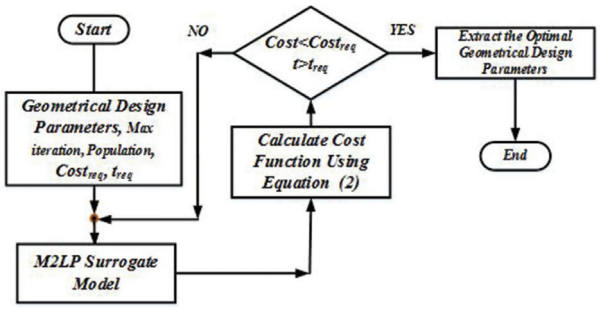

Fig. 3. Flow chart of the IWO search.

Table 3: Optimally selected design values in [mm]

***W*1**	19	***S*4**	13.8
***L*1**	15	***S*6**	3.6
***S*2**	8.5	***S*7**	5.5

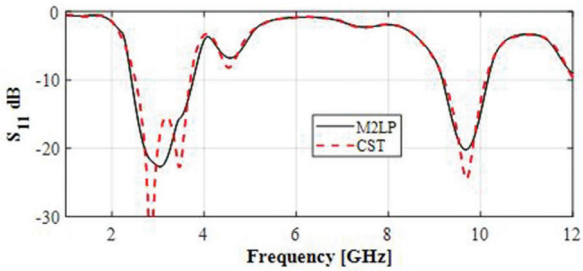

Fig. 4. Simulated results of multi-band antenna.

antennas [38]. The search protocol of the IWO algorithm is driven by cost function defined in the following equation:

$$\text{Cost} = \sum_{f_{\min_1}}^{f_{\max_1}} \frac{C_1}{|S_{11_i}(f)|} + \sum_{f_{\min_2}}^{f_{\max_2}} \frac{C_2}{|S_{11_i}(f)|}. \qquad (2)$$

Here, C values are weighing coefficients of cost function sub-criteria. Since, in this work, the importance of each of the bands is equal, these coefficients are taken equally as $C_1 = C_2 = 1$. Here, the goal is to maximize both of the S_{11} values in the given frequency ranges. The aimed operation bands of the multi-band antenna are taken as: (1) 2.4–3.6 GHz for ISM, LTE, and 5G sub-frequencies; (2) 9–10 GHz for X-band applications.

In Table 3, the optimally selected design variables obtained from IWO algorithm are presented.

The results obtained using the proposed M2LP-based optimization technique had been compared with the simulated results of 3D full-wave EM simulator CST (Figure 4).

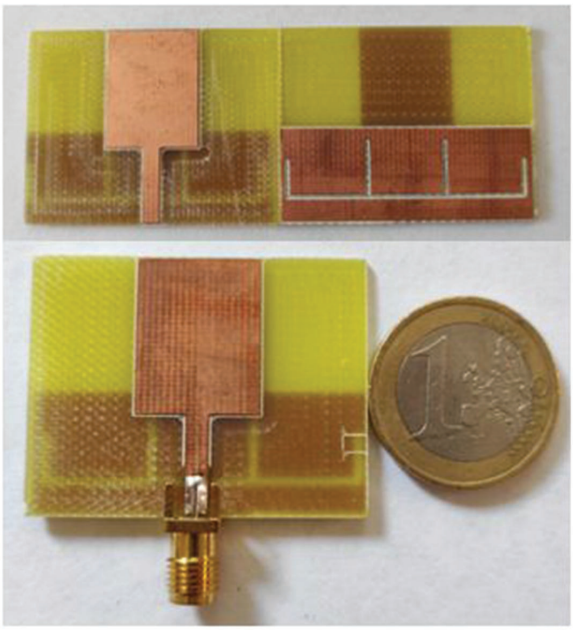

Fig. 5. The prototyped multi-band antenna.

IV. FABRICATION AND MEASUREMENT

For justification of the proposed designed methodology, the designed antenna in the previous section had been prototyped (Figure 5). The measurement devices (a network analyzer with a measurement bandwidth of 9 KHz to 13.5 GHz, and LB-8180-NF broadband horn antenna of 0.8–18 GHz as reference antenna) available in Microwave Laboratories of Yildiz Technical University had been used.

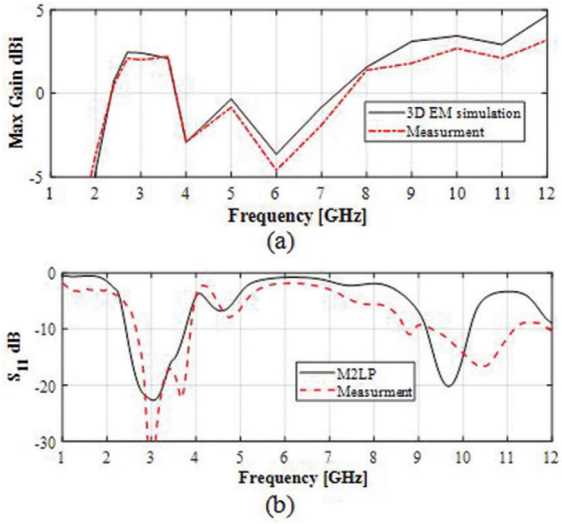

Fig. 6. Measured (a) maximum gain and (b) scattering parameters, over the operation band.

In Figure 6, the measured results of maximum gain over frequency and scattering parameter of prototyped antenna are presented. As it can be seen from the figure, the measured performances of the antenna are in agreement with the simulated results obtained in previous sections.

V. CONCLUSION

Herein, by using surrogate-based modeling technique, a computationally efficient design optimization of a multi-band microstrip antenna has been achieved. Toward this end, a M2LP regression model is used alongside of a meta-heuristic optimization algorithm IWO to determine the optimal design variables for selected operation bands of ISM, LTE, 5G sub-frequencies, and X-band applications. The obtained optimal design performance had been compared with both the simulated results from the 3D full-wave EM simulator tool and measured results of the prototyped antenna. Thus, in this work, computationally efficient design optimization process for having a multi-band microstrip antenna is achieved via the use of a novel regression model M2LP and a meta-heuristic optimization algorithm IWO.

ACKNOWLEDGMENT

We would like to express our special thanks of gratitude to the Aktif Neser Elektronik and DataRobot, for providing researcher licenses for CST and DataRobot.

REFERENCES

[1] A. C. K. Mak, C. R. Rowell, R. D. Murch, and C. Mak, "Reconfigurable multiband antenna designs for wireless communication devices," *IEEE Trans. on Antennas and Prop.*, vol. 55, no. 7, pp. 1919-1928, Jul. 2007.

[2] Y. X. Guo, M. Y. W. Chia, and Z. N. Chen, "Miniature built-in quadband antennas for mobile handsets," *IEEE Antenna Wireless Propag. Lett.*, vol. 2, pp. 30-32, 2004.

[3] I. Ang, Y. X. Guo, and Y. W. Chia, "Compact internal quad-band antenna for mobile phones," *Micro. Opt. Technol. Lett.*, vol. 38, no. 3, pp. 217-223, Aug. 2003.

[4] B. K. Yu, B. Jung, H. J. Lee, F. J. Harackiewicz, and B. Lee, "A folded and bent internal loop antenna for GSM/DCS/PCS operate of mobile handset applications," *Microw. Opt. Technol. Lett.*, vol. 48, no. 3, pp. 463-467, 2006.

[5] H. Hsieh, Y. Lee, K. Tiong, and J. Sun, "Design of a multiband antenna for mobile handset operations," *IEEE Antennas and Wireless Prop. Lett.*, vol. 8, pp. 200-203, 2009.

[6] A. E. Ahmed, and W. A. E. Ali, "A novel multiband antenna with 3D-printed multicircular substrate for wireless applications," *2020 International*

Conference on Electrical, Communication, and Computer Engineering (ICECCE), 2020, pp. 1-5.

[7] R. M. David, T. Ali, and P. A. Kumar, "Multiband antenna stacked with novel metamaterial SCSRR and CSSRR for WiMAX/WLAN applications," *Micromachines*, vol. 12, pp. 113, 2021.

[8] A. Bharathi, R. Shankar, and R. Gosula, "A novel compact multiband reconfigurable WLAN MIMO antenna," *IETE Journal of Research*, 2021.

[9] H. T. Sediq, and Y. N. Mohammed, "Performance analysis of novel multi-band monopole antenna for various broadband wireless applications," *Wireless Pers. Commun*., vol. 112, pp. 571-585, 2020.

[10] P. Mahouti, "Design optimization of a pattern reconfigurable microstrip antenna using differential evolution and 3D EM simulation-based neural network model," *Int. J. RF Microw. Comput. Aided Eng.*, vol. 29, no. 8, 2019.

[11] E. Hassan, D. Noreland, R. Augustine, E. Wadbro, and M. Berggren, "Topology optimization of planar antennas for wideband near-field coupling," *IEEE Trans. Ant. Prop.*, vol. 63, no. 9, pp. 4208-4213, 2015.

[12] J. Wang, X. S. Yang, and B. Z. Wang, "Efficient gradient-based optimization of pixel antenna with large-scale connections," *IET Microwaves Ant. Prop.*, vol. 12, no. 3, pp. 385-389, 2018.

[13] J. Du, and C. Roblin, "Statistical modeling of disturbed antennas based on the polynomial chaos expansion," *IEEE Ant. Wireless Prop. Lett*., vol. 16, p. 1843-1847, 2017.

[14] M. Rossi, A. Dierck, H. Rogier, and D. Vande Ginste, "A stochastic framework for the variability analysis of textile antennas," *IEEE Trans. Ant. Prop*., vol. 62, no. 16, pp. 6510-6514, 2014.

[15] J. S. Ochoa and A. C. Cangellaris, "Random-space dimensionality reduction for expedient yield estimation of passive microwave structures," *IEEE Trans. Microw. Theory. Techn.*, vol. 61, no. 12, pp. 4313-4321, 2013.

[16] J. A. Easum, J. Nagar, P. L. Werner, and D. H. Werner, "Efficient multiobjective antenna optimization with tolerance analysis through the use of surrogate models," *IEEE Trans. Ant. Prop.*, vol. 66, no. 12, pp. 6706-6715, 2018.

[17] J. Dong, W. Qin, and M. Wang, "Fast multi-objective optimization of multi-parameter antenna structures based on improved BPNN surrogate model," *IEEE Access*, vol. 7, pp. 77692-77701, 2019.

[18] S. Koziel and A. T. Sigurdsson, "Multi-fidelity EM simulations and constrained surrogate modeling for low-cost multi-objective design optimization of antennas," *IET Microwaves Ant. Prop*., vol. 12, no. 13, pp. 2025-2029, 2018.

[19] J. L. Chávez-Hurtado, and J. E. Rayas-Sánchez, "Polynomial-based surrogate modeling of RF and microwave circuits in frequency domain exploiting the multinomial theorem," *IEEE Trans. Microwave Theory Tech.,* vol. 64, no. 12, pp. 4371-4381, 2016.

[20] N. V. Queipo, R. T. Haftka, W. Shyy, T. Goel, R. Vaidynathan, and P. K. Tucker, "Surrogate-based analysis and optimization," *Progress in Aerospace Sciences*, vol. 41, no. 1, pp. 1-28, 2005.

[21] P. Barmuta, F. Ferranti, G. P. Gibiino, A. Lewandowski, and D. M. M. P. Schreurs, "Compact behavioral models of nonlinear active devices using response surface methodology," *IEEE Trans. Microwave Theory and Tech*., vol. 63, no. 1, pp. 56-64, 2015.

[22] J. Cai, J. King, C. Yu, J. Liu, and L. Sun, "Support vector regression based behavioral modeling technique for RF power transistors," *IEEE Microwave and Wireless Comp. Lett*., vol. 28, no. 5, pp. 428-430, 2018.

[23] A. Petrocchi, A. Kaintura, G. Avolio, D. Spina, T. Dhaene, A. Raffo, and D. M. P. -P. Schreurs, "Measurement uncertainty propagation in transistor model parameters via polynomial chaos expansion," *IEEE Microwave Wireless Comp. Lett.,* vol. 27, no. 6, pp. 572-574, 2017.

[24] J. E. Rayas-Sanchez, and V. Gutierrez-Ayala, "EM-based statistical analysis and yield estimation using linear-input and neural-output space mapping," *IEEE MTT-S Int. Microwave Symp. Digest (IMS*), pp. 1597-1600, 2006.

[25] N. Calik, M. A. Belen, and P. Mahouti, "Deep learning base modified MLP model for precise scattering parameter prediction of capacitive feed antenna," *Int. J. Numer. Model.*, vol. 33, no. 2, 2020.

[26] T. Mahouti, T. Yıldırım, and N. Kuþkonmaz, "Artificial intelligence–based design optimization of nonuniform microstrip line band pass filter," *Int. J. Numer. Model*. 2021; e2888, in press.

[27] A. Belen, O. Tari, P. Mahouti, M. A. Belen, "Surrogate Based Design Optimization of Multi-Band Antenna," *International Applied Computational Electromagnetics Society (ACES) Symposium*, August 1-5, 2021.

[28] G. Rushin, C. Stancil, M. Sun, S. Adams, and P. Beling, "Horse race analysis in credit card fraud—deep learning, logistic regression, and Gradient Boosted Tree," *In 2017 systems and information*

engineering design symposium (SIEDS), pp. 117-121. IEEE, 2017.

[29] H. Li, Z. Xu, G. Taylor, C. Studer, and T. Goldstein, "Visualizing the loss landscape of neural nets," *Adv Neural Inf Process Syst* , pp. 6389-6399, 2017.

[30] L. Bo, C. Sminchisescu. "Greed block coordinate descent for large scale Gaussian process regression," *In Proceedings of the Twenty Fourth Conference on Uncertainty in Artificial Intelligence* (UAI2008), http://arxiv.org/abs/1206.3238, 2012.

[31] M. Misaghi, and M. Yaghoobi, "Improved invasive weed optimization algorithm (IWO) based on chaos theory for optimal design of PID controller," *J. Comp. Design and Eng.*, vol. 6, no. 3, pp. 284-295, 2019.

[32] S. Karimkashi, and A. A. Kishk, "Invasive weed optimization and its features in electromagnetics," *IEEE Transactions on Antennas and Propagation*, vol.58, no. 4, pp. 1269-1278, 2010.

[33] S. Maddio, G. Pelosi, M. Righini, S. Selleri, and I. Vecchi, "Optimization of the shape of non-planar electronically scanned arrays for IFF applications via multi-objective invasive weed optimization algorithm," *Applied Computational Electromagnetic Society (ACES) Journal*, vol. 35, no. 5, 2020.

[34] A. R. R. Mallahzadeh, H. Oraizi, and Z. Davoodi-Rad, "Application of the invasive weed optimization technique for antenna configurations," *Progress in Electromagnetics Research*, vol. 79, pp. 137-150, 2008.

[35] M. Hayati, M. Amiri, S. H. Sedighy, "Design of compact and wideband suppression low pass elliptic filter by n-segment step impedance transmission line," *Applied Computational Electromagnetic Society (ACES) Journal*, vol. 30, no. 5, 2015.

[36] A. R. Mallahzadeh, and P. Taghikhani, P. "Cosecant squared pattern synthesis for reflector antenna using a stochastic method," *Applied Computational Electromagnetic Society (ACES) Journal,* vol. 26, no. 10, pp. 823-830, 2011.

[37] H. R. Khakzad, S. H. Sedighy, and M. K. Amirhosseini, "Design of compact SITLs low pass filter by using invasive weed optimization (IWO) technique," *Applied Computational Electromagnetic Society (ACES) Journal*, vol. 28, no. 3, pp. 228-233, 2013.

[38] A. Belen, P. Mahouti, F. Günes, F., and Ö. Tari, "Gain enhancement of a traditional horn antenna using 3D printed square-shaped multi-layer dielectric lens for X-band applications," *Applied Computational Electromagnetic Society (ACES) Journal*, vol. 36, no. 2, 2021.

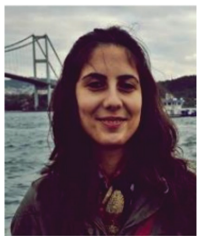

Aysu Belen received her Ph.D degree in Electronics and Communication Engineering from the Yıldız Technical University in 2021. She is currently an Assistant Prof. in İskenderun Technical University. Her main research areas are optimization of microwave circuits, circuits, device modeling, and computer aided circuit design and microwave amplifiers.

Özlem Tari received her B.Sc., M.Sc. and Ph.D. in Physics Engineering from the Istanbul Technical University (ITU). She was the recipient of the Universidad Carlos III de Madrid Research Fellowship award before accepting her position at Istanbul Arel University in 2010. Her research areas are the phase transitions and phase diagram of some physical systems, Multi-Objective Optimization problems and development of Meta-Heuristic Optimization Algorithms.

Peyman Mahouti received his M. Sc. And Ph.D. degree in Electronics and Communication Engineering from the Yıldız Technical University, Turkey, in 2013 and 2016, Respectivly. The main research areas are analytical and numerical modelling of microwave devices, optimization techniques for microwave stages, and application of artificial intelligence-based algorithms. His research interests include analytical and numerical modelling of microwave and antenna structures, surrogate-based optimization, and application of artificial intelligence algorithms.

Mehmet Ali Belen received his Ph.D degree in Electronics and Communication engineering from the Yıldız Technical University in 2016. He is currently an Associated Prof. in İskenderun Technical University. His current activities include teaching and researching

Electromagnetics and Microwaves along with developing Additive Manufacturing 3D Printed Microwave Components for Rapid Prototyping. His current research interests are in the areas of multivariable network theory, device modeling, computer aided microwave circuit design, monolithic microwave integrated circuits, and antenna arrays, active/passive microwave components especially in the field of metamaterial- based antennas and microwave filters.

Alper Çalışkan received his Ph.D. degree in Electronics and Communication Engineering from the Yıldız Technical University in 2019. The main research areas are optimization of microwave circuits, broadband matching circuits, device modeling, and computer aided circuit design, microwave amplifiers.

A Wide-Beam Metasurface Antenna Using Pattern Combination of Characteristic Modes

Shizhe Zhao, Xiuping Li, Yongxin Chen, Wenyu Zhao, and Zihang Qi

[1]State Key Laboratory of Information Photonics and Optical Communications, Beijing University of Posts and Telecommunications, Beijing 100876, China

[2]Key Laboratory of Universal Wireless Communications, Ministry of Education, Beijing 100816, China

[3]Beijing Key Laboratory of Work Safety Intelligent Monitoring, Beijing University of Posts and Telecommunications, Beijing 100876, China

[4]School of Electronic Engineering, Beijing University of Posts and Telecommunications, Beijing 100876, China
szzhao@bupt.edu.cn, xpli@bupt.edu.cn, yongxin.chen@bupt.edu.cn, wyzhao@bupt.edu.cn, qizihang@bupt.edu.cn

Abstract – In this paper, a new method based on characteristic mode analysis for designing wide-beam antennas is proposed. According to theory of characteristic modes, the total radiation pattern is the linear combination of modal currents. The phase of the excitation coefficient is demonstrated to be the characteristic angle. To get a wide-beam pattern, a fundamental mode and an even mode are selected to be excited and combined. The method is verified by the proposed antenna. First, two modes are selected based on characteristic mode analysis. Then the modes are excited separately using different feeding networks. Lastly, a 1-to-3 power divider is proposed to combine the feeding networks. The proposed antenna has a 3-dB beamwidth of over 200° in both 45° and 135° planes. The results have shown that the proposed antenna is suitable for a wide range of detection applications.

Keywords – Beamwidth, characteristic modes, wide-beam antennas.

I. INTRODUCTION

Microstrip antennas have been widely used in many communication systems such as mobile phones, satellite navigation systems, vehicular communication systems, and radar systems. In some cases, a wide beamwidth (half-power beamwidth, HPBW) is required to implement particular applications. For instance, in satellite navigation systems, each satellite is required to cover 120° in order to receive the satellite signal quickly [1]. Also, antennas on vehicles should be aware of its nearby situations; thus, the beamwidth needs to be larger than 150° in the horizontal plane [2]. Detection systems are used for vital signs testing after disasters like earthquakes and fires as well as human body induction for smart lights. Those applications need a wide detection range; so the antennas of the system need to be wide-beam.

There are many ways to enhance the 3-dB HPBW. In [3], the beamwidth of the microstrip patch is broadened by induced vertical currents on the vertical metal walls between the substrate and the ground. The vertical currents can generate a horizontal omnidirectional beam; thus, the outer side of the beam is enhanced. In recent years, some structures based on loading vias on microstrip patches have been proposed in the literature. As reported in [4], the HPBW is improved by decreasing the width of the equivalent slot between the microstrip patches. Based on a similar approach, beamwidth on both E- and H-planes can be extended by adding parasitic patches on both sides of the patch [5]. In [6], a microstrip patch with a blind-via fence has improved the beamwidth a little. In [7], the beamwidth and bandwidth are improved by placing three metallic posts inside the dielectric resonator. For a magnetoelectric tapered-slot antenna proposed in [8], ME modes of multiple slots in the TSA are used to improve the HPBW. Above all, there are plenty of ways to achieve a wide beamwidth, but the design techniques are based on instincts and inspirations of antenna developers, and none of the antennas are designed by clear and structural steps.

Characteristic mode analysis (CMA) is a method of modal decompositions originally proposed by Garbacz [9] and established as a complete theory based on the method of moments (MoM) by Harrington and Mautz [10, 11]. Due to limited computing speed, the theory had not been regarded as an antenna designing tool until 21st century. In 2007, Cabedo-Fabres [12] summarized her works on CMA and showed that CMA can be used as an insight of physical understanding to design antennas.

Submitted On: August 17, 2021
Accepted On: January 1, 2022

https://doi.org/10.13052/2022.ACES.J.370105

Later, researchers have found that CMA can be used to design various types of antennas such as wideband antennas [13, 14], circularly polarized antennas [15], high-gain antennas [16], multi-band antennas [17–19], and high polarization purity antennas [20]. Among the possible structures of antennas, metasurfaces are highly suitable for CMA [14, 17, 19, 20]. However, no work related to wide-beam antenna design using CMA has been reported. As there are many advantages in its nature, CMA is a good candidate for designing wide-beam antennas rigorously.

In this paper, a wide-beam metasurface antenna is designed using CMA. A novel method called modal pattern combination is proposed to design wide-beam antennas with physical insights of the antenna operating mechanisms. Section II introduces theory of characteristic modes (TCM) and the proposed theory of modal pattern combination is derived by analyzing the basic parameters of characteristic modes. A simple example of rectangular patch antenna is provided to show a practical prospect of the proposed theory. Section III describes the proposed wide-beam antenna from CMA to feeding network design. Finally, Section IV concludes the paper.

II. THEORY OF MODAL PATTERN COMBINATION

A. Theory of characteristic modes

The core of the TCM is to solve the generalized eigenvalue problem [10]:

$$X(J_n) = \lambda_n R(J_n). \tag{1}$$

The solution of the generalized eigenvalue problem is the doublet (λ_n, J_n). The resulting current of the antenna structure with a specific excitation can be expressed as a linear combination of the characteristic currents J_n. According to the TCM [10]:

$$J = \sum_n \frac{V_n^i J_n}{1+j\lambda_n} = \sum_n \alpha_n J_n, \tag{2}$$

where coefficient α_n is called the modal weighting coefficient (MWC) of mode n. The denominator is only relevant to the eigenvalues λ_n of the modes; so it does not depend on the excitations and can be considered as the intrinsic characteristic of the modes. Thus, the modal significance (MS) is defined as

$$\mathrm{MS}_n = \left| \frac{1}{1+j\lambda_n} \right|. \tag{3}$$

The numerator V_n^i of α_n is called the modal excitation coefficient (MEC) of mode n, which is defined as

$$V_n^i = \oint_s J_n \cdot E^i ds, \tag{4}$$

where E^i is the incident E field that excites the antenna structure. Thus, the MEC is relevant to the excitation. If the excitation E^i is orthogonal to a mode, then the mode is suppressed; otherwise, the mode is excited.

MWC is obviously a complex quantity; it has both magnitude and phase. The previously discussed definitions are all about the magnitude of the excitation properties, but the phase properties are also important in CMA.

B. The phase of the modal weighting coefficients

To solve the integral equation in reality, the generalized eigenvalue problem (1) is transferred into a matrix generalized eigenvalue problem. As the antenna structure is meshed, the characteristic currents can be expressed as the linear combination of the basis functions W_j (usually RWG functions [21])

$$J_n = \sum_j I_j W_j. \tag{5}$$

After the decomposition, the task of solving eqn (1) can be turned into solving [11]

$$[X][I]_n = \lambda_n [R][I]_n \tag{6}$$

where

$$[R] = [< W_i, RW_j >]. \tag{7}$$

$$[X] = [< W_i, XW_j >]. \tag{8}$$

Eqn (6) is a symmetric weighted matrix eigenvalue equation [11]. The solution of the equation is real; therefore, the calculated modal currents are real. In real implementations, the incident field E^i is always a real value on the mesh elements of the antenna structure. As a result, the MECs given by eqn (4) are real.

Then it is concluded that the phase of the MWCs depends only on its nominator. We can express it as a phasor:

$$1 + j\lambda_n = \frac{1}{\mathrm{MS}} \cdot e^{j \cdot \arctan\lambda_n}. \tag{9}$$

The characteristic angle (CA) of a mode is defined as

$$\mathrm{CA} = \pi - \arctan\lambda_n. \tag{10}$$

Thus, we can rewrite the MWC as

$$\mathrm{MWC}_n = \alpha_n = -V_n^i \cdot \mathrm{MS} \cdot e^{j \cdot \mathrm{CA}}. \tag{11}$$

So, the phase of the MWCs is the same as CAs of the same mode. This result is very important in the combination of modal patterns.

C. Modal pattern combination

The modal E field E_n of mode n is given by [10]

$$E_n = \frac{-j\omega\mu}{4\pi r} e^{jkr} F_n(\theta, \varphi), \tag{12}$$

where $F_n(\theta, \varphi)$ are the modal radiation patterns. The coefficient of eqn (12) does not change with a given structure and a given excitation. When we compute the combination of the modal E fields

$$E = \sum_n \alpha_n E_n = \frac{-j\omega\mu}{4\pi r} e^{jkr} \sum_n \alpha_n F_n(\theta, \varphi), \tag{13}$$

the modal radiation patterns $F_n(\theta, \varphi)$ are correspondingly combined with the same weighting coefficients. According to [10], the weighting coefficients of modal E

fields are the same as the weighting coefficients of characteristic currents, i.e., the MWCs α_n.

Thus, we can get the desired radiation pattern by controlling the MWCs.

D. Modal pattern combination of a rectangular patch antenna

It is useful to begin with a simple structure, as a square patch has many typical characteristic modes. The simulated model is shown in Figure 1. For simplicity, infinite substrate length is used in the simulation to avoid dielectric modes. CMA is performed on the patch using the commercial software Altair FEKO [22] and results are shown in Figures 2–4. CA is directly related to the eigenvalue. It has the advantage of preserving the phase information of the modes compared to the MS. The resonant point of a mode is on the 180° horizontal line of the graph and the resonant bandwidth (MS = 0.707) of a mode is defined within the region 135° = CA = 225°. Figure 2 shows the CAs of the square patch. The two

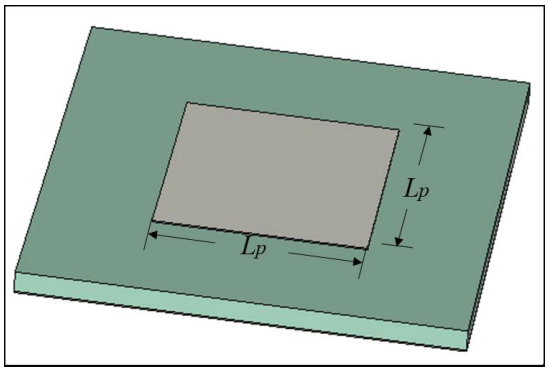

Fig. 1. Simulation configuration of the square patch. The size of the patch $L_p = 6.6$mm.

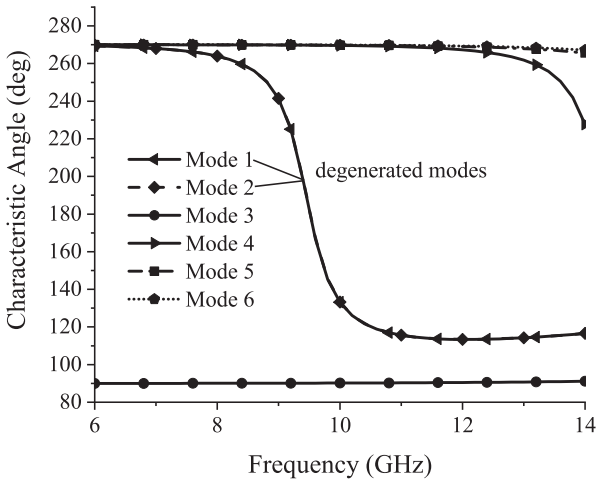

Fig. 2. Characteristic angle of the square patch.

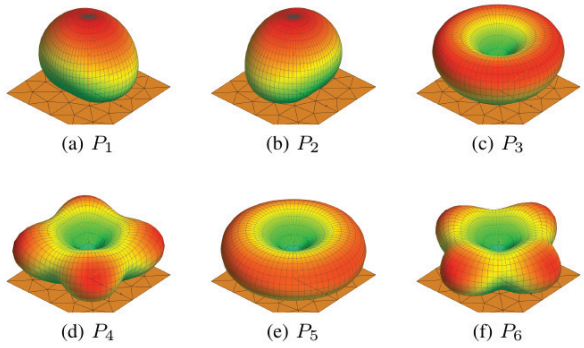

Fig. 3. Modal patterns of the square patch.

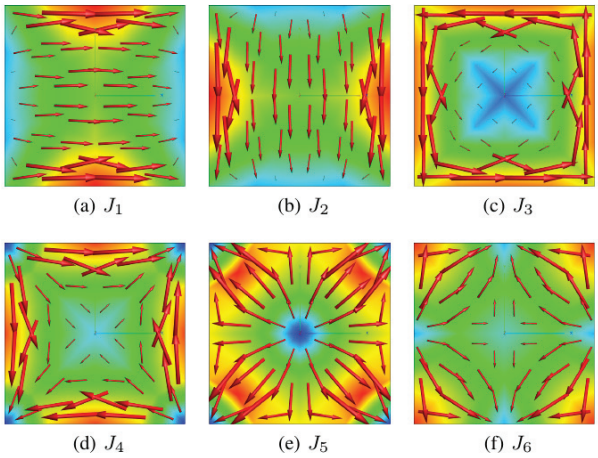

Fig. 4. Modal currents of the square patch.

fundamental modes, mode 1 and mode 2, are a pair of degenerated modes that resonate at 9.52 GHz. Other modes are higher-order modes each with a null point at the center of its modal pattern, as shown in Figure 3.

As a wide beamwidth is required, exciting one of the existing modes is not enough. The HPBW of mode 1/2 is only 134.1° in the E-plane and 83.9° in the H-plane. Thus, a modal combination is needed to achieve a wider beamwidth. Several possible combinations of modal patterns are shown in Figure 5. These combined patterns are calculated by a FEKO Lua script that performs the scalar

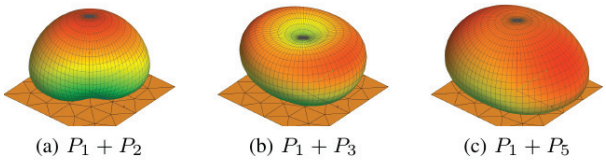

Fig. 5. Some combined modal patterns of the square patch.

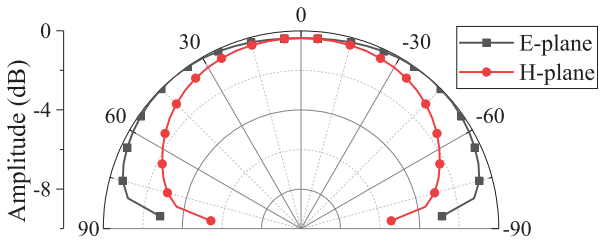

Fig. 6. Normalized E-plane and H-plane patterns of $P_1 + P_5$.

linear combination of modal patterns. In Figure 5(a), we can see that the combined pattern of the two degenerated fundamental modes P_1 and P_2 is simply a rotation of the modal pattern. This result can be seen as the pattern generated by a combined vector current distribution of the modal currents J_1 and J_2.

On the other hand, the combination of a fundamental mode with a perfect unidirectional pattern and a higher-order mode with an omnidirectional pattern leads to a pattern with wide beamwidth, as shown in Figures 5(b) and (c). Obviously the HPBWs of $P_1 + P_5$ in both E-plane and H-plane are wider than $P_1 + P_3$, as the maximal direction of the omnidirectional pattern of P_5 is closer to the horizontal plane. The simulated E- and H-plane patterns are shown in Figure 6. The HPBW of E- and H-plane patterns are 170.2° and 156.2°, with increases of 36.1° and 72.3° in both E- and H-planes, respectively. Due to the simulation configuration of infinite ground, the radiation patterns are restricted above the ground plane; thus, the HPBW cannot exceed 180°.

To summarize, with the combination of an omnidirectional pattern, a pattern with a wider beamwidth can be achieved. The only problem is to excite both the fundamental and the higher-order omnidirectional modes at the same time. It is difficult to excite both mode 1 and mode 5 properly, as mode 5 resonates at a far high frequency. Thus, the antenna structure should be changed to let both modes resonate at the desired frequency. In Section III, we propose a wide-beam metasurface antenna using the illustrated method.

III. WIDE-BEAM METASURFACE ANTENNA DESIGN

A. Characteristic mode analysis

To design a wide-beam antenna, a metasurface composed of 3×3 square patches is used as the radiating structure, as shown in Figure 7. The CMA is performed on the metasurface over an infinite grounded substrate. All the modal characteristics are calculated under the commercial software Altair FEKO [22]. Some important modal patterns of the metasurface are shown in Figure 8.

Modes 1 and 2 are degenerated fundamental modes of the 3×3 metasurface. They are horizontally polarized

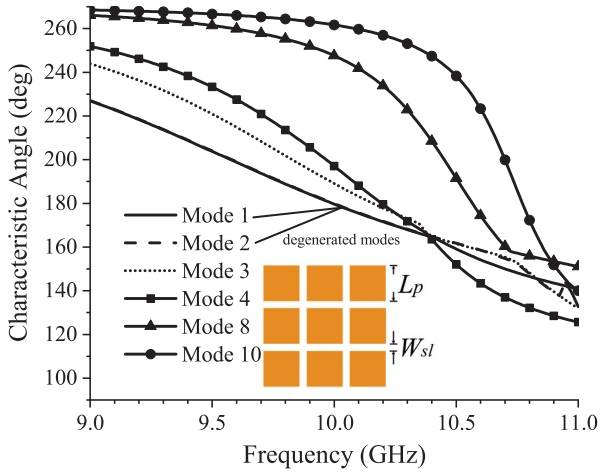

Fig. 7. Characteristic angle plot of the 3×3 metasurface. $L_p = 6.4$ mm, $W_{sl} = 1.2$ mm.

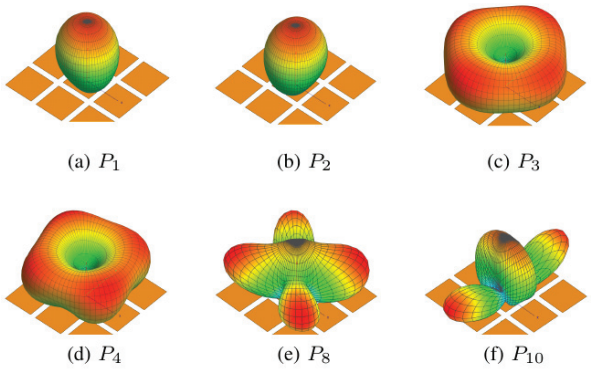

Fig. 8. Some modal patterns of the 3×3 metasurface.

(TM_{310}) and vertically polarized, respectively (TM_{130}). mode 3 is a mode with converging or diverging currents, whose pattern is omnidirectional but not as uniformly as the corresponding mode of a square patch. Mode 4 is also an omnidirectional mode, but its modal current is more irregular and harder to exploit. Other modes are less important in generating a radiation pattern with high quality. For example, the two third-order modes shown in Figures 8(e) and (f) have relatively larger sidelobes which can only cause distortions in the resulting pattern. As discussed earlier in Section II, a wide-beam pattern is achieved by combining a unidirectional mode and an omnidirectional one. In this case, mode 1 (or mode 2) and mode 3 are chosen to be excited. The combination effect can be shown in Figure 9. The resulting HPBWs in E- and H-planes are 141.3° and 140.7°. Thus, the metasurface is suitable for a wide-beam antenna.

The corresponding characteristic currents of the metasurface are shown in Figure 10. To excite two

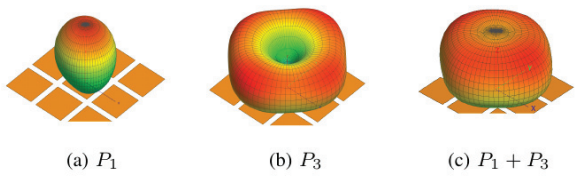

(a) P_1 (b) P_3 (c) $P_1 + P_3$

Fig. 9. Modal pattern combination of the 3×3 metasurface.

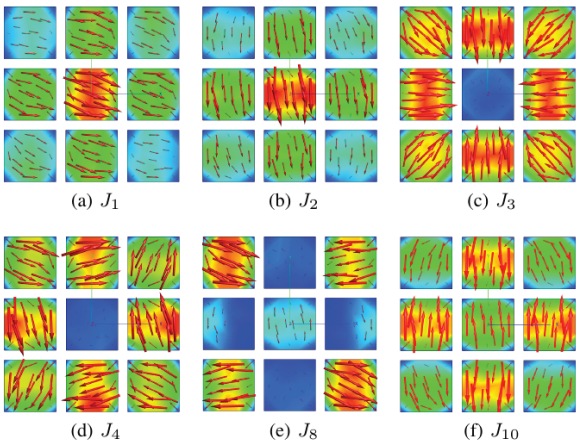

(a) J_1 (b) J_2 (c) J_3

(d) J_4 (e) J_8 (f) J_{10}

Fig. 10. Some modal currents of the 3×3 metasurface.

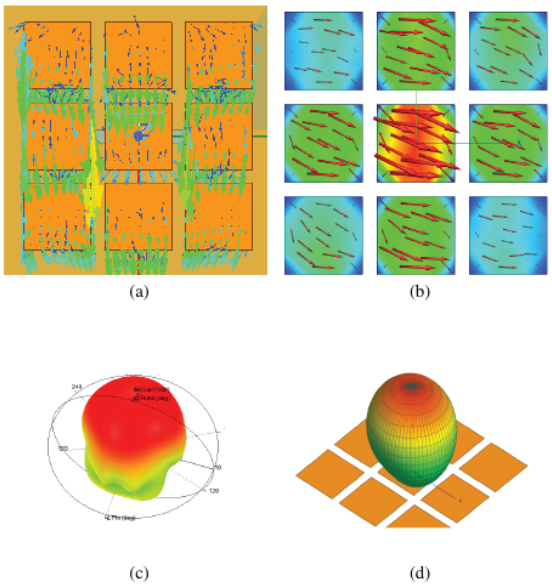

(a) (b) (c) (d)

Fig. 11. The comparison between excited currents and modal currents of unidirectional mode 1. (a) Excited currents. (b) Modal currents J_1. (c) Excited pattern. (d) Modal pattern P_1.

modes at the same time, we use the superposition principle. First, the feeding networks that excite single mode 1 and mode 3 are designed separately, and then a divider is designed to combine two feeding networks. These works are expressed in detail in the following sections.

B. Design of unidirectional mode antenna

The modal currents of mode 1 in Figure 10(a) are to be excited. The currents on nine subpatches are all parallel to the *x*-axis, along one edge of each patch. Therefore, the coupling slot is placed under the center of the metasurface perpendicular to the currents, in order to excite the fundamental mode. From Figure 11, the comparison between the modal and the excited currents and patterns show that mode 1 is successfully excited. The simulated gain of the antenna is 9.77 dBi at $\theta = 0°$, but when $|\theta| > 60°$, the gain is under 0 dBi, which can hardly be used in wide-beam applications.

C. Design of omnidirectional mode antenna

However, the higher-order omnidirectional mode is harder to exploit. The surface currents of mode 3 are not uniform, and they all point to the center. Compared to the surface currents of other modes, the current directions on the four corner patches are unique. Aiming at the corner patches of the metasurface, the feeding slot is designed to be a ring cut into four pieces. Due to the relative symmetric positions of the corner patches, the modal currents on the corner patches are nearly identical in magnitude. So, the exciting magnitude and phase of the feeding network should be the same. For simplicity, a simulation model with two ports and two 1-to-2 dividers are used, as shown in Figure 12(c).

The simulation results of the excited omnidirectional mode are shown in Figure 13. The results have shown that the omnidirectional mode is excited successfully by the feeding network. Note that the pattern of the excited mode can have beams greater than 90° and less than −90° because of finite ground.

D. Design of wide-beam antenna with combined modes

As analyzed in Section II, a wide-beam pattern can be achieved by combining mode 1 and mode 3. Thus, the desired wide-beam pattern can be obtained by combining the feeding networks in Sections III.B and III.C. To combine the two feeding networks, an unequal three-way power divider is needed. The proposed feeding network is shown in Figure 14(b). The omnidirectional pattern is excited by four symmetric slots with the same magnitude and phase; therefore, the two corresponding ports should have the same magnitude and phase output. The power divider is evolved from a normal two-way divider with a coupled microstrip between the branches, as shown in Figure 14(a). Power flows into Port 2 by coupling between Port 2 and Port 3/4. To further enhance the power

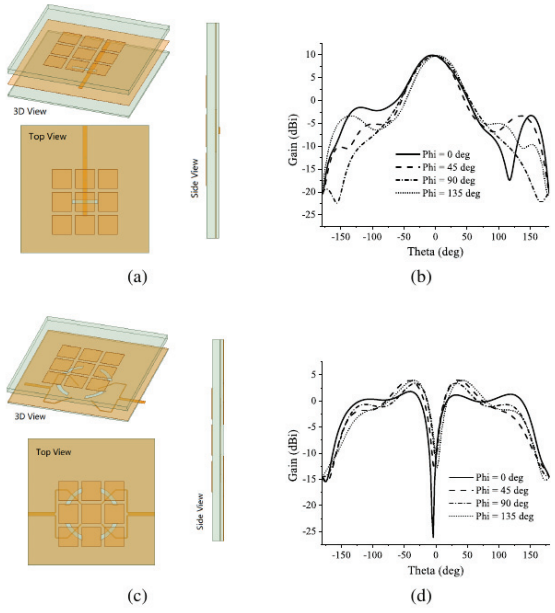

Fig. 12. Simulation configuration and gain of the metasurface antenna with mode 1 and mode 3 excited individually. (a) Simulation configuration of the excited mode 1. (b) Gain of the excited mode 1. (c) Simulation configuration of the excited mode 3. (d) Gain of the excited mode 3.

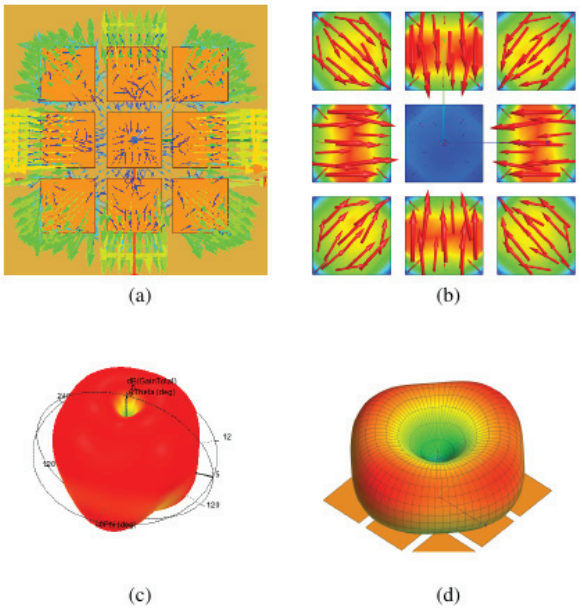

Fig. 13. The comparison between excited currents and modal currents of unidirectional mode 3. (a) Excited currents. (b) Modal currents J_3. (c) Excited pattern. (d) Modal pattern P_3.

flowing into Port 2, a connection is added to Port 2, as shown in Figure 14(b). The simulated S parameters of the divider are shown in Figure 15. The magnitude ratio between S_{21} and S_{31} is 1.1:1 and the phase difference is relatively stable within 9−11 GHz.

The configuration of the proposed antenna is shown in Figure 16. The feeding network is a combination of the three-way unequal power divider and the feeding networks of the individually excited modes. According to the superposition principle, the result of the combined feeding network can be seen as a linear combination of the two antennas in Sections III.B and III.C. The amplitude of the combination is determined by the unequal power divider and the phase difference between ports can be tuned by the lengths of the feeding branches. The return losses of the combined antenna compared with single mode antennas are shown in Figure 17.

The simulated radiation pattern is shown in Figure 18. The 3-dB beamwidth of the 45° and 135° planes are 200.9° and 200.6°, respectively. The beamwidth of E- and H-planes suffered some loss because of the coupling and unideal characteristics of the combination. On the other hand, the beamwidths in 45° and 135° planes are increased but with an asymmetric pattern. The $|S_{11}|$ bandwidth is 9.81−10.27 GHz (4.6%). The maximum gain of the wide-beam antenna is 4.25 dBi, which is slightly larger than the

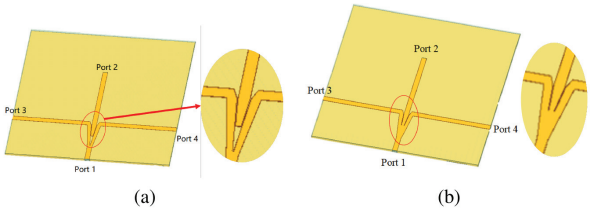

Fig. 14. Power divider configuration of the proposed antenna. (a) Divider 1. (b) Proposed divider.

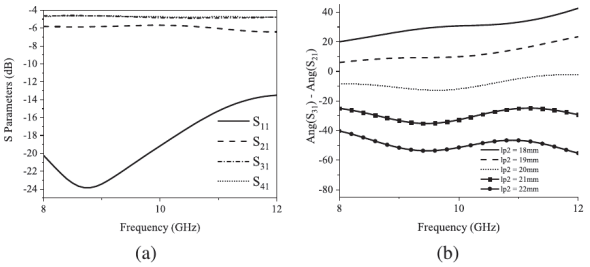

Fig. 15. S parameters of the unequal power divider. (a) Magnitudes of S_{11}, S_{21}, S_{31}, and S_{41}. (b) Phase difference between S_{21} and S_{31} with varied length l_{p2} of the microstrip line connected to port 2.

omnidirectional antenna. Overall, a wide-beam pattern is successfully obtained.

Table 1 Comparisons among the proposed metasurface antenna and related antennas

Ref	Type	Size(λ^3)	HPBW (E-/H-plane)	Ground size (mm^2)	HPBW/ground size E-/H-plane) ($^\circ/mm^2$)
[1]	MS ring	$0.54 \times 0.54 \times 0.11$	$140^\circ/-$	$\pi \times 68 \times 68$	$0.0096/-$
[3]	MS	$0.63 \times 0.63 \times 0.21$	$236^\circ/124^\circ$	27×27	$0.324/0.170$
[4]	MS	$1.17 \times 1.87 \times 0.03$	$140^\circ/-$	125×200	$0.0056/-$
[5]	MS	$0.52 \times 0.52 \times 0.03$	$135^\circ/132^\circ$	32.1×32.1	$0.131/0.128$
[6]	MS	$0.19 \times 0.19 \times 0.07$	$107^\circ/105^\circ$	170×170	$0.0037/0.0036$
[7]	DRA	$2.0 \times 2.0 \times 0.16$	$168^\circ/177^\circ$	40×40	$0.105/0.111$
[8]	ME TSA	$0.73 \times 0.67 \times 0.03$	$135^\circ/-$	$-$	$-$
This work	**MTS**	$\mathbf{1.4 \times 1.4 \times 0.07}$	$200^\circ/200^\circ(45^\circ/135^\circ)$	$\mathbf{42 \times 42}$	$0.113/0.113(45^\circ/135^\circ)$

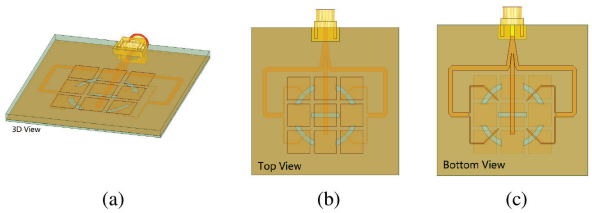

Fig. 16. Simulation configuration of the proposed antenna. (a) 3D view. (b) Top view. (c) Bottom view.

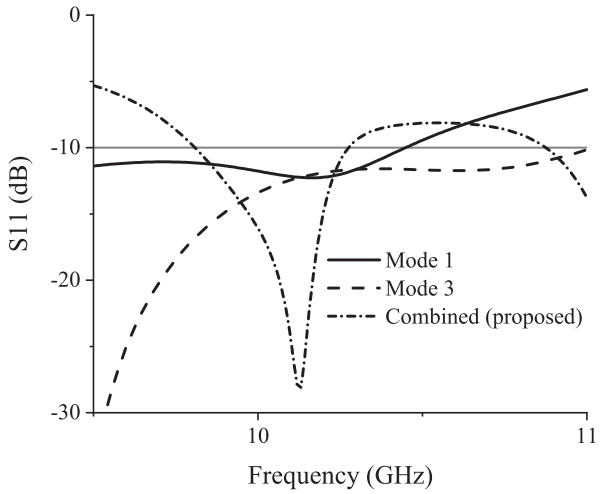

Fig. 17. Return loss (S_{11}) of the metasurface antenna.

Comparisons among the proposed antenna and related wide-beam antennas are given in Table 1. As shown in the table, low-profile structures using microstrip structures with grounding vias in [4–6] and magneto-electric tapered slot antenna in [8] can hardly generate a wide-beam pattern above 140°. Structures with wider beamwidths in [3, 7] have higher profiles $h > 0.1\lambda$. The resulting HPBW is larger than most of the structures. Compared with the dielectric resonator antenna (DRA) in [7], metasurface structures based on microstrips are easy to fabricate and have smaller size.

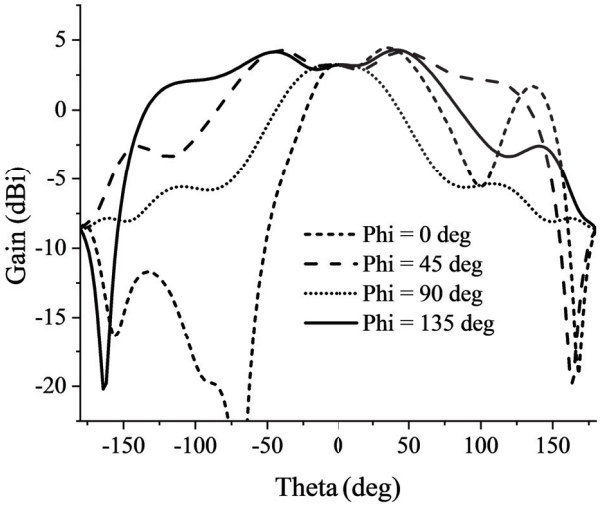

Fig. 18. Gain of the proposed antenna.

IV. CONCLUSION

A low-profile wide-beam metasurface antenna for detection purpose has been proposed. The 3-dB beamwidth of the 45° and 135° planes are 200.9° and 200.6°, respectively. The maximum gain of the wide-beam antenna is 4.25 dBi. The results have shown that the proposed antenna is capable of detection applications near 10 GHz.

ACKNOWLEDGEMENT

This work is supported by the project of 61971051 from the National Natural Science Foundation of China (NSFC).

REFERENCES

[1] Z. Pan, W. Lin, and Q. Chu, "Compact wide-beam circularly-polarized microstrip antenna with a parasitic ring for cnss application," *IEEE Transactions*

on Antennas and Propagation, vol. 62, no. 5, pp. 2847–2850, 2014

[2] C. Yu, E. S. Li, H. Jin, Y. Cao, G. Su, W. Che, and K. Chin, "24 ghz horizontally polarized automotive antenna arrays with wide fan beam and high gain," *IEEE Transactions on Antennas and Propagation*, vol. 67, no. 2, pp. 892–904, 2019.

[3] G. Yang, J. Li, D. Wei, S. Zhou, and J. Yang, "Broadening the beamwidth of microstrip antenna by the induced vertical currents," *IET Microwaves, Antennas Propagation*, vol. 12, no. 2, pp. 190–194, 2018.

[4] N. Liu, S. Gao, L. Zhu, L. Ji, L. Yang, and H. Zheng, "Low profile microstrip patch antenna with simultaneous enhanced bandwidth, beamwidth, and cross-polarisation under dual resonance," *IET Microwaves, Antennas Propagation*, vol. 14, no. 5, pp. 360–365, 2020.

[5] J. Ou, S. Dong, J. Huang, X. Y. Zhang, W. Che, and Q. Xue, "A compact microstrip antenna with extended half-power beamwidth and harmonic suppression," *IEEE Transactions on Antennas and Propagation*, vol. 68, no. 6, pp. 4312–4319, 2020.

[6] Y. He and Y. Li, "Dual-polarized microstrip antennas with capacitive via fence for wide beamwidth and high isolation," *IEEE Transactions on Antennas and Propagation*, vol. 68, no. 7, pp. 5095–5103, 2020.

[7] N. Yang, Z. Weng, L. Wang, and T. Liao, "A hybrid dual-mode dielectric resonator antenna with wide beamwidth," *International Journal of RF and Microwave Computer-Aided Engineering*, vol. 30, no. 10, p. e22337, 2020. [Online]. Available: https://onlinelibrary.wiley.com/doi/abs/10.1002/mmce.22337

[8] K.-W. Yang, F.-S. Zhang, C. Li, G. Zhao, and F. Zhang, "A wideband planar magneto-electric tapered slot antenna with wide beamwidth," *International Journal of RF and Microwave Computer-Aided Engineering*, vol. 29, no. 11, p. e21910, 2019. [Online]. Available: https://onlinelibrary.wiley.com/doi/abs/10.1002/mmce.21910

[9] R. J. Garbacz, "Modal expansions for resonance scattering phenomena," *Proceedings of the IEEE*, vol. 53, no. 8, pp. 856–864, 1965.

[10] R. Harrington and J. Mautz, "Theory of characteristic modes for conducting bodies," *IEEE Transactions on Antennas and Propagation*, vol. 19, no. 5, pp. 622–628, 1971.

[11] R. Harrington and J. Mautz, "Computation of characteristic modes for conducting bodies," *IEEE Transactions on Antennas and Propagation*, vol. 19, no. 5, pp. 629–639, 1971.

[12] M. Cabedo-Fabres, E. Antonino-Daviu, A. Valero-Nogueira, and M. F. Bataller, "The theory of characteristic modes revisited: A contribution to the design of antennas for modern applications," *IEEE Antennas and Propagation Magazine*, vol. 49, no. 5, pp. 52–68, 2007.

[13] F. H. Lin and Z. N. Chen, "Low-profile wideband metasurface antennas using characteristic mode analysis," *in IEEE Transactions on Antennas and Propagation*, vol. 65, no. 4, pp. 1706–1713, April 2017, doi: 10.1109/TAP.2017.2671036.

[14] J. Lin and Q. Chu, "Increasing bandwidth of slot antennas with combined characteristic modes," *IEEE Transactions on Antennas and Propagation*, vol. 66, no. 6, pp. 3148–3153, 2018.

[15] Y. Chen and C. Wang, "Characteristic-mode-based improvement of circularly polarized u-slot and e-shaped patch antennas," *IEEE Antennas and Wireless Propagation Letters*, vol. 11, pp. 1474–1477, 2012.

[16] Y. Luo, Z. N. Chen, and K. Ma, "Enhanced bandwidth and directivity of a dual-mode compressed high-order mode stub-loaded dipole using characteristic mode analysis," *IEEE Transactions on Antennas and Propagation*, vol. 67, no. 3, pp. 1922–1925, 2019.

[17] T. Li and Z. N. Chen, "A dual-band metasurface antenna using characteristic mode analysis," *IEEE Transactions on Antennas and Propagation*, vol. 66, no. 10, pp. 5620–5624, 2018.

[18] S. Liu, D. Yang, and J. Pan, "A low-profile broadband dual-circularly polarized metasurface antenna," *IEEE Antennas and Wireless Propagation Letters*, vol. 18, no. 7, pp. 1395–1399, 2019.

[19] T. Li and Z. N. Chen, "Shared-surface dual-band antenna for 5g applications," *IEEE Transactions on Antennas and Propagation*, vol. 68, no. 2, pp. 1128–1133, 2020.

[20] F. H. Lin and Z. N. Chen, "A method of suppressing higher order modes for improving radiation performance of metasurface multiport antennas using characteristic mode analysis," *IEEE Transactions on Antennas and Propagation*, vol. 66, no. 4, pp. 1894–1902, 2018.

[21] S. Rao, D. Wilton, and A. Glisson, "Electromagnetic scattering by surfaces of arbitrary shape," *IEEE Transactions on Antennas and Propagation*, vol. 30, no. 3, pp. 409–418, 1982.

[22] D. J. Ludick, E. Lezar, and U. Jakobus, "Characteristic mode analysis of arbitrary electromagnetic structures using feko," in 2012 International Conference on Electromagnetics in Advanced Applications, 2012, pp. 208–211.

Shizhe Zhao received the B.S. degree in communication engineering from the Beijing University of Posts and Telecommunications, Beijing, China, in 2019. He is currently working toward the M.S. degree in electronic engineering from the Beijing University of Posts and Telecommunications.

His research interests include but not limited to theory of characteristic modes and millimeter wave antennas.

Xiuping Li received the B.S. degree from Shandong University, Jinan, China, in 1996 and the Ph.D. degree from the Beijing Institute of Technology, Beijing, China, in 2001.

From 2001 to 2003, she was with the Positioning and Wireless Technology Center, Nanyang Technological University, Singapore, where she was a Research Fellow and involved in the research and development of RFID system. In 2003, she was a Research Professor with Yonsei University, Seoul, South Korea. Since 2004, she has been with the Beijing University of Posts and Telecommunications, Beijing, China, as an Associate Professor and was promoted to Professor in 2009.

Dr. Li has been selected into the New Century Excellent Talents Support Plan in National Ministry of Education and the Beijing Science and Technology Nova Support Plan in 2007 and 2008, respectively. She won the second prize of the Progress in Science and Technology of China Institute of Communications and the Excellent Achievements in Scientific Research of Colleges and Universities in 2015 and 2018, respectively. She is the author of four books, over 100 journal and conference papers. She is also awarded more than 20 PRC patents. Her current research interests include millimeter-wave antennas, THz antennas, RFID systems, and MMIC design.

Yongxin Chen received the B.S. degree in electronic information science and technology from the Nanjing University of Aeronautics and Astronautics, Nanjing, China, in 2015. He is currently working toward the M.S. degree in electronic engineering with the Beijing University of Posts and Telecommunications, Beijing, China.

His current research interests include characteristic modes theory.

Wenyu Zhao received the B.S. degree from the Beijing University of Posts and Telecommunications, Beijing, China, in 2018. He is currently working toward the Ph.D. degree with the School of Electronic Engineering and the Beijing Key Laboratory of Work Safety Intelligent Monitoring, Beijing University of Posts and Telecommunications.

His current research interests include dual-polarized antennas, millimeter-wave antennas, and reflect array antennas.

Zihang Qi received the B.E. degree in electronic and information engineering from China Three Gorges University, Yichang, China, in 2013, and the Ph.D. degree in electronic science and technology from the Beijing University of Posts and Telecommunications, Beijing, China, in 2019.

He is currently an Associate Research Fellow with the Beijing University of Posts and Telecommunications. His current research interests include OAM antennas, millimeter-wave/THz antennas, and microwave filters.

Dr. Qi was a recipient of the 2018 National Scholarship of China for Doctoral Students.

Modeling the Performance Impact of Anisotropic Unit Cells Used in Additively Manufactured Luneburg Lenses

Brian F. LaRocca[1] and Mark S. Mirotznik[2]

[1]Department of the Army,
Aberdeen Proving Ground, Aberdeen, MD 21005, USA
brian.f.larocca.civ@army.mil

[2]Electrical Engineering Department,
University of Delaware, Newark, DE 19716, USA
mirotzni@udel.edu

Abstract – Additively manufactured graded index lenses, such as the Luneburg lens, often result in some degree of uniaxial anisotropy in the effective permittivity distribution. A uniaxially anisotropic Luneburg lens modifies the polarization state of an incident electromagnetic field, thus giving rise to a polarization mismatch at the receiving antenna. Using 3D finite element simulation, the lens focal point polarization is analyzed and a model that fits the simulation data is created. The model allows prediction of polarization mismatch loss given any incident field and any receiving antenna polarization without resorting to further time-consuming simulations.

Index Terms – Anisotropic lens, finite element analysis, Luneburg lens, 3D printing.

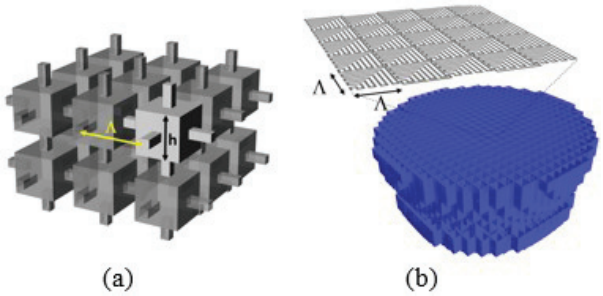

Fig. 1. Unit cell geometries that have been created for 3D printing of graded index components. (a) UV-curable polymer cubes with interconnecting rods and (b) planer unit cell. A indicates the size of the unit cell, which is much smaller than the free-space wavelength at the intended operating frequency

I. INTRODUCTION

Numerous researchers have reported on the use of sub-wavelength unit cells as fundamental building blocks to additively manufacture graded index components such as the Luneburg lens [1–9]. In these accounts, a 3D printer dispenses precise amounts of material within each unit cell volume, thus controlling the effective permittivity of the cell. Depending upon the complexity of the design, certain fabrication techniques and cell geometries are best suited in terms of manufacturability. Figure 1 provides sketches of two successful unit cell geometries that have been implemented. In (a), the researchers employ a lattice of ultraviolet-curable polymer cubes with interconnecting rods [3], and, indeed, this design is isotropic. The implementation uses a polymer-jetting technique that requires an interposed water-soluble polymer that supports the lattice as it is being printed. This material must then be thoroughly flushed out of the part before use. For complex or large designs with small unit cells, this flushing process of removing support material may be problematic. Furthermore, the UV curable polymers used in polymer-jetting have significantly higher loss tangents than thermoplastics [10]. For large designs, this results in an appreciable reduction in radiation efficiency. In (b), the authors in [1, 2] overcome these difficulties by using a planar unit cell, which is printed from a filament of melted thermoplastic, in a process known as fused deposition modeling. This technique produces a cost-effective, low loss, and sturdy design, without the need for a support material. However, the planar unit cell is uniaxially anisotropic. This anisotropy has been recognized by the authors in [1, 2], but its impact on lens performance has yet to be investigated.

Thus, this work uses 3D finite element simulations and post-processing to examine the performance impact of this unit cell anisotropy. A model is created to fit the field at the focal point, which then enables prediction of polarization state without further finite element simulation. The outline for the subsequent portion of the paper

Submitted On: September 24, 2021
Accepted On: January 28, 2022

https://doi.org/10.13052/2022.ACES.J.370106

is as follows. Section II discusses the simulation environment, including an analysis of error. Section III provides the details of the anisotropy model that is incorporated into the simulations. Section IV develops the simplifying focal point model and Section V applies this model to predict polarization loss. Section VI then discusses the primary results.

II. SIMULATION ENVIRONMENT

The MATLAB partial differential equation (PDE) toolbox [11] is used to perform 3D finite element analysis of an anisotropic Luneburg lens illuminated by a monochromatic uniform plane wave. The toolbox is used to mesh the computational domain composed of the lens and free space and solve for the scattered field. Upon completion, the scattered field is summed with the incident field to obtain the total field solution [12].

The computational domain is meshed using tetrahedral elements that have a maximum edge length of $l_{\max} \leq 0.1\lambda$, where λ is the free-space wavelength of the incident field. The computational domain is bounded by a sphere of radius $r_b = r_l + 0.5\lambda$ that is concentric around the lens of radius r_l. A first-order absorbing boundary condition [12] is used over the bounding spheres surface. Due to the rotational symmetry of the lens about the z-axis, the direction vector $\vec{k}$ of the incident field is confined to the x, z plane. The sketch in Figure 2 identifies the geometry of the simulation scenario excluding the outer spherical boundary, and a summary of simulation parameters is provided in Table 1.

Referring to the solver category in Table 1, lsqr() and equilibrate() are both core MATLAB functions designed

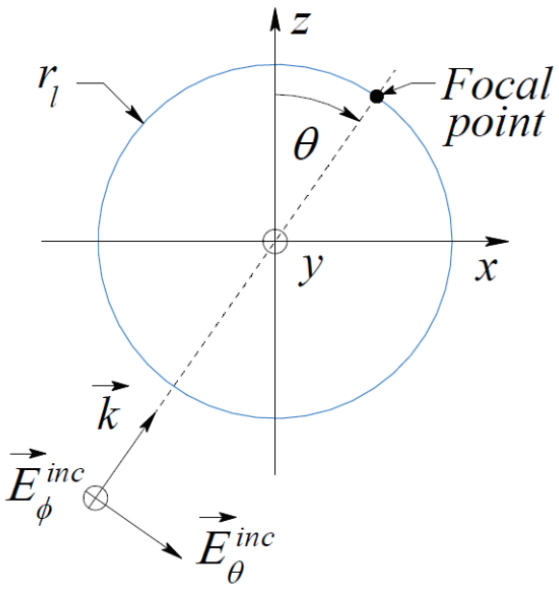

Fig. 2. Incident plane wave, lens, and focal point.

Table 1: Simulation parameters

Category	Parameter	Value
Model	Frequency	15 GHz
	Plane wave polarization	Left hand circular
	Domain radius	$r_l + 0.5\lambda$
	Boundary conditions	First-order absorbing
Mesh	Max. edge length	0.1λ
	Nodes per element	4
	Growth rate	1.5
Solver	Type	lsqr()
	Tolerance	0.1×10^{-3}
	Matrix conditioning	equilibrate()

Table 2: Evaluation of simulation error with isotropic reference lens

r_l	$\angle E_\phi - \angle E_\theta - 90^\circ$	$\lvert E_\phi \rvert / \lvert E_\theta \rvert - 1$
2.5λ	$+3.37^\circ$	$+0.011$
3.5λ	-2.25°	-0.017
5.0λ	-1.21°	$+0.001$
RMS error	2.44°	0.012

to operate on sparse matrices. lsqr() implements the least squares method to solve the linear matrix equation $Ax = b$ for x. equilibrate(A) is used to the transform the linear system into an equivalent system that is very stable, prior to solution with lsqr(). Although the PDE toolbox provides solvepde() for this purpose, the underlying solveStationary() routine is not suitable for large problems, and in such cases, it is necessary to substitute an iterative solver such as gmres() or lsqr(). For the problems in this study, it was found that lsqr() performed the best. Another PDE toolbox function that is very useful is createPDEResults(). This utility function packs the solution x into a structure that is identical to that returned by solvepde(). Drop-in compatibility is achieved by invoking this function before returning from a custom solver routine which may itself call either gmres() or lsqr().

Parameters $l_{\max}$ and r_b have been chosen after experimentation, with the intent of striking a balance between solution fidelity and simulation efficiency. This experimentation includes evaluating isotropic reference lens simulations, which are shown in Table 2.

In this evaluation, three isotropic lenses of varying radii are illuminated with a left hand circularly polarized (LCP) plane wave. Given the incident field is LCP, the phase difference $\angle E_\phi - \angle E_\theta$ at the focal point should precisely be equal to 90°, and the polarization ratio $\lvert E_\phi \rvert / \lvert E_\theta \rvert$ should precisely be equal to 1.0. However, since $r_b < \infty$ and $l_{\max} > 0$, the observed root mean square (RMS) error is 2.44° in phase and 0.012 in polarization ratio.

Table 3: Evaluation of simulation error with polar illumination of anisotropic lens

r_l	$\angle E_\phi - \angle E_\theta - 90^\circ$	$\lvert E_\phi\rvert/\lvert E_\theta\rvert - 1$
2.5λ	-0.43°	$+0.013$
3.5λ	$+0.94^\circ$	-0.018
5.0λ	$+1.60^\circ$	-0.026
RMS error	1.10°	0.020

A similar evaluation involves illuminating three uniaxially anisotropic lenses of varying radii, with an LCP plane wave at a polar angle of $\theta = 0^\circ$. The results of this test are shown in Table 3. Since the illumination is parallel to the optic axis of the lens, both E_ϕ and E_θ experience equivalent material properties. Ideally then, the polarization state at the focal point should equal that of the incident wave, i.e., a $+90^\circ$ phase difference with a polarization ratio of 1.0 (just as in the isotropic case). The observed RMS error in this case is 1.10° in phase and 0.02 in polarization ratio. The observed errors in both the isotropic and anisotropic tests are deemed acceptable.

III. MODELING OF LENS ANISOTROPY

The model used herein follows the findings of researchers in [1, 2] who showed that because of the additive manufacturing process and choice of cell geometry, the lens exhibits a negative uniaxial anisotropy in which

$$\varepsilon_x = \varepsilon_y = \varepsilon_{xy} \geq \varepsilon_z. \tag{1}$$

Moreover, the permittivities along the x- and y-axes of the lens follow the Luneburg profile exactly. That is, for any point within the lens at a radial distance r from the lens center

$$\varepsilon_{xy} = 2 - \left(\frac{r}{r_l}\right)^2. \tag{2}$$

The permittivity of the lens along the z-axis is modeled by the fractional mixing formula

$$\varepsilon_z = \varepsilon_{xy}\,(1-\alpha) + \alpha\,\varepsilon_{\mathrm{MG}}, \tag{3}$$

where α is a parameter (the purpose of which is explained shortly) and $\varepsilon_{\mathrm{MG}}$ represents the effective relative permittivity determined by the Maxwell Garnett (MG) mixing rule for spherical inclusions embedded in a host medium [13]. For a host medium of free space, it is given by

$$\varepsilon_{\mathrm{MG}} = 1 + 3f\frac{(\varepsilon_i - 1)}{\varepsilon_i + 2 - f(\varepsilon_i - 1)}\,. \tag{4}$$

Here, ε_i represents the relative permittivity of the inclusions, and f represents the volume fill fraction of a unit cell, i.e., the volumetric ratio of material to free space within the cell. In the context of this work, ε_i is the relative permittivity of the dielectric material used to print the lens, which is taken as pure thermoplastic with a ε_i of 2.60. The authors in [1, 2] determined ε_z for the exact unit cell geometry of Figure 1(b) using rigorous coupled wave analysis (RCWA). It is a testament to the scope of Equation (4) in that it generates results that closely match their analysis. It is also fortunate since the alternative is to model the structural geometry of the lens down to the unit cell. To do so accurately would require a mesh fine enough to accurately capture its smallest feature, that being the cell thickness of 0.12 mm [1]. Ultimately, this requires a mesh $l_{\max}$ 160 times smaller and a memory requirement on the order of 160^3 times greater than that used for the present study. This is not feasible since for a lens with $r_l = 2.5\lambda$, this amounts to a memory requirement of 2.2×160^3 gigabytes or equivalently 8.6 petabytes.

Table 4: Comparison of mixing rules to RCWA

Mixing rule	RMS difference
Maxwell Garnett	0.064
Bruggeman	0.098
Coherent-potential	0.109

Table 4 compares the MG mixing rule to the Bruggeman and coherent-potential mixing rules [13] in terms of fitting the RCWA predictions of ε_z as reported in [1, 2]. The table provides the RMS difference between the respective mixing rule and those results. The MG mixing rule has the least RMS difference, thus providing the best fit.

A linear relationship between f and ε_{xy} is assumed, such that

$$f = \frac{(\varepsilon_{xy} - 1)}{(\varepsilon_i - 1)}. \tag{5}$$

Finally, in Equation (3), the parameter α can range from 0 to 1 and is used to simulate designs that exhibit lesser degrees of anisotropy. For example, setting α equal 0 generates a fully isotropic lens design since $\varepsilon_z = \varepsilon_{xy}$, whereas setting α equal 1 generates the highest degree of anisotropy producing $\varepsilon_z = \varepsilon_{MG}$. The MG equation with $\varepsilon_i = 2.60$ is plotted in Figure 3 for four values of α. The plot highlights the fact that for a chosen ε_i, the maximum fill fraction is 0.625 which occurs at the lens center where $\varepsilon_z = 2.0$.

IV. MODELING OF POLARIZATION

A. Illumination normal to optic axis

In this subsection, the lens is examined when it is illuminated with a plane wave normal to the z-axis of the lens. Referring to Figure 2, θ is therefore 90° and the incident field is simply directed along the x-axis of the lens. The incident field is represented as

$$\overrightarrow{E}^{\mathrm{inc}} = \begin{bmatrix} E_\theta^{\mathrm{inc}} \\ E_\phi^{\mathrm{inc}} \end{bmatrix} = \begin{bmatrix} a_\theta^{\mathrm{inc}} e^{j\psi_\theta^{\mathrm{inc}}} \\ a_\phi^{\mathrm{inc}} e^{j\psi_\phi^{\mathrm{inc}}} \end{bmatrix} e^{-jk_0 x}, \tag{6}$$

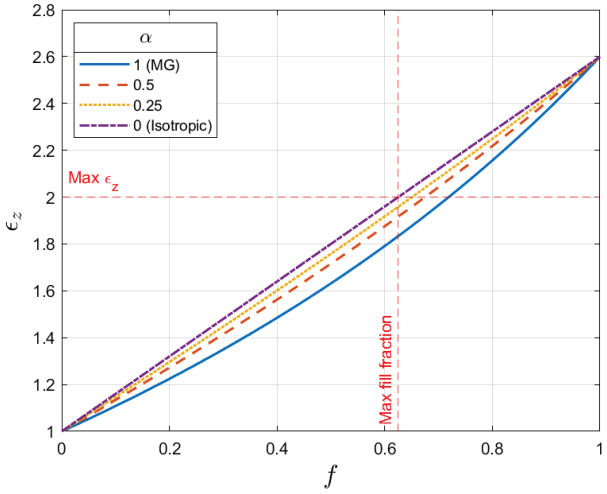

Fig. 3. ε_z vs. f for different α. Maximum ε_z occurs at lens center where $f = 0.625$.

where a_θ^{inc} and a_ϕ^{inc} are real positive constants, ψ_θ^{inc} and ψ_ϕ^{inc} are real phase constants, and $k_0 = 2\pi/\lambda$. The illumination is LCP, where $a_\theta^{\text{inc}} = a_\phi^{\text{inc}}$, and the phase difference $\psi_\phi^{\text{inc}} - \psi_\theta^{\text{inc}} = 90^\circ$. For a lens of radius r_l, the focal point is located on the surface of the lens, at the cartesian coordinate $(r_l, 0, 0)$. To assess the polarization at the focal point, the radial component of the resultant field at the focal point is ignored, leaving

$$\vec{E} = \begin{bmatrix} a_\theta e^{j\varphi_\theta} \\ a_\phi e^{j\varphi_\phi} \end{bmatrix}, \tag{7}$$

where a_θ and a_ϕ are real positive values, and φ_θ and φ_ϕ are real phase terms and are different from the incident field constants in Equation (6). To describe the polarization state of the focal point, only the ratio $\sigma = a_\phi/a_\theta$ and the phase difference $\delta = \varphi_\phi - \varphi_\theta$ are required [15]. To create a simplifying polarization model of the lens that is independent of the incident field polarization state, the phase imbalance attributed to the lens itself is distinguished from δ. We refer to this as the retardance of the lens $\acute{\delta}$, which is defined here as

$$\acute{\delta} = \delta - (\psi_\phi^{\text{inc}} - \psi_\theta^{\text{inc}}). \tag{8}$$

A similar distinction is required for the polarization ratio σ. Thus, we define the lens polarization ratio $\acute{\sigma}$ as being the polarization ratio measured at the focal point to σ^{inc}, the polarization ratio of the incident field:

$$\acute{\sigma} = \frac{\sigma}{\sigma^{\text{inc}}} = \frac{a_\phi/a_\theta}{a_\phi^{\text{inc}}/a_\theta^{\text{inc}}}. \tag{9}$$

Both $\acute{\sigma}$ and $\left|\acute{\delta}\right|$ take on maximum values when the illumination is normal to the optic axis. Under this condition, $\acute{\sigma}$ is referred to as $\acute{\sigma}_m$, and $\acute{\delta}$ is referred to as $\acute{\delta}_m$. Note that when the illumination is parallel, the optic axis $\acute{\sigma} = 1$ and $\acute{\delta} = 0$.

Table 5: Polynomial coefficients for $\acute{\delta}_m$

α	p_1	p_2
1.0	−0.5209	0.0828
0.5	−0.2433	0.0264
0.25	−0.1195	0.01118

In the following two figures, the simulation results for $\acute{\delta}_m$ and $\acute{\sigma}_m$ are plotted using an r_l from 0.5λ to 6λ, in 0.5λ increments. These results are shown for three values of the MG fractional anisotropy constant α. This data is plotted with solid lines and markers. Additionally, polynomial least square fits to $\acute{\delta}_m$ and $\acute{\sigma}_m$ are plotted using dashed curves without markers; this data is comparatively smooth and sampled at a much finer resolution.

The least square fit for $\acute{\delta}_m$ is given by the first-order polynomial below and plotted with simulation data in Figure 4:

$$\acute{\delta}_m = p_1[\alpha]\,\bar{r}_l + p_2[\alpha], \tag{10}$$

where $\acute{\delta}_m$ is specified in radians, $\bar{r}_l = r_l/\lambda$ and is unitless, and p_1 and p_2 are real coefficients given in Table 5. Note that in Equation (10), the square brackets indicate that α is being treated as a lookup table index − not a continuous variable.

$\acute{\sigma}_m$ is treated as a function of $\acute{\delta}_m$, and, as can be inferred from Figure 4, $\acute{\delta}_m < 0^\circ$. Moreover, a piecewise model of $\acute{\sigma}_m$ is necessary, expressed herein as

$$\acute{\sigma}_m = \begin{cases} \acute{\sigma}_m^a, & \text{if } -180^\circ \le \acute{\delta}_m \\ \acute{\sigma}_m^b, & \text{otherwise.} \end{cases} \tag{11}$$

As $\acute{\delta}_m$ is varied from 0° to -180°, it is observed that a_ϕ increases linearly, whereas a_θ increases non-linearly and settles into a plateau as $\acute{\delta}_m$ approaches -180°. For $-180^\circ \le \acute{\delta}_m$, the least square fit for $\acute{\sigma}_m$ is given by the

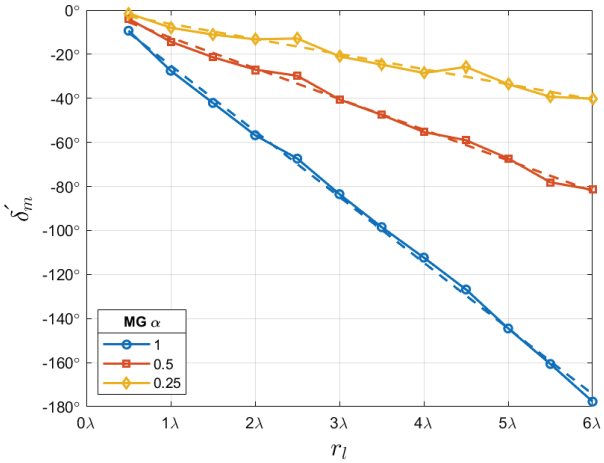

Fig. 4. $\acute{\delta}_m$ vs. r_l for different α. Dashed lines are model given by least square fit in Equation (10).

Table 6: Polynomial coefficients for $\acute{\sigma}_m^a$

q_1	q_2	q_3
0.07122	−0.1148	0.9999

second-order polynomial below, and plotted with simulation data in Figure 5:

$$\acute{\sigma}_m^a = q_1\acute{\delta}_m^2 + q_2\acute{\delta}_m + q_3, \tag{12}$$

where q_1, q_2, and q_3 are the real coefficients given in Table 6.

As $\acute{\delta}_m$ decreases beyond -180°, a_ϕ continues to increase linearly, whereas a_θ is fixed at the plateau value. Therefore, $\acute{\sigma}_m$ is linear in this region and is given by

$$\acute{\sigma}_m^b = q_4\acute{\delta}_m + q_5, \tag{13}$$

where the coefficients q_4 and q_5 are determined as follows. To ensure a differentiable, and thus continuous, piecewise model, the slope of the line defined by Equation (13) must equal the derivative of Equation (12) at $\acute{\delta}_m = -\pi$. Therefore

$$q_4 = \left.\frac{d\acute{\sigma}_m^a}{d\acute{\delta}_m}\right|_{\acute{\delta}_m=-\pi} = -2q_1\pi + q_2. \tag{14}$$

Now, upon substituting Equation (14) into Equation (13), setting $\acute{\sigma}_m^b = \acute{\sigma}_m^a$ and solving for q_5 at $\acute{\delta}_m = -\pi$ yields

$$q_5 = \left(\acute{\sigma}_m^a - q_4\acute{\delta}_m\right)\Big|_{\acute{\delta}_m=-\pi} = q_3 - q_1\pi^2. \tag{15}$$

The piecewise model for $\acute{\sigma}_m$ therefore transitions smoothly between a second-order and a first-order polynomial at $\acute{\delta}_m = 180^\circ$.

Equation (10) and (11), therefore, predict the extent to which the incident polarization state is altered when the incident wave is normal to the optic axis of the lens.

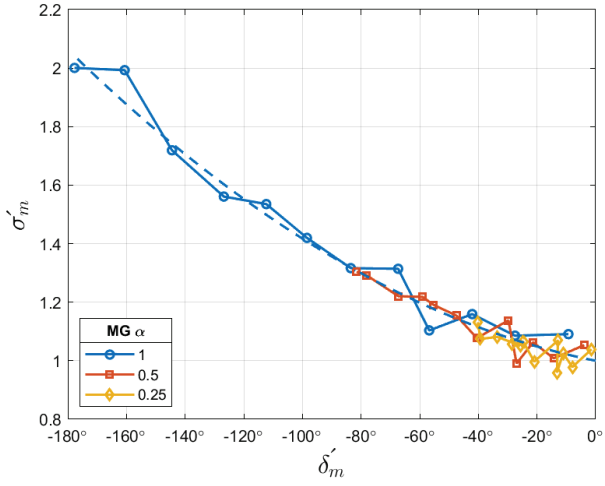

Fig. 5. $\acute{\sigma}_m$ vs. $\acute{\delta}_m$ for different α. Dashed curve is the model given by least square fit in Equation (12). For $\acute{\delta}_m < -180^\circ$, the model transitions smoothly into the linear relationship given by Equation (13).

B. Illumination at arbitrary polar angle

In this subsection, the impact of the lens anisotropy is examined as the polar angle θ of the incident field is swept from 0° to 90° in 11.25° increments. The incident field is therefore defined as

$$\overrightarrow{E}^{\text{inc}} = \begin{bmatrix} a_\theta^{\text{inc}} e^{j\psi_\theta^{\text{inc}}} \\ a_\phi^{\text{inc}} e^{j\psi_\phi^{\text{inc}}} \end{bmatrix} e^{-jk_0(x\sin(\theta)+z\cos(\theta))}. \tag{16}$$

In this experiment, three different lens radii are studied: 2.5λ, 3.5λ, and 5λ. It is observed that $\acute{\delta} = 0$ when the incident field is parallel to the optic axis, i.e., $\theta = 0^\circ$, and $\acute{\delta} = \acute{\delta}_m$ when the incident field is normal to it, i.e., $\theta = 90^\circ$. Moreover, the retardance is approximated by

$$\acute{\delta} = \acute{\delta}_m \sin^2(\theta). \tag{17}$$

The retardance computed directly from the 3D finite element simulations and the approximation given in Equation (17) are plotted in Figure 6.

Correspondingly, $\acute{\sigma} = 1$ when the incident field is parallel to the optic axis and $\acute{\sigma} = \acute{\sigma}_m$ when the incident field is normal to it. After experimenting with several approximating functions, the following provides the best fit of $\acute{\sigma}$ to the simulation data:

$$\acute{\sigma} = 1 + \frac{(\acute{\sigma}_m - 1)\left(1 - e^{-(\theta/\tau)^2}\right)}{1 - e^{-(\pi/2\tau)^2}}. \tag{18}$$

In the above equation, θ is specified in radians and τ is a parameter that has been set to 0.6 radians through experimentation. In Figure 7, both the results computed from the 3D finite element simulations and the approximation of Equation (18) are plotted.

Equation (17) and (18), therefore, predict the extent to which the incident polarization state is altered when

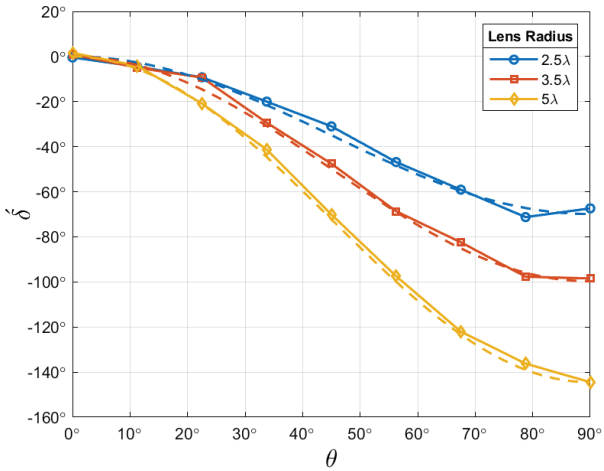

Fig. 6. $\acute{\delta}$ vs. θ for different r_l. Dashed curves are model given by Equation (17).

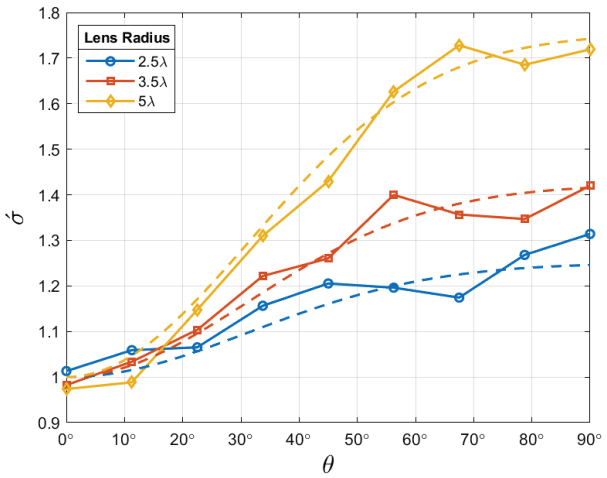

Fig. 7. $\acute{\sigma}$ vs. θ for different r_l. Dashed curves are model given by Equation (18).

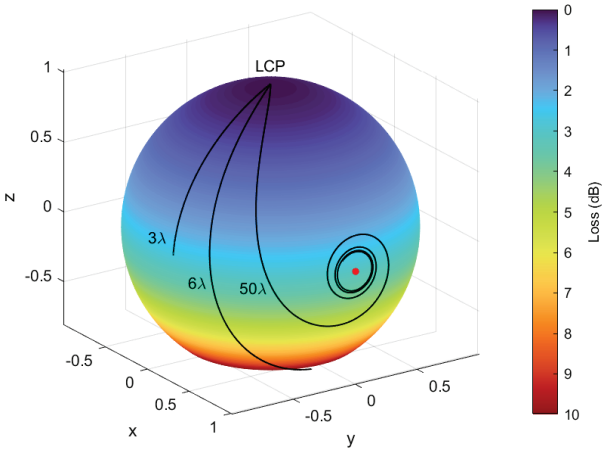

Fig. 8. Paths on Poincarè sphere for different r_l, as θ is swept from 0° to 90°. Surface of sphere indicates the PLF. Red dot is LHP marker. Illumination is LCP.

the incident wave arrives at an arbitrary angle relative to the optic axis of the lens.

V. POLARIZATION LOSS

Other than for the degenerate cases in which either $a_\theta^{\text{inc}} = 0$ or $a_\phi^{\text{inc}} = 0$, the anisotropy of the lens creates a mismatch between the incident and focal point polarizations. Normally, the receiving antenna has a polarization matched to that of the incident field. When the lens alters the incident polarization, the ability of the antenna to transfer focal power to the load is reduced. A non-dissipative loss is associated with this inefficiency and is termed the polarization loss factor (PLF). It is defined as follows [14]:

$$\text{PLF} = 10\log_{10}(\Gamma), \tag{19}$$

Finally, in Figure 9, the model provides PLF for a relatively wide range of lens radii with LCP illumination.

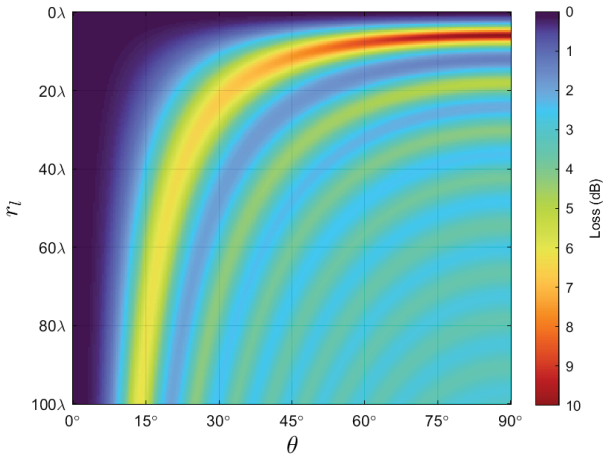

Fig. 9. PLFs as r_l and θ are varied. Compare with results on Poincarè sphere. Illumination is LCP.

The loss over most of the image is ≈ 3 dB, indicating a focal point that is nearly horizontally polarized.
where

$$\Gamma = |\hat{\rho}\cdot\hat{\rho}_r^*|^2 = |\cos(\psi_r)|^2. \tag{20}$$

In Equation (20), $\hat{\rho}$ is the unit polarization vector of the field at the focal point, $\hat{\rho}_r^*$ is the complex conjugate of the unit polarization vector for the receiving antenna, and ψ_r is the angle between the two. Since Equation (7) can be expressed as

$$\vec{E} = a_\theta e^{j\varphi_\theta}\begin{bmatrix}1\\ \sigma e^{j\delta}\end{bmatrix}, \tag{21}$$

then the direction of $\vec{E}$, and therefore $\hat{\rho}$, must depend only on σ and δ. Thus

$$\hat{\rho} = \frac{1}{\sqrt{1+\sigma^2}}\begin{bmatrix}1\\ \sigma e^{j\delta}\end{bmatrix}. \tag{22}$$

To compute the PLF using the focal point polarization model developed in the previous section, we first use Equation (17) to compute $\acute{\delta}$ and Equation (18) to compute $\acute{\sigma}$. Both values are independent of the incident field's polarization; therefore, we use Equation (8) to solve for δ and Equation (9) to solve for σ. In other words

$$\delta = \acute{\delta} + \left(\psi_\phi^{\text{inc}} - \psi_\theta^{\text{inc}}\right), \tag{23}$$

and

$$\sigma = \acute{\sigma}\,\sigma^{\text{inc}}. \tag{24}$$

An insight into the dependence of the PLF on r_l and θ is obtained by tracing the focal point polarization state on a Poincarè sphere that is PLF colorized according to the incident field. This is accomplished efficiently using the model developed in the previous section along with Equation (19), (23), and (24). Figure 8 provides such results for lens radii of 3λ, 6λ, and 50λ, all illuminated with LCP. For each lens, as θ is swept from 0° to 90°, the state moves away from the zero loss LCP

state. A maximum loss of ≈ 10 dB is observed when $r_l = 6\lambda$. For $r_l = 50\lambda$, the maximum loss drops to ≈ 6 dB, and the state follows a spiraling path toward the linear horizontally polarized (LHP) state, denoted as a red dot. Larger lenses produce even tighter spirals around the LHP state and incur a maximum loss that asymptotically approaches 3 dB.

VI. CONCLUSION

A uniaxially anisotropic Luneburg lens modifies the polarization state of an incident wave, thus introducing a polarization mismatch loss at the focal point. This mismatch is dependent upon the wave polarization, the degree of anisotropy, the radius of the lens, and the wave angle of arrival. For $r_l \gg \lambda$, the anisotropy strongly polarizes the focal point along the horizontal plane. This mismatch is undesirable in most circumstances, and minimizing it requires prediction of the unit cell permittivities along the x-, y- and z-axes.

We show that curve fitting of 3D finite element simulations provides an efficient method to model the retardance and polarization ratio of the lens. This model and knowledge of the incident wave and receiving antenna polarizations are sufficient to predict the amount of polarization mismatch loss, enabling the selection of isotropic unit cell geometries that are suitable for fused deposition modeling.

REFERENCES

[1] Z. Larimore, S. Jensen, A. Good, J. Suarez and M. S. Mirotznik, "Additive manufacturing of Luneburg lens antennas using space filling curves and fused filament fabrication," *IEEE Transactions on Antennas and Propagation*, vol. 66, no. 6, pp. 2818-2827, June 2018.

[2] S. Biswas, A. Lu, Z. Larimore, P. Parsons, A. Good, N. Hudak, B. Garrett, J. Suarez and M. S. Mirotznik, "Realization of modified Luneburg lens antenna using quasi-conformal transformation optics and additive manufacturing," *Microwave and Optical Technology Letters*, vol. 61, no. 4, pp. 1022-1029, 2019.

[3] M. Liang, W. R. Ng, K. Chang, K. Gbele, M. E. Gehm, and H. Xin, "A 3-D Luneburg lens antenna fabricated by polymer jetting rapid prototyping," *IEEE Transactions on Antennas and Propagation*, vol. 62, no. 4, pp. 1799-1807, April 2014.

[4] Y. Li, L. Ge, M. Chen, Z. Zhang, Z. Li, and J. Wang, "Multibeam 3-D-Printed Luneburg lens fed by magnetoelectric dipole antennas for millimeter-wave MIMO applications," *IEEE Transactions on Antennas and Propagation*, vol. 67, no. 4, pp. 2923-2933, May 2019.

[5] S. Lei, K. Han, X. Li, and G. Wei, "A design of broadband 3-D-Printed circularly polarized spherical Luneburg lens antenna for X-Band," *IEEE Antennas and Wireless Propagation Letters*, vol. 20, no. 4, April 2021.

[6] C. Wang, J. Wu, and Y. Guo, "A 3-D-Printed wideband circularly polarized parallel-plate Luneburg lens antenna," *IEEE Transactions on Antennas and Propagation*, vol. 68, no. 6, June 2020.

[7] J. Chen, H. Chu, Y. Zhang, Y. Lai, M. Chen, and D. Fang, "Modified Luneburg lens for achromatic sub-diffraction focusing and directional emission," *IEEE Transactions on Antennas and Propagation*, vol. 69, no. 11, November 2021.

[8] M. Yin, X. Y. Tian, L. L. Wu, and D. C. Li, "All-dielectric three-dimensional broadband Eaton lens with large refractive index range," Applied Physics Letters 104, 094101 (2014).

[9] C. Babayiğit, A. S. Evren, E. Bor, H. Kurt, and M. Turduev, "Analytical, numerical, and experimental investigation of a Luneburg lens system for directional cloaking," *Physical Review*, vol. 99, iss. 4, April 2019.

[10] P. I. Deffenbaugh, R. C. Rumpf, K. H. Church, "Broadband microwave frequency characterization of 3-D printed materials," *IEEE Transactions on Components, Packaging and Manufacturing Technology*, vol. 3, no. 12, pp. 2147-2155, December 2013.

[11] MATLAB, ver. 2021a, The Mathworks Inc., Natick, Massachusetts, 2021.

[12] J. M. Jin, D. Riley. Finite Element Analysis Of Antennas And Arrays. John Wiley & Sons Inc., New Jersey, 2009.

[13] A. Sihvola, Electromagnetic Mixing Formulas And Applications, The Institution of Engineering and Technology, London, 2008.

[14] C. A. Balanis, Antenna Theory - Analysis And Design, John Wiley & Sons Inc., New Jersey, 2005

[15] F. T. Ulaby, U. Ravaioli, Fundamentals Of Applied Electromagnetics, Pearson, 2015.

Brian F. LaRocca received the B.S.E.E. and M.S.E.E. degrees from the New Jersey Institute of Technology, Newark, NJ, USA in 1985 and 2000 respectively. He is currently working toward the Ph.D. degree in electrical engineering with the University of Delaware, Newark, DE, USA.

From 1985 to 1996, he worked in industry, from 1996 to 2004 as a government contractor, and from 2004 to present as a civilian engineer with the Department of the Army, Ft. Monmouth, NJ, USA and Aberdeen Proving Ground, MD, USA.

Mark S. Mirotznik (Senior Member, IEEE) received the B.S.E.E. degree from Bradley University, Peoria, IL, USA, in 1988, and the M.S.E.E. and the Ph.D. degrees from the University of Pennsylvania, Philadelphia, PA, USA, in 1991 and 1992, respectively.

From 1992 to 2009, he was a Faculty Member with the Department of Electrical Engineering,The Catholic University of America, Washington, DC, USA. Since 2009, he has been a Professor and an Associate Chair for Undergraduate Programs with the Department of Electrical and Computer Engineering, University of Delaware, Newark, DE, USA. He holds the position of Senior Research Engineer with the Naval Surface Warfare Center, Carderock Division. His current research interests include applied electromagnetics and photonics, computational electromagnetics, multifunctional engineered materials, and additive manufacturing.

Electronically Steerable Parasitic Patches for Dual-Polarization Reconfigurable Antenna Using Varactors

Yajie Mu, Jiaqi Han, Dexiao Xia, Xiangjin Ma, Haixia Liu, and Long Li

Key Laboratory of High-Speed Circuit Design and EMC of Ministry of Education, School of Electronic Engineering, Xidian University, Xi'an 710071, China
hxliu@xidian.edu.cn, lilong@mail.xidian.edu.cn

***Abstract* –** This paper presents a dual-polarized reconfigurable antenna loading electronically steerable parasitic patches. The proposed dual-polarized antenna is surrounded by four parasitic patches each of which is mounted by two varactor diodes on the ground. By tuning the varactors, continuous two-dimensional beam-steering can be achieved for each of the polarization. A prototype of the proposed antenna is fabricated and measured. Excellent agreement between the simulated and measured results is observed. It is observed that the maximum beam-scanning angles in *E*-plane and *H*-plane are greater than $\pm 25^{\circ}$, which is suitable for 5G base station applications.

***Keywords* –** Dual-polarized antenna, reconfigurable pattern antenna, parasitic patch, varactor.

I. INTRODUCTION

With the rapid development of wireless communication, there are increasing needs for high-speed, low-latency, and large-capacity wireless communications. The widely used dual-polarized antenna can effectively improve the communication capacity through polarization diversity [1–8]. Additionally, the pattern reconfigurable antennas are capable of steering the beam pointing, reducing noise interference and increasing signal coverage [9, 10]. Therefore, a dual-polarized pattern reconfigurable antenna can improve channel capacity and mitigate multi-path propagation fading.

Essentially, the pattern reconfigurable antennas can be achieved by adding active components (e.g., PIN diode, varactor, MEMS, etc.) on parasitic patches indirectly [9–12] or radiator directly [13–15]. The directly loaded manner affects the surface current flow path, while the indirectly loaded manner tunes parasitic patches to realize pattern reconfigurability. The active tuned parasitic patches are more flexible and transplantable compared to directly loaded manner. The main reason is that the parasitic patches do not change the structure of the driven antenna. The parasitic patches in the pattern reconfigurable antenna have various structures, such as rectangle, circle, and octagon, etc. Among them, the rectangular parasitic structure is the most commonly used. In the papers [16] and [20], the rectangular parasitic patches are adopted to achieve pattern reconfigurable antenna. In the paper [9], the parasitic patches are octagon structures that can obtain four pattern modes by adjusting the connection state of the parasitic patches and the ground. Moreover, there are very few dual-polarized pattern reconfigurable antennas. In the paper [9], a dual-polarized pattern reconfigurable Yagi patch antenna was proposed, which can achieve four-mode patterns in both polarizations. However, it uses eight PIN diodes to implement two deflection modes and only one can achieve one-dimensional beam-steering. In the papers [13] and [21], the directly loaded manner is used to tune the current of antenna radiators which can achieve pattern reconfigurable antenna.

In addition, there are many ways to realize a reconfigurable antenna pattern [18–24]. An artificial ground structure was reconfigured with PIN diodes inserted on the bottom ground to adjust the pattern of the antenna [18]. A broadside radiation pattern and a conical pattern were obtained when it alternatively operates in the TM10 mode and TM02 mode of the rectangular patch [19]. The optically transparent and compact dual-band, polarization-angle-independent metasurfaces have reconfigurable patterns for ambient energy harvesting and wireless power transfer [25, 26].

In this paper, electronically tuned parasitic patches using varactors are assigned in the surrounding area of a driven dual-polarized antenna to implement pattern reconfigurability. This work aims to design a two-dimensional dual-polarized pattern reconfigurable antenna. We propose a single antenna model that can explain the pattern reconfigurable principle of the capacitance-loaded parasitic patches. An antenna prototype is fabricated and measured. Continuously two-dimensional dual-polarized beam pointing adjustment is achieved.

Submitted On: October 2, 2021
Accepted On: January 28, 2022

https://doi.org/10.13052/2022.ACES.J.370107

This paper is organized as follows. Section II introduces the design principle of pattern reconfigurable antenna and the steps to achieve the dual-polarization pattern reconfigurable antenna. The dual-polarization reconfigurable antenna is introduced in great detail in Section III. Section IV describes the pattern reconfigurable results. The measured results of the dual-polarization pattern reconfigurable antenna are given in Section V. The conclusion is given in Section VI.

II. DESIGN PRINCIPLE

Fundamentally, the pattern reconfigurable principle of the proposed antenna is to change the surface current phase of the parasitic patches by loading unequal capacitance. The induced current with unequal phases would reradiate to form the desired patterns. Although numerous studies have discussed the parasitic patches tuned antennas [27], the mechanism by loading lumped components on parasitic patches has not been established.

In this paper, we qualitatively analyze the antenna which is tuned by capacitance-loaded parasitic patches. The proposed antenna for each polarization can be regarded as the three-point source. The central source is the driven source and the sibling two are parasitic sources, as shown in Figure 1. The driven source is referred to as the phase center point. Thereby, as the theory of point sources array [28], the far-field pattern can be expressed as

$$\vec{E} = \vec{E}_d + \vec{E}_p e^{-jk_0 D\cos\theta} + \vec{E}_p e^{j(k_0 D\cos\theta + \Delta\varphi)}, \quad (1)$$

where $\vec{E}_d$ and $\vec{E}_p$ are the driven and parasitic source amplitude at far-field, $k_0 D\cos\theta$ is the phase difference of parasitic source referring to the driven source, and $\Delta\varphi$ is the tunable phase. Based on these assumptions, patterns of the three-point sources are calculated and shown in Figure 2. Distance between the driven source and the parasitic source is $D = 0.32\ \lambda$ and $\left|\vec{E}_p\right| = 0.6\left|\vec{E}_d\right|$. It can be seen that the main beam pattern deflects when the tunable phase changes. This indicates that a pattern reconfigurable antenna can be achieved when we introduce unbalanced capacitance which results in an unbalanced phase on either side of parasitic arms.

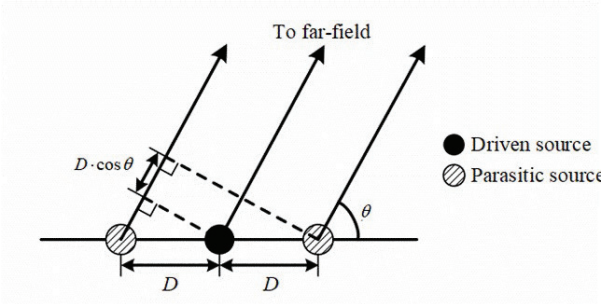

Fig. 1. Qualitative analysis for one driven source and two varactor-loaded parasitic sources.

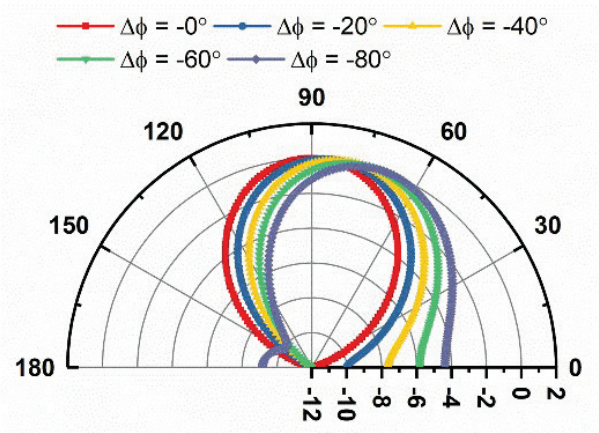

Fig. 2. Normalized patterns for different $\Delta\varphi$ on the parasitic source.

In this paper, electronically tuned parasitic patches using varactors are assigned in the surrounding area of a driven dual-polarization antenna to implement pattern reconfigurability. The unbalanced phase for achieving pattern reconfigurability on the parasitic patches is achieved by the unbalanced capacitance. The unbalanced capacitance is represented by ΔC which is the capacitance difference of each pair of varactors.

The dual-polarization pattern reconfigurable antenna can be decomposed into two single-polarization patterns reconfigurable antenna. Due to the two polarizations being symmetrical, we only need to analyze how one of the single polarization antennas realizes the reconfigurable pattern. The single polarization antenna can achieve the reconfigurable pattern when parasitic patches are assigned in H-plane and E-plane, respectively, as shown in Figure 3(a) and (b), where the electronically tuned arms must be parallel to the antenna polarization direction to control the antenna pattern. In Figure 3(a), the antenna can achieve the reconfigurable pattern with different ΔC in H-plane, as shown in Figure 4(a) and (b). When $\Delta C = 1$ pF and $\Delta C = -1$ pF, the beam deflection angles are 36° and −37° in H-plane, respectively. Similarly, when $\Delta C = 0.5$ pF and $\Delta C = -0.5$ pF, the beam deflection angles are 21° and −21° in H-plane, respectively. Therefore, the single polarization antenna can achieve the reconfigurable pattern in H-plane when the capacitance differences are introduced on parasitic patches in H-plane. In addition, the antenna can achieve the reconfigurable pattern with different ΔC in E-plane, as shown in Figure 3(b). In Figure 4(c), when ΔC =1 pF and $\Delta C = -1$ pF, the beam deflection angles are 20° and −18° in E-plane, respectively. Similarly, in Figure 4(d),

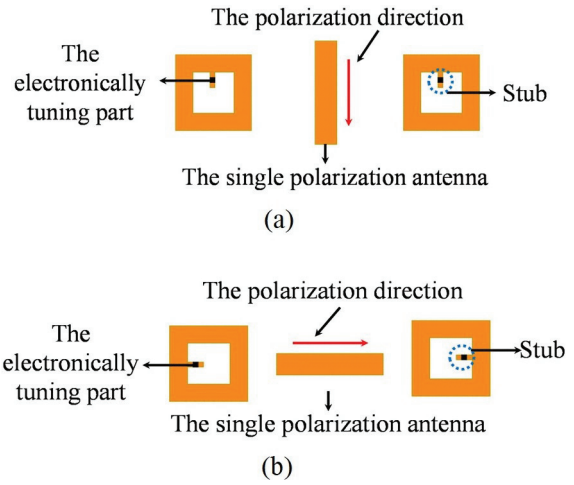

Fig. 3. (a) The reconfigurable pattern of the single-polarization antenna in H-plane. (a) The reconfigurable pattern of the single-polarization antenna in E-plane.

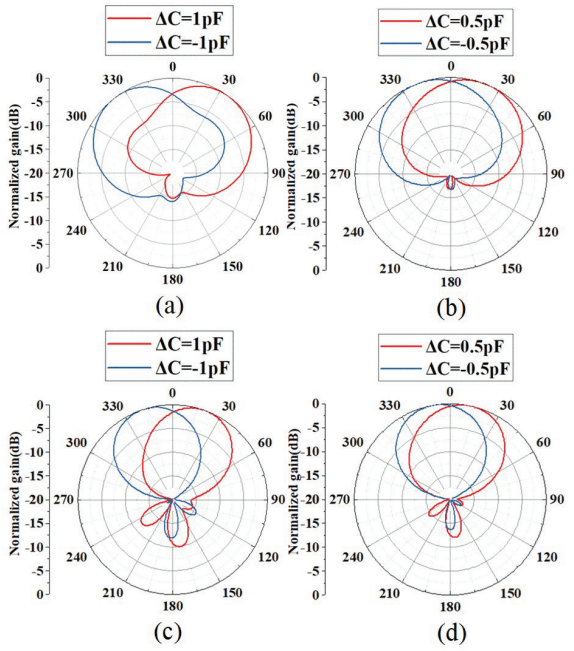

Fig. 4. (a) and (b) The reconfigurable patterns of the single-polarization antenna with different capacitance values in the H-plane. (c) and (d) The reconfigurable pattern of the single-polarization antenna with different capacitance values in E-plane.

when ΔC = 0.5 pF and ΔC = −0.5 pF, the beam deflection angles are 13° and −11° in E-plane, respectively. Therefore, the single polarization antenna can achieve the reconfigurable pattern in E-plane when the capacitance differences are introduced on parasitic patches in E-plane. According to the above analysis, the single polarization antenna can realize the reconfigurable pattern in two-dimensional directions by loading two electrically tuned parasitic patches in the E-plane and H-plane, respectively.

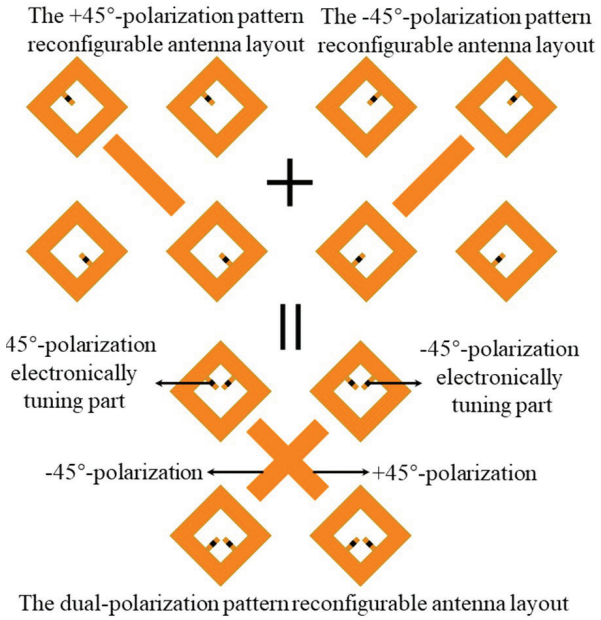

Fig. 5. The single polarization pattern reconfigurable antenna layout and the dual-polarization pattern reconfigurable antenna layout with two-dimensional beam-steering.

For E-plane or H-plane reconfigurable pattern, two parasitic patches are needed at least, which are placed on scanning plane. Hence, four parasitic patches are arranged to achieve the two-dimensional reconfigurable pattern in a single polarization antenna. Therefore, the two-dimensional dual-polarization pattern reconfigurable antenna is made of two orthogonal single-polarized antennas that have two-dimensional pattern reconfigurability, as shown in Figure 5. For a ±45° dual-polarization antenna, the E-plane of +45°-polarization is the H-plane of −45°-polarization. Therefore, the E-plane parasitic patches of +45° polarization and the H-plane parasitic patches of the −45° polarization are in the same area where the +45° and −45° polarization can share a parasitic patch. These shared parasitic patches have the electronically tuning parts along each polarization direction. Therefore, the dual-polarization antenna has pattern reconfigurability in two-dimensional directions by shared parasitic patches, as shown in Figure 5.

III. ANTENNA DESIGN

As mentioned before, the indirectly loaded pattern reconfigurable antennas are composed of a driven antenna and parasitic patches. And the two-dimensional

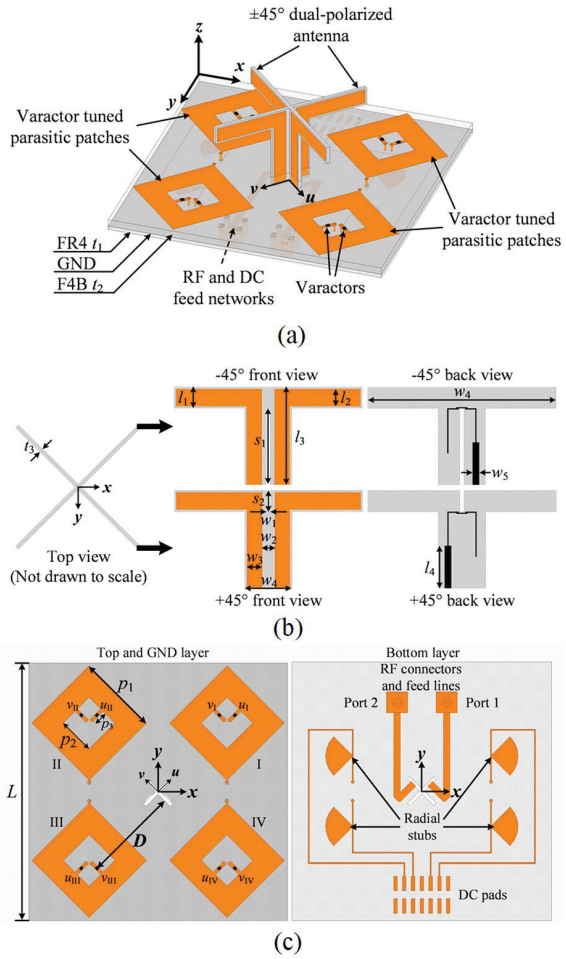

Fig. 6. Topology of the proposed antenna. (a) Perspective view, (b) dual-polarized antenna, and (c) varactor-tuned parasitic patches with DC bias lines (the four patches are labeled as I, II, III, and IV anticlockwise).

beam-steering scheme of dual-polarized antennas is also analyzed in the previous section. In this section, the specific design scheme of the dual-polarization antenna with a two-dimensional reconfigurable pattern is presented.

The geometrical topology of the proposed antenna is shown in Figure 6(a). It can be seen that it has a ±45° dual-polarized dipole antenna and four parasitic patches, which are tuned by eight varactors. The orthogonal *u*- and *v*-directions are defined to represent the $\varphi = +45°$ and $\varphi = -45°$ polarization directions, respectively.

Detailed geometrical structure of the dual-polarized antenna located at the center is shown in Figure 6(b). The printed dipole antennas have compact configurations for dual-polarized operations. The structure of the two dipole antennas is almost the same except for substrate shape and feed lines. The substrate for the printed dipole

Table 1 Parameter values (λ_0 at 3.4 GHz)

Parameters	Values	Parameters	Values
t_1	1 mm	w_3	3.5 mm
t_2	2 mm	w_4	44 mm
t_3	1 mm	s_1	18 mm
l_1	5 mm	s_2	5 mm
l_2	4 mm	L	75 mm
l_3	23 mm	D	28.3 mm
l_4	10 mm	p_1	23.5 mm
w_1	1 mm	p_2	10.6 mm
w_2	3 mm	p_3	4.3 mm

antennas is FR4 ($\varepsilon_r = 4.4$, $\tan\delta = 0.02$). For each polarization, the dipole is integrated with a balun which connects to a 50-Ω SMA connector [26].

The parasitic patches, reflective ground plane, and direct circuit (DC) bias lines are shown in Figure 4(c). The four capacitance-loaded parasitic patches are etched on an FR4 substrate, which is assigned along with two polarizations. It can be seen that patches I and III lie in the *u*-plane, while patches II and IV lie in the *v*-plane. To realize a two-dimensional dual-polarized pattern reconfigurable, two arms along *u*- and *v*-directions, which are mounted by varactors, are designed on each parasitic patch.

The model of the varactor used in this design is Skyworks SMV1430 whose junction capacitance ranges from 0.31 to 1.24 pF as reverse voltage changes from 30 to 0 V. Package series inductance is 0.45 nH. The varactors are soldered in the 0.5-mm gap of parasitic patches arms. A F4B substrate ($\varepsilon_r = 2.5$; $\tan\delta = 0.005$) separates the ground layer and feed networks. The radio frequency (RF) connectors and DC feed lines are integrated into the bottom layer as shown in Figure 6(c). Four radial stubs are designed to choke RF signals.

For simplicity, we label the varactor by direction combined with the patch index. For example, the pattern of the dipole in the *u*-plane (+45° polarization) can be steered to scan in *u*-plane by using u_I and u_{III} varactors, while as u_{II} and u_{IV} varactors are used, the pattern can scan in *v*-plane. In other words, there are four tuned arms to steer the radiation pattern of each polarization. A pair of varactors steer the pattern scanning in *E*-plane and the other pair of varactors steer the pattern scanning in *H*-plane. All the structural parameters are listed in Table 1. Central operating frequency of the proposed antenna is 3.4 GHz.

IV. PATTERN RECONFIGURABLE RESULT

Ansys HFSS 15.0 is applied to simulate the proposed antenna. The varactor is simulated by a capacitor in series with an inductor using lumped *RLC* boundary conditions. The varactor is characterized by the varying

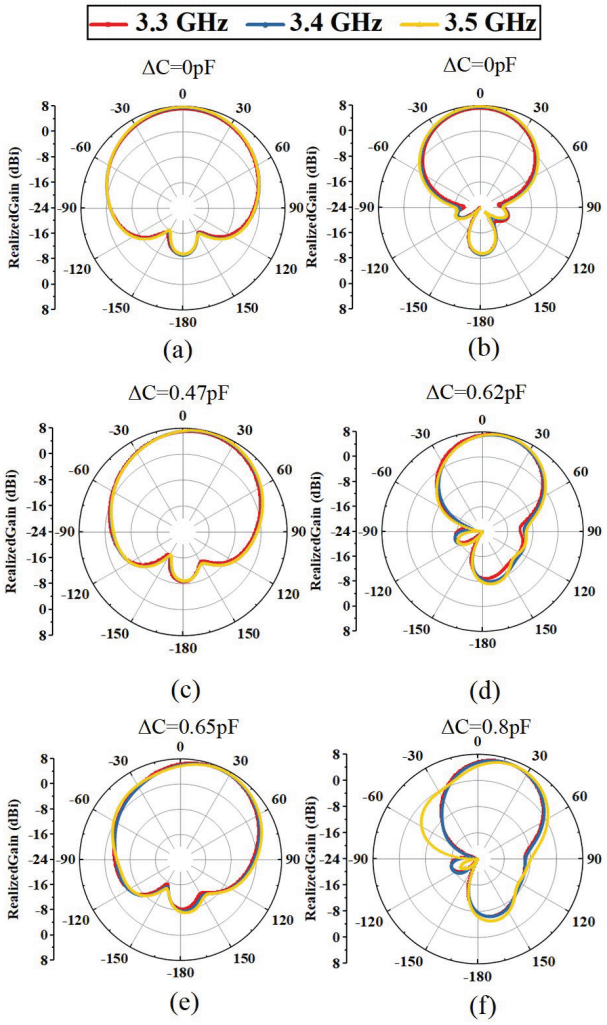

Fig. 7. Simulated gain patterns deflection in *E*-plane and *H*-plane at different frequencies when Δ*C* varies. (a), (c), and (e) Patterns in *E*-plane. (b), (d), and (f) Patterns in *H*-plane.

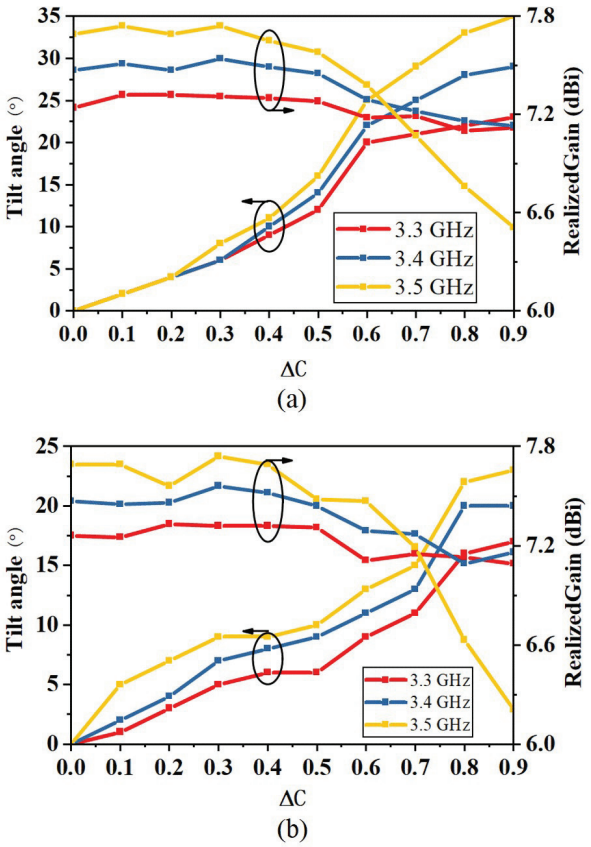

Fig. 8. Tilt angle and peak gain in (a) *E*-plane and (b) *H*-plane versus Δ*C* at different frequencies.

capacitance value of the capacitor. Here, the capacitance difference of each pair of varactors is defined as Δ*C* for simplicity. As shown in Figure 7, the simulated gain patterns, which take into the mismatch loss account, with different deflection angles are presented for different Δ*C*. Both *E*-plane and *H*-plane simulated results are plotted. It can be seen that the tilt patterns show similarly reconfigurable results within the working frequency band. In this case, only Port 1 is excited and Port 2 has similar results. Varactor pair of u_I and u_{III} controls the pattern tilt in *E*-plane, while u_{II} and u_{IV} control the pattern tilt in *H*-plane, which can be controlled independently. Pattern tilt angles at 3.5 GHz are 0°, 16°, and 27° in *E*-plane, while in *H*-plane, they are 0°, 13°, and 22° for different Δ*C*, as shown in Figure 7. The peak gains are 7.69, 7.58, and 7.21 dBi in *E*-plane, while in *H*-plane 7.69, 7.37, and 6.63 dBi, respectively. It should be noted that for the same Δ*C*, the pattern deflection angles are not identical in *E*-plane and *H*-plane.

For the detailed variation of the pattern tilt angle versus Δ*C*, we simulated the proposed antenna under different Δ*C* when Port 1 is excited, as shown in Figure 8. From the results, it suggests that pattern deflection angle increases with Δ*C*. Meanwhile, peak gain decreases due to scanning loss and mismatch loss. At 3.5 GHz, the proposed antenna possesses a maximum deflection angle of 35° and its peak gain drops to 6.5 dBi accordingly in *E*-plane, as shown in Figure 8(a). Similar results can be obtained for *H*-plane deflection that the proposed antenna possesses a maximum deflection angle of 28° and its peak gain drops to 6.21 dBi accordingly at 3.5 GHz, as shown in Figure 8(b). Similar results can be obtained for Port 2 which is a +45° polarization antenna. The different deflection angles of the *E*-plane and *H*-plane patterns are caused by the different coupling of the antenna to the *E*-plane and *H*-plane. Through the above simulation

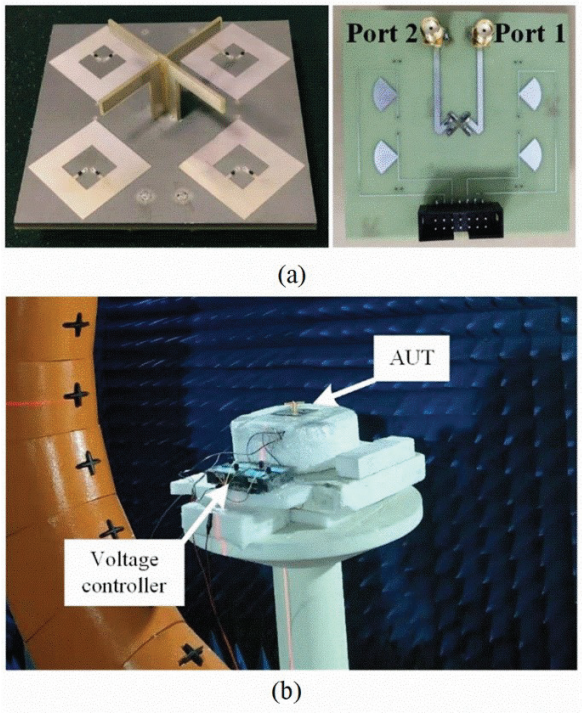

Fig. 9. Fabricated two-dimensional dual-polarized pattern reconfigurable antenna. (a) Fabricated antenna prototype. (b) Measurement scene.

results, it can be analyzed to get that we proposed antenna possess two-dimensional dual-polarization pattern reconfigurability.

V. MEASUREMENT RESULTS

The fabricated prototype of the proposed antenna is shown in Figure 9(a). Simulated and measured reflection coefficients for different ΔC are shown in Figure 10. Note that Port 1 ΔC represents the capacitance difference of u_I and u_{III}, while Port 2 ΔC represents the capacitance difference of v_{II} and v_{IV}. It can be observed that the measured results agree with the simulated ones as ΔC changed. However, the measured reflection coefficients of the two ports are not overlapped exactly. A possible explanation for this might be the variation of actual capacitance of the varactor and designed data obtained from the manufacturer's datasheet.

The antenna is measured in a multi-probe anechoic chamber, as shown in Figure 9(b). Four voltage controllers that can continuously generate 0−30 V voltage are applied to bias the varactors for two-dimensional beam-steering. The measured and simulated E-plane patterns within the working frequency band as Port 1 excited are shown in Figure 11. For simplicity, only the deflection pattern under a certain capacitance difference on the E-plane is given. We tuned the voltage controller

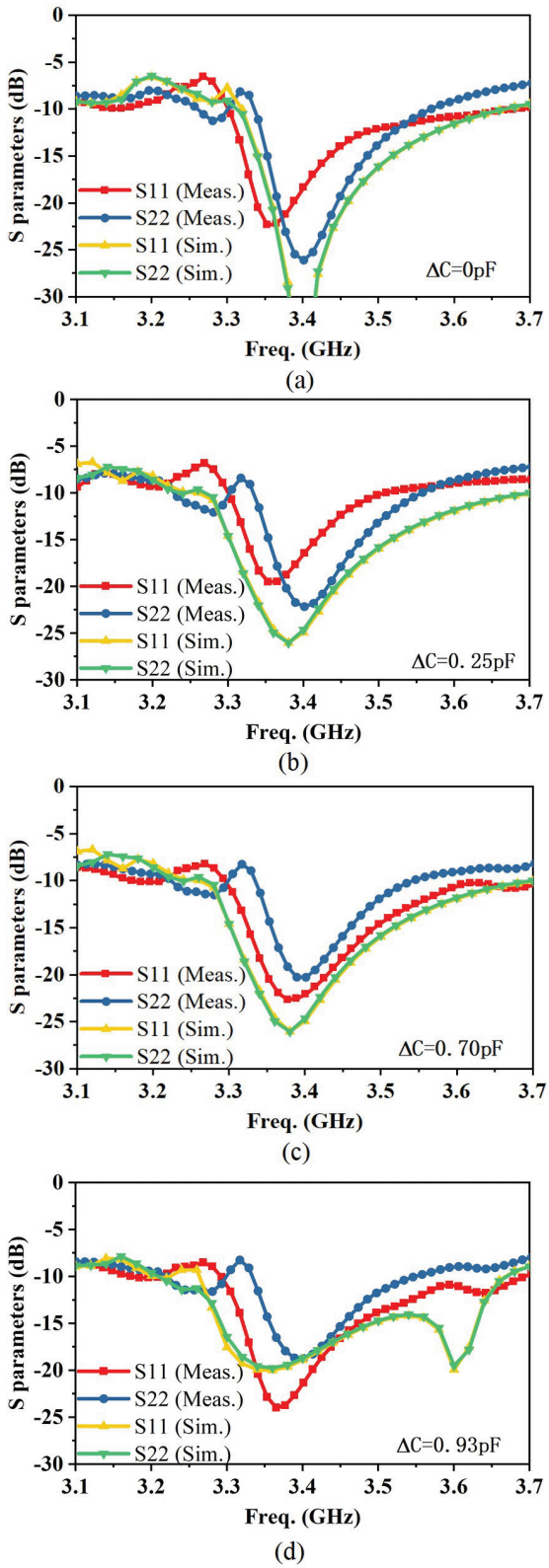

Fig. 10. Simulated and measured reflection coefficients for different ΔC. (a) ΔC = 0 pF. (a) ΔC = 0.25 pF. (a) ΔC = 0.70 pF. (a) ΔC = 0.93 pF.

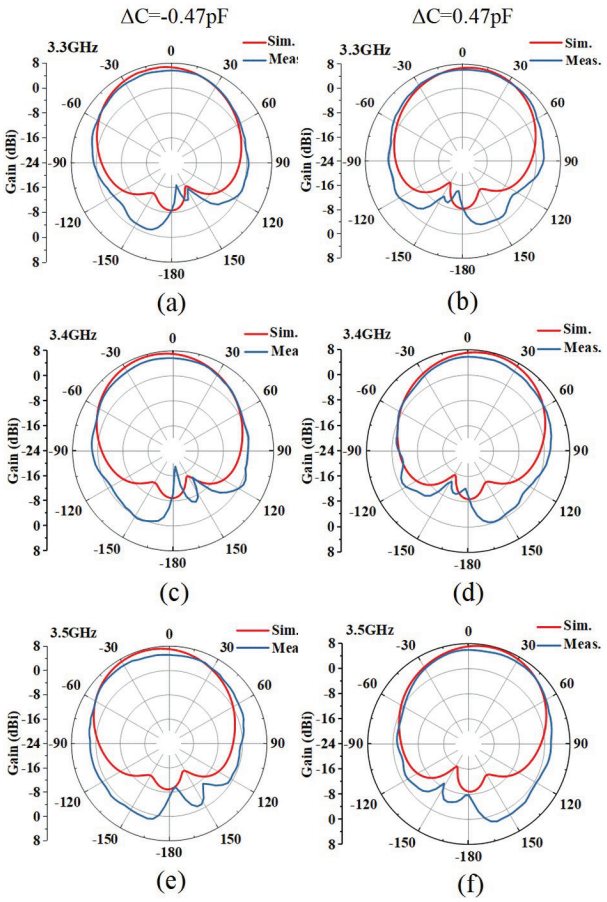

Fig. 11. Simulated and measured E-plane gain patterns for $\Delta C = -0.47$ pF and $\Delta C = 0.47$ pF at different frequencies with Port 1 excited. (a), (c), and (e) Patterns at 3.3, 3.4, and 3.5 GHz for $\Delta C = -0.47$ pF. (b), (d), and (f) Patterns at 3.3, 3.4, and 3.5 GHz for $\Delta C = 0.47$ pF.

to set ΔC of u_I and u_{III} as -0.47 and 0.47 pF. From the comparisons, we can clearly see that measured patterns are deflected to the intended directions for each frequency. At 3.3 GHz, peak gains, which are 5.80 and 5.92 dBi, occur at $\theta = -16^\circ$ and $\theta = 18^\circ$ when ΔC is equal to -0.47 and 0.47 pF, respectively. At 3.4 GHz, peak gains, which are 5.89 and 5.81 dBi, occur at $\theta = -14^\circ$ and $\theta = 16^\circ$ when ΔC is equal to -0.47 and 0.47 pF, respectively. At 3.5 GHz, peak gains, which are 5.74 and 5.96 dBi, occur at $\theta = -24^\circ$ and $\theta = 28^\circ$ when ΔC is equal to -0.47 and 0.47 pF, respectively. There exists a discrepancy of beam pointing and gain-loss between simulated and measured results. They are caused by fabrication errors and measurement tolerance. The back lobes of the measured patterns are larger than simulated ones. This may be due to the support platform. The measured efficiency of the antenna is above 50%, a little lower than that of the simulated one. Nevertheless, the measured results validate the good performance of the proposed antenna. In addition, the measured cross-polarization discriminations are higher than 12.5 dB, which satisfies the requirement of communication.

Table 2 Comparison of this work with some existing works

Ref.	DP	PR	PR dim.	BW (%)
[3]	Yes	No	NA	44.5%
[9]	Yes	Yes	1	5.6%
[14]	No	Yes	1	58%
[15]	No	Yes	1	0.6%
[24]	No	Yes	1	20.8%
This work	Yes	Yes	2	5.9%

Note: DP: Dual polarization; PR: polarization reconfigurability; PR dim.: PR dimension; BW: bandwidth.

In Table 2, the proposed antenna is compared with some existing works. It can be seen that only [9] and the work of this paper are about the reconfigurable pattern of dual-polarization antennas, and the bandwidth of this paper is wider. In addition, only the proposed antenna has a two-dimensional dual-polarization pattern reconfigurable ability. And the antenna can achieve continuous steering.

VI. CONCLUSION

A dual-polarized pattern reconfigurable antenna has been proposed and fabricated in this paper. This antenna is capable of continuously steering patterns in E- and H-planes by using varactors tuned parasitic patches. The proposed parasitic patches topology can be transplanted to other frequency bands. Two-dimensional pattern deflection exceeds 50°. Measured reflection coefficients are less than -10 dB from 3.3 to 3.5 GHz for two ports when continuously steering the beam pointing. Validation of the prototyped antenna indicates that the proposed varactor-tuned parasitic patches can effectively direct the pattern of the driven antenna, which is coincident with the qualitative analysis.

ACKNOWLEDGEMENT

The authors acknowledge the National Key Research and Development Program of China under Grant 2021YFA1401001, the National Natural Science Foundation of China under Grant 62001342, the Key Research and Development Program of Shaanxi under Grant 2021TD-07, and the Outstanding Youth Science Foundation of Shaanxi Province under Grant 2019JC-15.

REFERENCES

[1] S. Kozono, T. Tsuruhara, and M. Sakamoto, "Base station polarization diversity reception for mobile radio," *IEEE Transactions. Vehicle Technology*, vol. 33, no. 4, pp. 301-306, 1984.

[2] Q. Chu, D. Wen, and Y. Luo, "A broadband ±45° dual-polarized antenna with Y-shaped feeding lines," *IEEE Transactions on Antennas and Propagation*, vol. 63, no. 2, pp. 483-490, 2015.

[3] Y. Liu, H. Yi, F. Wang, and S. Gong, "A novel miniaturized broadband dual-polarized dipole antenna for base station," *IEEE Antennas and Wireless Propagation Letters*, vol. 12, pp. 1335-1338, 2013.

[4] Z. Bao, Z. Nie and X. Zong, "A novel broadband dual-polarization antenna utilizing strong mutual coupling," *IEEE Transactions on Antennas and Propagation*, vol. 62, no. 1, pp. 450-454, 2014.

[5] Q. Zhang and Y. Gao, "A compact broadband dual-polarized antenna array for base stations," *IEEE Antennas and Wireless Propagation Letters*, vol. 17, no. 6, pp. 1073-1076, 2018.

[6] W. Chen et al., "A low-profile broadband dual-polarized base station antenna using folded dipole radiation element," *IEEE Access*, vol. 7, pp. 67679-67685, 2019.

[7] Y. -L. Chen, Y. -Z. Sui, Z. -Q. Yang, X. -Y. Qu, and W. -H. Zong, "A broadband dual-polarized antenna for 2G/3G/4G/5G base station applications," *Applied Computational Electromagnetics Society Journal*, vol. 36, no. 9, pp. 1202-1208, 2021.

[8] J. Yin, H. Sun, and L. Zhang, "A wideband wide-beam dual polarized dipole antenna and its application in wideband wide-angle scanning array," *Applied Computational Electromagnetics Society Journal*, vol. 35, no. 6, pp. 692-699, 2020.

[9] W. Deng, X. Yang, C. Shen, J. Zhao and B. Wang, "A dual-polarized pattern reconfigurable Yagi patch antenna for microbase stations," *IEEE Transactions on Antennas and Propagation*, vol. 65, no. 10, pp. 5095-5102, 2017.

[10] M. A. Hossain, I. Bahceci and B. A. Cetiner, "Parasitic layer-based radiation pattern reconfigurable antenna for 5G communications," *IEEE Transactions on Antennas and Propagation*, vol. 65, no. 2, pp. 6444-6452, 2017.

[11] L. Marantis, D. Rongas, A. Paraskevopoulos, C. Oikonomopoulos-Zachos and A. Kanatas, "Pattern reconfigurable ESPAR antenna for vehicle-to-vehicle communications," *IET Microwaves, Antennas and Propagation*, vol. 12, no. 3, pp. 280-286, 2018.

[12] S. Raman, N. Timmons and J. Morrison, "Gain enhanced pattern reconfigurable planar yagi-uda antenna on coplanar structure," *Electronics Letters*, vol 49, no. 25, pp. 1593 -1595, 2013.

[13] S. Shi and W. Ding, "Radiation pattern reconfigurable microstrip antenna for WiMAX application," *Electronics Letters*, vol. 51, no. 9, pp. 662-664, 2015.

[14] S. Ahdi Rezaeieh and A. M. Abbosh, "Pattern-reconfigurable magnetoelectric antenna utilizing asymmetrical dipole arms," *IEEE Antennas and Wireless Propagation Letters*, vol. 18, no. 4, pp. 688-692, 2019.

[15] Z. Ding, R. Jin, J. Geng, W. Zhu and X. Liang, "Varactor loaded pattern reconfigurable patch antenna with shorting pins," *IEEE Transactions on Antennas and Propagation*, vol. 67, no. 10, pp. 6267-6277, 2019.

[16] S. Xiao, C. Zheng, M. Li, J. Xiong and B. Wang, "Varactor-loaded pattern reconfigurable array for wide-angle scanning with low gain fluctuation," *IEEE Transactions on Antennas and Propagation*, vol. 63, no. 5, pp. 2364-2369, 2015.

[17] F. Farzami, S. Khaledian, B. Smida and D. Erricolo, "Pattern-reconfigurable printed dipole antenna using loaded parasitic patches," *IEEE Antennas and Wireless Propagation Letters*, vol. 16, pp. 1151-1154, 2017.

[18] Y.-F. Cheng, X. Ding, W. Shao, and C. Liao, "A novel beam-steerable antenna using HIS-SWG reconfigurable artificial ground structure," *Applied Computational Electromagnetics Society Journal*, vol. 34, no. 1, pp. 107-114, 2019.

[19] H.-Y. Huang, B.-Z. W. Wang, X. Ding, and W. Shao, "A pattern reconfigurable antenna based on TM10 and TM02 modes of rectangular patch," *Applied Computational Electromagnetics Society*, vol. 28, no. 8, pp. 693-699, 2013.

[20] W. Li, L. Bao, and Y. Li, "A novel frequency and radiation pattern reconfigurable antenna for portable device applications," *Applied Computational Electromagnetics Society Journal*, vol. 30, no. 12, pp. 1276-1285, 2015.

[21] M. Saravanan and M. J. S. Rangachar, "Design of Pin loaded reconfigurable patch antenna for wireless communications," *Applied Computational Electromagnetics Society Journal*, vol. 34, no. 10, pp. 1535-1541, 2019.

[22] M. A. Wazie, A.-F. A. Sheta, and W. A. Malik, "RF MEMS switches enabled H-shaped beam reconfigurable antenna," *Applied Computational Electromagnetics Society Journal*, vol. 34, no. 9, pp. 1312-1318. 2019.

[23] Y. Zhang, D. Sun, T. Dong, and J. Yin, "Design of reconfigurable patch antenna in frequency, pattern, and switchable polarization," *Applied Computational Electromagnetics Society Journal*, vol. 35, no. 9, pp. 1037-1046, 2020.

[24] R. Li, H. Yang, B. Liu, Y. Qin and Y. Cui, "Theory and realization of a pattern-reconfigurable antenna based on two dipoles," *IEEE Antennas and Wireless Propagation Letters*, vol. 17, no. 9, pp. 1291-1295, 2018.

[25] L. Li, X. Zhang, C. Song, W. Zhang, T. Jia and Y. Huang, "Compact dual-band, wide-angle, polarization-angle-independent rectifying metasurface for ambient energy harvesting and wireless power transfer," *IEEE Transactions on Microwave Theory and Techniques*, vol. 69, no. 3, pp. 1518-1528, March 2021.
[26] L. Li, P. Zhang, F. Cheng, M. Chang, and T. J. Cui, "An optically transparent near-field focusing metasurface," *IEEE Transactions on Microwave Theory and Techniques*, vol. 69, no. 4, pp. 2015-2027, April 2021.
[27] Y. Gou, S. Yang, J. Li and Z. Nie, "A compact dual-polarized printed dipole antenna with high isolation for wideband base station applications," *IEEE Transactions on Antennas and Propagation*, vol. 62, no. 8, pp. 4392-4395, 2014.
[28] J. D. Kraus and R. J. Marhefkas, "Antennas: For all applications" (New York, NY, USA: McGraw-Hill, 2002, 3rd ed.)

Yajie Mu was born in Gansu, China, in 1997. She received the B.E. and M.S. degrees in electromagnetic fields and microwave technology from Xidian University, Xi'an, China, in 2018 and 2021, respectively.

Her current research interests include antenna decoupling, pattern reconfigurable antenna, and large angle scanning array.

Jiaqi Han was born in Henan, China, in 1991. He received the B.E. degree in electronic and information engineering from Henan Normal University, Xinxiang, China, in 2014, and the Ph.D. degree in electromagnetic fields and microwave technology from Xidian University, Xi'an, China, in 2019.

He is currently a Postdoctoral Fellow with the School of Electronic Engineering, Xidian University. His research interests include the design of programmable metasurfaces and their applications on wireless power transfer and computational imaging.

Dexiao Xia was born in Jiangxi, China, in 1998. He received the B.E. degree in electronic and information engineering in 2019. He is currently working toward the Ph.D. degree in electromagnetic fields and microwave technology with Xidian University, Xi'an, China, since 2021.

His current research interests include pattern reconfigurable antenna, metasurface antenna decoupling, and array antenna optimization.

Xiangjin Ma was born in Anhui, China, in 1998. He received the B.E. degree in communication engineering from the Nanchang Institute of Technology, Nanchang, China, in 2019. He is currently working toward the Ph.D. degree in electromagnetic field and microwave technology with Xidian University, Xi'an, China.

His current research interests include analysis and application of programmable metasurfaces, design of high-performance programmable metasurfaces, and microwave holographic imaging.

Haixia Liu Haixia Liu received the B.S. and M.S. degrees in test and measurement technique and instrumentation and the Ph.D. degree in electromagnetic fields and microwave technology from Xidian University, Xi'an, China, in 1998, 2001, and 2014, respectively.

She studied at Shizuoka University, Shizuoka, Japan, as a cooperative graduate in 2001. Since 2002, she has been working with Xidian University. His research interests include circuit analysis, frequency measurement and control, wireless power transfer, antennas, and electromagnetic compatibility.

Long Li Long Li received the B.E. and Ph.D. degrees in electromagnetic fields and microwave technology from Xidian University, Xi'an, China, in 1998 and 2005, respectively.

He was a Senior Research Associate with the Wireless Communications Research Center, City University of Hong Kong, Hong Kong, in 2006. He received the Japan Society for Promotion of Science (JSPS) Postdoctoral Fellowship and visited Tohoku University, Sendai, Japan, as a JSPS Fellow from 2006 to 2008. He was a Senior Visiting Scholar with the Pennsylvania State University, State College, PA, USA, in 2014. He is currently a Professor with the School of Electronic Engineering, Xidian University. He is the Director of Key Laboratory of High-Speed Circuit Design and EMC, Ministry of Education, China, and the Dean of Hai-Tang No.9 Academy of Xidian University. His research interests

include metamaterials/metasurfaces, antennas and microwave devices, field-circuit collaborative design and EMC, wireless power transfer and harvesting technology, and OAM vortex waves. He has authored or coauthored more than 120 papers in journals and held more than 20 patents.

Dr. Li received Nomination Award of National Excellent Doctoral Dissertation of China in 2007. He won the Best Paper Award in the International Symposium on Antennas and Propagation in 2008. He received the Program for New Century Excellent Talents in University of the Ministry of Education of China in 2010. He won the First Prize of Awards for Scientific Research Results offered by Shaanxi Provincial Department of Education, China, in 2013. He received the IEEE APS Raj Mittra Travel Grant Senior Researcher Award in 2015. He received Shaanxi Youth Science and Technology Award in 2016, and Distinguished Young Scholars Foundation of Shaanxi Province of China, in 2019. He was awarded a Chang-Jiang Distinguished Scholar by the Ministry of Education, China, in 2021. He is the Vice-President of MTT-Chapter in IEEE Xi'an Section. He is a TPC Co-Chair of APCAP2017 and a General Co-Chair of AWPT2019. He serves as an Associate Editor for *ACES Journal and Guest Editor for IEEE J-ERM Special Issue*.

Compact Cauliflower-Shaped Antenna for Ultra-Wideband Applications

Boumediene Guenad[1,2], Abdelhalim Chaabane[3], Djelloul Aissaoui[4], Abdelhafid Bouacha[2], and Tayeb A. Denidni[5]

[1]Faculté des Technologiques,
Université Hassiba Benbouali de Chlef, N19 Ouled Fares, Chlef, Algeria
b.guenad@univ-chlef.dz

[2]Laboratoire De Télécommunications,
Université De Tlemcen, BP 230, Pole Chetouane, Tlemcen 13000, Algeria
abdelhafid.bouacha@gmail.com

[3]Laboratoire des Télécommunications, Département d'Electronique et Télécommunications, Faculté des Sciences et de la Technologie, Université 8 Mai 1945 Guelma, BP 401, Guelma 24000, Algeria
abdelhalim.chaabane@univ-guelma.dz

[4]Faculté des sciences Technologiques,
Université Ziane-Achour de Djelfa, Djelfa 17000, Algeria
djelloul.aissaoui@univ-djelfa.dz

[5]Institut National de la Recherche Scientifique
Centre EMT, 800 Rue De La Gauchetière West, Suite 6900, Montreal, Quebec, H5A-1K6, Canada
denidni@emt.inrs.ca

***Abstract* –** A compact coplanar waveguide (CPW) fed cauliflower-shaped antenna is presented and discussed in this paper. To extend the impedance bandwidth and to improve the impedance matching, fractal geometry having a cauliflower shape is introduced along the edges of the radiator. To validate the simulated results by experimental ones, a prototype of the designed antenna was fabricated on the RO-4350B substrate having a compact size of $0.3623\lambda_0 \times 0.41\lambda_0 \times 0.01524\lambda_0$ at 3 GHz. An Agilent 8722ES vector network was used for the reflection coefficient measurement revealing that the –10 dB bandwidth of the fabricated antenna offers an impedance bandwidth of 113% extending from 3.05 to 10.96 GHz. Besides, the antenna's radiation patterns are measured in an anechoic chamber showing consistent radiation patterns characteristic over the entire working band. Furthermore, the proposed antenna has a peak gain of around 6 dBi and an average radiation efficiency almost over 90% across the entire operating band. Thus, the proposed antenna could be useful in many modern ultra-wideband (UWB) communication systems.

***Index Terms* –** Cauliflower-shaped antenna, coplanar waveguide (CPW) fed, hexagonal patch antenna, fractal geometry, ultra-wideband (UWB) antenna.

I. INTRODUCTION

In recent years, telecommunication systems have undergone significant technological change mainly due to the multiplication and growth of newer consumer markets. However, the emergence of the communication markets and the growth of the number of consumers have been accompanied by strict specifications to meet the requirements of the new users. Indeed, the new transmission/reception systems must today provide a maximum of services over different frequency bands and bit rates. The rise of planar technologies (microstrip, coplanar, etc.) for low-power applications is a part of the response to these new requirements. In these contexts, an ultra-wideband (UWB) technology has been purported as a promising solution for the new communication systems. UWB technology has many advantages, including high-speed transmission and low energy profile [1]. Since the definition of the frequency band from 3.1 to 10.6 GHz for UWB communication systems by the FCC in 2002 [2], several antenna structures have been reported by many researchers to enhance the bandwidth of the antennas [4–9].

However, the design of a UWB antenna presents various challenges to meet the different requirements: low profile, low cost, low radiated power, low power

Submitted On: June 27, 2021
Accepted On: December 28, 2021

https://doi.org/10.13052/2022.ACES.J.370108

consumption, broadband operability, high data rate transmission, and stable radiation patterns. Various solutions have been proposed to ensure these requirements; the most promising is the introduction of fractal geometries.

The use of these geometries increases the bandwidth and the gain and can introduce the multiband properties without changing the dimensions of the antenna which remains very compact. This allows us to produce miniature broadband antennas with performances similar to those of large antennas. Recently, many fractal structures have been proposed like those proposed in [10–18]. In [10], an antenna with Koch fractal geometry has been proposed to enhance the bandwidth. However, only 3.3 GHz (3-6.3 GHz) bandwidth has been achieved. A fractal antenna based on an octagonal patch and a semi-elliptical ground plane has been proposed in [11]. Unfortunately, this antenna has low gain which does not exceed 3 dBi and its efficiency is below 90% along the working bandwidth. More recently, in [12], a circular cross-slot AMC has been assembled with a fractal antenna to improve the bandwidth and the gain. The overall impedance bandwidth attained is 129.49% extending from 2.4 to 11.2 GHz. The main disadvantageous of the designed structure are the complexity and the large thickness which is about 9.4 mm. A novel wideband fractal antenna based on a hexagonal-circular geometry with large size of $80.6 \times 80.6 \times 1.6$ ^{3} has been proposed in [13]. The iterations of circular slots inside a hexagonal metallic patch have allowed to achieve a bandwidth of around 2 GHz extending from 1.34 to 3.44 GHz. A compact flexible fractal UWB antenna printed on a 12.5-μm flexible polyimide substrate has been presented in [14]. An impedance bandwidth of 15.48 GHz (3.6-19.08 GHz) has been achieved, but it suffers from a low gain which does not exceed 3.5 dBi along the interested frequency band. In [15], a hybrid of Sierpinski and Minkowski geometries has been exploited into a wide antenna for multiband applications. In [16], an antenna with Jerusalem crosses as fractal slots has been introduced to achieve wide bandwidth; no more than 0.6 GHz bandwidth with only 3.5 dBi peak gain and an efficiency value of 70% have been achieved at the resonating frequency. In [17], Minkowski fractal structures are introduced into a flexible antenna for improving the return loss and the impedance bandwidth. This flexible antenna that has been printed into large substrate ($97.48 \times 80 \times 0.5$ mm^3) is operating in two narrow bands with bandwidths < 0.6 GHz. Carpet geometry has been exploited in [18] for improving the bandwidth of a monopole antenna with defected ground structure. However, only 3.13 GHz bandwidth has been obtained.

In the present work, a cauliflower-shaped structure is exploited to achieve size-compactness and the UWB response. The fractal geometry was introduced along the edges of the patch and on the outer corners of the truncated ground plane. A prototype was fabricated and measured showing a good concordance between the measured and the simulated results. The fabricated prototype has an impedance bandwidth of 7.91 GHz extending from 3.05 to 10.96 GHz and stable omni-directional radiation patterns. In addition, the simulated antenna has a reasonable gain (1.39-5.68 dBi) and high radiation efficiency (>90%) values over the entire operating frequency band. The designed antenna was calculated and optimized by using the commercial software CST Microwave Studio^{TM} [19]. The following section will present fractal length generations, describe the proposed antenna geometry, and depict the obtained results.

II. ANTENNA DESCRIPTION AND RESULTS

A. Process of antenna design

The proposed antenna is generated by combining the fractal concept and the hexagonal geometry. The geometrical configuration of this new fractal curve begins with a straight line, called the initiator, which is shown in Figure 1 (iteration 0). The first iteration divides the initial length into four equal parts, and the two centric segments are replaced by three other segments of the same length by forming a regular trapezoid with an angle $\theta = 60^\circ$ as shown in Figure 1 (iteration 1). This iterative process is repeated for the higher-order iteration which is shown in Figure 1 (iteration 2).

Each segment of iteration 1 (generator) is one-fourth the length of the initiator. There are five such segments. Thus, for iteration n, the total length of the curve is $(5/4)^n$.

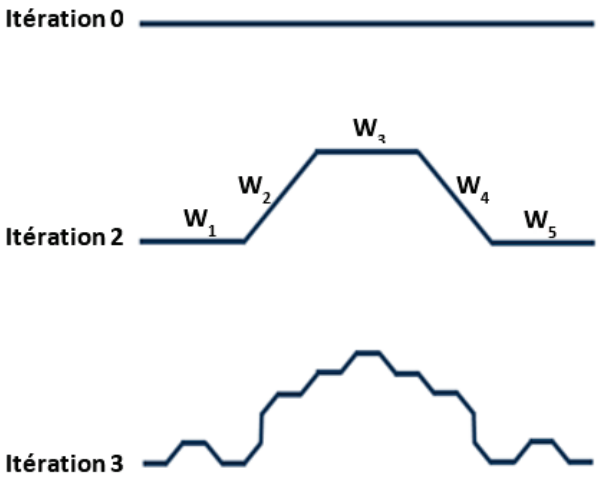

Fig. 1. Iteration-wise evolution of cauliflower-shaped structure.

B. Generating fractal geometry using iterative function system (IFS)

An IFS can be used to define the generator. The transformations used to obtain the generator segments are given by the following equations:

$$W_1\begin{pmatrix}x\\y\end{pmatrix}=\begin{bmatrix}\frac{1}{4}&0\\0&\frac{1}{4}\end{bmatrix}\begin{pmatrix}x\\y\end{pmatrix}, \tag{1}$$

$$W_2\begin{pmatrix}x\\y\end{pmatrix}=\begin{bmatrix}\frac{1}{4}\cos 60^\circ&-\frac{1}{4}\sin 60^\circ\\\frac{1}{4}\sin 60^\circ&\frac{1}{4}\cos 60^\circ\end{bmatrix}\begin{pmatrix}x\\y\end{pmatrix}+\begin{pmatrix}\frac{1}{4}\\0\end{pmatrix}, \tag{2}$$

$$W_3\begin{pmatrix}x\\y\end{pmatrix}=\begin{bmatrix}\frac{1}{4}&0\\0&\frac{1}{4}\end{bmatrix}\begin{pmatrix}x\\y\end{pmatrix}+\begin{pmatrix}\frac{3}{8}\\\frac{1}{4}\sin 60^\circ\end{pmatrix}, \tag{3}$$

$$W_4\begin{pmatrix}x\\y\end{pmatrix}=\begin{bmatrix}\frac{1}{4}\cos 60^\circ&\frac{1}{4}\sin 60^\circ\\-\frac{1}{4}\sin 60^\circ&\frac{1}{4}\cos 60^\circ\end{bmatrix}\begin{pmatrix}x\\y\end{pmatrix}+\begin{pmatrix}\frac{5}{8}\\\frac{1}{4}\sin 60^\circ\end{pmatrix}, \tag{4}$$

$$W_5\begin{pmatrix}x\\y\end{pmatrix}=\begin{bmatrix}\frac{1}{4}&0\\0&\frac{1}{4}\end{bmatrix}\begin{pmatrix}x\\y\end{pmatrix}+\begin{pmatrix}\frac{3}{4}\\0\end{pmatrix}. \tag{5}$$

The generator is then obtained with the union of these five transformations:

$$W(A)=W_1(A)\bigcup W_2(A)\bigcup W_3(A)\bigcup W_4(A)\bigcup W_5(A). \tag{6}$$

C. Geometry of the proposed cauliflower-shaped antenna

The geometrical structure and the dimensions of the designed antenna are presented in Figure 2. The antenna radiator is constructed by a set of successive assemblies of hexagons that create a cauliflower shape. The antenna structure progress during the design stages is shown in Figure 3. The substrate used for the designed antenna is RO-4350B substrate (relative dielectric constant of 3.48 with the loss tangent of 0.0037 and thickness of 1.524 mm). The overall size of the designed antenna is $0.3623\lambda_0 \times 0.41\lambda_0 \times 0.01524\lambda_0$ at 3 GHz as a result of the introduction of a fractal geometry along the edge of the radiating patch and along with the outer corners of the truncated ground plane, an enhanced impedance matching and an extended impedance bandwidth are attained. According to other published works like[1], the resonant frequency f_r of a comparable antenna with a hexagonal patch can be predicted using eqn (7). In addition, the length of each edge constructing the hexagonal patch can be calculated by eqn (8)

$$f_r \approx \frac{U_{mn}\,c}{2\pi r_e\sqrt{\varepsilon_r}}. \tag{7}$$

The equivalent radius r_e is given by the following formula:

$$r_e=\sqrt{r^2+\frac{2hr}{\pi\varepsilon_r}\left(\ln\frac{\pi r}{2h}+1.7726\right)}. \tag{8}$$

The side length of the hexagonal patch can be calculated using the following formula:

$$q \approx 1.1\,r_e, \tag{9}$$

where ε_r is the dielectric constant of the substrate, c is the speed of light in free space, h is the thickness of the substrate, q is the side length of the hexagonal radiating patch, r is the radius of a comparable circular patch, and U_{mn} is the mth zero of the derivative of the Bessel function of order n. The values of U_{mn} are given as in Table 1.

Table 1: Parameters of roots for different modes

Mode (n, m)	U_{mn}
0,1	0
1,1	1.84118
2,1	3.05424
0,2	3.83171
3,1	4.20119

The dimensions of the designed cauliflower-shaped antenna were optimized to attain the desirable performances.

The physical dimensions of the proposed cauliflower-shaped antenna were set as follows: A = 11.5 mm, d = 0.85 mm, g = 0.25 mm, W_f = 4 mm, W_g = 18.25 mm, and h_g = 9.5 mm.

Figure 4 indicates that the working bandwidth is improved by 17.5% and the impedance matching is highly improved at higher frequencies by inserting the cauliflower-shaped structure along the edge of the hexagonal radiating element and on the outer corners of the truncated ground plane. The working bandwidth of the proposed antenna and the initial designs are given in Table 2.

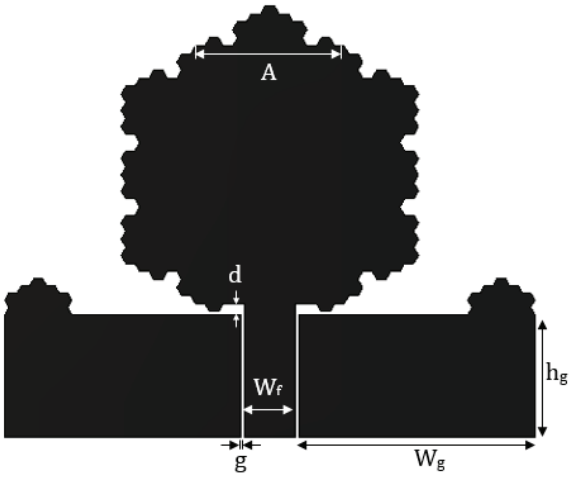

Fig. 2. Detailed configuration of the designed CPW cauliflower-shaped antenna.

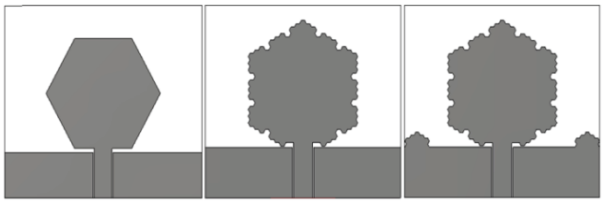

Fig. 3. Antenna geometry development during the design steps. (a) Antenna 1. (b) Antenna 2. (c) Antenna 3.

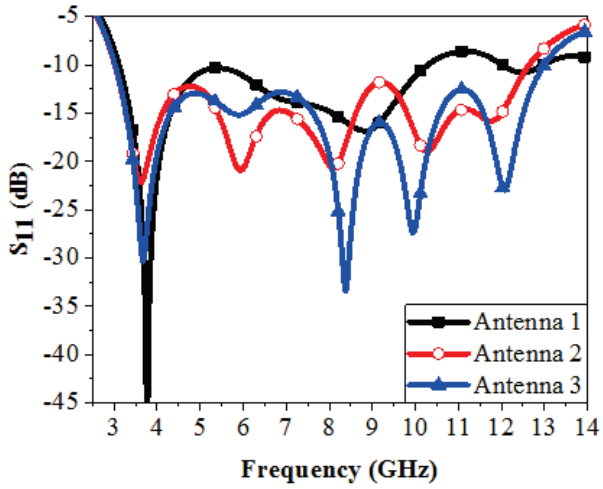

Fig. 4. Influence of the fractal structure on the reflection coefficient of the antenna.

Figure 5 indicates that the real part of the impedance is nearer, fluctuating around 50 Ω value which is the input impedance of the excitation port. Whereas, the imaginary part is narrowly fluctuating near zero bar during the working bandwidth. Thus, the designed antenna is well adapted throughout the entire working frequency range. At the input of the antenna, the accepted power is compared with the no-transmitted powers and the obtained results are presented in Figure 6. Compared to the level of the accepted power, negligible powers are recorded which prove the well adaptation of the designed antenna. In order to show the utility of the used fractal geometry, the current distribution on the antenna's surface is presented in Figure 7. At higher frequencies, there is more concentration of the current at the

Table 2: Antennas working bandwidth comparisons

Antennas	Working band (GHz)	Bandwidth (GHz)	Bandwidth (%)
Antenna 1	3.12-10.30	7.18	107
Antenna 2	3.02-12.64	9.62	122.86
Antenna 3	3.02-12.98	9.96	124.4

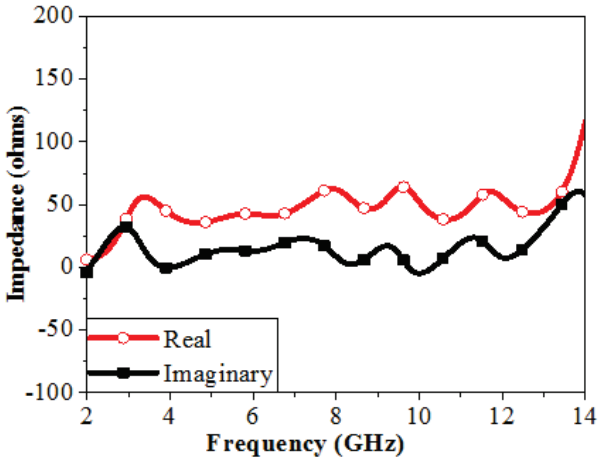

Fig. 5. Real and imaginary parts of the impedance.

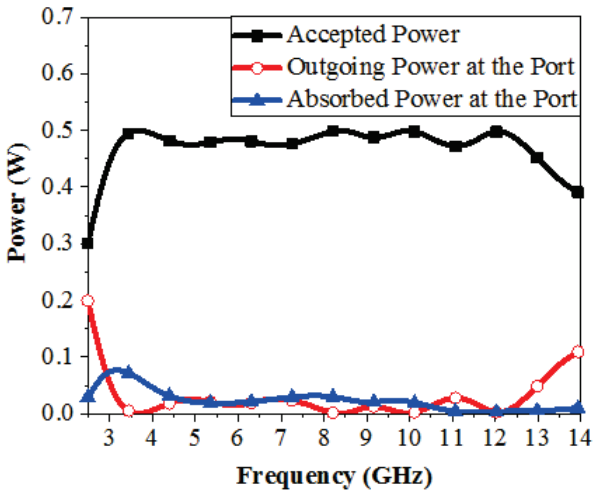

Fig. 6. Powers at the input of the antenna.

edge of the radiating patch and along the upper edge of the ground plane. The reflections at the edges of the antenna permit creation of other resonant frequencies, which is confirmed by Figure 4. Thus, the fractal geometry has a high contribution to the antenna's performance improvement by engendering additional resonances and allowing to extend the operational bandwidth.

Figure 8 represents a photograph of the fabricated prototype which was printed on the RO-4350B substrate with a total size of $0.3623\lambda_0 \times 0.41\lambda_0 \times 0.01524\lambda_0$ at 3 GHz. To confirm the UWB feature of the designed antenna, the reflection coefficient of the fabricated prototype was measured using an Agilent 8722ES vector network analyzer (VNA) with the specifications given in Table 3. High concordance between the simulation and experimental results is detected and the UWB characteristic of the proposed antenna is validated. Figure 9

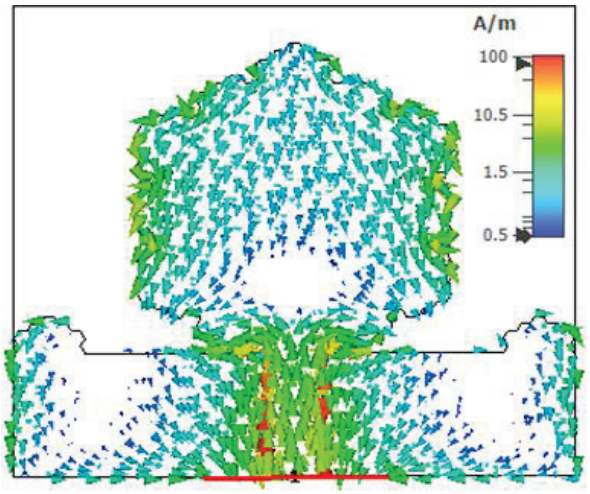

(a)

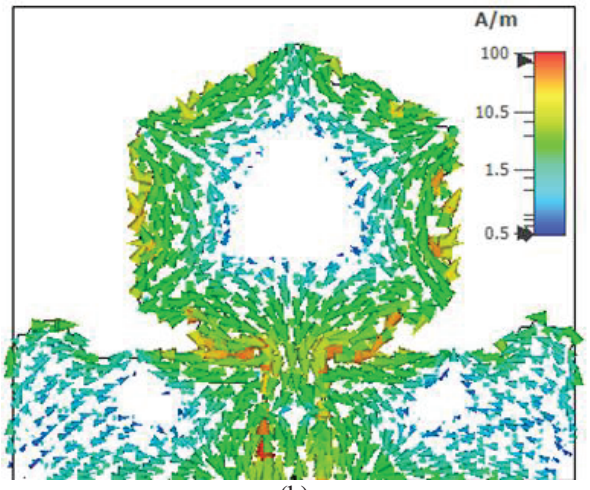

(b)

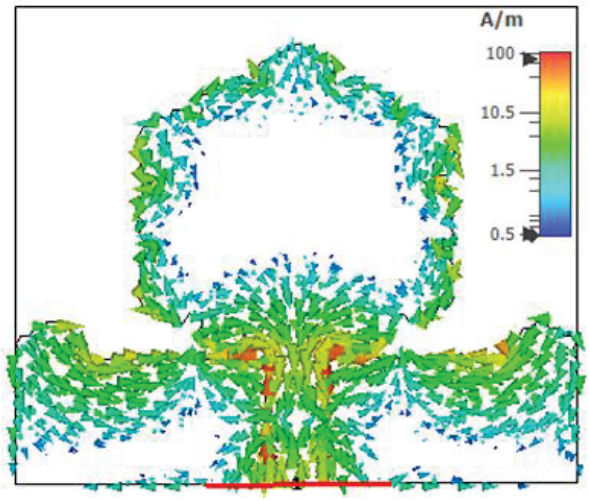

(c)

Fig. 7. Current distribution at three frequencies. (a) 3.65 GHz. (b) 8.37 GHz. (c) 9.89 GHz.

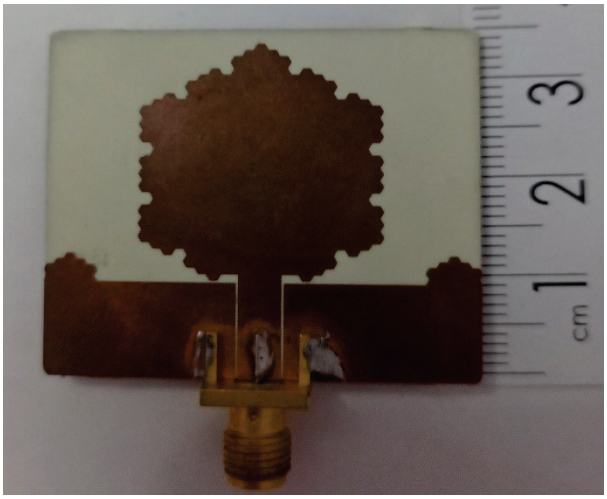

Fig. 8. Fabricated prototype of the proposed UWB CPW cauliflower-shaped antenna.

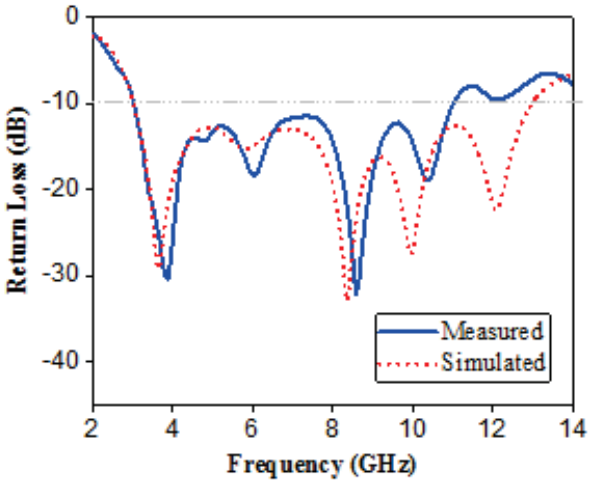

Fig. 9. Measured and simulated reflection coefficient of the proposed UWB CPW cauliflower-shaped antenna.

indicates that the measured reflection coefficient of the fabricated prototype covers a large bandwidth extending from 3.05 to 10.96 GHz (113%), which is wider than the reserved UWB frequency band of 110% (3.1−10.6 GHz).

The experimental co-polar and cross-polar radiation patterns of the fabricated prototype were measured in an anechoic chamber by using two-antenna measurement setup. A double ridged horn antenna (model AH-118 working in the range 1-18 GHz) is used for transmitting electromagnetic waves, whereas the fabricated coplanar waveguide (CPW) cauliflower-shaped antenna is used for receiving them.

The radiation patterns were measured in both the *H* (*xz*-plane) and the *E* (*yz*-plane) planes at three

Table 3: Specifications of the used VNA

Parameters	Values
Frequency range	0.05−40 GHz
IF bandwidth	10 Hz
Maximum input level	10 dBm
Maximum output power	−5 dBm
Power resolution	0.01 dB
Output power range	70 dB (0.05−20 GHz) 65 dB (20−40 GHz)
Output impedance	50 Ω

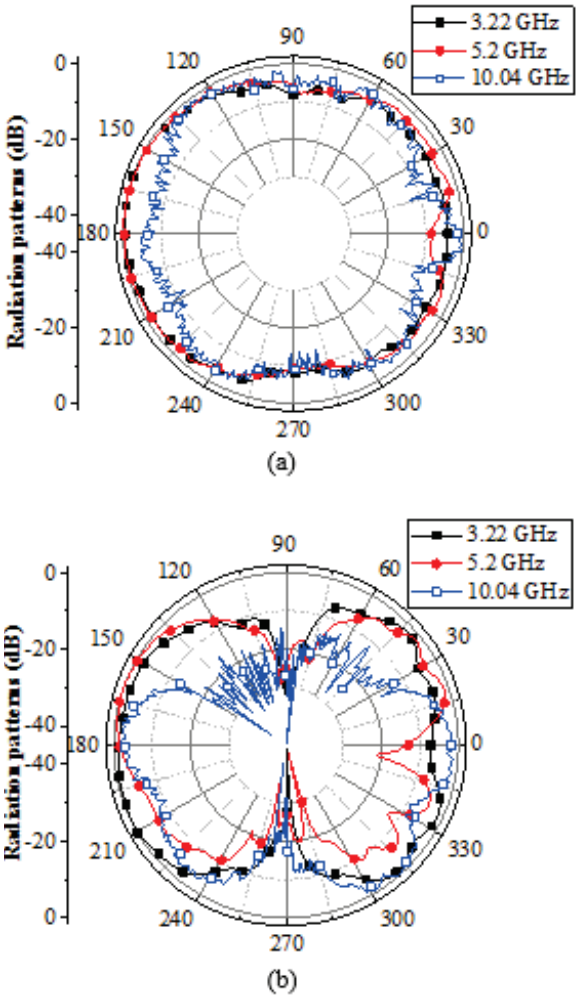

Fig. 10. Measured normalized co-polar radiation patterns at three frequencies from the working bandwidth. (a) *xz*-plane. (b) *yz*-plane.

frequencies from the operating bands 3.22, 5.2, and 10.04 GHz. Figure 10 and 11 indicate that the fabricated prototype has nearly consistent omni-directional radiation characteristics in the *H*-plane and bidirectional radiation patterns, like-dumbbell-shaped ones as a conventional monopole, in the *E*-plane. At higher frequencies, the radiation patterns undergo small distortions due to the reflections along the introduced like-cauliflower-structure and along the upper edge of the ground plane and also due to the excitation of higher-order mode [22].

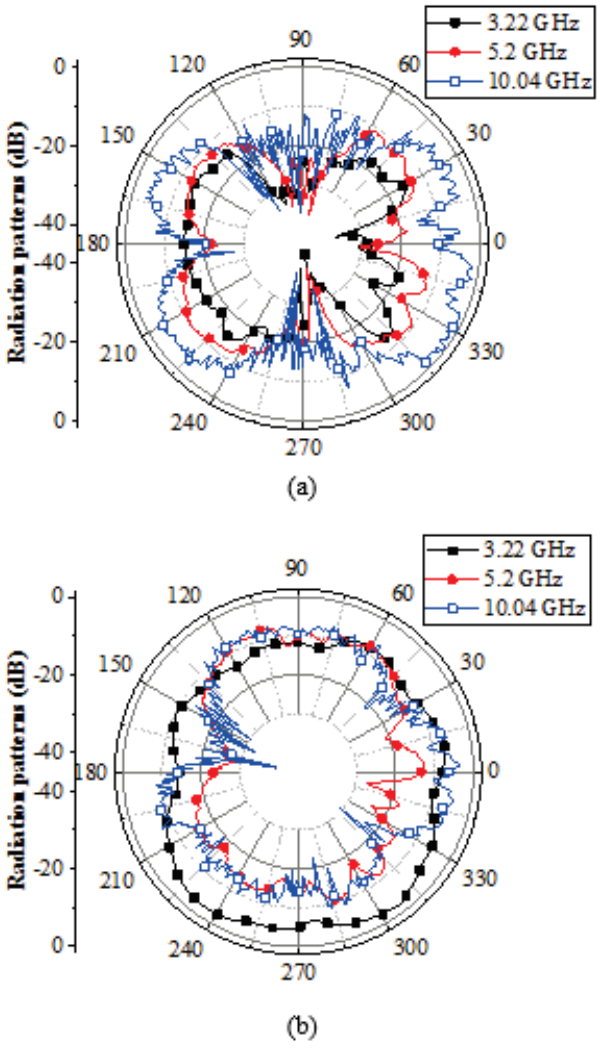

Fig. 11. Measured normalized cross-polar radiation patterns at three frequencies from the working bandwidth. (a) *xz*-plane. (b) *yz*-plane.

The cross-polar radiation patterns in the H-plane retain their star shape over the entire working band with low levels compared to those of co-polar radiation patterns, despite the augmentation of their levels with increasing the frequency, which is due to the excitation of hybrid currents [23].

Figure 12 indicates that the gain and the radiation efficiency simulated by the designed antenna throughout the operating frequency are acceptable and rea-

Table 4: Comparison of the fabricated antenna with other recently published antennas

Antennas	**Substrates**	**Sizes (mm^3)**	**Bandwidths**	**Ease of fabrication**
Ref. [26]	FR4	$100 \times 100 \times 15$ mm^3 ($\lambda_0 \times \lambda_0 \times 0.15\lambda_0$)	2.7−11.8 GHz (125.52%)	Hard
Ref. [27]	FR4	$49 \times 48.5 \times 0.8$ mm^3 ($0.49\lambda_0 \times 0.485\lambda_0 \times 0.008\lambda_0$)	2.9−10.4 GHz (112.78%)	Easy
Ref. [28]	FR4	$169 \times 169 \times 38.46$ mm^3 ($1.69\lambda_0 \times 1.69\lambda_0 \times 0.3846\lambda_0$)	3.8–8.8 GHz (79.36%)	Hard
Ref. [29]	FR4	$50 \times 50 \times 1.6$ mm^3 ($0.5\lambda_0 \times 0.5\lambda_0 \times 0.016\lambda_0$)	1.5–11 GHz (152%)	Easy
Ref. [30]	RO-4003	$100 \times 104 \times 1.5$ mm^3 ($\lambda_0 \times 1.04\lambda_0 \times 0.015\lambda_0$)	2–9 GHz (127.27%)	Hard
Ref. [31]	FR4	$100 \times 100 \times 16$ mm^3 ($\lambda_0 \times \lambda_0 \times 0.16\lambda_0$)	4.7−12.4 GHz (90%)	Hard
Ref. [32]	FR4	$45 \times 40 \times 1.6$ mm^3 ($0.45\lambda_0 \times 0.4\lambda_0 \times 0.016\lambda_0$)	1.31–6.81 GHz (135%)	Hard
Ref. [33]	FR4	$50 \times 50 \times 11.6$ mm^3 ($0.5\lambda_0 \times 0.5\lambda_0 \times 0.116\lambda_0$)	4.3−9.10 GHz (71.64%)	Easy
Ref. [34]	FR4	$40 \times 40 \times 3.2$ mm^3 ($0.4\lambda_0 \times 0.4\lambda_0 \times 0.032\lambda_0$)	5.64–8.63GHz (41.90%)	Easy
Ref. [35]	Taconic RF-35	$120 \times 120 \times 1.6$ mm^3 ($1.2\lambda_0 \times 1.2\lambda_0 \times 0.016\lambda_0$)	1.45–4.86 GHz (108.08%)	Easy
This work	RO-4350B	$36.23 \times 41 \times 1.524$ mm^3 ($0.3623\lambda_0 \times 0.41\lambda_0 \times 0.01524\lambda_0$)	3.05–10.96 GHz (113%)	Easy

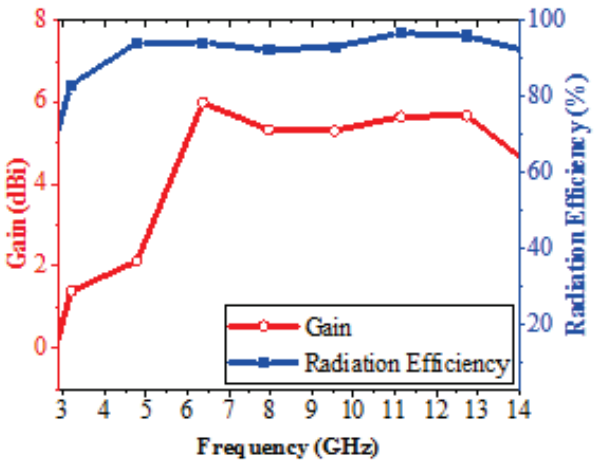

Fig. 12. Gain and radiation efficiency achieved by the designed antenna.

sonable because their values are better than the values obtained by some recently published works. The gain is varying between 1.39 and 5.68 dBi which is better than the one attained in [24]. Whereas, the radiation efficiency is almost over 90% during the working bandwidth which is better than the one achieved in [25].

In Table 4, the main parameters of the proposed antenna are compared with the ones of some recently published printed antennas. It can be deduced that the parameters of the proposed antenna are better or comparable to those of other antennas. With the above mentioned parameters, it could be deduced that the proposed antenna can be very convenient for many UWB systems.

III. CONCLUSION

In this paper, the utility of the fractal concept is investigated for designing a printed CPW-fed cauliflower-shaped antenna for UWB communication applications and systems. The simulation and measurement results have demonstrated that the working bandwidth and the impedance matching have been improved by inserting fractal geometry along the edge of the radiating patch and on the outer corners of the truncated ground plane. A prototype was fabricated and printed in a compact size of $0.3623\lambda_0 \times 0.41\lambda_0 \times 0.01524\lambda_0$ at 3 GHz. The measured results indicated that the cauliflower-shaped fractal antenna is well matched along a large bandwidth extending from 3.05 to 10.96 GHz, which is about 113% enclosing the UWB frequency range. Furthermore, the experimental radiation patterns of the fabricated prototype measured in an anechoic chamber showed stable omni-directional radiation patterns along the operating bandwidth. Besides, reasonable gain (1.39−5.68 dBi) and high radiation efficiency values (>90%) were simulated over the entire operating frequency band. Consequently, the proposed antenna

could be useful for many modern UWB communication systems.

ACKNOWLEDGMENT

This work was supported by the Directorate-General for Scientific Research and Technological Development (DG-RSDT) of Algeria.

REFERENCES

[1] M. Kantharia, A. Desai, T. Upadhyaya, R. Patel, P. Mankodi, and M. Kantharia, "High gain flexible cpw fed fractal antenna for Bluetooth/WLAN/WPAN/WiMAX pplications," *Progress In Electromagnetics Research Letters*, vol. 79, pp. 87–93, 2018.

[2] D. Aissaoui, N. Boukli-Hacen, and T.A. Denidni, "UWB hexagonal monopole fractal antenna with additional trapezoidal elements," *IEEE Int. Conf. on Ubiquitous Wireless Broadband, ICUWB*, pp.1-4, Oct. 2015.

[3] D. Aissaoui, A. Chaabane, A. Boualleg, and M. Guerroui, "Coplanar waveguide-fed UWB slotted antenna with notched-band performance," *Periodica Polytechnica Electrical Engineering and Computer Science.*, vol. 65, no. 1, pp. 69-73, Jan. 2021.

[4] D. Aissaoui, L. M. Abdelghani, N. Boukli-Hacen, and T. A. Denidni, "CPW-fed UWB hexagonal shaped antenna with additional fractal elements," *Microwave and Optical Technology Letters* vol. 58, no. 10, pp. 2370-2374, Jul. 2016.

[5] A. Chaabane and A. Babouri, "Dual-Band Notched UWB MiMo Antenna for Surfaces Penetrating," *Application .Advanced Electromagnetics*, vol. 8, no. 3, pp. 6-15, Jun. 2019.

[6] Y. Zehforoosh and M. Naser-Moghadasi, "CPW-fed fractal monopole antenna for UWB communication applications," *Applied Computational Electromagnetic Society (ACES) Journal*, vol. 29, no. 2, pp. 748-754, 2014.

[7] M. Guerroui, A. Chaabane, and A. Boualleg, "Super UWB grooved and corrugated antenna for GPR application," *Periodica Polytechnica Electrical Engineering and Computer Science*, vol. 66, no. 1, 2022.

[8] A. Chaabane and M. Guerroui "Printed UWB rhombus shaped antenna for GPR applications," *Iranian Journal of Electrical and Electronic Engineering*, vol. 73, no. 4, 2021.

[9] X. Bai, J. Zhang, L. Xu, and B. Zhao, "A broadband CPW fractal antenna for RF energy harvesting," *Applied Computational Electromagnetic Society (ACES) Journal*, vol. 33, no. 5, pp. 482-487, 2018.

[10] A. Bhattacharya, B. Roy, S. K. Chowdhury, and A. K. Bhattacharjee, "Design and analysis of a Koch Snowflake fractal monopole antenna for wideband communication," *Applied Computational Electromagnetic Society (ACES) Journal*, vol. 32, no. 6, Jun. 2017.

[11] G. Geetha, S. K. Palaniswamy, M. G. N. Alsath, M. Kanagasabai, and T. R. Rao, "Compact and flexible monopole antenna for ultra-wideband applications deploying fractal geometry," *Journal of Electrical Engineering and Technology*, vol. 13, no. 1, pp. 400-405, 2018.

[12] R.P. Dwivedi, M.Z. Khan, and U.K. Kommuri, "UWB circular cross slot AMC design for radiation improvement of UWB antenna," *International Journal of Electronics and Communications (AEÜ)*, vol. 117, no. 1, reference: AEUE 153092, 2020.

[13] M. A. Dorostkar, R. Azim, M. T. Islam, and Z. H. Firouzeh, "Wideband hexagonal fractal antenna on epoxy reinforced woven glass material," *Applied Computational Electromagnetic Society (ACES) Journal*, vol. 30, pp. 645-652, 2015.

[14] Q. Zou and S. Jiang, "A compact flexible fractal ultra-wideband antenna with band notch characteristic," *Microwave and Optical Technology Letters*, vol. 63, no. 3, pp. 1-7, 2020.

[15] N. Sharma, V. Sharma, and S. S. Bhatia, "A novel hybrid fractal antenna for wireless applications," *Progress In Electromagnetics Research M*, vol. 73, pp. 25–35, 2018.

[16] S. Heydari, P. Jahangiri, A. S. Arezoomand, and F. B. Zarrabi, "Circular polarization fractal slot by Jerusalem cross slot for wireless applications," *Progress In Electromagnetics Research Letters*, vol. 63, pp. 79-84, 2016.

[17] M. Kantharia, A. Desai, T. Upadhyaya, R. Patel, P. Mankodi, and M. Kantharia, "High gain flexible CPW fed fractal antenna for Bluetooth/WLAN/WPAN/WiMAX applications," *Progress In Electromagnetics Research Letters*, vol. 79, pp. 87-93, 2018.

[18] A. Bhattacharya, B. Roy, S. K. Chowdhury, and A. K. Bhattacharjee, "A compact fractal monopole antenna with defected ground structure for wideband communication," *Applied Computational Electromagnetic Society (ACES) Express Journal*, vol. 1, no. 8, pp. 228-231, Aug. 2016.

[19] CST Microwave Studio, ver. 2019, Computer Simulation Technology, 2019.

[20] D. H Werner and S. Ganguly, "An overview of fractal antenna engineering research," *IEEE Antennas Propagation Magazine*, vol. 45, pp. 38-57, 2003.

[21] M. Gupta and V. Mathur, "Hexagonal fractal antenna using koch for wireless applications," *Frequenz*, vol. 72, pp. 443-453, Aug. 2018.

[22] S. Singhal and A.K. Singh, "Elliptical monopole based super wideband fractal antenna," *Microwave*

and Optical Technology Letters, vol. 62, no. 3, pp. 1324-1328, Nov. 2020.

[23] A. Chaabane, O. Mahri, D. Aissaoui, and N. Guebgoub, "Multiband stepped antenna for wireless communication applications," *Informacije MIDEM*, vol. 50, no. 4, pp. 275-285, Dec. 2021.

[24] M. M. Hosain, S. Kumari, and A. K. Tiwary, "Sunflower shaped fractal filtenna for WLAN and ARN application," *Microwave and Optical Technology Letters*, vol. 62, no. 1, pp. 346-354, Aug. 2020.

[25] S. Hota, S. Baudha, B. B. Mangaraj, and M. A. Varun-Yadav, "Novel compact planar antenna for ultra-wideband application," *Journal of Electromagnetic Waves and Applications*, vol. 34, no. 1, pp. 116-128, Apr. 2019.

[26] A. Joshi and R. Singhal, "Gain enhancement in probe-fed hexagonal ultra wideband antenna using AMC reflector," *Journal of Electromagnetic Waves and Applications*, vol. 33, no. 9, pp. 1185-1196, Mar. 2018.

[27] S. Guruswamy, R. BChinniah, and K. A. Thangavelu, "A printed compact UWB Vivaldi antenna with hemi cylindrical slots and directors for microwave imaging applications," *International Journal of Electronics and Communications (AEÜ)*, vol. 110, Oct. 2019.

[28] P. R. Prajapati and S. B. Khant, "Gain enhancement of UWB antenna using partially reflective surface," *International Journal of Microwave and Wireless Technologies*, vol. 10, no. 7, pp. 835-842, Mar. 2018.

[29] D. M. Elsheakh and E. A. Abdallah, "Ultra-wide-bandwidth (UWB) microstrip monopole antenna using split ring resonator (SRR) structure," *International Journal of Microwave and Wireless Technologies*, vol. 10, no. 1, Feb. 2018.

[30] Z. Yang, H. Jingjianti, and Y. Naichang, "An antipodal Vivaldi antenna with band-notched characteristics for ultra-wideband applications," *International Journal of Electronics and Communications (AEÜ)*, vol. 76, pp. 152-157, Jun. 2017.

[31] D. Sankaranarayanan, D. Venkatakir and B. Mukherjee, "A novel compact fractal ring based cylindrical dielectric resonator antenna for ultra wideband application," *Prog. in Electromagnetics Res.* vol. 67, pp. 71-83, Sep. 2016.

[32] A. Kumar, S. Dwari, G. P. Pandey, and B. K. Kanaujia, "A high gain wideband circularly polarized microstrip antenna," *International Journal of Microwave and Wireless Technologies*, vol. 74, pp. 125-130, Jun. 2018.

[33] A. Desai, T. K. Upadhyaya, R. H. Masotti, and P. Mankodi, "Wideband high gain fractal antenna for wireless applications," *Progress In Electromagnetics Research*, vol. 12, no. 7, pp. 678-687, Mar. 2019.

[34] R. Anand and P. Chawla, "Optimization of inscribed hexagonal fractal slotted microstrip antenna using modified lightning attachment procedure optimization," *Microwave and Wireless Technologies*, vol. 12, no. 6, pp. 519-530, Mar. 2020.

[35] G. Liu, J. Gu, Z. Gao, and M. Xu, "Wideband printed slot antenna using Koch fractal metasurface structure," International Journal of RF and Microwave Computer-Aided Engineering, vol. 30, no. 3, Nov. 2020.

Boumediene Guenad received the magister degree in signals and systems and the Ph.D. degree in telecommunications science from the University of Tlemcen, Tlemcen, Algeria, in 2005 and 2013, respectively.

He is currently working as an Assistant Professor with the Department of Electronic Engineering, Faculty of Technology, University of Chlef, Ouled Farès, Algeria, and a Researcher Member of the Telecommunications Laboratory of Tlemcen (LTT), Tlemcen, Algeria. His current research areas of interest include multi-beam antenna arrays, fractal antennas, ultra-wideband antennas, and meta material antennas.

Abdelhalim Chaabane received the Ph.D. degree and completed his habilitation in electronics in 2017 and 2020, respectively.

He is currently working as an Associate Professor with the Université 8 Mai 1945 Guelma, Algeria. He is a member of Telecommunications Laboratory, Université 8 Mai 1945 Guelma. His current research areas of interest include fractal antennas, ultra-wideband antennas, meta material antennas, and ground-penetrating radar antennas.

Djelloul Aissaoui received the magister degree in signals and systems and the Ph.D. degree in telecommunications science from the University of Tlemcen, Tlemcen, Algeria, in 2007 and 2019, respectively.

He is currently working as an Assistant Professor with the Department of Electrical Engineering, Faculty of Science and Technology, University of Djelfa, Djelfa, Algeria. His current research areas of interest include fractal

antennas, ultra-wideband antennas, and meta material antennas.

Abdelhafid Bouacha received the magister degree in signals and systems and the Ph.D. degree in telecommunications science from the University of Tlemcen, Tlemcen, Algeria, in 2005 and 2012, respectively.

He is currently an Assistant Professor with the Telecommunications Department, Faculty of Technology, University of Tlemcen and a Research Member of the Telecommunications Laboratory of Tlemcen (LTT). His current research activities are focused on advanced antenna systems for 5G network and beyond.

Tayeb A. Denidni received the M.Sc. and Ph.D. degrees in electrical engineering from Laval University, Quebec City, QC, Canada, in 1990 and 1994, respectively.

From 1994 to 2000, he was a Professor with the Engineering Department, Université du Quebec in Rimouski (UQAR), Rimouski, QC, Canada, where he founded the Telecommunications Laboratory. Since August 2000, he has been with the Institut National de la Recherche Scientifique (INRS), Université du Quebec, Montreal, QC, Canada. His current research areas of interest include reconfigurable antennas using EBG and FSS structures, dielectric resonator antennas, meta material antennas, adaptive arrays, switched multi-beam antenna arrays, ultra-wideband antennas, microwave and development for wireless communications systems.

A Broadband Dual-Polarized Magneto-Electric Dipole Antenna Element for Low-Frequency Astronomical Arrays

Akila Murugesan[1], Divya Natarajan[2], S. Abishek[3], V. Lingasamy[4], K. Hariharan[5], and Krishnasamy T. Selvan[1]

[1]Department of Electronics and Communication Engineering, Sri Sivasubramaniya Nadar College of Engineering, Kalavakkam 603110, India
selvankt@ssn.edu.in

[2]Oracle Financial Services Software Limited, Chennai 600086, India

[3]Johnson Electric Private Limited, Chennai 600123, India

[4]Sterlite Technologies Limited, Gurgaon 122002, India

[5]L & T Infotech, Navi Mumbai 400710, India

Abstract – This paper presents simulation-based design and analysis of a broadband dual-polarized magneto-electric dipole antenna element that can be used to construct VHF astronomical antenna arrays. The antenna consists of two pairs of radiating structures, each fed by a Γ-shaped feeding section. The feeding section and radiating parts are physically disconnected from each other. The antenna is evaluated by simulation, and its −10 dB impedance matching bandwidth ranges from 115 to 340 MHz. The maximum gain of the antenna is about 8 dB over the operating range. Isolation of about 20 dB is observed between the two input ports.

Keywords – Array, astronomy, broadband, dual-polarization, magneto-electric dipole, VHF.

I. INTRODUCTION

Radio astronomy has always been one of the most explored research topics. It deals with the measurement of electromagnetic radiation emitted from cosmic sources, where the emissions are irregularly varying as a function of time. The emissions are spread over a wide range of frequencies from a few MHz to the far-infrared. Since the signals of interest are very weak, antenna arrays are designed and distributed over large effective apertures covering hundreds of meters/kilometers [1]. The first step in the array modeling of an astronomical array is the design of the element. The element design is pretty challenging as it should have a good impedance match and stable gain over a wide range of frequencies.

Various antenna elements have been reported in the literature for astronomical purposes, which include Bowtie antenna, log-periodic dipole array, Vivaldi antenna, parabolic reflector antenna, and magneto-electric dipole (MD) antenna.

Log-periodic antennas [2, 3] are used when simultaneous multi-frequency observations of radio emissions from celestial radio sources must be monitored. But they offer narrow bandwidth and are also susceptible to winds due to their height, especially when designed for low frequencies. Although parabolic reflector antennas play a major role in microwave satellite and space communications, from [4–6], it is noted that these are primarily designed for transmitting and receiving pencil beams. Also, designing a parabolic reflector antenna in the VHF band is a complex process. Other wideband antenna elements like Vivaldi [7, 8] and Bowtie [9], when designed for astronomical purposes, require a complex feeding mechanism that includes the design of baluns for impedance matching. Furthermore, they are usually printed on dielectrics, which reduces the likeliness of being deployed in an outside environment.

A wideband magneto-electric dipole (ME) antenna reported in [10] exhibits wide bandwidth and seems to be appropriate for astronomical arrays considering its metallic construction. It also offers better radiation characteristics such as low cross-polarization and back radiation, symmetric *E*- and *H*-plane radiation patterns, and stable gain across the operating band. These are achieved by exciting both electric and magnetic dipoles with suitable amplitudes and phases [11, 12]. A variant of dual-polarized ME antenna reported in [13] combats multipath fading effects and enhances the polarization diversity. Also, the Γ-shaped probe feed of the ME antenna employed in [14] improves the impedance

Submitted On: July 19, 2021
Accepted On: November 25, 2021

https://doi.org/10.13052/2022.ACES.J.370109

characteristics of the antenna. A dual-band shared-aperture base station antenna array reported in [15] is based on ME elements.

Considering the advantages and performance characteristics of a dual-polarized ME antenna, in this work, a simulation-based modified [16] dual-polarized ME antenna operating over the frequency range of 115–340 MHz is designed. The novelty aspects of the proposed design are: (1) the design of horizontal plates with a curvature at the corners which enhances the impedance match, (2) design of the feeding sections passing below the horizontal plates that improves matching, and (3) design of dielectric stubs that provide mechanical strength to the feeding sections without altering the matching. The proposed element design has the practical benefit of being employed as the basic building block of an electronically steerable square kilometer array [17, 18]. The array so designed could be used to study the fast and slow transient radio radiation originating from astronomical sources as well as to conduct high angular resolution imaging of discrete galactic and extragalactic sources at low radio frequencies. The transient sky at low frequencies (in MHz) remains relatively unexplored [19]; therefore, the antenna is designed to operate from 115 to 340 MHz.

This work is presented in various sections. Section II presents the element design, and Section III discusses the operating principle. The computational aspects of the designed antenna and the simulation results are discussed in Sections IV and V, respectively, while Section VI concludes the paper.

II. ELEMENT DESIGN

The antenna is designed at a center frequency of 160 MHz, as shown in Figure 1. The antenna is composed of three components, namely, (1) radiating structures, (2) feeding section, and (3) support structures. The radiating structures and the feeding section are made of aluminum, while the support structures are made of Teflon ($\varepsilon_r = 2.1$). A detailed description of each of the antenna components is elaborated below.

A. Radiating structures

The size of the ground plane considered for this design is 2.5×2.5 m^2. The radiating structure constitutes the horizontal plates and the vertical plates, as presented in Figure 2. The four radiating structures are placed over the ground plane in the four quadrants, as depicted in Figure 1. As per Figure 1, a pair of vertically oriented rectangular plates shorted to the ground form a shorted patch antenna which constitutes the magnetic dipole. In contrast, the pair of horizontal square plates form the electric dipole. The dimension of resonant dipole or patch antenna is approximately $\lambda/2$. Hence, we started the design with a size of $\lambda/2$ at the center frequency. Later, the dimensions were optimized for a -10 dB impedance bandwidth over the operational band.

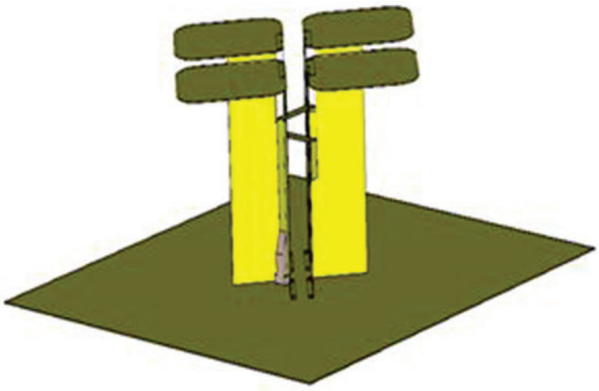

Fig. 1. Perspective view of the antenna.

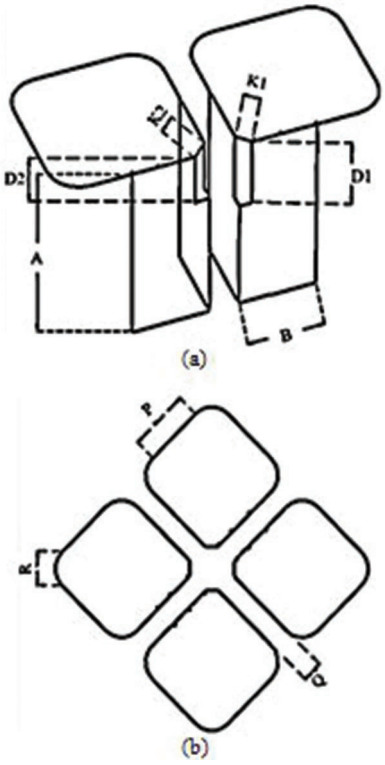

Fig. 2. (a) Perspective view of the radiating structures. (b) Top view of the radiating structures.

The dimensions of the horizontal and vertical plates determine the lower and upper cutoff frequencies. When the height of the vertical plate (A) is increased, a better impedance match is observed at the lower frequency and the bandwidth is pushed toward the lower frequency. Similarly, increasing the length of the horizontal plates results in the impedance bandwidth being shifted toward

the lower frequency. After the parametric investigations, the vertical plates' heights and lengths are optimally chosen as 515.58 and 273.90 mm. The overall size of the radiating structure is 1040×1040 mm^2. The two diagonal radiating structures constitute one polarization. Each radiating part consists of two vertically oriented plates connected such as to form a 90° corner. The bottom edges of the plates are connected to the ground plane, and the top edges are connected to the horizontal plate, as shown in Figure 2(a). The width of the two vertically oriented plates, when decreased, increases the impedance bandwidth. The optimized width of the two vertically oriented plates is 244.9 mm. The four radiating structures are positioned in each quadrant with a gap of 90 mm between them, as depicted in Figure 2(b). One corner (inner) of each horizontal plate has a slot to insert the feed, maintaining the physical disconnectivity between the feed and the radiating structures. When the widths w1 and w2 of the slot are increased, the impedance match moves toward the lower cutoff frequency. The other corners of the horizontal plates are curved to improve impedance matching. The dimensions of the radiating structures are tabulated in Table 1.

B. Feeding section

Each pair of diagonally opposite radiating structures is fed with a Γ-shaped feeding section which forms two feeding ports for the entire antenna. The feeding section is physically disconnected from the radiating structures. Each Γ-shaped feeding section has three parts, as shown in Figures 3(a) and (b). The long vertical strip is the transmission line. Its bottom end is 3 mm from the ground plane, connected to the coaxial connector through a small horizontal stub, as shown in the figure. The top end of the transmission line is bent to form the horizontal coupling strip, which is further bent down on the other side, forming a short vertical impedance matching strip. Parametric studies were performed to understand the role of the feed section on the impedance characteristics. A decrease in the transmission line length results in a shift in the lower cutoff frequency, while a decrease in the coupling strip length provides a shift in the upper cutoff frequency. The final optimized dimensions of the feeding sections are tabulated in Table 2.

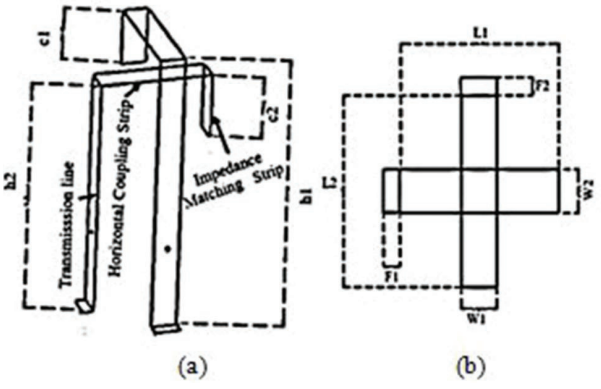

Fig. 3. Geometrical description of the feeding section. (a) Perspective view. (b) Top view.

The transmission line part of the feeding section is placed within one of the radiating structures close to the corner of the vertical plates connected to the edge. The horizontal coupling strip protrudes out of the top horizontal plate through a slot cut at the top corner. The coupling strip enters the other diagonal radiating structure through a triangular slot cut on the top, without physically touching the vertical or the horizontal plates, as shown in Figure 1.

C. Support structures

Mechanical stability is essential to the feeding section and is provided using dielectric support structures made of Teflon ($\varepsilon_r = 2.1$), as shown in Figure 4(a). A dielectric slab, starting from the ground plane, is placed along the width of the transmission line of the feeding section, which is tapered in the top portion. The tapered section is fastened to the feed strip using metallic screws, and the bottom of the slab is attached to the ground with Teflon screws with an additional sidestep, as shown in Figure 4(b). The support structure dimensions are optimally chosen such that the antenna's performance is not affected, and the same are tabulated in Table 3.

III. OPERATING PRINCIPLE

The pair of vertically oriented rectangular plates shorted to the ground form the magnetic dipole, and the pair of horizontal square plates form the electric dipole. A combined effect of the electric dipole and the magnetic dipole provides a uniform unidirectional radiation pattern [20]. The radiating structures are excited by the fields coupled with the feeding section.

The significance of the three parts of the feeding section is explained as follows:

1. The transmission line section and the shorted vertical plates act as an air microstrip line of 50-Ω characteristic impedance, which transmits the electrical signal from the coaxial launcher to the second portion of the feed.
2. The electrical energy from the transmission line is coupled to the horizontal and vertical plates via the horizontal coupling strip. The length of the coupling strip contributes to the inductive reactance, thereby altering the antenna's input impedance.
3. The impedance matching section is an open-circuited transmission line, which can be modeled as a capacitor and contributes to the capacitive

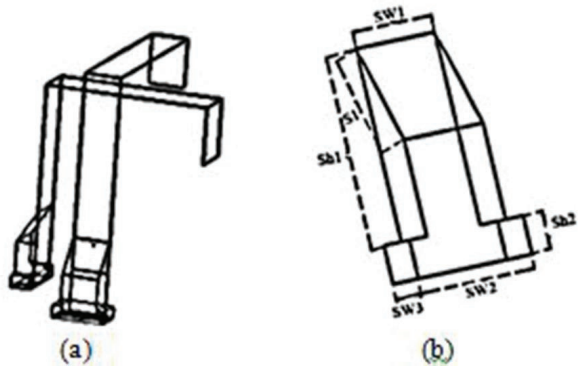

Fig. 4. (a) Feed sections with the support structures. (b) Perspective view of support structure.

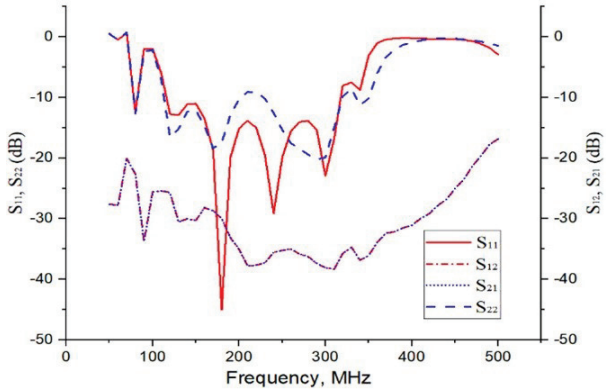

Fig. 5. S-parameters of the ME antenna.

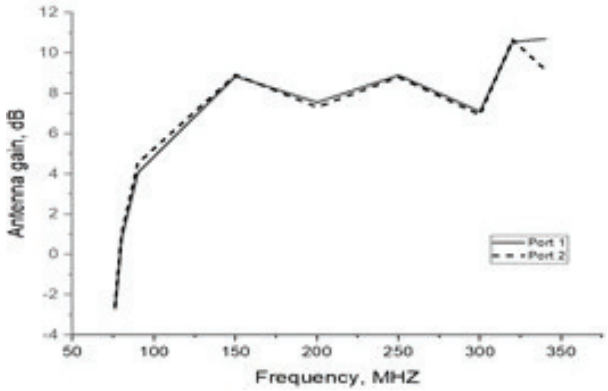

Fig. 6. Antenna gain versus frequency plot.

reactance. Appropriate choice of its length compensates for the inductive reactance caused by the coupling strip and thereby enhances the impedance bandwidth.

In summary, the operation starts with the excitation of the feeding strips, which couple fields to the corresponding radiating structures and induce currents. The current-induced horizontal radiating plates act as a planar electric dipole, while the shorted vertical radiating structures act as a magnetic dipole, resulting in the overall radiation.

IV. COMPUTATIONAL ASPECTS OF THE DESIGNED ANTENNA

This paper reports a broadband antenna design, and, hence, the solver chosen in the CST simulation tool is the time domain. The accuracy level maintained is -30 dB, and the number of pulses to 50. The mesh type used for the simulation is hexahedral. The mesh cell setting in the tool is an essential parameter – the more the mesh cells, the better the accuracy, with the disadvantage of longer computational time. Taking account of these considerations, the cells per wavelength for the maximum cell calculation are optimally set to 15 for the proposed antenna simulation.

The port mode solver supports inhomogeneous port accuracy as we received a warning from the solver indicating that dispersive materials are detected at the ports. Also, the number of pulses is set to 50 as the steady-state criteria are not met with fewer pulses.

V. RESULTS AND DISCUSSION

The antenna design and simulation are performed using the CST Microwave Studio 2018. The simulated results of the designed antenna are discussed in the following sub-sections.

A. Impedance matching performance

The simulated antenna's reflection and coupling coefficients with respect to ports 1 and 2 are shown in Figure 5. It is observed that the -10 dB reflection coefficient with respect to the two ports is over the frequency range of $115-340$ MHz.

B. Gain and radiation pattern

The antenna gain as a function of frequency is depicted in Figure 6 for both the ports. The maximum gain of the antenna is around 8 dB over the operating band. The 3-dB gain bandwidth is observed over the frequency range of $115-340$ MHz. The simulated radiation patterns of the proposed antenna are plotted at 150 and 250 MHz in Figure 7. The simulations are performed by exciting each port separately to obtain radiation patterns in each polarization. An extensive simulation-based study is carried out to validate the sensitivity of the proposed antenna to determine the fabrication tolerance of the design parameters. The parameters in the feeding section have a tolerance of ± 2 mm, and all the remaining dimensions have a tolerance of ± 5 mm.

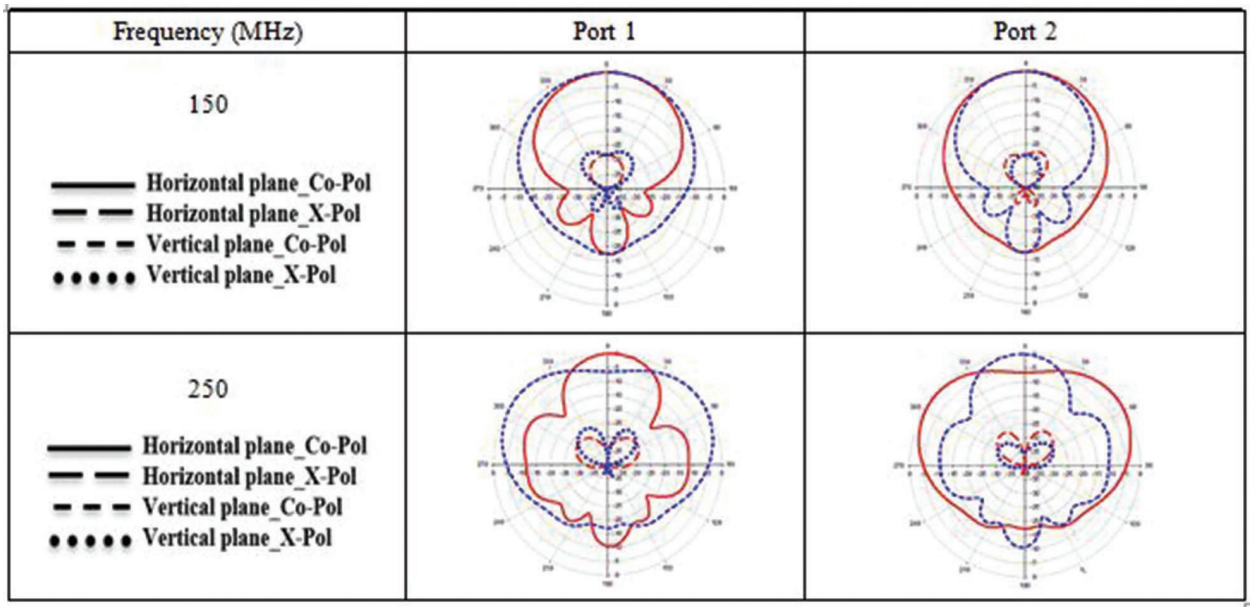

Fig. 7. Simulated radiation patterns when ports 1 and 2 excited individually.

Table 1 Dimensions of the radiating structures in mm

Parameters	*P*	*R*	*q*	K1	K2	D1	D2	A	B
Values	273.90	141.42	92.20	56.15	66.92	198.58	146.58	515.58	244.90

Table 2 Dimensions of feeding section in mm

Parameters	c1	c2	h1	h2	L1	L2	F1	F2	w1	w2
Values	76.37	89.37	376	319	201.85	201.85	21.51	19.88	45.36	45.36

Table 3 Dimensions of the support structure in mm

Parameters	Sw1	Sw2	Sw3	Sh1	Sh2	S1
Values	45.36	65.36	25	100	20	55.90

VI. CONCLUSION

Simulation-based design of broadband dual-polarized ME antenna element is presented in this paper for very low-frequency astronomical array applications. The antenna designed offers a -10 dB impedance bandwidth over the frequency range of $115-340$ MHz. The broadside gain of the antenna is about 8 dB, and the isolation between the input ports is about 20 dB over the operating frequency range. It may be noted that the antenna element could not be fabricated, given its size and also the current pandemic situation.

VII. ACKNOWLEDGMENT

The design study reported in this paper was undertaken when the authors participated in SWANtenna20, an antenna design competition organized by the Teaching Learning Centre of the Inter-University Centre for Astronomy and Astrophysics (IUCAA), Pune, India. Based on a detailed assessment by a jury of eminent antenna experts, the team was one of the five to be invited for presentation and interactions with the jury. The authors would like to acknowledge the experts' valuable inputs, which have gone into preparing this manuscript. They would also like to thank S. Shyam Krishna for proof-reading the manuscript.

REFERENCES

[1] S. W. Ellingson., "Antennas in radio telescope systems," *Handbook of Antenna Technologies Springer Singapore*, 2015.

[2] K. Sasikumar Raja, C. Kathiravan, R. Ramesh, M. Rajalingam and I. V. Barve, "Design and

performance of a low-frequency cross-polarized log-periodic dipole antenna," *The Astrophysical Journal Supplement Series*, vol. 27, no. 1, June 2013.

[3] S. Lin, S. Luan, Y. Wang, X. Luo, X. Han, X. Q. Zhang, Y. Tian, and X. Y. Zhang, "A printed log-periodic tree-dipole antenna (Plptda)," *Progress In Electromagnetics Research M*, vol. 21, pp. 19-32, 2011.

[4] P. S. Kildal, "Radiation characteristics of the EISCAT VHF parabolic cylindrical reflector antenna," *IEEE Transactions on Antennas and Propagation*, vol. 32, no. 6, pp. 541-552, June 1984.

[5] P. S. Kildal and E. Sorngard, "Circularly polarized feed for cylindrical parabolic reflector antennas," *EEE Transactions on Antennas and Propagation*, vol. 28, no. 2, pp. 210-215, March 1980.

[6] W. Jacob and M. Baars, "The paraboloidal reflector antenna in radio astronomy and communication: theory and practice," *Astrophysics and Space Scienced Library*, 2007.

[7] G. Virone, R. Sarkis, C. Craeye, G. Addamo and O. A. Peverini, "Gridded vivaldi antenna feed system for the Northern Cross radio telescope," *IEEE Transactions on Antennas and Propagation*, vol. 59, no. 6, pp. 1963-1971, June 2011.

[8] K. Ma, Z. Zhao, J. Wu, S. Mubarak Ellis, and Z. P. Nie, "A printed vivaldi antenna with improved radiation patterns by using two pairs of eye-shaped slots for UWB applications," *Progress In Electromagnetics Research*, vol. 148, pp. 63-71, 2014.

[9] C. Lonsdale, R. Cappallo, M. Morales, F. Briggs, L. Benkevitch, , J. Bowman, J. Bunton, S. Burns, B. Corey and L. deSouza, "The Murchison widefield array: design overview," *IEEE Proceedings*, vol. 97, no. 8, pp. 1497–1506, Mar. 2009.

[10] K. M. Luk and H. Wong, "A new wideband unidirectional antenna element," *International journal of Microwave and optical technology*, vol. 1, pp. 35–44, Apr. 2006.

[11] A. Clavin, "A new antenna feed having equal E-and H-plane patterns," *IRE Transactions on Antennas and Propagation*, vol. 2, no. 3 pp. 113–119, Jul. 1954.

[12] P. King, G. Owyang, "The slot antenna with coupled dipoles," *IRE Transactions on Antennas and Propagation*, vol. 8, no. 2, pp. 136-143, Mar. 1960.

[13] M. Li, K. M. Luk, "Wideband Magneto-electric Dipole Antennas : Chen Z. (eds) Handbook of Antenna Technologies," *Springer, Singapore*, April 2015.

[14] Z. Y. Zhang, G. Fu, S. L. Zuo and S. X. Gong, "Wideband unidirectional patch antenna with Γ-shaped strip feed," *Electronics Letters IET Digital Library*, vol. 46, no. 1, pp. 24-26, Jan. 2010.

[15] D. He, Q. Yu, Y. Chen, and S. Yang., "Dual-band shared-aperture base station antenna array with electromagnetic transparent antenna elements," *IEEE Transactions on Antennas and Propagation*, vol. 69, no. 9, pp. 5596-5606, Sep. 2021.

[16] B. Q. Wu, and K. M. Luk, "A broadband dual-polarized magneto-electric dipole antenna with simple feeds," *IEEE Antennas and Wireless Propagation Letters*, vol. 8, pp. 60–63, 2009.

[17] http://www.rri.res.in/SWAN/Strategic_Initiatives.html

[18] R. Maaskant, R. Mittra and A.G. Tijhuis, "Fast solution of multi-scale antenna problems for the square kilometre array (SKA) radio telescope using the characteristic basis function method (CBFM)," *Applied Computational Electromagnetics Society Journal*, vol. 24, pp. 174, 2009.

[19] National Academies of Sciences, Engineering, and Medicine, "Handbook of frequency allocations and spectrum protection for scientific uses," *The National Academies Press, Second Edition*, Washington, DC.

[20] L. Ge, and K. M. Luk., "A wideband magneto-electric dipole antenna," *IEEE Transactions on Antennas and Propagation*, vol. 60, no. 11, pp. 4987-4991, Nov. 2012.

M. Akila is currently working toward the Ph.D. degree with the Department of Electronics and Communication Engineering, Sri Sivasubramaniya Nadar College of Engineering, Kalavakkam, India.

Her current research interests include metasurfaces for RCS reduction and shared aperture phased array antennas.

Divya N. graduated from Sri Sivasubramaniya Nadar College of Engineering, Kalavakkam, India.

She is currently with Oracle Financial Services Software Limited, Chennai, India.

S. Abishek graduated from Sri Sivasubramaniya Nadar College of Engineering, Kalavakkam, India.

He is currently associated with Johnson Electric Private Limited, Chennai, India.

V. Lingasamy is currently working as a Senior Technical Lead with Sterlite Technologies Limited on LTE/5G radio unit and massive MIMO development.

Hariharan K. graduated from Sri Sivasubramaniya Nadar College of Engineering, Kalavakkam, India.

He is currently with L & T Infotech, Navi Mumbai, India.

Krishnasamy T. Selvan was with SAMEER – Centre for Electromagnetics, Chennai, India, a government of India's microwave research institution, from 1988 to 2005. From early 2005 to mid-2012, he was with the Department of Electrical & Electronic Engineering, University of Nottingham Malaysia, Semenyih, Malaysia. Since then, he has been a Professor with the Department of Electronics & Communication Engineering, Sri Sivasubramaniya Nadar College of Engineering, Kalavakkam, India.

Design and Optimization of a Wideband Rectangular TEM Device for Cell Experiments

Shiqi Wang, Shaojun Fang, and Peng Chen

Department of Information Science and Technology
Dalian Maritime University, Dalian, Liaoning 116026, China
1609900643@qq.com, fangshj@dlmu.edu.cn, chenpeng213@126.com

***Abstract* –** The influence of electromagnetic waves on living things has been of great concern in recent years. Traditionally, electromagnetic radiation device for cell experiments has a narrow frequency range and small radiation space. In this paper, a DC to 5.2-GHz rectangular transverse electromagnetic (TEM) device for cell experiments is proposed. The novelty of this research lies in the wide frequency range and sufficient radiation space under the condition of ensuring the transmission performance. The rectangular device is composed of a closed rectangular coaxial transmission line, tapered transition regions, inner plate structure, and dielectric supports. After simulation, optimization, and measurement, both the results of the simulated and measured studies indicate that reflection coefficient S_{11} is below -10 dB and transmission coefficient S_{21} is nearly 0 dB. It is demonstrated that the device has a good transmission performance from DC to 5.2 GHz, which meets the requirement for wideband cell radiation experiments. The proposed rectangular device is a good candidate for cell radiation experiment device.

***Index Terms* –** Rectangular TEM, radiation space, wideband, cell experiments.

I. INTRODUCTION

With the development of digital devices and integrated circuits, electrical equipment and systems are widely used in our daily life. And the electromagnetic signals with high density and wide spectrum constitute the extremely complicated electromagnetic environment [1]. People pay more and more attention to the problem of electromagnetic pollution, the relationship between electromagnetic waves, and the biological effects of biological systems, such as human, animal, and cell samples, etc. Therefore, the research on the effect and mechanism of electromagnetic field on human health has been carried out. Bioelectromagnetic research requires a complete and specific device for radiation experiment. In the middle of the 1960s, people used the transverse electromagnetic (TEM) wave chamber (Parallel Plates TEM cell) as an experimental device. But because of its open structure, electromagnetic energy radiated to the surrounding area is susceptible to environmental and external interference; thus, the accuracy and reliability of the test are not enough. Later, based on the principle of rectangular coaxial line, a symmetrical TEM cell for simulating electromagnetic wave propagation in closed space was proposed [2–4]. It consists of a square outer conductor, a main segment of the inner conductor of the mounting plate, and a tapered transition section at both ends, which can be respectively connected with the excitation source and the matching load. The radiation device based on TEM cell provides radiation conditions similar to that in free space and has the advantages of convenient use, uniform electromagnetic field, and low cost.

For the vitro studies of RF interaction with biological cells, the TEM chamber is generally used as radiation device. In [5], a vivo exposure system based on TEM cell is designed at 2.45 GHz and its size is 1700 mm $\times$ 120 mm $\times$ 120 mm. The system can be used for small animals' exposure experiments in 2.45 GHz. In [6], a new technique for establishing standard, uniform, and electromagnetic fields in a shielded environment employs TEM cells that operate as 50-Ω impedance-matched systems. An open TEM cell suitable for exposure frequencies from DC to 1 GHz is shown in [7], and its size is 200 mm $\times$ 100 mm $\times$ 30 mm. In [8], a 1800-MHz TEM cell is introduced for experiments investigating effects on biological samples, whose size is 198.8 mm $\times$ 78 mm $\times$ 82 mm. In [9], a TEM cell used for experimental biological samples exposure to radiofrequency field in the 100 MHz to 1 GHz range is designed. In [10], an open TEM cell is used as a pulse delivery system. Its size is 202 mm $\times$ 85 mm $\times$ 20 mm and its return loss is below -10 dB up to 3 GHz. The main disadvantages of the above TEM cells are their limited radiation space and lower upper frequency range. When the size of the TEM cell increases, the frequency will decrease accordingly. Nowadays, due to the quick development of communication systems operating at frequency ranges up to 5 GHz,

Submitted On: July 13, 2021
Accepted On: October 18, 2021

https://doi.org/10.13052/2022.ACES.J.370110

a new experimental radiation device should be planned.

In this paper, a rectangular TEM device with wideband and sufficient space is proposed for cell experiments. The proposed rectangular device is capable of producing a uniform planar electromagnetic wave with wideband property in a limited enclosed space. In order to not only obtain more accurate measured results but also expand application range of the device in practical needs [11], the proposed rectangular TEM device is aiming to overcome the restrictions on available testing space. The rectangular TEM device proposed can operate at the frequency range from DC up to 5.2 GHz. And it forms a uniform TEM electromagnetic field in the radiation space, which can be used to detect cell electromagnetic properties in electromagnetic radiation experiments.

II. THEORY ANALYSIS OF THE PROPOSED DEVICE

The proposed structure is a coaxial cavity structure. The outer conductor is composed of a rectangular cavity in the middle and a square cone cavity on both sides, and the inner conductor is composed of a rectangular conductor plate in the middle and two trapezoidal conductor plates on both sides, as shown in Figure 1(a). The coaxial structure is a dual conductor guiding system, which consists of internal and external systems. It mainly transmits TEM wave. When there is discontinuity or high-frequency operation, it will excite TE mode or TM mode. The device has two coaxial ports at the ends of the cell. The external dimension of the proposed rectangular square cone coaxial cavity is 1176 mm $\times$ 220 mm $\times$ 220 mm, with coaxial connectors at both ends. The middle section of the inner conductor is a rectangular conductor plate with thickness of 8 mm and width of 131 mm, and the inner conductors on both sides are trapezoidal conductor plates with thickness of 8 mm and width from 131 mm gradually changing to 8 mm, as shown in Figures 1(b) and (c). When a certain frequency and power signal is added to the excitation port, the electromagnetic wave inside the device is excited in the form of TEM. In order to achieve uniform field distribution, the device adopts a symmetrical structure. The inner and outer conductors of the device are made of aluminum, the wall thickness of the outer conductor is 10 mm, and the dielectric supports are composed of two 10-mm-thick PTFE materials. The cell dish is placed in the middle of the radiation space.

One port of rectangular square cone coaxial cavity is connected with RF signal generator, and the other port is connected with 50-Ω load to ensure good impedance matching. The calculation model of middle section of radiation device is illustrated in Figure 2. The cross-sectional size for the middle part of the inner conductor of the rectangular square cone coaxial cavity is obtained by the following formula [12]:

$$Z_0 = \frac{188.31}{2\frac{C}{\varepsilon_0} + \frac{w}{h} + \frac{t}{g}}, \tag{1}$$

$$\frac{w}{h} + \frac{b}{g} = 3.7662 - 2\frac{C}{\varepsilon_0}, \tag{2}$$

where C is the unit capacitance between inner and outer conductors, ε_0 is the dielectric constant of media between inner and outer conductors, w is the cross-sectional width of inner conductor plate, t is the thickness of inner conductor, g is the distance from the inner conductor to the outer conductors on sides, and h is the distance from the inner conductor to the top or bottom outer conductors. At first, the values are calculated based on formulae (1) and (2). It is then further optimized in CST software.

The transition section design is mainly to make a good match between the input end of the cell and the power supply. The traditional transition section of TEM cell adopts stepped transition structure, which is generally circular coaxial and circular coaxial transition. Because of the step discontinuity of the structure, the transition structure will have a great reflection, which will affect the transmission and other performance of the TEM cell. In order to solve this problem, a new type of gradual transition structure is proposed, which is circular coaxial rectangular coaxial tapered structure. This structure has low reflection loss and can be used in cell electromagnetic radiation structure to improve transmission performance.

The input port of the transition section of the device is connected with the N-type coaxial RF connector, and the output port is connected with the rectangular coaxial cavity of the device. In order to make the working frequency of the device reach 5.2 GHz, the design of the transition section should ensure to meet the 50-Ω characteristic impedance matching. It is also necessary to make sure that the cut-off frequency of the transition section should be greater than the working frequency and suppress the high-order noise when working in the high-frequency section [17–20]. A slow gradual structure is adopted to minimize the discontinuity caused by the gradual transition [13–16].

III. SIMULATION AND ANALYSIS

A. Simulation and optimization

The electromagnetic simulation for the rectangular square cone coaxial cavity is carried out with CST Microwave Studio Suite TM 2013. The impedance matching of the structure is mainly affected by the width w of the middle section of the inner conductor plate and the length $H1$ of the transition section; thus, the optimization and parameter scanning analysis of w and $H1$ is carried out. Figure 3 shows the structure diagram of iden-

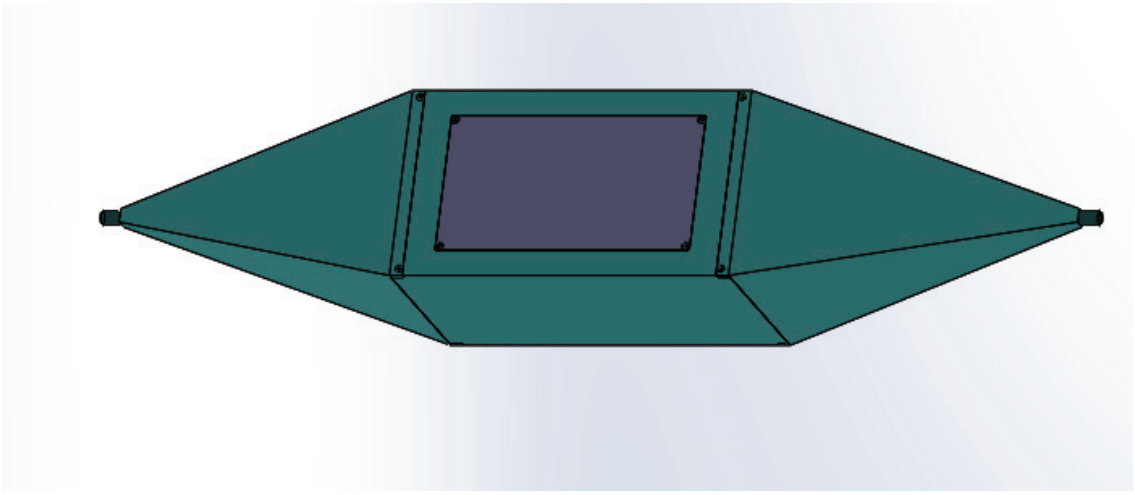

(a)

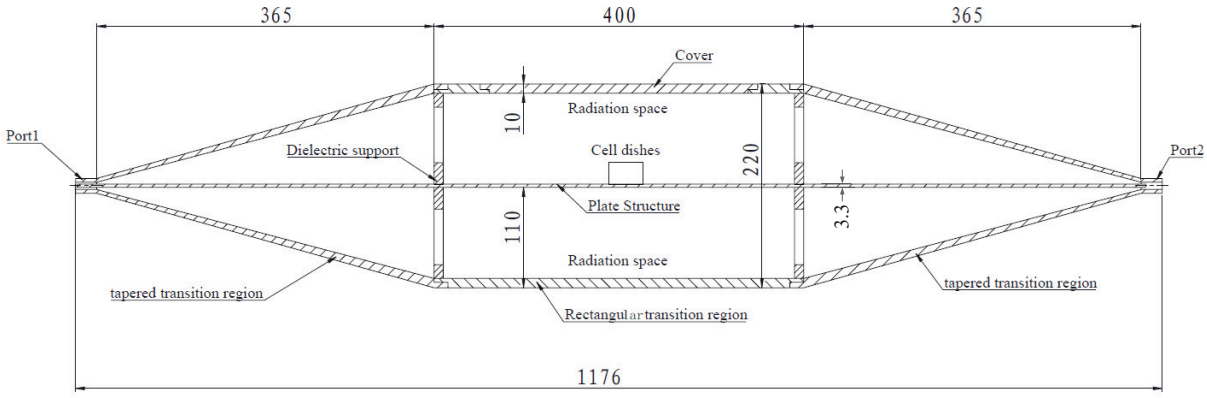

(b)

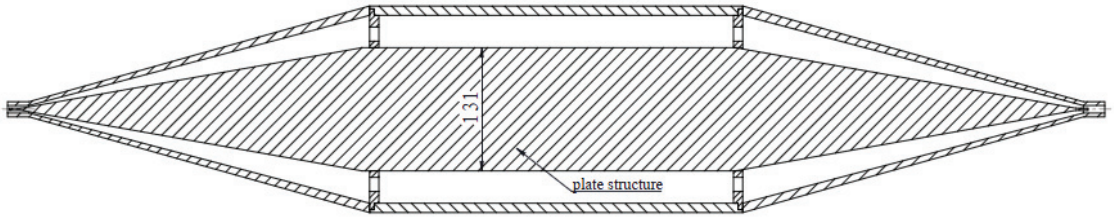

(c)

Fig. 1. (a) 3D structure diagram of the device. (b) Side view dimensions of the device (mm). (c) Top view dimensions of the device (mm).

tification $H1$. Figure 4 shows the S_{11} for different $H1$ and w. When other structural parameters of rectangular square cone coaxial cavity are fixed and $H1$ is changed, the curve of S_{11} is shown in Figure 4(a). It can be seen that the best $H1$ value is 36.5 cm, which makes S_{11} below -10 dB in the range of DC to 5.2 GHz. In the frequency range of 5.2−6 GHz, S_{11} is slightly higher than -10dB, which is caused by higher order modes. When w changes

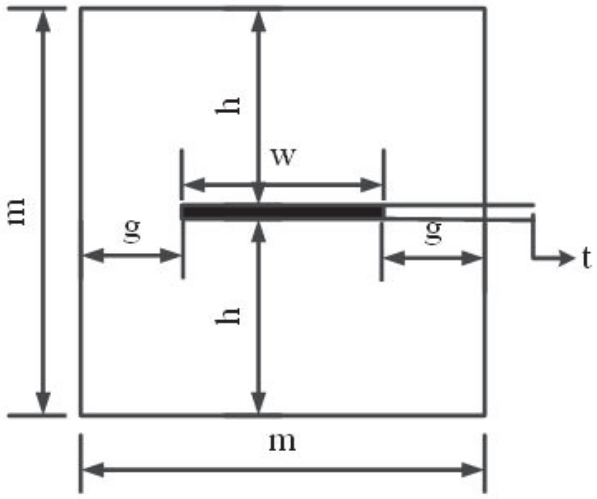

Fig. 2. Calculation model of middle section of radiation device.

and other structural parameters are fixed, the curve of S_{11} is shown in Figure 4(b). It can be seen that the optimal w value is 13.1 cm, which makes S_{11} lower than -10dB

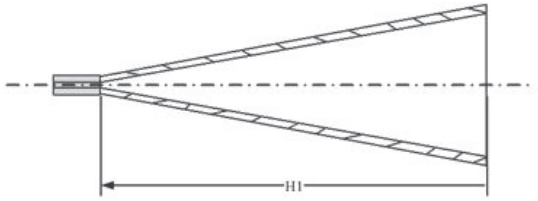

Fig. 3. Structure diagram of identification $H1$.

in the DC to 5.2 GHz range. In the frequency range of 5.2−6 GHz, S_{11} is also slightly higher than -10dB. Due to the large size and wide frequency range of the structure, high-order modes will appear in the high-frequency band, and the influences of dielectric supports, which will have a certain impact on the transmission of electromagnetic waves, and the results of S_{11} will also fluctuate accordingly.

B. Experimental results and discussions

According to the optimization results, the rectangular square cone coaxial cavity is fabricated, and the experimental prototype is shown in Figure 5. It is tested with vector network analyzer AV3629B.

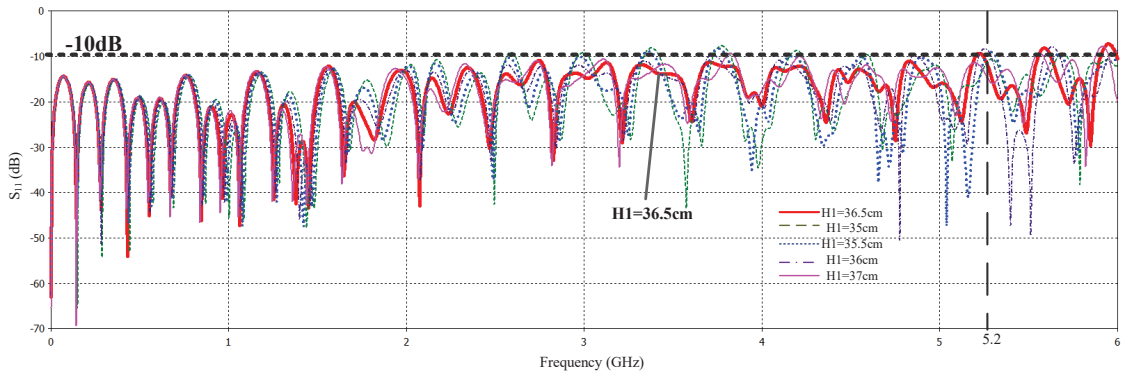

(a)

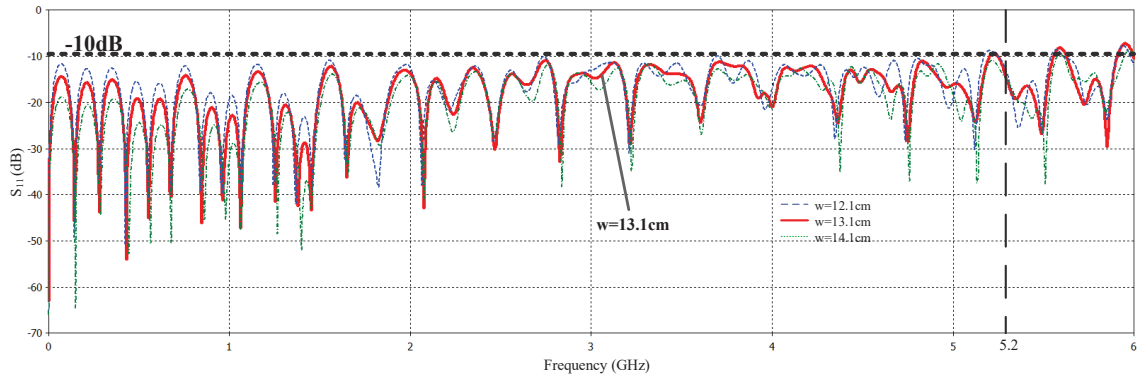

(b)

Fig. 4. Simulated S_{11} versus frequency with (a) the length of the tapered transition $H1$ and (b) the width of the inner plate structure.

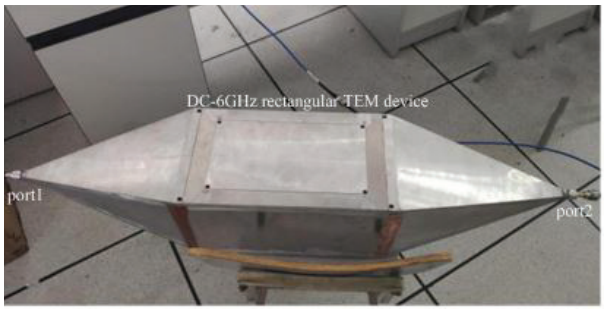

Fig. 5. Photograph of the rectangular device.

The simulated and measured results of the device are depicted in Figure 6. The reflection coefficient S_{11} is depicted in Figure 6(a) and the transmission coefficient S_{21} is depicted in Figure 6(b). It depicts that the S_{11} is better than -10 dB in the frequency range of DC to 5.2 GHz, S_{21} is nearly 0 dB in the frequency range of DC to 2 GHz, and S_{21} is between 0 and 1 in the frequency range of 2−5.2 GHz. As can be seen from Figure 6(a), the matching bandwidth of a radiation system is typically defined by the frequency bandwidth where the reflection coefficient is lower than -10 dB. Note that some of the S_{11} values for the radiation device within its bandwidth are slightly greater than -10 dB. This is probably because there is little reflection at the junction of the transmission section and the joint of the rectangular device. And higher order modes occur at some high frequency, which will influence the transmission performance in reality. As can be seen from Figure 6(b), good consistency has been obtained between the simulations and measurements. Due to the machining error, measured results are slightly biased at individual frequencies. Both the simulated and measured results show that the device has a good transmission performance and impedance matching from DC to 5.2 GHz.

The distribution of E-fields at $Z = 0$ in the device is depicted in Figure 6(c). It can be seen that distribution of the electromagnetic field is mostly green, and the electric

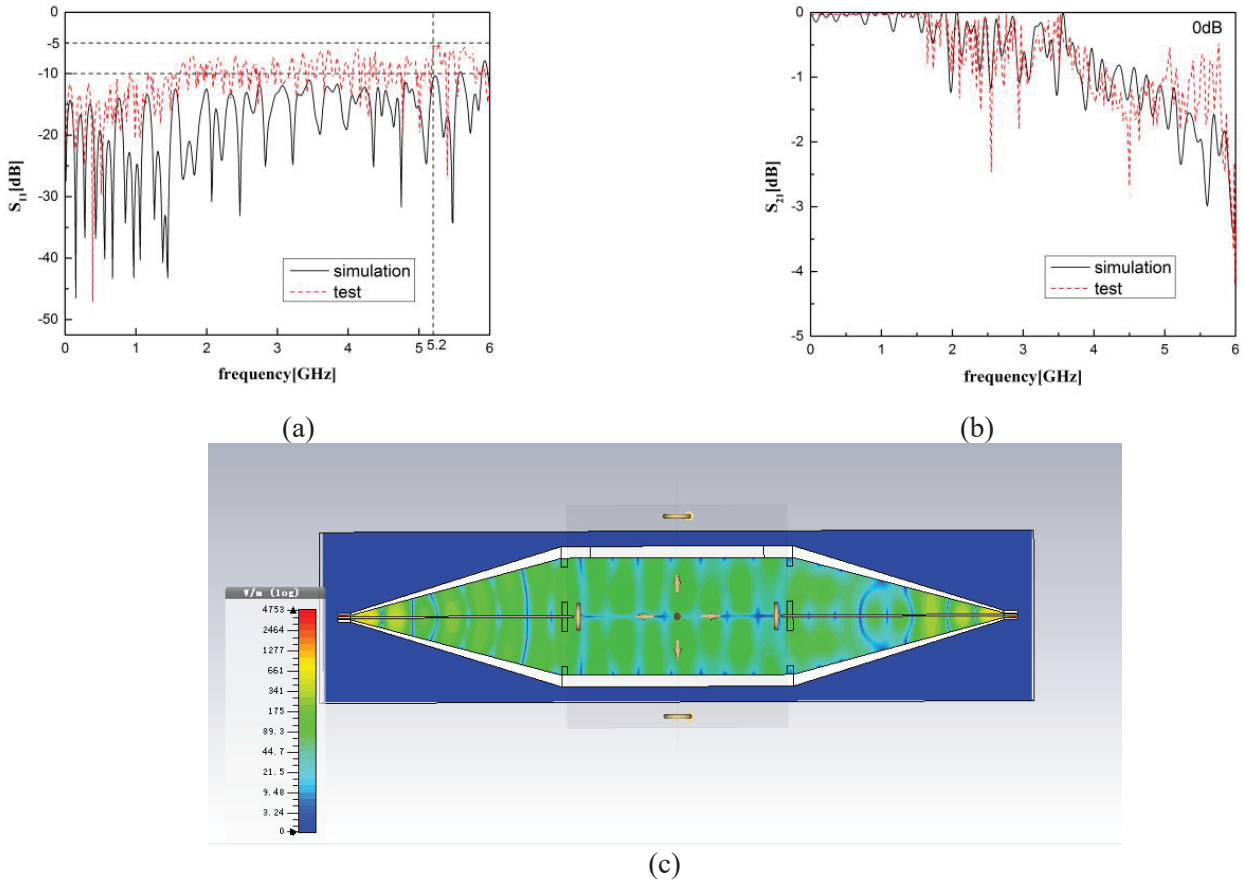

Fig. 6. (a) The simulated and measured results of reflection coefficient S_{11} from DC to 6 GHz. (b) The simulated and measured results of transmission coefficient S_{21} from DC to 6 GHz. (c) E-field distribution at $Z = 0$.

Table 1: Comparison between the proposed rectangular device and previously reported designs

Ref.	Structure	Frequency range (GHz)	Size ($\lambda_0 \times \lambda_0 \times \lambda_0$) ($mm^3$)	S_{11}(dB)
[2]	Open TEM cell	0.5 to 3	$200 \times 85 \times 20$	Below -7.5
[5]	TEM cell	2.5	$1700 \times 120 \times 120$	
[7]	Open TEM cell	DC to 1	$200 \times 100 \times 30$	
[8]	TEM cell	1.8	$198.8 \times 78 \times 82$	
[9]	TEM cell	DC to 1	$410 \times 260 \times 150$	Below -9
[10]	Open TEM cell	DC to 3	$202 \times 85 \times 20$	Below -10
[11]	Twin TEM cells	1	$300 \times 300 \times 200$	
[13]	Cylindrical TEM cell	DC to 1	$1021.2 \times 150 \times 150$	Below -13
[14]	Two-port rectangular TEM cell	$0.5-3$	$444 \times 364 \times 360$	
[16]	TEM cell	DC to 3	$280 \times 150 \times 90$	Below -15
This work	**Closed rectangular device**	**DC to 5.2**	**$1176 \times 220 \times 220$**	**Below -10**

field distributions are formed uniformly along the transverse plate. And we can conclude that there is a relatively uniform electromagnetic field inside the cavity. A uniform electromagnetic field is generated inside the outer conductor, and the outer conductor shell does not produce electromagnetic field. The uniform electric field distribution is essential for the radiation space and cell experiments.

Compared with the traditional TEM cells, simulated and measured results of this device show a good performance in the frequency range. And the device has advantages in sufficient radiation space and wide frequency band.

IV. COMPARISON OF THE TRADITIONAL TEM DEVICES

Table 1 summarizes the performance comparison between the proposed rectangular device and previously reported designs for radiation experiments.

The proposed rectangular device shows the widest frequency range compared with other designs [5, 8, 11] for the radiation frequency range. In the item of structure, the proposed rectangular device is a closed Pdevice, which can eliminate electromagnetic leakage and play a shielding role compared with [2]. Compared with [9, 13, 15], the proposed rectangular device not only broadens the frequency range but also increases the radiation space. In general, the proposed rectangular device has obvious advantages in the sufficient radiation space and broadband aspect.

V. CONCLUSION

In this paper, a rectangular TEM device for cell experiments is proposed, which uses a rectangular coaxial structure as the radiation section. Its configuration is given, and the related key parameters are discussed. The measurements show that S_{11} is better than -10 dB in the frequency range of DC to 5.2 GHz, and S_{21} is nearly 0 dB which shows the proposed device can be used for the broadband cell radiation experiments. Compared with other designs, the overall performance of the proposed device is better. The proposed device successfully upgrades the frequency to a wideband range and expands the space for cell experiments. The proposed prototype is expected to have a very broad prospect in cell radiation experiments of the wide frequency range.

REFERENCES

[1] G. Shi, Y. Zhang, Y. Liao and X. Ying, "Characteristics of the electromagnetic radiation emission from coaxial cable of a type inverter," *2015 IEEE 6th International Symposium on Microwave, Antenna, Propagation, and EMC Technologies (MAPE)*, Shanghai, pp. 458-461, 2015.

[2] M. Soueid, S. Kohler, L. Carr, S. M. Bardet, R. P. O' Connor, P. Leveque, and D. A. Cormos, "Electromagnetic analysis of an aperture modified TEM cell including an ITO layer for real-time observation of biological cells exposed to microwaves". *Progress in Electromagnetics Research*. vol. 149, pp. 193-204, 2014.

[3] S. Kohler, N. Ticaud, M. M. Iordache, M. G. Moisescu, T. Savopol, P. Leveque, and D. Arnaud-Cormos, "Setup for simultaneous microwave heating and real-time spectrofluorometric measurements in biological systems". *Progress in Electromagnetics Research*. vol. 145, pp. 229-240, 2014.

[4] C. Merla, N. Ticaud, D. Arnaud-Cormos, B. Veyret, and P. Leveque, "Real-time RF exposure setup based on a multiple electrode array (MEA) for electrophysiological recording of neuronal networks". *IEEE Transactions on Microwave Theory and Techniques*. vol. 59, no. 3, pp. 755-762, 2011.

[5] A. Paffi, M. Liberti, F. Fratta, F. Apollonio, C. Merla, R. Pinto, and G. Lovisolo, "A TEM cell system for in vivo exposure at 2.45 GHz". *In Proceeding of the 2012 6th European Conference on Antennas and Propagation (EUCAP)*, Prague, Czech Republic, pp. 1099-1101, 2012.

[6] M. L. Crawford, "Generation of standard EM fields using TEM transmission cells". *IEEE Transactions on Electromagnetic Compatibility*, vol. 16, pp. 189-195, 1974.

[7] R. P. O'Connor, S. D. Madison, P. Leveque, H. L. Roderick, and M. D. Bootman, "Exposure to GSM RF fields does not affect calcium homeostasis in human endothelial cells, rat pheocromocytoma cells or rat hippocampal neurons". *Plos One*. vol. 5, no. 7, pp. e11828, 2010.

[8] X. Z. Jian, H Lu, and J Deng, "Dosimetry and temperature evaluations of a1800 MHz TEM cell for in vitro exposure with standing waves". *Progress in Electromagnetics Research*. vol. 124, pp. 487-510, 2012.

[9] C. Iftode and S. Miclaus, "Design and validation of a TEM cell used for radio frequency dosimetric studies". *Progress in Electromagnetics Research*. vol. 132, pp. 369-388, 2012.

[10] S. Kohler, R.P. O'Connor, T.D.T. Vu, P. Leveque, and D. Arnaud-Cormos, "Experimental microdosimetry techniques for biological cells exposed to nanosecond pusled electric fields using microfluorimetry". *IEEE Transactions on Microwave Theory and Techniques*. vol. 61, no. 5, pp. 2015-2022, 2013.

[11] C. Song and X. Feng, "A new design and implementation of expanding testing space of a transverse electromagnetic cell," *2016 IEEE International Conference on Microwave and Millimeter Wave Technology (ICMMT)*, Beijing, pp. 967-969, 2016.

[12] Q. Huang, Research of gigahertz transverse electromagnetic cell[D]. School of Physical Electronics, 2013.

[13] M. Arezoomand, M. K. Meybodi and N. Noori, "Design of a TEM cell using both multi-step and piecewise linear tapering," *2016 8th International Symposium on Telecommunications (IST)*, Tehran, pp. 571-574, 2016.

[14] P. Alotto, D. Desideri and A. Mashio, "Parametric analysis and optimization of the shape of the transitions of a two-port rectangular TEM cell". *In the Proceeding of the 2012 International Symposium on Electromagnetic Compatibility (EMC EUROPE)*, Rome, Italy, pp. 1-6, 2012.

[15] Q. Y. Guo, Q. C. Liang, D. H. Luo, and Q. G. Liu, "An electric field probe calibration based on TEM cell and evaluation of its uncertainty". *Journal of Guangdong University of Technology*. vol. 33, pp. 19-25, 2016.

[16] S. H. Wen, J. L. Zhang, and Y. H. Lv, "The optimization design of septum in TEM cells for IC EMC Measurement". *In the Proceeding of the 2015 7th Asia-Pacific Conference on Environmental Electromagnetics (CEEM)*, Hangzhou, China, pp. 250-253, 2015.

[17] S. B. Deng, D. Pommerenke, B. T. Hu and D. Shin, "An experimental investigation of higher order mode suppression in TEM cells," *IEEE Transactions on Electromagnetic Compatibility*, vol. 50, no. 2, pp. 416-419, 2008.

[18] V. Chechetkin, A. Korotkov, E. Golubenko, E. Sychugov and P. Smirnov, "Investigation of the characteristics of the TEM cell model," *2019 Ural Symposium on Biomedical Engineering, Radioelectronics and Information Technology (USBEREIT)*, pp. 439-441, 2019.

[19] X. M. Wang, X. K. Kong, S. L. Jiang, L. Q. Kong, W. H. Lin and B. R. Bian, "A wideband open TEM cell to measure the frequency response of a frequency selective surface," *2020 IEEE 3rd International Conference on Electronic*, pp. 321-323, 2020.

[20] M. Mierka, "Realization of a TEM cell," *2019 12th International Conference on Measurement*, pp. 162-166, 2019.

Shiqi Wang was born in Shenyang, China. She received the B.Eng. and M.Eng. degrees in information and communication engineering from Dalian Maritime University, Liaoning, China, in 2014 and 2017, respectively. She is currently working toward the Ph.D. degree with the Dalian Maritime University. Her current research interests include wideband electromagnetic field, bioelectromagnetics, and optimization method.

Shaojun Fang received the Ph.D. degree in communication and information systems from Dalian Maritime University (DLMU), Liaoning, China, in 2001.

Since 1982, he has been with DLMU, where he is currently the Head Professor with the School of Information Science and Technology. His recent research interests include passive RF components, patch antennas, and computational electromagnetics. He has authored or coauthored three books and over 100 journal and conference papers.

Dr. Fang was a recipient of the Best Doctor's Dissertation Award of Liaoning Province in 2002 and the Outstanding Teacher Award of the Ministry of Transport of China.

Peng Chen received the Ph.D. degree in communication and information systems from Dalian Maritime University (DLMU), Liaoning, China, in 2007.

He is currently an Associate Professor with the School of Information Science and Technology, DLMU. His current research interests include wireless sensor network, ultra-broadband wireless communication technology, and antenna.

Design of Electronically Controlled Filter Power Divider Based on Liquid Crystal

Wenjie Shen[1,2], Ying Han[1], Weirong Chen[1], Di Jiang[3], Sha Luo[3], and Tianming Bai[3]

[1]School of Electrical Engineering, Southwest Jiaotong University, Chengdu 610031, China
29788165@qq.com, hanying@swjtu.edu.cn, wrchen@swjtu.edu.cn

[2]China Railway Engineering Consulting Group Co., Ltd., Beijing 100055, China

[3]School of Information and Communication Engineering, University of Electronic Science and Technology of China, Chengdu 611731, China
dijiang@uestc.edu.cn, luosha109@163.com, tianyumingfeng@163.com

Abstract – The wireless communication system is one of the most important facilities of fuel cell hybrid power tram (FCHPT), which provides a strong guarantee for efficient and safe operation. As an indispensable part of the RF front-end of the transmitter and receiver, the miniaturization and high-performance trends of filtering power dividers are becoming evident. Based on the principle of filter power divider, a capacitor loaded power divider filter is designed and fabricated in this paper. The center frequency of the designed power divider filter is 30 GHz, the return loss S_{11} is less than -10 dB in the range from 29.2 to 31.6 GHz, and the insertion losses S_{21} and S_{31} are less than 5.3 dB. The frequency shift of 1.8 GHz can be achieved by changing the dielectric constant of the liquid crystal with an applied bias voltage, which can be used in millimeter wave communication system.

Keywords – Electronically controlled tuning, filter power divider, liquid crystal material.

I. INTRODUCTION

Fuel cells as a promising technology that provide electrical power with high efficiency, less noise, and near-zero emissions have been successfully used in vehicle, rail traffic, ship, and distributed generation. Fuel cell hybrid power tram (FCHPT) is a new type of urban rail transit locomotive, which has been widely studied and successfully applied in the world. The wireless communication system is one of the most important facilities of FCHPT, which is the core guarantee to ensure the safe, reliable, and efficient operation of the tram.

In the wireless communication system of FCHPT, the filtering power divider is an indispensable part of the RF front-end of the transmitter and receiver. The filter can let the desired signal through and suppress the spurious signal, while the power divider can realize the distribution and synthesis of power [1, 2]. In modern wireless communication systems, these two devices are generally designed independently and then cascaded by additional matching networks or transmission lines. The traditional design method makes the circuit have a larger physical size, and the cascade between devices will introduce additional mismatch and loss. The characteristics of filter power divider are mainly determined by the design of filter. The filter with multi-frequency band can save space and meet the needs of most work [3], but the working frequency band is often fixed after the structure is determined. As an extension of multi-band filter, the adjustable filtering power divider has the characteristics of high integration, dynamic frequency selection, low loss, and so on [4]. The technology is to realize reconfigurable performance mainly including PIN [5], varactor tuning technology [6], ideal switches [7, 8], MEMS system tuning technology [9, 10], graphite [11], iron or ferrite tuning technology [12, 13], and so on. In addition, as a new type of electromagnetic material, liquid crystal material holds the characteristics of anisotropy of dielectric constant, stable electromagnetic performance, and low loss. Liquid crystal tuned microwave passive devices are based primarily on liquid crystal electromagnetic effect. When the low frequency bias voltage is applied to it, under the action of the electric field, the director of the liquid crystal molecule is driven to be consistent with the bias voltage of the external electric field, which changes the distribution state of the liquid crystal pointing vector in space. At the same time, for the electromagnetic wave with a certain polarization direction with liquid crystal as the medium, the change of the spatial director of the liquid crystal means that the refractive index of the incident wave is changed, so as to modulate the transmission state of the electromagnetic wave transmitted in the liquid crystal. At present, researchers at home and abroad

Submitted On: July 23, 2021
Accepted On: December 12, 2021

https://doi.org/10.13052/2022.ACES.J.370111

have carried out a lot of research work on passive devices based on liquid crystal materials, such as tunable phase shift [14], adaptive filter [15], tunable planar reflection array antenna [16, 17], phased array antenna [18–20], and frequency selective surface [21–23]. Liquid crystal tunable technology has great application potential and development prospects.

The traditional filter resonant structures include end coupling [24], parallel coupling line [25], comb line [26], hairpin type [27], cross toe type [28], etc. All of the above structures are realized by coupling lines, and the input and output of traditional coupling line structures are not on the same straight line. The end coupling size is usually larger, comb line, hairpin type, or cross toe type, and other structures require high machining accuracy, especially in the millimeter wave band. For the purpose of integration and miniaturization of wireless communication system, an electronically controlled adjustable filtering power divider is proposed in this paper. A capacitive electromagnetic cross-coupling resonator structure is designed, and the capacitive coupling resonator is integrated into the two output terminals of the first-order Wilkinson power divider. Then, by using the liquid crystal material and electrifying the electrodes on the upper and lower surface of the liquid crystal. The liquid crystal molecular orientation will change with the voltage value, which changes the dielectric constant of the liquid crystal material, so as to tune the central frequency of the filtering power divider. Its structure is relatively simple, which meets the requirements of broadband miniaturization of current electronic communication technology, and adapts to a wider range of application scenarios.

II. THEORY AND DESIGN

A. Capacitor loaded power divider bandpass filter

Ideally, the structure of the capacitive loaded lossless transmission line resonator is shown in Figure 1. Denoting the transmission coefficient by $\beta = \omega_0\sqrt{LC} = 2\pi/\lambda g$, where ω_0 is the angular frequency, L and C are expressed as distributed series inductors and parallel capacitors, respectively. If the capacitance C becomes larger in the circuit, transmission coefficient will decrease, and the slow-wave effect will appear, thus reducing the size of the circuit. If the capacitance C increases periodically, it can reduce the circuit size and have band-stop characteristics. It has a good effect on the suppression of some frequencies. Coupling equivalent circuits of two resonators are shown in Figure 2.

By using the two-port network theory to analyze the coupling between two resonators, the capacitive coupling between stages can be further equivalent to an admittance converter, and the equivalent circuit of interstage coupling is shown in Figure 3.

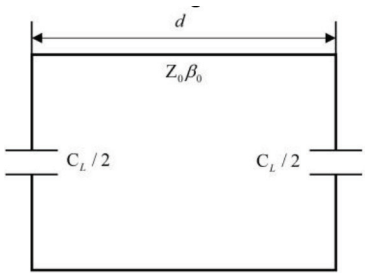

Fig. 1. Ideally loaded capacitive transmission line resonator.

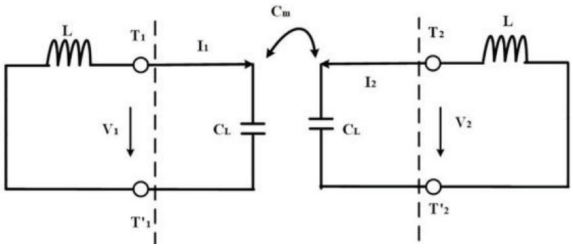

Fig. 2. Coupling equivalent circuit of two resonators.

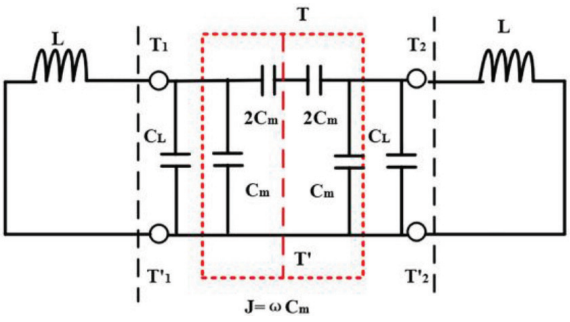

Fig. 3. Coupling equivalent circuit of two resonators.

If T-T' is equivalent to an electric wall, the resonant frequency is

$$f_e = \frac{1}{2\pi\sqrt{L(C_L + C_m)}}. \tag{1}$$

If T-T' is equivalent to a magnetic wall, the resonant frequency is

$$f_m = \frac{1}{2\pi\sqrt{L(C_L - C_m)}}. \tag{2}$$

Therefore, the coupling coefficient between the two resonators is

$$K = \frac{f_m^2 - f_e^2}{f_m^2 + f_e^2} = \frac{C_m}{C_L}. \tag{3}$$

A capacitor loaded filter coupled with a resonant unit, as shown in Figure 4, is adopted. In the design of this structure, the multipath effect caused by the coupling between multiple resonators makes the signal synthesize with the same amplitude and phase at the output port.

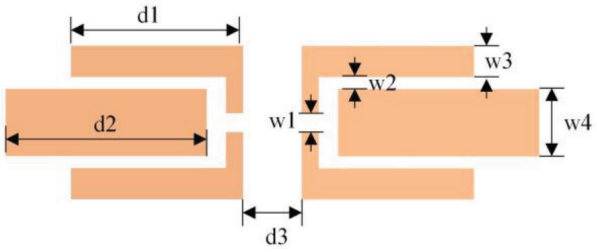

Fig. 4. The structure of capacitor loaded power divider bandpass filter.

Table 1 Design parameters and their values

Parameters	Value (mm)
d1	2.7
d2	3.7
d3	0.15
w1	0.15
w2	0.07
w3	0.27
w4	1.07

Through two identical coupling paths, not only compact structure can be realized but also lower loss can be realized. Based on this structure, modeling and simulation are carried out in HFSS. The specific design parameters are shown in Table 1.

The filter uses a Rogers 5880 substrate with a thickness of h = 0.254 mm, with a relative dielectric constant of 2.2 and a dielectric loss tangent of 0.0009. After the above theoretical analysis, through the loading capacitance introduced by the microstrip gap, the S parameter of the filter is obtained according to the parameters of Table 1. The results of equivalent circuit model and HFSS simulation model are compared as shown in Figure 5. Considering the limit of actual fabricated accuracy, the simulation results in HFSS are poor compared with the ideal circuit simulation results. But they still meet the requirements and are basically consistent with the expectation, which verifies the effectiveness of the circuit. In the HFSS simulation, the central frequency is at 30.9 GHz, the insertion loss in the passband is less than 1.4 dB, and the return loss is greater than 13 dB.

B. Filter-based Wilkinson power divider

The Wilkinson power divider's function is to distribute the input signal equally or unequally to each output port and maintain the same output phase. Although the ring has similar functions, the Wilkinson power divider has a broader bandwidth in the application.

The circuit structure of the microstrip Wilkinson power divider is shown in Figure 6. Among them, the characteristic impedance of the input port is Z_0. According to the quarter wavelength impedance transformation theory, the electrical length of the two branch microstrip lines is $\lambda/4$, the characteristic impedance is $\sqrt{2}Z_0$, and the characteristic impedance of the output port is Z_0.

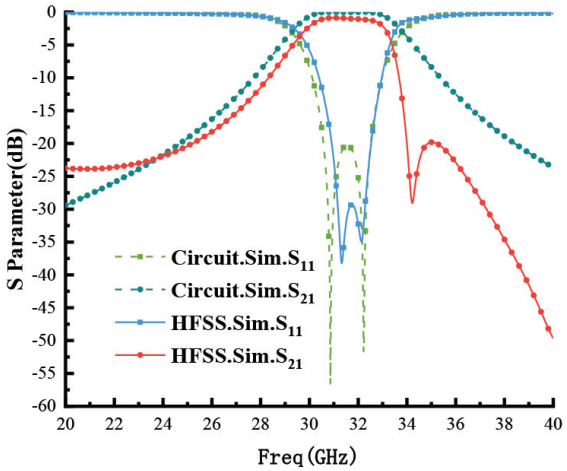

Fig. 5. Comparison of S parameter simulation results.

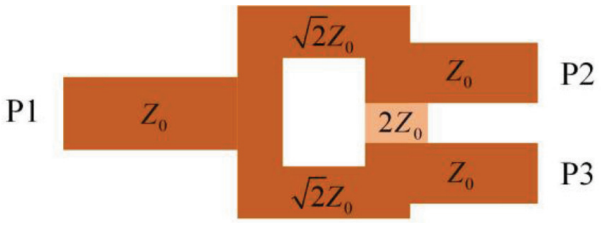

Fig. 6. Circuit structure of microstrip Wilkinson power divider.

The characteristic impedance of the microstrip lines is 50 Ω. The value of isolation resistance can be obtained from the following formula:

$$R = Z_0 k + 1/k, \tag{4}$$

where $k = \sqrt{P3/P2}$, and when the power is evenly distributed, k is 1, then R = 2 Z_0.

The linewidth of 50 Ω mounted microstrip lines can be calculated by the empirical formula

$$Z_0 = \frac{87}{\sqrt{\varepsilon + 1.41}} \ln\left[\frac{5.98h}{0.8w + t)}\right], \tag{5}$$

where h is the height of the substrate, t is the line height, and w is the width of the microstrip lines.

When the input signal enters from P1, P2 and P3 have equal amplitude and in-phase output. The power divider is designed based on microstrip line; so transmission mode is quasi-TEM mode. The simulation results of the frequency response of the first-order Wilkinson power divider are shown in Figure 7, including isolation and transmission characteristics. As can be seen in Figure 7, the energy is evenly divided within the effective

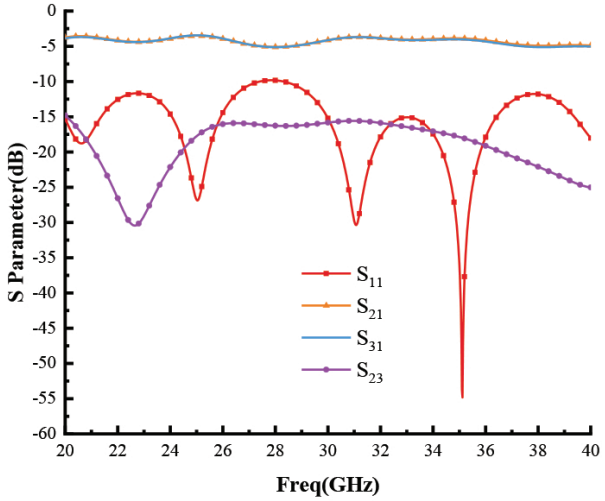

Fig. 7. Simulation results of the first-order Wilkinson power divider.

frequency band, the transmission attenuation of port is 4 dB, the curves of S_{21} and S_{31} are basically consistent, and the isolation of ports 2 and 3 is greater than 15 dB.

C. Adjustable filter power divider

The frequency selection performance of the filtering power divider mainly depends on the filter. The loading capacitor filter introduced above is cascaded at the two outputs of the first-order Wilkinson power divider to form the filtering power divider. The overall structure model is shown in Figure 8. The size of the whole structure of the filtering power divider is 35 mm $\times$ 20 mm. Two layers of Rogers 5880 dielectric substrate with a thickness of 0.254 mm and a dielectric constant of 2.2 are used, and the second layer substrate is slotted in the middle to fill the liquid crystal material. The liquid crystal block area is 22 mm $\times$ 6 mm, and the thickness is set to 0.254 mm. The frequency response results are shown in Figure 8. The center frequency of the filter is 30 GHz, the return loss S_{11} is less than -10 dB in the range of 29.02$-$31.64 GHz, and the insertion losses S_{21} and S_{31} are less than 5 dB. It can be seen from Figure 9 that the designed filtering power divider achieves equal power division performance in the operating frequency band and has the same amplitude and phase.

Liquid crystal is an electromagnetic tuning material. As shown in Figure 10(a), with the different applied bias voltage, the molecular orientation in it will change, resulting in the change of dielectric constant. And then, the corresponding resonant frequency of microstrip lines with the same size will change, that is, frequency reconfiguration is realized. When the liquid crystal molecule is perpendicular to the direction of the electric field, the

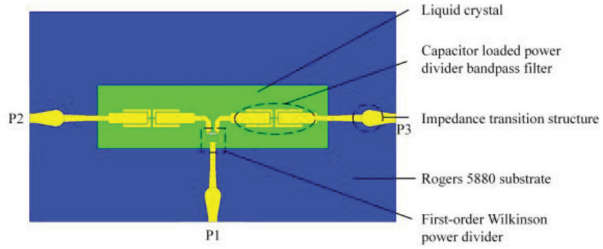

Fig. 8. Structure of adjustable filtering power divider.

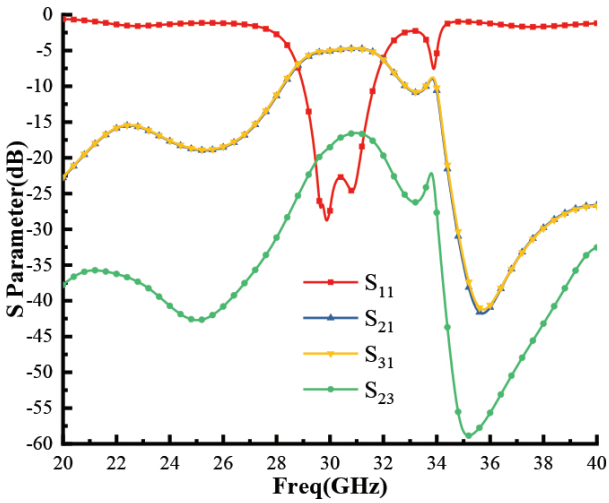

Fig. 9. Simulation results of S parameter.

corresponding dielectric constant is $\varepsilon_{\perp}$, the liquid crystal molecule is parallel to the direction of the electric field, and the corresponding dielectric constant is $\varepsilon_{\parallel}$. In the simulation, the liquid crystal is set as a new material and its dielectric constant is set as a variable for simulation. In the actual measurement, the metal of the filter layer is grounded and the metal base is loaded with bias voltage, as shown in Figure 10(b). The dielectric constant of liquid crystal is adjusted by adjusting the bias voltage, so as to realize the frequency reconfigurable characteristics of filter power divider.

Then the dielectric constant of the liquid crystal varies uniformly in the range of 2.2$-$2.8. As shown in Figure 11, the center frequency of the passband of the filter power divider moves from 30 to 28.1 GHz to achieve the 1.9-GHz frequency shift.

III. RESULTS AND DISCUSSION

To verify the feasibility of the filtering power divider, it is processed and tested according to the structure size of the filtering power divider. The prototype of the filtering power divider is shown in Figure 12. The circuit structure shown in Figure 12 is attached to the lower surface of the upper dielectric substrate in the form of

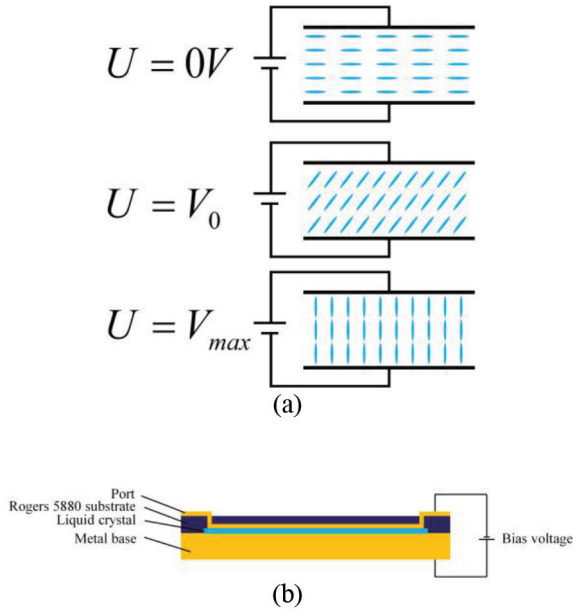

Fig. 10. Schematic diagram of liquid crystal bias voltage control. (a) Tuning process. (b) Bias voltage loading structure.

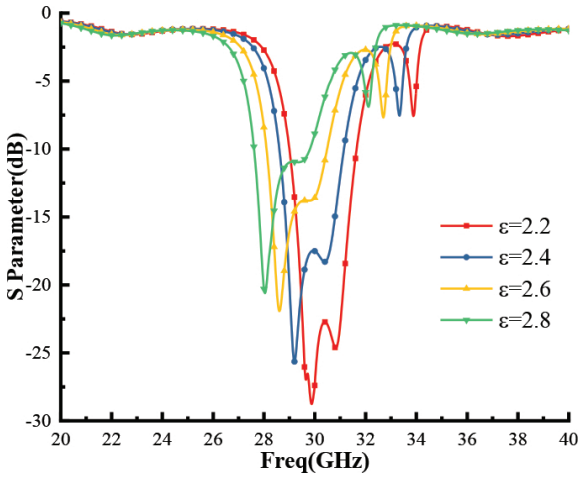

Fig. 11. Simulation results of S_{11} tuning.

inverted microstrip, and the dielectric constant of the liquid crystal is controlled by the bias voltage between the inverted microstrip patch and the metal base, to realize the change of the resonance point. The orientation of liquid crystal molecules is matched by coating a layer of polyimide film on the metal copper foil of the filter power splitter. After completing the phase matching, the direction of all liquid crystal molecules is perpendicular to the electric field.

The test platform is shown in Figure 13, which includes the PNA-X vector network analyzer and function

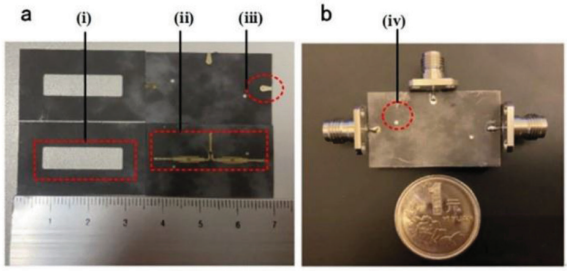

Fig. 12. Prototype of adjustable filtering power divider. (a) Layered structure: (i) liquid crystal slot; (ii) inverted microstrip filter; (iii) transition structure. (b) Integral structure: (iv) liquid crystal injection hole.

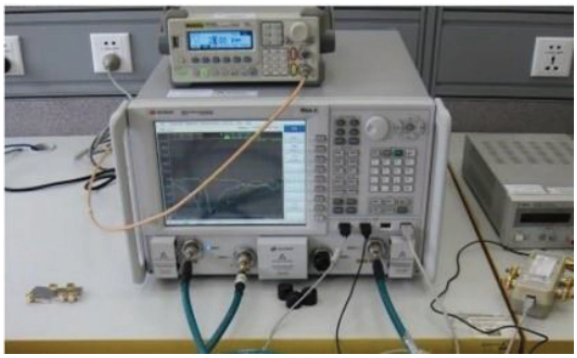

Fig. 13. Measurement of power divider filter.

waveform generator. The function waveform signal generator provides 1-KHz low-frequency square wave signal modulation voltage (0−20 V) for the experiment. The dielectric constant of liquid crystal varies with the applied voltage, but excessive voltage will destroy the internal structure of liquid crystal molecules. Generally, the applied voltage range is 0−20 V, and its electrical tuning ability can be expressed as follows:

$$\tau = \frac{\varepsilon - \varepsilon_{\perp}}{\varepsilon}. \tag{6}$$

As can be seen from Figure 14, the bandwidth of the filtering power divider is 2.46 GHz, the return loss S_{11} is less than −10 dB in the range from 29.2 to 31.6 GHz, and the insertion losses S_{21} and S_{31} are less than 5.3 dB. It can be seen that the designed filtering power divider achieves equal power division performance in the working frequency band. Then, by changing the voltage range of 0−20 V at both ends of the liquid crystal, as shown in Figure 15, the center frequency of the passband of the filtering power divider is shifted from 29.9 to 28.1 GHz to achieve 1.8-GHz frequency shift. Compared with the simulation results, the measurement results are slightly worse, which may be due to the generation of some bubbles during liquid crys-

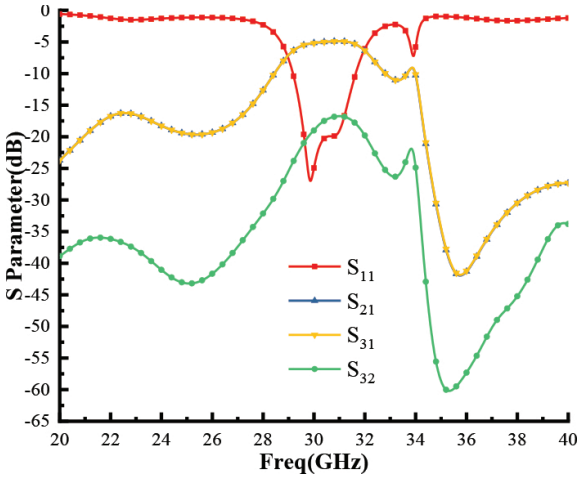

Fig. 14. Measurement results of S parameter.

Table 2 Comparison of proposed work with others

Ref.	Frequency (GHz)	Bandwidth (GHz)	Tuning bandwidth (GHz)
[29]	1.2	0.04	No
[30]	1.4	<0.2	No
[31]	1.4	<0.25	0.2
[32]	1	<0.2	0.4
This work	30	2.46	1.8

tal filling, which affects the performance, but it is still within the acceptable range. The measurement results show that the proposed liquid crystal filter power divider can realize frequency tuning. The performance comparison with similar power division filters is shown in Table 2.

IV. CONCLUSION

In this paper, an electronically controlled filter power divider of FCHPT based on liquid crystal is designed by cascading the Wilkinson power divider with the output port of the filter unit. Compared with most of the low frequency filters, the designed power divider filter integrates power distribution and filtering and can work at 30 GHz. In addition, by changing the voltage value, the liquid crystal pointing vector can be changed, so as to change the effective dielectric constant of the liquid crystal material, and then tune the center frequency of the filter power divider. The tuning bandwidth of the filtering power divider is 1.8 GHz (29.9−28.1 GHz), and the port isolation is less than 18 dB. In the continuously adjustable range, the maximum insertion loss is 5.3 dB. It realizes dynamic frequency selection and power distribution, effectively simplifies the structure and size of the system, and realizes the miniaturization and lightweight characteristics of the electronic system, thus reducing the cost and suitable for millimeter-wave electronic communication systems.

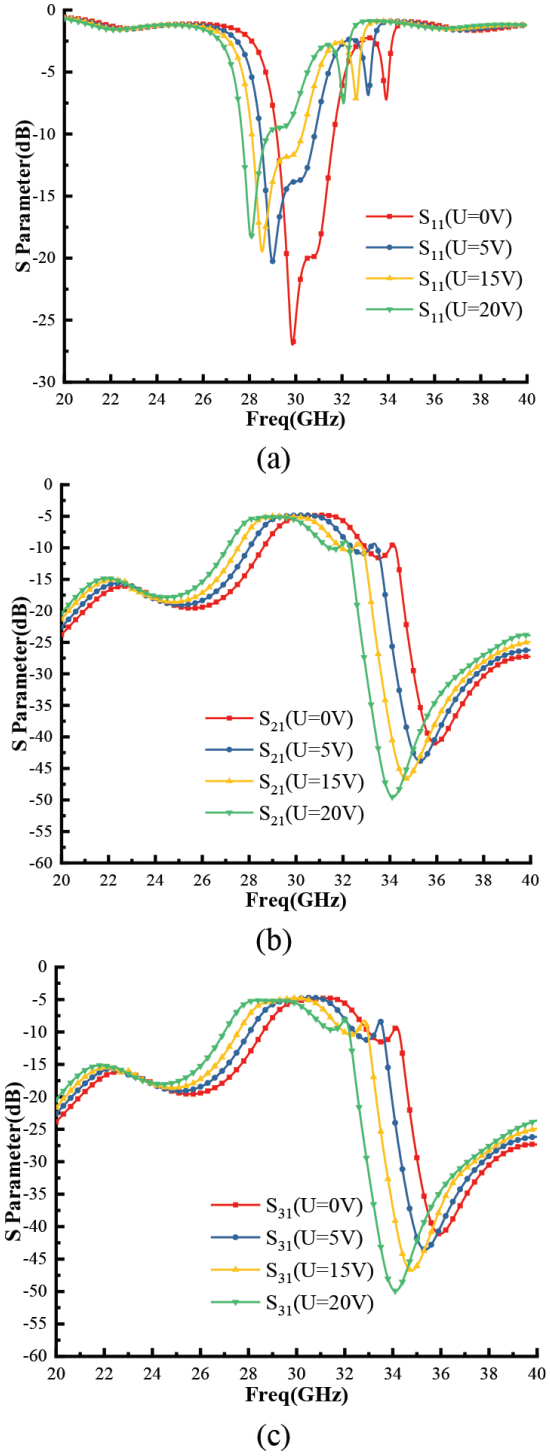

Fig. 15. Measurement tuning results of S parameter. (a) S_{11}. (b) S_{21}. (c) S_{31}.

REFERENCES

[1] R. Gómez-García, L. Yang, J.-M. Muñoz-Ferreras, and W. Feng, "Lossy signal-interference filters and applications," *IEEE Transactions on Microwave Theory and Techniques*, vol. 68, no. 2, pp. 516-529, Dec. 2020.

[2] K. Song, F. Xia, Y. Zhou, S. Guo, and Y. Fan, "Microstrip/slotline-coupling substrate integrated waveguide power divider with high output isolation," in *IEEE Microwave and Wireless Components Letters*, vol. 29, no. 2, pp. 95-97, Feb. 2019.

[3] Y. Li, S. Luo, and W. Yu, "A compact tunable triple stop-band filter based on different defected microstrip structures," *Applied Computational Electromagnetics Society Journal*, vol. 33, no. 7, pp. 752-757, Apr. 2018.

[4] P. Wen, Z. Ma, H. Liu, S. Zhu, B. Ren, Y. Song, X. Wang, and M. Ohira, "Dual-band filtering power divider using dual-resonance resonators with ultra-wide stopband and good isolation," in *IEEE Microwave and Wireless Components Letters*, vol. 29, no. 2, pp. 101-103, Feb. 2019.

[5] E. Abiri, M. R. Salehi, S. Kohan, and M. Mirzazadeh, "Multi-application PIN diode," *2010 Second Pacific-Asia Conference on Circuits, Communications and System*, pp. 60-62, Aug. 2010.

[6] Q. Xiang, Q. Feng, and X. Huang, "Tunable band-stop filter based on split ring resonators loaded coplanar waveguide," *Applied Computational Electromagnetics Society Journal*, vol. 28, no. 7, pp. 591-596, Jul. 2013.

[7] Y. Li, W. Li, and W. Yu, "A switchable UWB slot antenna using SIS-HSIR and SIS-SIR for multi-mode wireless communications applications," *Applied Computational Electromagnetics Society Journal*, vol. 27, no. 4, pp. 340-351, Apr. 2012.

[8] Y. Li, W. Li, and Q. Ye, "A reconfigurable wide slot antenna integrated with sirs for UWB/multiband communication applications," *Microwave & Optical Technology Letters*, vol. 55, no. 1, pp. 52-55, Jan. 2013.

[9] S. Fouladi, F. Huang, W. D. Yan, and R. R. Mansour, "High-Q narrowband tunable combline bandpass filters using MEMS capacitor banks and piezomotors," *IEEE Transactions on Microwave Theory and Techniques*, vol. 61, no. 1, pp. 393-402, Jan. 2013.

[10] E. Erdil, K. Topalli, M. Unlu, O. A. Civi, and T. Akin, "Frequency tunable microstrip patch antenna using RF MEMS technology," in *IEEE Transactions on Antennas and Propagation*, vol. 55, no. 4, pp. 1193-1196, Apr. 2007.

[11] C. Huang, J. Song, C. Ji, J. Yang, and X. Luo, "Simultaneous control of absorbing frequency and amplitude using graphene capacitor and active frequency-selective surface," in *IEEE Transactions on Antennas and Propagation*, vol. 69, no. 3, pp. 1793-1798, Mar. 2021.

[12] J. D. Adam, L. E. Davis, G. F. Dionne, E. F. Schloemann, and S. N. Stitzer, "Ferrite devices and materials," in *IEEE Transactions on Microwave Theory and Techniques*, vol. 50, no. 3, pp. 721-737, Mar. 2002.

[13] Q. D. Huang and Y. J. Cheng, "Ferrite-loaded substrate integrated waveguide frequency-agile bandpass filter," *Applied Computational Electromagnetics Society Journal*, vol. 31, no. 7, pp. 823-828, Jul. 2016.

[14] B. S.-Y. Ung, X. Liu, E. P. J. Parrott, A. K. Srivastava, H. Park, V. G. Chigrinov, and E. Pickwell-MacPherson, "Towards a rapid terahertz liquid crystal phase shifter: terahertz in-plane and terahertz out-plane (TIP-TOP) switching," in *IEEE Transactions on Terahertz Science and Technology*, vol. 8, no. 2, pp. 209-214, March 2018.

[15] D. Jiang, X. Li, Z. Fu, G. Wang, Z. Zheng, T. Zhang, and W.-Q. Wang, "Millimeter-wave broadband tunable band-pass filter based on liquid crystal materials," in *IEEE Access*, vol. 8, pp. 1339-1346, Nov. 2020.

[16] G. Perez-Palomino, P. Baine, R. Dickie, M. Bain, J. A. Encinar, R. Cahill, M. Barba, and G. Toso, "Design and experimental validation of liquid crystal-based reconfigurable reflectarray elements with improved bandwidth in F-band," in *IEEE Transactions on Antennas and Propagation*, vol. 61, no. 4, pp. 1704-1713, Apr. 2013.

[17] S. Bildik, S. Dieter, C. Fritzsch, W. Menzel, and R. Jakoby, "Reconfigurable folded reflectarray antenna based upon liquid crystal technology," in *IEEE Transactions on Antennas and Propagation*, vol. 63, no. 1, pp. 122-132, Jan. 2015.

[18] G. Perez-Palomino, P. Baine, R. Dickie, M. Bain, J. A. Encinar, R. Cahill, M. Barba, and G. Toso, "Design and experimental validation of liquid crystal-based reconfigurable reflectarray elements with improved bandwidth in F-band," in *IEEE Transactions on Antennas and Propagation*, vol. 61, no. 4, pp. 1704-1713, Apr. 2013.

[19] R. Reese, E. Polat, H. Tesmer, J. Strobl, C. Schuster, M. Nickel, A. B. Granja, R. Jakoby, and H. Maune, "Liquid crystal based dielectric waveguide phase shifters for phased arrays at W-band," in *IEEE Access*, vol. 7, pp. 127032-127041, Sep. 2019.

[20] Y. Zhao, C. Huang, A. Qing, and X. Luo, "A frequency and pattern reconfigurable antenna array based on liquid crystal technology," *IEEE Photonics Journal*, vol. 9, no. 3, pp. 1-7, Jun. 2017.

[21] W. Hu, R. Dickie, R. Cahill, H. Gamble, Y. Ismail, V. Fusco, D. Linton, N. Grant, and S. Rea "Liquid crystal tunable mm wave frequency selective surface," *IEEE Microwave and Wireless Components Letters*, vol. 17, no. 9, pp. 667-669, Sept. 2007.

[22] J. A. Bossard, X. Liang, L. Li, S. Yun, D. H. Werner, B. Weiner, T. S. Mayer, A. Diaz, and I. C. Khoo, "Tunable frequency selective surfaces and negative-zero-positive index metamaterials based on liquid crystals," in *IEEE Transactions on Antennas and Propagation*, vol. 56, no. 5, pp. 1308-1320, May 2008.

[23] S. N. Novin, S. Jarchi, and P. Yaghmaee, "Tunable frequency selective surface based on IDC-loaded electric-LC resonator incorporated with liquid crystal," *2017 Conference on Microwave Techniques (COMITE)*, pp. 1-4, May 2017.

[24] A. Vosoogh, A. A. Brazález, and P. Kildal, "A V-band inverted microstrip gap waveguide end-coupled bandpass filter," in *IEEE Microwave and Wireless Components Letters*, vol. 26, no. 4, pp. 261-263, Apr. 2016.

[25] S. Lin, Y. Chen, P. Chiou, and S. Chang, "Tunable Wilkinson power divider utilizing parallel-coupled-line-based phase shifters," in *IEEE Microwave and Wireless Components Letters*, vol. 27, no. 4, pp. 335-337, Apr. 2017.

[26] L. Zhou, S. Liu, J. Duan, and M. Xun, "A novel tunable combline bandpass filter based on external quality factor and internal coupling tunings," *Applied Computational Electromagnetics Society Journal*, vol. 33, no. 6, pp. 591-596, Jun. 2018.

[27] J.-S. Hong and M. J. Lancaster, "Cross-coupled microstrip hairpin-resonator filters," *IEEE Transactions on Microwave Theory and Techniques,* vol. 46, no. 1, pp. 118-122, Jan. 1998.

[28] T. Cheng and K. Tam, "A wideband bandpass filter with reconfigurable bandwidth based on cross-shaped resonator," in *IEEE Microwave and Wireless Components Letters*, vol. 27, no. 10, pp. 909-911, Oct. 2017.

[29] C. Chen and C. Lin, "Compact microstrip filtering power dividers with good in-band isolation performance," in *IEEE Microwave and Wireless Components Letters*, vol. 24, no. 1, pp. 17-19, Jan. 2014.

[30] X. Zhao, L. Gao, X. Y. Zhang, and J. Xu, "Novel filtering power divider with wide stopband using discriminating coupling," in *IEEE Microwave and Wireless Components Letters*, vol. 26, no. 8, pp. 580-582, Aug. 2016.

[31] Y.-H. Chun, J.-S. Hong, P. Bao, T. J. Jackson, and M. J. Lancaster, "BST varactor tuned bandstop filter with slotted ground structure," *2008 IEEE MTT-S International Microwave Symposium Digest*, pp. 1115-1118, Jun. 2008

[32] D. Psychogiou, R. Gómez-García, A. C. Guyette, and D. Peroulis, "Reconfigurable single/multi-band filtering power divider based on quasi-bandpass sections," in *IEEE Microwave and Wireless Components Letters*, vol. 26, no. 9, pp. 684-686, Sep. 2016.

Wenjie Shen received the bachelor's degree in electrical engineering from Beijing Jiaotong University, Beijing, China, in 2004, and the master's degree in electrical engineering from Tsinghua University, Beijing, China, in 2013. He is currently working toward the doctor's degree.

He is currently a Senior Engineer and Vice President of China Railway Engineering Consulting Group Co., Ltd. His research interests include the design of railway and metro traction power supply systems.

Ying Han received the B.S. and Ph.D. degrees from the School of Electrical Engineering, Southwest Jiaotong University, Chengdu, China, in 2013 and 2019, respectively.

He is a Visiting Scholar with the School of Information Technology and Electrical Engineering, University of Queensland, Brisbane, Australia. He is a Senior Member of IEEE and an Assistant Professor with the School of Electrical Engineering, Southwest Jiaotong University. His research interests include optimal control of fuel cell locomotives, energy management of hybrid systems, and optimization and control of integrated energy systems.

Weirong Chen received the B.S. and M.S. degrees in electronic engineering from the Electronic Science and Technology University, Chengdu, China, in 1985 and 1988, respectively, and the Ph.D. degree in power system and its automation from Southwest Jiaotong University, Chengdu, China, in 1998.

He is currently a Senior Visiting Scholar with Brunel University, London, U.K., in 1999. He is an IET Fellow and Professor with the School of Electrical Engineering, Southwest Jiaotong University. His research interests include renewable energy and its applications, fuel cell locomotive technology, and power system control.

Di Jiang is currently an Associate Professor and Doctoral Advisor of Information and Communication Engineering with the University of Electronic Science and Technology of China, Chengdu, China. He is mainly engaged in broadband reconfigurable microwave devices, array antennas, and other research.

Sha Luo is currently a graduate student of Information and Communication Engineering with the University of Electronic Science and Technology of China, Chengdu, China. He loves learning new knowledge, likes to contact new things, is willing to communicate with people, and have a sense of responsibility. In the graduate stage, he studied in the direction of RF and microwave. His main research topics are reconfigurable antenna and passive components. He designed passive phased array antenna, holographic antenna, phase shifter, filter power divider, microstrip log periodic antenna, waveguide slot antenna, etc.

Tianming Bai is currently a graduate student of Information and Communication Engineering with the University of Electronic Science and Technology of China, Chengdu, China. His main research direction is conformal antenna, reflection array antenna, phased array antenna, etc.

Research and Design of Radar System for Respiratory and Heartbeat Signal Detection

Ziliang Xia, Xinhuai Wang, Xin Li, and Yin Xu

National Key Laboratory of Science and Technology on Antennas and Microwave
Xidian University, Xi'an, Shaanxi 710071, China
zlxia@stu.xidian.edu.cn, xinhuaiwang@xidian.edu.cn, xli7@stu.xidian.edu.cn, xuyin@xidian.edu.cn

Abstract – The respiratory and heartbeat signals can accurately reflect the health status of the tester, which is of great clinical significance. Compared with the traditional contact detection method, the non-contact radar detection method does not require the tester to wear any sensor equipment and will not cause any discomfort to the tester. The frequency modulated continuous wave (FMCW) radar has the characteristics of simple structure, high resolution, strong stability, and low transmission power and is used for the detection of respiratory and heartbeat signals. This paper designs a low-power, low-cost respiratory, and heartbeat signal detection system based on FMCW radar. In addition, the variational modal decomposition (VMD) method is used to separate respiration and heartbeat signals to obtain accurate respiration and heartbeat rates. The results show that the radar system for detecting respiratory and heartbeat signals has high detection accuracy.

Keywords – Frequency modulated continuous wave (FMCW), heartbeat signals, respiratory signals, variational modal decomposition (VMD).

I. INTRODUCTION

According to the latest report, 330 million people have cardiovascular disease in China, and the death rate of this disease ranks first [1]. Real-time monitoring of patients' respiratory and heartbeat signals can effectively reduce accidents caused by this disease. Therefore, a detection device is needed to monitor the human body's respiratory and heartbeat rate in real time. Traditional medical contact detection equipment requires the tester to wear electrodes or sensors during the detection process, and the tester's physical activity is restricted by the device [2]. The non-contact detection device does not need to wear any sensors and mainly realizes the detection of the tester's physical information through wireless signals. The respiratory and heartbeat signal detection radar system is based on electromagnetic signals for measurement, which can penetrate obstacles such as clothes and quilts. It can be used in medical diagnosis, home health monitoring, and other occasions [3].

At present, non-contact radar detection technology has developed rapidly in the field of physiological detection. Biological radar was designed to detect abnormalities in cardiopulmonary information in 2004 [4]. A 5.8-GHz continuous wave radar detects the baby's vital signs in [5, 6]. Zito's research team has carried out research on the non-contact detection device based on ultra-wideband radar and successfully developed a set of cardiopulmonary signal detection device [7]. In [8], a 9.6-GHz frequency modulated continuous wave (FMCW) radar is used to detect respiration and heart rate, and the influence of harmonic of respiratory signal on estimation of heart rate is not eliminated. Zhang *et al*. used FMCW radar of 24.15 GHz to extract the heart rate signal, and the method used to extract the heartbeat signal is not accurate [9]. In [10], the author evaluated the results of vital signs detection by typical antennas.

During normal cardiopulmonary activities such as respiratory and heartbeat, the surface of the human thoracic cavity will produce periodic weak movements. The electromagnetic signal emitted by the radar passes through the slightly moved thoracic cavity and undergoes a Doppler effect, which causes the phase of the echo signal to change. The phase change corresponds to the micro-movement of the chest cavity, hiding the respiratory and heartbeat signals. Due to the close frequency band range of respiratory and heartbeat signals, the use of band-pass filter to separate respiratory and heartbeat signals cannot effectively solve the problem of respiratory harmonic interference on heartbeat signals [11]. Wavelet transform can extract respiratory and heartbeat signals from life signals by selecting appropriate wavelet basis functions, and it is difficult to select appropriate wavelet basis functions [12]. Empirical mode decomposition (EMD) is an adaptive signal processing method proposed by Huang *et al*. in 1998 [13], which can deal with nonlinear and non-stationary signals very well. The disadvantage of EMD is that the decomposed intrinsic modal functions (IMFs) have modal aliasing.

Submitted On: November 26, 2021
Accepted On: January 13, 2022

https://doi.org/10.13052/2022.ACES.J.370112

Ensemble empirical mode decomposition (EEMD) proposed by Wu *et al*. [14, 15] reduces the problem of modal aliasing by adding white noise. However, due to the limited number of noise additions, noise residue is prone to appear. Complete ensemble empirical mode decomposition with adaptive noise (CEEMDAN) proposed by Torres *et al*. [16] can solve the noise residual problem with less averaging by adding adaptive white noise at each stage of the decomposition. There may be false components in the result of its decomposition. Variational modal decomposition (VMD) [17] can effectively avoid modal aliasing and false components. Therefore, this paper proposes an algorithm based on VMD to process radar life signals to realize the separation and extraction of respiratory and heartbeat signals.

II. DETECTION SCHEME

A. Respiration and heartbeat signal detection

The detection of respiratory and heartbeat signals uses FMCW radar, which can measure the distance and speed of the target. In addition, the electromagnetic wave signal emitted by the radar has a very narrow wavelength and a wide bandwidth, which can improve the system's high sensitivity and range resolution. Shown in Figure 1 is the detection schematic diagram of FMCW radar.

FMCW is generated by the voltage-controlled oscillator (VCO) as the local oscillator signal of the radar system. The power divider is divided into two parts. One part of the signal is used as the transmitting signal to radiate outward through the transmitting antenna, and the other part is used as the local oscillator input of the receiver to mix with the echo signal received by the receiving antenna to obtain an intermediate frequency signal. The frequency and phase information of the intermediate frequency signal contains the information of the chest cavity micro-movement. Figure 2 shows the FMCW using sawtooth modulation.

The transmitted signal can be expressed as

$$s(t) = e^{j(2\pi f_c t + \pi B t^2/T)}, \tag{1}$$

where f_c is the working frequency of sensor, B is the bandwidth of radar, and T is the period of saw tooth wave

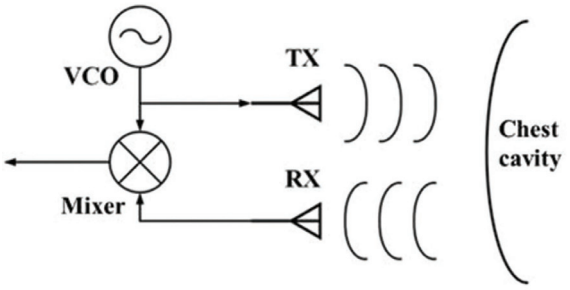

Fig. 1. Schematic diagram of FMCW radar detection.

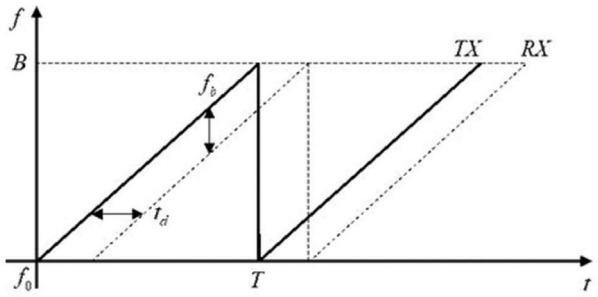

Fig. 2. The FMCW using sawtooth modulation.

transmitting signal. When the signal is reflected after it encounters an object, the reflected signal can be regarded as the delay form of the transmitting signal:

$$r(t) = e^{j(2\pi f_c(t-t_d)+\pi B(t-t_d)^2/T)}. \tag{2}$$

$t_d = 2R/c$ is the time taken for the electromagnetic wave from transmitting to receiving, R is the distance between the sensor and the object under test, and c is the speed of light. The intermediate frequency signal $b(t)$ of the object to be measured is obtained by mixing and filtering the received signal

$$b(t) = s^{'}(t)r(t) \approx e^{j(4\pi BRt/cT+4\pi R/\lambda)} = e^{j(2\pi f_b t+\phi_b)}. \tag{3}$$

For a single object, the intermediate frequency signal after mixing is a sine curve with frequency $f_b = 4\pi BRt/cT$ and phase $\phi_b = 4\pi R/\lambda$. When the chest wall displacement of human body is detected, the phase of intermediate frequency signal in the distance unit of the measured object can be measured with time. The phase change is

$$\Delta\phi_b = 4\pi\Delta R/\lambda. \tag{4}$$

Since the amplitude of chest wall vibration is very small, it can be assumed that the vibration signal $x(t)$ is in the same distance element during vibration. Assuming that the object is in the mth distance element, the vibration signal can be obtained by calculating the phase information corresponding to the mth distance element at time nT_s

$$x(m,nT_s) = \lambda/4\pi\phi_b(m,nT_s), \tag{5}$$

where n is the index of LFM pulse and T_s is the time interval of continuous measurement.

B. Respiration and heartbeat signal decomposition

Since the human heart and lungs have a certain physiological coupling relationship, the higher harmonics of the respiratory signal may overlap with the heartbeat signal; so the separation of the respiratory signal and the heartbeat signal based on VMD are proposed. The VMD method is used to solve the variational problem. Its purpose is to decompose the original signal f into k IMFs with a finite bandwidth and a center frequency.

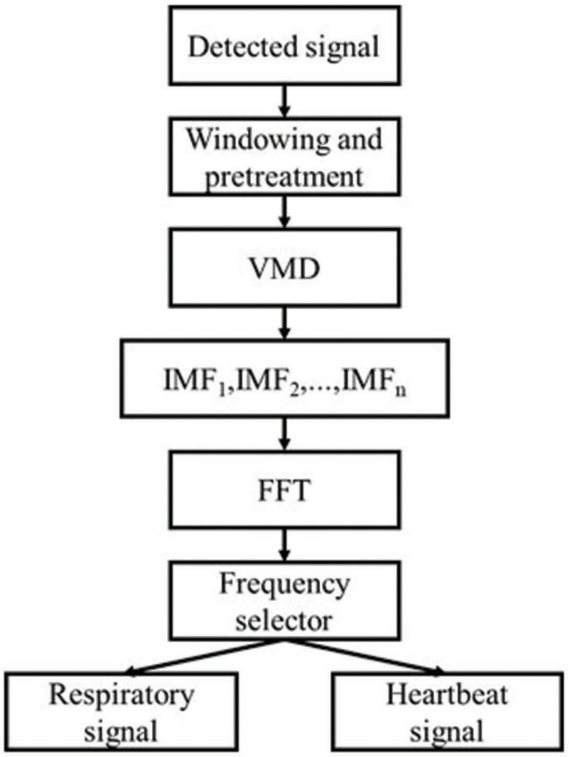

Fig. 3. The algorithm flow of decomposition of respiratory and heartbeat signals.

The algorithm flow of decomposition of respiratory and heartbeat signals is shown in Figure 3. After passing through the rectangular window, the vital signs need to be preprocessed by filtering and de-noising to be used as the input signal of VMD. The appropriate decomposition level k is set to reduce the aliasing phenomenon of decomposed natural mode components. The value of k is selected according to the actual measured signals. The decomposed natural mode components are transformed by 1024 points fast Fourier transform (FFT) to obtain the spectrum information. Since the frequency of the normal person's breathing component ranges from 0.2 to 0.8 Hz, and the frequency range of the heartbeat component ranges from 0.8 to 2 Hz, the frequency selector can be used to obtain the breathing signal and the heartbeat signal.

III. RADAR SYSTEM DESIGN

A. Hardware circuit design

The key indicators of FMCW radar include the start frequency of the radio frequency signal, the signal bandwidth, the slope of the ramp signal, and the repetition period. Table 1 shows the relevant parameters of the radar system hardware platform.

The detection range of the radar is designed to be 5 m, and the signal bandwidth is selected to be 500 MHz under a certain range resolution, and the corresponding range resolution is 0.3 m. The slope of the ramp signal is set to 0.5 MHz/μs, and the corresponding intermediate frequency signal frequency is about 16 kHz, thereby reducing the requirements of the backend circuit. The start frequency affects the detection accuracy of weak motion information. When there is a 1-mm micro-movement, the phase of the 24-GHz radio frequency signal changes 0.32π. The re-frequency period determines the update frequency of the demodulation information, and it is set to 100 Hz to meet the frequency estimation requirement. The framework of the radar system is shown in Figure 4. The entire radar system includes transceivers, antennas, intermediate frequency conditioning circuits, and microcontrollers. The system is based on the following integrated chips: radio frequency transceiver chip BGT24MTR11, phase-locked loop chip LMX2491, operational amplifier chip LMX321, and microcontroller chip STM32F303.

Table 1 The relevant parameters of the radar system hardware platform

Index	Numerical value
Start frequency	24 GHz
Bandwidth	500 MHz
Ramp signal slope	0.5 MHz/μs
Repeat frequency	100 Hz

The overall working principle of the circuit is as follows: First, the RF transmitter generates a 24-GHz FMCW signal and radiates it through the transmitting antenna. The FMCW start frequency, signal bandwidth, and repetition period are adjusted through the phase-locked loop to adjust the VCO input voltage control; then the receiving antenna receives the radio frequency signal carrying the test target information, through the quadrature mixer and the transmitted signal down-mixing to obtain two orthogonal intermediate

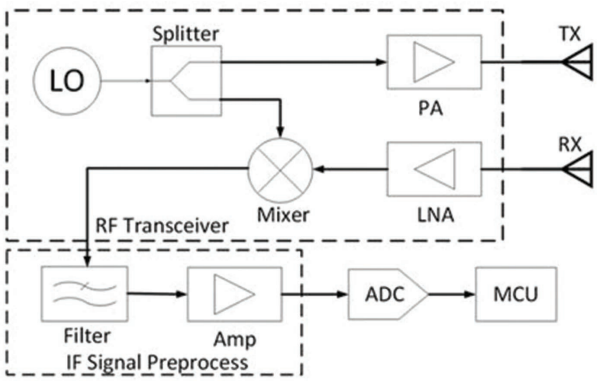

Fig. 4. The framework of the radar system.

frequency signals; the intermediate frequency signal is amplified and filtered by the intermediate frequency conditioning circuit. The analog-to-digital converter samples the digital signal; the final digital signal is analyzed and processed in the microprocessor.

B. System flow control

The system control process includes the system initialization process, the judgment waiting process, and the signal processing process. Figure 5 shows the system control process. In the initialization process, the microcontroller clock system and internal storage unit are first configured, the preset radio frequency signal parameters are read, and the internal registers of the phase-locked loop chip and the radio frequency transceiver chip are configured through the analog serial peripheral interface (SPI). The judgment waiting process is used to judge the following two events, that is, whether there is a user command to be responded to and whether there is radar data to be processed. When there is a user command to be responded to, parse the command and jump to the initialization process to reinitialize the system parameters with new parameters. When there is a radar signal to be processed, jump to the signal processing process. If neither event occurs, continue to wait until the event happened. The signal processing flow is used to process the radar data analysis, including the extraction of the micromotion signal parameters and upload the detection results through the universal asynchronous receiver/transmitter (UART) or SPI.

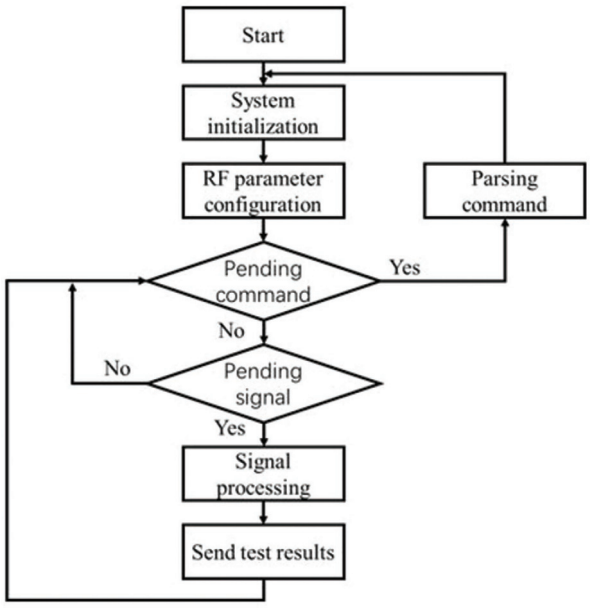

Fig. 5. The system control process.

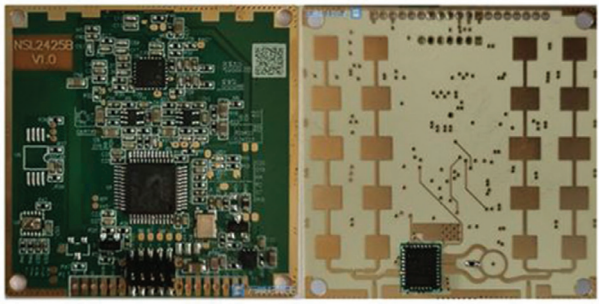

Fig. 6. The respiratory and heartbeat signal detection radar system.

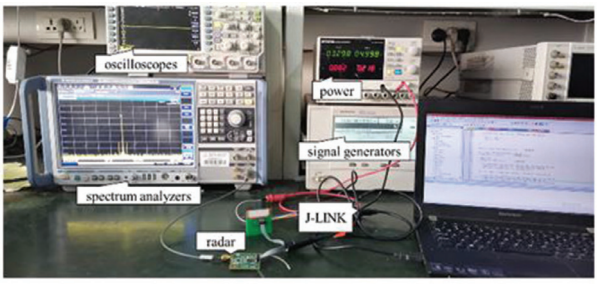

Fig. 7. Testing scenarios.

IV. EXPERIMENT AND ANALYSIS

A. Device and experiment

The designed respiratory and heartbeat signal detection radar system is shown in Figure 6. The physical size of the PCB board is 40 mm $\times$ 40 mm.

In order to test the system's power consumption and RF signal quality, we built a test scenario as shown in Figure 7. Test instruments include laptop computers, J-LINK simulators, power supplies, oscilloscopes, signal generators, and spectrum analyzers. The maximum power of the system is 1.25 W, and the standard universal serial bus (USB) interface can meet the power supply requirements of the system. Two 2 $\times$ 5 microstrip patch antennas are used for Tx and Rx.

The parameters of the radio frequency signal emitted by the radar system are shown in Table 1. Figure 8 shows the frequency spectrum of the FMCW signal under power peak hold. It can be seen from the figure that the parameters of the actual transmitted signal are basically consistent with the preset values.

B. Results and analysis

During the test, the tester remains at rest and is 1.5 m away from the antenna. The ADC with a sampling rate of 20 Hz is used to sample the chest micro-movement information detected by the radar system. The signal after windowing and preprocessing is shown in Figure 9. Since the human body's normal respiratory and heart-

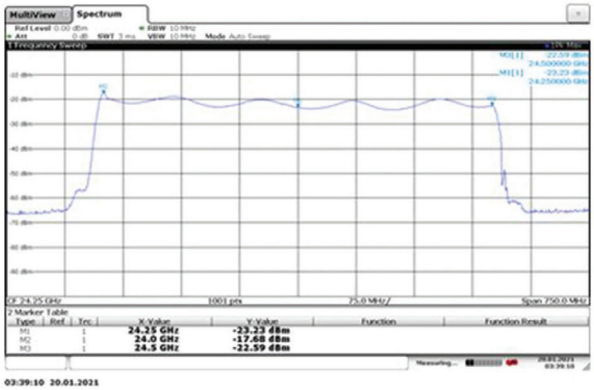

Fig. 8. FMCW output power test.

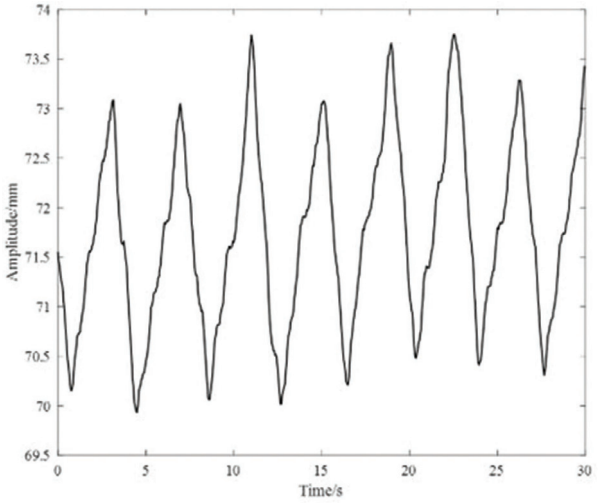

Fig. 9. Chest micromotion signal detected by radar system.

beat frequencies are below 3 Hz, when using the VMD algorithm to decompose the processed signal, the number of IMFs does not need to be too much. The value of k adopts an adaptive method. In this signal, the value of k is 4. As shown in Figure 10, VMD can successfully decompose the respiratory and heartbeat signals in the signal. The IMF_1 is the same frequency as the peak of the chest wall displacement signal spectrum. The IMF_2 is twice the frequency of the peak of the IMF_1 spectrum; so IMF_2 is the second harmonic of IMF_1. The frequency of the peak of the IMF_3 spectrum is 1.426 Hz. The corresponding heart rate is 42 beats, which is consistent with half of the pulse rate. The IMF_4 is five times the frequency of the peak of the IMF_3 spectrum; so IMF_4 is the fifth harmonic of IMF_3.

Eight different testers at the same distance are detected. Compared with the ECG monitor, the correct

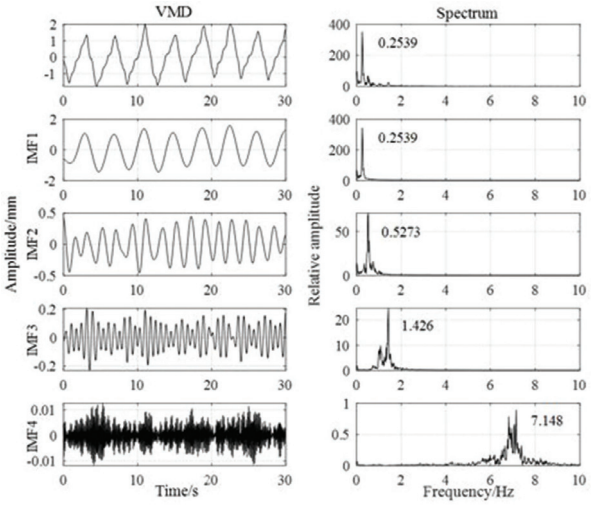

Fig. 10. IMFs of VMD and spectrums.

Table 2 Frequency and correct rates of the separated respiratory and heartbeat signals

Testers	**Respiratory frequency /Hz**	**Heartbeat frequency /Hz**	**Respiratory/ heartbeat accuracy /%**	
1	0.1953	1.221	97.7	96.9
2	0.2539	1.426	98.4	97.0
3	0.3418	1.514	97.8	96.8
4	0.2441	1.536	97.6	97.7
5	0.2667	1.367	99.9	97.0
6	0.2510	1.27	97.7	97.1
7	0.2344	1.346	99.8	98.5
8	0.3167	1.420	99.0	98.2

rates of respiratory frequency and heart frequency of VMD decomposition are obtained in Table 2. It can be seen that the accuracy of respiratory rate and heart rate of eight testers are all above 97% and 96%, respectively. The results show that the FMCW radar system designed to detect human respiratory and heartbeat signals has achieved the expected purpose. The separation algorithm based on the VMD method we designed is very effective for separating the respiratory and heartbeat signals from the thoracic micromotion signals.

V. CONCLUSION

In this paper, a respiration and heartbeat signal detection radar system is designed. The radar transmits FMCW signals to the chest cavity of the human body and uses the Doppler frequency offset effect to obtain the information of the chest cavity micro-movements caused by respiration and heartbeat movement, thereby

achieving the purpose of non-contact detection of the target's respiration and heartbeat rate. In order to separate the respiration and heartbeat signals from the thoracic micromotion signals, we propose a method for separating respiration and heartbeat signals based on VMD. The detection results are very accurate, the correct rate of respiratory rate is more than 97%, and the correct rate of heart rate is more than 96%. The system can provide help for the monitoring of cardiovascular patients.

REFERENCES

[1] The Writing Committee of the Report on Cardiovascular Health and Diseases in China, "Report on cardiovascular health and diseases burden in china: an updated summary of 2020," *Chinese Circulation Journal*., vol. 36, pp. 521–545, Jun. 2021.

[2] Y. H. Kwak, et al., "Flexible heartbeat sensor for wearable device," *Biosensors & Bioelectronics.,* vol. 94, pp. 250–255, Mar 2017.

[3] F. Q. Qi, et al., "Detection and classification of finer-Grained human activities based on stepped-frequency continuous-wave through-wall radar," *Sensors.,* vol. 16, no. 6, pp. 885–901, Jun. 2016.

[4] A. D. Droitcour, et al., "Range correlation and I/Q performance benefits in single-chip silicon Doppler radars for noncontact cardiopulmonary monitoring," *IEEE Transactions on Microwave Theory & Techniques.,* vol. 52, no. 3, pp. 838–848, Mar. 2004.

[5] M. Brink, C. H. Müller, and C. Schierz, "Contact-free measurement of heart rate, respiration rate, and body movements during sleep," *Behavior Research Methods.,* vol.38, no. 3, pp. 511–521, Aug. 2006.

[6] M. Uenoyama, T. Matsui, K. Yamada, et al., "Non-contact respiratory monitoring system using a ceiling-attached microwave antenna," *Medical & Biological Engineering & Computing.,* vol. 44, no. 9, pp. 835–840, 2006.

[7] Y. Xu, J. Chen, S. Dai, et al., "Experimental study of UWB pulse radar for life detection," *Instrumentation, Measurement, Computer, Communication and Control.,* 2011 pp. 729–732.

[8] L. Anitori, A. D. Jong, F. Nennie, "FMCW radar for life-sign detection," *IEEE Radar Conference.,* 2009. pp. 1–6.

[9] D. Zhang, M. Kurata, T. Inaba, "FMCW radar for small displacement detection of vital signal using projection matrix method," *International Journal of Antennas and Propagation.,* 2013, pp. 1–5.

[10] R. S. Mpanda, et al. "Design and evaluation of typical antennas for monitoring vital signs," *Applied Computational Electromagnetics Society journal.,* vol. 34, no. 3, pp. 497-505, Mar. 2019.

[11] D. R. Morgan, M. G. Zierdt, "Novel signal processing techniques for Doppler radar cardiopulmonary sensing," *Signal Processing.,* vol. 89, no. 1, pp. 45–66, 2009.

[12] M. Y. Li, J. Lin, "Wavelet-transform-based data-length-variation technique for fast heart rate detection using 5.8-ghz CW Doppler radar," *IEEE Transactions on Microwave Theory and Techniques.,* vol.66, no. 1, pp. 568–576, 2018.

[13] N. E. Huang, Z. Shen, S. R. Long, et al., "The empirical mode decomposition and the Hilbert spectrum for nonlinear and non-stationary time series analysis," *Proceedings of the Royal Society of London. Series A: Mathematical, Physical and Engineering Sciences.,* vol. 454, no. 1971, pp. 903–995, 1998.

[14] Z. Wu, N. E. Huang, X. Chen, "The multi-dimensional ensemble empirical mode decomposition method," *Advances in Adaptive Data Analysis.,* vol. 1, no. 3, pp. 339–372, 2009.

[15] Z. Wu, N. E. Huang, "Ensemble empirical mode decomposition: a noise-assisted data analysis method," *Advances in adaptive data analysis.,* vol.1, no. 1, pp. 1–41, 2009.

[16] M. E. Torre, M. A. Colominas, et al., "A completeensemble empirical mode decomposition with adaptive noise," *IEEE International Conference on Acoustics, Speech and Signal Processing.,* 2011, pp. 4144–4147.

[17] K. Dragomiretskiy, D. Zosso, "Variational mode decomposition," *IEEE Transactions on Signal Processing.,* vol.62, no. 3, pp. 531–544, 2014.

Ziliang Xia received the B.S. degree from the Xidian University, Xi'an, China, in 2019. He is currently working toward the M.S. degree in electromagnetic field and microwave technology with the same university. His recent research interests are mainly in the design of circuits and algorithms.

Xinhuai Wang received the B.Eng., M.Eng., and Ph.D. degrees from Xidian University, Xi'an, China, in 2004, 2007, and 2011, respectively. Since 2011, he has been with Collaborative Innovation Center of Information Sensing and Understanding, Xidian University and

Science and Technology on Antenna and Microwave Laboratory, Xidian University, as a Lecturer and Associate Professor. He has authored or coauthored more than 60 international and regional refereed journal papers. His recent research interests are mainly in the design of microwave components system.

Dr. Wang is a member of IEEE and a senior member of CIE.

Xin Li was born in 1995. He received the B.S. degree from the Xidian University, Xi'an, China, in 2019. He is currently working toward the M.S. degree in electromagnetic field and microwave technology with the same university. His recent research interests are mainly in the signal processing and the design of circuits.

Yin Xu received the B.Eng., M.Eng., and Ph.D. degrees from Xidian University, Xi'an, China, in 2006, 2009, and 2013, respectively.

She is working at Xidian University as an associate professor.Her recent research interests are mainly in the electromagnetic field and microwave technology.

Simulation of High Frequency Twisted Pair Cable Using DDM-FEM Hybrid Algorithm

S. Khan, Y. Zhao*, Y. Wei, A. Mueed, Z. Ullah, and A. Khan

Department of Electrical and Automation Engineering, Nanjing Normal University, Nanjing 210046, China
engrshumail456@yahoo.com, zhaoyang2@njnu.edu.cn, 61197@njnu.edu.cn, engr.mueed@live.com,
engrzakirullah@yahoo.com, Abubakarkhan92064@gmail.com
*Corresponding author from Nanjing Normal University, Nanjing, China.

***Abstract* –** In this article, an efficient domain decomposition method finite element method (DDM-FEM) algorithm is presented for the lossy twisted pair cable. In harsh environment and anti-interface ability, cables need high toughness, noise immunity, and extraordinary strength. We, in this paper, simulate a physical model of twisted pair cable and apply a hybrid solver of DDM-FEM to analyze these problems by compression and approximation of matrix-vector product. The DDM-FEM solver along with matrix compression is used to compute the *RLCG*, propagation constant in the twisted pair cable, and to reduce the computational time and memory size. Therefore, in the proposed algorithm, the complexities of the system become linear. The study compares the calculated results with the existing standard to verify the effectiveness of the proposed algorithm.

***Index Terms* –** Domain decomposition method (DDM), finite element method (FEM), hybrid solver, propagation constant, *RLCG* parameter, twisted pair cable.

I. INTRODUCTION

With the advancement of technology, means of data and information transfer is improving day by day. To ensure maximum and reliable data, communication signals need a secure way to transfer data with minimum interface. This can be achieved through twisted pair cable, coaxial cable, and optical fiber cable, which are developed to bear higher frequency signal with minimum interface.

Twisted pair cable has been used for a long time due to its high toughness, good noise immunity, and high strength. Twisted pair cables are usually used in harsh environment due to robustness and anti-interface ability to conduct noise. Over the years, twisted pair cables have been used with different frequencies ranging from 16 MHz to 1.8 GHz [1–3]. Our focus in this paper is to further increase the frequency to 5 GHz in shielded category of twisted pair cables, which will reduce propagation loss. To evaluate the performance, we analyze the primary (electrical) and secondary parameters in this paper. Resistance (R), inductance (L), capacitance (C), and conductance (G) matrices give the electrical parameters. Similarly, secondary parameters are propagation constant (δ), attenuation constant (α), phase constant (β), characteristic impedance (z_0), scattering parameter (s) and permeability constant of free space Epsilon (ε_0) [4–7].

To compute the electrical and secondary parameter of twisted pair cable, different numerical techniques are used such as method moment [8], frequency domain and time domain (FDTD) techniques [9, 10], advanced modeling (AM) techniques [11], domain decomposition method (DDM) [12], and traditional finite element method (FEM) approach [13].

Among the above-mentioned techniques, the DDM decomposes the domain into subdomains and then create a mesh to solve each of these subdomains separately. On the other hand, FEM uses triangular mesh method to solve inhomogeneous structure effectively and efficiently. We thus combine the two methods (FEM and DDM) to first divide given structure subdomains and then apply FEM method to solve for each subdomain. This way, we exploit the advantages of both the methods to reduce the propagation loss.

Parallel computing system requires a much smaller amount of computation memory than the conventional FEM for structure, which is bent or twisted. DDM represents a large potential for parallelization of the FEMs. It also serves as a basis for distributed, parallel computations with high performance (over 90%) which is achieved even in a large-scale finite element calculation with irregular domain decomposition [14, 15].

This article is structured as follows. In Section II, the mathematical equations of twisted pair cable performance parameters are described. In Sections III and IV, DDM and FEM implementation are described, respectively. In Section V, numerical simulation using

Submitted On: July 27, 2021
Accepted On: October 18, 2021

https://doi.org/10.13052/2022.ACES.J.370113

proposed algorithm and validation result are presented. Finally, Section VI concludes the work.

II. SHIELDED TWISTED PAIR CABLE

Shielded twisted pair (STP) cable is a type of guided transmission medium, which consists of individual pair of wires, each having two conductor wires twisted together in a regular spiral pattern. Individual pair or collection of pair are shielded with foil or braided wire to reduce the electromagnetic (EM) interference. The shield further connects to ground reference, which protects the induced current to wire and attenuates the EM wave for external shielding. The propagation matrix (γ) for the STP cable is given as

$$\gamma=\alpha+j\beta, \tag{1}$$

where α is the attenuation constant and β is the phase constant and both are in matrix form. We can also write it as

$$\gamma=K_1 f\sqrt{\left(\frac{RG}{K_1{}^2 f^2}\right)-LC+\frac{J}{K_1 f}(RC+LG)}, \tag{2}$$

where $K_1 = 2\pi$ and R, L, C, and G are the electrical parameter of twisted pair (STP) cable and are given as

$$R=K_2\frac{R_1 D}{d\sqrt{D^2-d^2}}, \tag{3}$$

$$L=K_3 U_r \cos h^{-1}\left(\frac{D}{d}\right), \tag{4}$$

$$G=\pi\sigma_d \sec h^{-1}\left(\frac{D}{d}\right), \tag{5}$$

$$C=K_4\varepsilon_r \sec h^{-1}\left(\frac{D}{d}\right), \tag{6}$$

where D is the distance between the center of two conductor cables for multi-twist, d is the diameter of each conductor, and R_1 is the surface resistance of conductor and is given as ($R_1=R_k f^{\frac{1}{2}}$), where R_k is constant and its value is 2.16×10^{-7}. Here, σ is the conductivity of the conductor material, and δ is skin depth. The conductivity of the dielectric can be given as ($\sigma_d=\omega\varepsilon= 2\pi f\varepsilon$). The other constants are: $K_2 = 2/\pi$, $K_3 = 2 \times 10^{-7}$, and $K_4 = \pi \times 8.85 \times 10^{-12}$.

Comparing eqn (1) and (2) of propagation constant, we can find the attenuation and phase constant, where the real part is attenuation and the imaginary part is phase constant described as

$$\alpha=K_1 f\sqrt{\left[\frac{RG}{K_1^2 f^2}-LC\right]}. \tag{7}$$

If t is the thickness of the dielectric, then the ratio of $\frac{D}{d}=\frac{2t}{d}+1$ and the attenuation constant in dB is given as

$$\alpha = 2\pi f^{\frac{7}{4}}\left\{\sqrt{\frac{26.13\times\varepsilon \sec h^{-1}(\frac{2t}{d}+1)}{d\sqrt{D^2-d^2}}}\right\}- 2\pi f\{\sqrt{5.56\times10^{-18}\mu_r\varepsilon_r}\}, \tag{8}$$

where

$$\alpha_1= 8.686\sqrt{\frac{4.16\times10^{-7}\varepsilon \sec h^{-1}(\frac{2t}{d}+1)}{d\sqrt{D^2-d^2}}}, \tag{9}$$

and

$$\alpha_2= 8.686\sqrt{5.56\times10^{-18}u_r\varepsilon_r}\,. \tag{10}$$

Eqn (8) will become

$$A= 2\pi f^{\frac{7}{4}}\alpha_1-2\pi f\alpha_2. \tag{11}$$

From the imaginary part of eqn (2), phase constant of the cable can be found as

$$\beta=K_1 f\sqrt{\frac{\mathrm{J}}{K1f}(RC+LG)}. \tag{12}$$

Let us assume

$$\beta_1=f^{-\frac{1}{2}}\sqrt{\frac{15D\varepsilon_r \sec h^{-1}(\frac{2t}{d}+1)}{d\sqrt{D^2-d^2}}}, \tag{13}$$

and

$$\beta_2=\sqrt{6.28\times10^{-7}u_r\varepsilon}. \tag{14}$$

Hence, eqn (12) will become

$$\beta = f^{-\frac{1}{2}}\beta_1+ f^{-1}\beta_2. \tag{15}$$

A. Propagation constant of STP cable

STP cable propagation constant can be found by putting the value of eqn (11) and (15) in eqn (1), resulting in the propagation constant as

$$\gamma = 2\pi f^{\frac{7}{4}}\alpha_1 + jf^{-\frac{1}{2}}\beta_1 - 2\pi f\alpha_2 + jf^{-1}\beta_2. \tag{16}$$

III. DOMAIN DECOMPOSITION METHOD

DDM is applied to solve, which solves the boundary value problem (BVP) by decomposing the domain to subdomain. The domain contains the information about the proposed model. Each domain has different configuration of material as well as geometry. The subdomains are further divided which make the partitions even smaller. These subdomains are easily solvable by the DDM. The domain contains the information locally; so it is convenient to solve the performance parameters. As they accelerate the solution to convergence point. Due to the locally connected domain, the performance parameters are calculated speedily. It also decreases the memory size and CPU time.

If we consider decomposition on the domain of S belong to $\mathbb{R}^3$ ($S \subset \mathbb{R}^3$), S is decomposed into two subdomains (S_1 and S_2). The subdomains (S_1 and S_2) have different material properties than domain S. Excitation of the problem may be discreet or fast or both of them.

In this manuscript, the grid-based approach for matching algorithms of DDM. The grid-based approach is used for defining the subdomain. A domain is divided into subdomains and artificial boundaries known as "interface". It means that each subdomain is independently solved. To get proper solution, the appropriate boundary condition must be given on the interface of

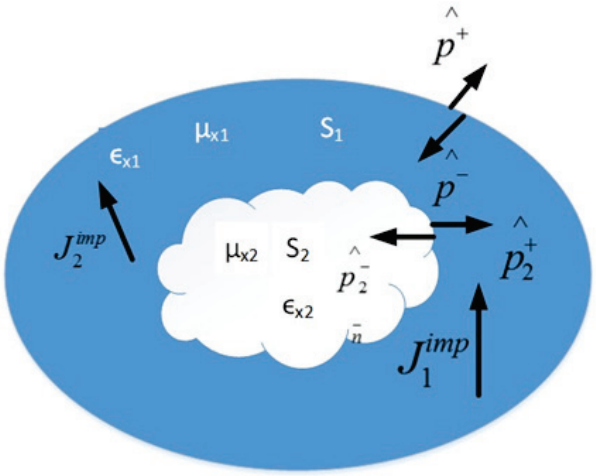

Fig. 1. Domain S with boundary value problem.

subdomains. The DDM based on natural boundary conditions reduces the approximation under the matching condition. We use the grid-based approach for matching purpose. To obtain the accuracy of the solution, it is necessary to use high refinements of the finite element grids near the concave vertices. So the solution is improved by using the grid approach near the concave vertex. Therefore, the solution offers good approximation by using the grid matching approach.

As shown in Figure 1, the domain S is divided into subdomains (S_1 and S_2). The shape of subdomain S_1 has the same geometrical shape as that of domain S, but the shape of subdomain S_2 has a different geometrical shape from domain S, having no geometrical information.

The same material as $\frac{S}{S_2}$ is meshed in subdomains S_1 and S_2 separately. The surface subdomain, initially decomposed BVPs are without connection between them. Moreover, for subdomain S_1 is given as follows:

$$\pi^+ \times (\mu_{x1}\nabla \times E_1) - jk\frac{1}{\eta_{x1}}\pi_t(E_1) = \pi^+ \times \left(\frac{1}{\mu_{x1}}\nabla \times E_1^{\text{inc}}\right) - jk\frac{1}{\eta_{x1}}\pi_t\left(E_1^{\text{inc}}\right), \text{ on } \partial S_1. \tag{17}$$

For S_2

$$\begin{aligned} &\nabla \times \frac{1}{\mu_{x2}}\nabla \times E_2 - k^2\varepsilon_{x2}E_2 = -jk\eta j_2^{\text{imp}}, \text{ in } S_2 \\ &\pi(E_2) = 0, \text{ on } \Gamma_{\text{PEC}} \\ &\left[\left[\frac{1}{\mu_{x2}} \times E_2\right]\right]_x = -jk\eta j^{\text{port}}, \text{ on } \Gamma_{\text{port}} \end{aligned} \tag{18}$$

Intrinsic impedance η for free space, ε_{xi} and μ_{xi} are the relative permittivity and permeability of material in S_i, $\eta_{xi} = \sqrt{\mu_{xi}/\varepsilon_{xi}}$ express the relative wave impedance, $i\varepsilon\{1,2\}$. Moreover, the tangential element trace operator $\pi_t(.)$ and twist tangential trace operator $\pi_\times(.)$ are adopted in our analysis, defined as

$$\pi_t(\mu) := \hat{p} \times \mu \times \hat{p}, \tag{19}$$

$$\pi_\times^{\pm}(\mu) := \hat{p}^{\pm} \times \mu, \tag{20}$$

where $\hat{p}^+$ and $\hat{p}^-$ are the unit outward and inward normal to domain S_i and subdomain (S_1 and S_2), respectively. $[[\mu]]_\times$ refers to the field jump across a surface

$$[\![\mu]\!]_\times := \pi_\times^+(\mu^+) + \pi_\times^-(\mu^-). \tag{21}$$

In eqn (18), Γ_{PEC} expresses the collection of PEC surface where the tangential component of electric field finishes. Γ_{Port} expresses the surface of internal port on which a specific current density ι^{port} exists. If (curl; S_i) is the proper space E_i, the normal curl conforming function space is

$$H(\text{curl};\, S_i) = \left\{ \frac{u\varepsilon\left(L^2(S_i)\right)^3}{\nabla} \times u\varepsilon\left(L^2(S_i)\right)^3 \right\}. \tag{22}$$

Contribute to the progress of the volume and surface time product as $(u,v)_S = \int_S u.vdV$ and $(u,v)_{\partial S} = \int_{\partial S} u.vdA$, respectively.

The information sent and received are between the subdomains S_1 and S_2. It includes transfer of information or data in two directions, i.e., from S_1 to S_2 and from S_2 to S_1.

A. Coupling from S_1 to S_2

As ∂S_2 is the field continuity between subdomains S_1 and S_2, it will be observed and applied through the Robin transmission condition on ∂S_2 as

$$k j_2^{(n)} - \frac{jk}{\overline{\eta}_x}\pi_t\left(E_2^{(n)}\right) = \pi_\times^+\left(\frac{1}{\mu_{x1}}\nabla \times E_1^{(n)}\right) - \frac{jk}{\overline{\eta}_x}\pi_t\left(E_1^{(n)}\right). \tag{23}$$

Here, the $\overline{\eta}_x = \sqrt{(\mu_{x1}+\mu_{x2})/(\varepsilon_{x1}+\varepsilon_{x2})}$.

As the j_2 expresses the auxiliary variable, the surface electric current on ∂s_2, so

$$j_2 = \frac{1}{k}\pi_\times^+\left(\frac{1}{\mu_{x2}}\nabla \times E_2\right).$$

As $v_2\varepsilon H^{-\frac{1}{2}}(\text{curl}_t;\, \partial s_2)$ and obtained below as

$$\left\langle \pi_2(v_2), kj_2^{(n)} - jk\frac{1}{\overline{\eta}_x}\pi_x(E_2^{(n)}) \right\rangle_{\partial s_2} = \left\langle \pi_t(v_2), \pi_\times^+\left(\frac{1}{\mu_{x1}}\nabla \times E_1^{(n)}\right) - jk\frac{1}{\overline{\eta}_x}\pi_x(E_1^{(n)}) \right\rangle_{\partial s_2}. \tag{24}$$

B. Coupling from S_2 to S_1

Transmission of information from S_2 to S_1 requires polarization of subdomain S_1, which will also depict the material difference, and the use of surface domain current to justify surface subdomain. This embedded subdomain contains the data of material properties.

C. Material difference

As for the solution of BVP surface subdomain S_2, E_2 and H_2 are the electric and magnetic fields. We apply $j\omega(\varepsilon_2-\varepsilon_1)$ and $j\omega(\mu_2-\mu_1)H_2$ into the Maxwell equation of surface subdomain S_1 as

$$\nabla\times E_1=-j\omega\mu_1 H_1-j\omega(\mu_2-\mu_1)H_2, \tag{25}$$

$$\nabla\times H_1=-j\omega\varepsilon_1 E_1+j\omega(\varepsilon_2-\varepsilon_1)E_2+j_1^{\text{imp}}. \tag{26}$$

The above two equations (25) and (26) are the electric and magnetic polarizations due to change of material properties from ε_{x1}, μ_{x1} to ε_{x2}, μ_{x2}. Moreover, subdomain surface S_1 and vector wave equation are improved by combining eqn (25) and (26) as

$$\nabla\times\frac{1}{\mu_{x1}}\nabla\times E_1^{(n)}-k^2\varepsilon_{x1}E_1^{(n)}=-jk\eta\, j_1{}^{\text{imp}}+ L_v^{(n-1)}+M_v^{(n-1)}. \tag{27}$$

L_v and M_v are two volume sources as

$$L_v^{(n-1)}=-k^2(\varepsilon_2-\varepsilon_1)E_2{}^{(n-1)}, \tag{28}$$

$$M_v^{(n-1)}=\nabla\times\left(\frac{1}{\mu_{x1}}-\frac{1}{\mu_{x2}}\right)\nabla\times E_2{}^{(n-1)}. \tag{29}$$

Eqn (27) with $v_1\varepsilon H\,(curl;\ S_1)$;so

$$\left(\nabla\times v_1,\frac{1}{\mu_{x1}}\nabla\times E_1{}^{(n-1)}\right)_{S_1}-k\left(v_1,\varepsilon_{x1},E_1{}^{(n)}\right)_{S_1}+ k\left\langle\pi_t(v_1),j_1^{(n)}\right\rangle_{\partial s_1}=-jk\eta\left(v_1,j_1^{(\text{imp})}\right)_{S_1}+ \left(v_1,L_v^{(n-1)}\right)_{S_2}+\left(v_1,G_v^{(n-1)}\right)_{S_2}. \tag{30}$$

Therefore, at the $(n-1)$th iteration, we make $L_v^{(n-1)}$ and $G_v^{(n-1)}$ based on the simulation result of surface subdomain S_2. This will be applied on subdivided surface subdomain S_1 for the local FEM simulation at the nth iteration.

IV. FINITE ELEMENT METHOD IMPLEMENTATION

As discussed in Section III.B.I, full discrete embedded system DDM will make matrix equation by applying Galerkin testings as

$$\begin{pmatrix}B_1 & -D_{12}\\ -D_{21} & B_2\end{pmatrix}\begin{pmatrix}x_1^{(n)}\\ x_2^{n}\end{pmatrix}=\begin{pmatrix}b_1^{(n)}\\ b_2^{(n)}\end{pmatrix}. \tag{31}$$

Here, x_i is the solution vector coefficient of the basic functions in S_i, and b_i is the excitation vector. B_1 and B_2 are the block matrices that stand for the FEM matrices of subdivided surfaces' area S_1 and S_2. D_{12} and D_{21} are off-diagonal matrices used as coupling between subdivided surface areas S_1 and S_2.

Here, we will use to mesh triangular/tetrahedral the subdivided surface area S_2.

However, the Gaussian quadrature integration is used to solve discrete system in eqn (31). Gaussian Seidel matrix symmetric block is used for preconditioner system as

$$P^{-1}Bx^{(n)}=P^{-1}b^{(n)}, \tag{32}$$

$$P=\begin{pmatrix}B_1 & 0\\ -D_{21} & B_2\end{pmatrix}\begin{pmatrix}B_1^{-1} & 0\\ 0 & B_2^{-1}\end{pmatrix}\begin{pmatrix}B_1 & -D_{12}\\ 0 & B_2\end{pmatrix}. \tag{33}$$

Preconditioner needs inversion of subdivided matrices B_1 and B_2. By using the multifrontal solution process [16, 17], we can factorize the subdomain matrices.

Moreover, embedded DDM has many advantages; it can discretize one domain into subdomains. Therefore, we can make embedded mesh of complicated geometries by dividing them into too many small subdomains, from which we get good quality of mesh. The small subdomain meshes and matrix assembly are independent. Therefore, if we want to move subdivided area S_2 with respect to S_1, only the matrices D_{12} and D_{21} in eqn (31) need to be re-calculated. As DDM subdomain needs to be recomputed by modifying or adding other subdomains. This will help us in EM modeling, designing, and in solving practical problems.

V. NUMERICAL SIMULATION USING PROPOSED ALGORITHM

In this section, we discuss numerical simulations of shield twisted pair cable to evaluate the electrical parameter (*RLCG*) and secondary parameter (propagation constant). Therefore, the shield multi-twisted pair cable(s) are chosen for research work. The shield twisted pair conductors are composed of seven pairs cable model as shown in Figure 2.

In overlapping DDMs, the subdomains overlap by more than one interface. Overlapping DDMs include the Schwarz alternating method and the additive Schwarz method.

The simulation frequency is 5 GHz, and the step size is 451. The convergence criteria of maximum delta are 0.02, and the number of passes for the convergence of solution is 10.

A. RLCG constant based on DDM-FEM algorithm

In this section, comparison among different methods regarding efficiency and strength of proposed algorithm

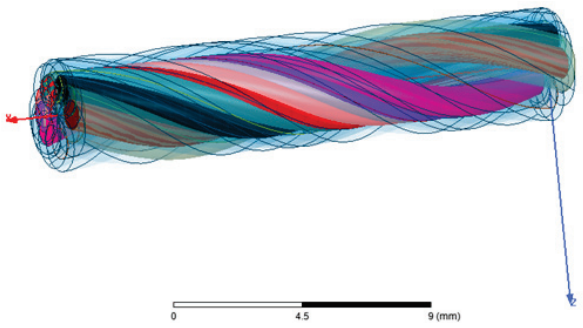

Fig. 2. Study model of twisted pair cables.

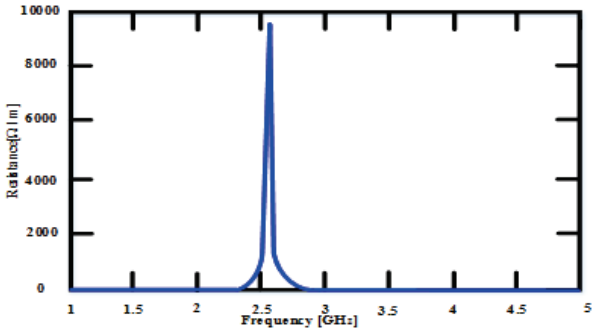

Fig. 3. Resistance of twisted pair.

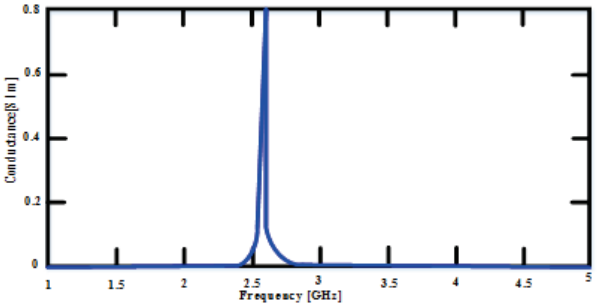

Fig. 4. Conductance of twisted pair.

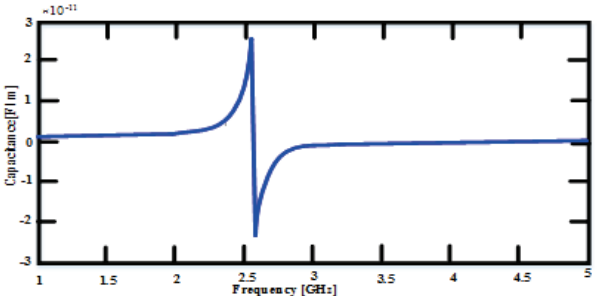

Fig. 5. Capacitance of twisted pair.

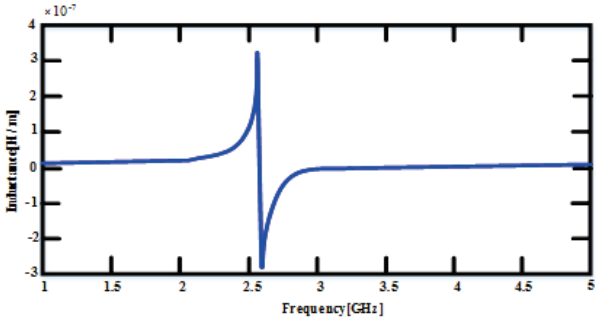

Fig. 6. Inductance of twisted pair cable.

is checked. Here, all simulation results are taken from ANSYS EM environment and MATLAB. The suggested method is used to determine the twisted cable effect in the test example. All the conductors are discretized into triangular and tetrahedral structure with refined mesh. The matrix is reduced up to 1:29%, by the DDM-FEM. The minimum residuals for the tolerance are 1 e^{06}.

Using the proposed algorithm, the twisted pair level effect and multi-layer effect are estimated. The DDM-FEM algorithm is suitable for calculating the *RLCG* parameter using different iterations. Based on the result, mutual capacitance and mutual inductance are calculated by the DDM-FEM approach. The mutual capacitance and inductance (impedance) are shown in Figures 5 and 6.

Initially, the resistance is zero at $1-2.5$ GHz, but as the frequency increases from 2.5 GHz, the resistance also increases. It shoots up to 1000 Ω/m and becomes 0 Ω/m again at 2.7 GHz. Moreover, as it is shown in Figure 3 that further increase in the frequency up to 5 GHz is not showing any deviation in the resistance. In addition, this is same for conductance as well as shown in Figure 4.

As shown in Figures 5 and 6, the shape of the graph is almost same for inductance and capacitance. Initially, at zero frequency, we have some residual inductance and capacitance, but as the frequency increases up to 2.3 GHz, its values gradually increase and reach its peak of inductance and capacitance value and then abruptly decrease the inductance to -3 H/m and capacitance -2.9 F/m at frequency of 2.6 GHz. As the frequency increases more, the inductance and capacitance also increase and reach up to inductance and capacitance of -1.5 H/m and -1.5 F/m.

At 3 GHz up to 5 GHz, the inductance and capacitance are at steady state.

B. Propagation constant based on hybrid algorithm

In this subsection, the propagation matrix and attenuation matrix of the twisted pair cable are estimated. The characteristic parameters of twisted pair model are shown in Table 1.

Table 1 describes the model of twisted pair cable. The number of adaptive passes and significant value of delta can be adjusted for the convergence of solution.

Table 1: Characteristics of twisted pair

Radius	**0.28**
No of twisted (under test)	1
Total number of twisted pair	7
Material	Copper
Dielectric	Polyester
No of adaptive passes	10
Frequency	5 GHz

Table 2: Computational memory of twisted pair cable

No of unknown	Memory (MBs)	No of adaptive passes
349,722	30.103	1
428,992	32.337	2
428,992	31.200	3
545,330	42.343	4

Table 3: Computational time of twisted pair cable

No of unknown	CPU time (matrix assembly)	No. of adaptive passes
349,722	00:00:06	1
428,992	00:00:08	2
428,992	00:00:08	3
545,330	00:00:10	4

Table 2 and 3 describe the memory and time computation of twisted pair cable. This information gives the real and imaginary values to analyze the propagation constant and attenuation constant using FEM-DDM. To verify the algorithm result, comparison takes place with the numerical analysis techniques using FEM [18]. ANSYS environment models and compared the result. Figure 7 shows the comparison of propagation loss. The *X*-axis represents the propagation loss and *Y*-axis represents the frequency in GHz and normalized values. Figure 8 shows the simulation of phase constant. Here, FEM-DDM results are adequate with respect to FEM results as shown in Figures 7 and 8.

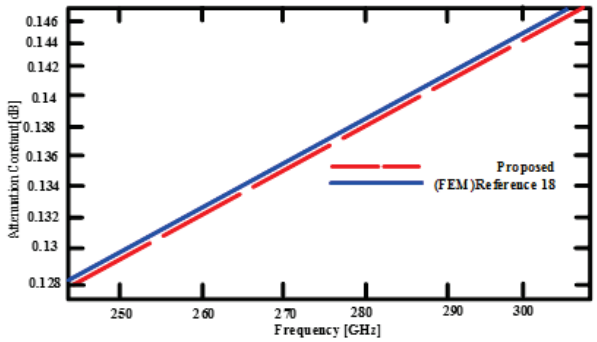

Fig. 7. Attenuation constant of twisted pair cable.

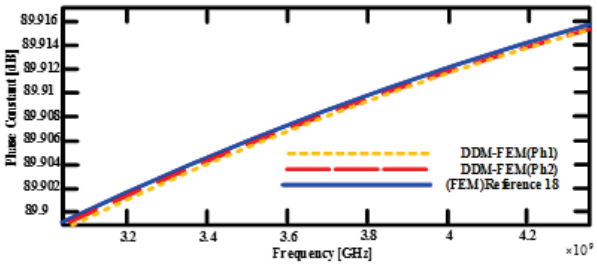

Fig. 8. Phase constant of twisted pair cable.

VI. CONCLUSION

In this article, the DDM-FEM algorithm calculates the *RLCG* parameters and propagation loss of STP cable. The versatile nature of FEM with integral equation solver gives good approximation of *RLCG* matrix and propagation matrix. The computing efficiency parameter of the STP cable is estimated through the DDM-FEM algorithm and offers less computational time and memory than the traditional method. The approximation is 1:85% than matrix transmission line theory.

ACKNOWLEDGMENT

National Natural Science Foundation of China under Grant 52107005 and "Open Fund Project of State Key Laboratory of Power Grid Environmental Protection (GYW51202001558)" supported the paper.

REFERENCES

[1] S. Abdolhamid, M. Rubinstein, A. Rubinstein, C. Romero, N. Mora, and F. Rachidi, "Application of the cascaded transmission line theory of Paul and McKnight to the evaluation of NEXT and FEXT in twisted wire pair bundles," *IEEE transactions on electromagnetic compatibility*, vol. 55, no. 4, pp. 648-656, 2013.

[2] A. Mueed, Y. Zhao, Y. Wei, Z. B. Zhu, and Q. L. Liu, "Analysis of lossy multiconductor transmission lines (MTL) using adaptive cross approximation (ACA)," *Applied Computational Electromagnetics Society Journal*, vol. 34, no. 11, 2019.

[3] H. Ali Mohajer, G.-J. Stockman, Y. Lefevre, V. Ginis, and W. Coomans, "Calculating millimeter-wave modes of copper twisted-pair cables using transformation optics," *IEEE Access*, vol. 9, pp. 52079-52088, 2021.

[4] A. Mueed, Y. Zhao, W. Yan, S. Khan, Q. Q. Liu, and C. Huang, "Skin effect and proximity effect analysis of stranded conductor based on mixed order MoM with adaptive cross approximation algorithm," *Engineering Analysis with Boundary Elements*, vol. 120, pp. 52-58, 2020.

[5] J. E. Schutt-Ainé, "High-frequency characterization of twisted-pair cables," *IEEE Transactions on Communications*, vol. 49, no. 4, pp. 598-601, 2001.

[6] M. Yamamura, Y. Kami, K. Murano, and F. Xiao, "Analysis of transmission characteristics for twisted pair cables using the RLGC parameters of the cable," Asia-Pacific Symposium on Electromagnetic Compatibility (APEMC), Taipei, pp. 720-723, 2015.

[7] C. Yang, W. Yan, Y. Zhao, Y. Chen, C. Zhu, and Z. Zhu, "Analysis on RLCG parameter matrix extraction for multi-core twisted cable based on back propagation neural network algorithm," in *IEEE Access*, vol. 7, pp. 126315-126322, 2019.

[8] D.A. Weston, Electromagnetic Compatibility: Methods, Analysis, Circuits, and Measurement, Third Edition (3rd ed.). Crc Press. 2016.

[9] Y. Yan, L. Meng, X. Liu, T. Jiang, J. Chen, and G. Zhang, "An FDTD method for the transient terminal response of twisted-wire pairs illuminated by an external electromagnetic field," in *IEEE Transactions on Electromagnetic Compatibility*, vol. 60, no. 2, pp. 435-443, Apr. 2018.

[10] Q. Q. Liu, Y. Zhao, C. Huang, W. Yan, and J. M. Zhou, "A new method for stranded cable crosstalk estimation based on BAS-BP neural network algorithm combined with FDTD method," *Applied Computational Electromagnetics Society Journal*, vol. 35, no. 2, Feb. 2020.

[11] C. Jullien, P. Besnier, M. Dunand, and I. Junqua, "Advanced modeling of crosstalk between an unshielded twisted pair cable and an unshielded wire above a ground plane," in *IEEE Transactions on Electromagnetic Compatibility*, vol. 55, no. 1, pp. 183-194, Feb. 2013.

[12] I. Hänninen, F. Wolfheimer, A. Barchanski, and D. Kostka, "High performance computing techniques for efficient 3D full-wave simulation of EMC problems," *International Symposium on Electromagnetic Compatibility*, Tokyo, Tokyo, pp. 828-831, 2014.

[13] C. Buccella, M. Feliziani, and G. Manzi, "Three-dimensional FEM approach to model twisted wire pair cables," in *IEEE Transactions on Magnetics*, vol. 43, no. 4, pp. 1373-1376, Apr. 2007.

[14] A. Amor-Martin, L. E. Garcia-Castillo, and J. F. Lee, "Study of accuracy of a non-conformal finite element domain decomposition method," *Journal of Computational Physics*, vol. 429, p. 109989, Mar. 2021.

[15] S. Yizhong, W. Sun, and H. Zheng, "Domain decomposition method for the fully-mixed Stokes–Darcy coupled problem," *Computer Methods in Applied Mechanics and Engineering*, vol. 374, p. 113578, Feb. 2021.

[16] E. Lundquist, S. Wu, C. Furse, and B. Jones. "Aging wire fault diagnosis using faster, higher-precision methods," In The 2011 Aircraft Airworthiness and Sustainment Conference, 2011.

[17] P. R. Amestoy, I. S. Duff, J.-Y. L'Excellent, and J. Koster, "A fully asynchronous multifrontal solver using distributed dynamic scheduling," *SIAM Journal on Matrix Analysis and Applications*, vol. 23, no. 1, pp. 15-41, 2001.

[18] M. M. Al-Asadi, A. P. Duffy, K. G. Hodge, and A. J. Willis, "Twisted pair cable design analysis and simulation," In 49th IWCS conference, Atlantic City, NJ, USA, pp. 13-16. 2000.

Shumail Khan received the B.E. degree from CECOS University, Peshawar, Pakistan, in 2005-2010 and the master's degree from Southeast University, Nanjing China, in 2015-2017.

He then worked as an Assistant Plant Engineer with Hydral Power station Malkand-III, his Dargi Pakistan in 2011-2015. He is currently a Ph.D. Research Scholar with Nanjing Normal University, Nanjing, China, under the supervision of Prof. Zhao Yang. His research interests include electromagnetic compatibility problems, computational electromagnetics, transient analysis, and crosstalk issues.

Zhao Yang received the B.E., M.E., and Ph.D. degrees in power electronic technology from the Nanjing University of Aeronautics and Astronautics, Nanjing, China, in 1989, 1992, and 1995, respectively.

He is currently a Professor with Nanjing Normal University, Nanjing, China. His research interests are in the areas of electromagnetic compatibility, power electronics, and automotive electronics.

Yan Wei received the M.S. degree in electrical engineering and the Ph.D. degree in physics and electronics from Nanjing Normal University, Nanjing, China, in 2011 and 2014, respectively.

Since 2014, he has been with the Jiangsu Electrical Equipment EMC Engineering Laboratory, Nanjing Normal University, where he is presently working as an Associate Professor. His current research interests include integrated circuit electromagnetic compatibility testing, bioelectromagnetic technology, and automotive electromagnetic compatibility design.

Abdul Mueed received the master's degree in electrical engineering from the University of Engineering and Technology, Taxila, Pakistan, in 2015.

From 2009 to 2017, he worked as a Lecturer in Electrical Engineering with the Dr A Q Khan Institute of Technology, Mianwali, Pakistan. He is currently working as a Research Scholar with Nanjing Normal University, Nanjing, China. His primary research interests include the electromagnetic compatibility problems, computational electromagnetic techniques, artificial intelligence application in EMC, and EMC-related issues in biomedical.

Eddy Current Microsensor Dedicated to the Nondestructive Testing of Conductive Plates

Chifaa Aber[1], Azzedine Hamid[2], Mokhtar Elchikh[1], and Tierry Lebey[3]

[1]Physical Engineering Department, Applied Power Electronics Laboratory,
University of Science and Technology USTO-MB, Oran 31000, Algeria
aber_ch@hotmail.com, m.elchikh@gmail.com

[2]Department of Electrical Engineering,
University of Science and Technology USTO-MB, Oran 31000, Algeria
hamidazdean@yahoo.fr

[3]Laplace Laboratory,
University of Paul Sabatier, Toulouse Cedex 9, France
thierry.lebey@laplace.univ-tlse.fr

Abstract **–** To ensure the safety of transportation and prevent accidents, nondestructive testing by Eddy current (EC) is proposed to check the conditions of industrial parts. EC sensors are used for the inspection of defects in conductive parts using coil fed by alternative current. These sensors are sensitive to defects, easy to implement, and robust for industrial applications. In order to satisfy the requirement for both reliability and speed during inspection operations, innovative EC sensors that can provide higher sensitivity, better spatial resolution, and more information about the defect characteristics, such as microsensors, are developed. The miniaturization of these sensors' coils conforms the sensor for micro-defects in critical parts and in complex materials. In this paper, a microsensor dedicated to EC application is studied and characterized to identify the coil parameters and to optimize the geometry of the probe. An approach for the modeling of microsensor dedicated to EC nondestructive applications is proposed. The moving band finite element method is implemented for this purpose to take into account the movement of the sensor and to simplify the modeling of EC testing configurations that use this kind of sensor. Experimental validations were conducted on a nickel-based alloy specimen. The real and imaginary parts of the impedance at every position of the sensor computed by experiments and simulations were consistent with each other. Simulation results proved that the sensor was capable of detecting micro-defects with a size starting from 0.1 mm under the optimal excitation frequency of 0.8 MHz. It is not only sensitive to micro-cracks, but also it distinguishes the different crack sizes (length, width, and depth).

Keywords **–** Defect inspection, Eddy current (EC), finite element method (FEM), microsensor, moving band method, NDT.

I. INTRODUCTION

Most of the failures observed in industrial installations are associated with failure by the propagation of cracks initiated in areas of mechanical field concentration as in the case of bogie systems in the railways or areas under cyclic and thermal loads as in the case of the engine blades in the aircraft which affect directly the transport operation and cause dramatical accidents.

Failures and defects can not only be always observed; while the crack is small enough, the structure can keep working despite its "illness." Nondestructive evaluation (NDE) systems have been proposed and developed against this background to ensure safety and prevent accidents [1–5]. NDE is, above all, a tool for quality and reliability control. Their aim is to check the condition of industrial parts without the corresponding examinations being able to affect their future use.

Condition-based maintenance (CBM) is a maintenance strategy based on information and evaluation status given by the NDE devices [6–9]. The detection of micro-cracks or initiators of rupture can prevent not only material disasters but also loss of human life and eliminate failure within the embryonic stage.

Eddy current (EC) sensors are widely used for the nondestructive inspection of electrically conducting materials [10–14]. The investigation is done by scanning the conductive plate with a coil fed by a time-harmonic source current and then measuring the impedance variation of the same coil or another one. These sensors

Submitted On: July 15, 2021
Accepted On: December 13, 2021

https://doi.org/10.13052/2022.ACES.J.370114

are sensitive to defects such as fatigue cracks, inclusions, or corrosion, and they are also easy to implement and robust for industrial applications. However, the increasing need for both reliability and speed during inspection operations requires developing innovative EC sensors that can provide higher sensitivity, better spatial resolution, and more information about the defect characteristics, such as the microsensors [15–17]. The miniaturization of these sensors' coils allows integrating multi-coil systems on a single substrate [18–22]. Furthermore, it enhances the magnetic coupling by reducing the lift-off (the distance between the coil and the conductive specimen) [23–25].

In the context of Eddy current nondestructive testing (ECNDT), it is interesting to use modeling, looking for a model that reacts similarly to the component we are studying [26–31]. This model will make it possible to deduce the desired results. Modeling involves creating a mathematical representation of a real problem using certain assumptions. This representation allows users to predict the behavior of the studied systems. The modeling tools allow the design of sensors and the prediction of their behavior without actual realization. These tools have consequences on the development of production tools, making it possible to reduce the cost of the experimental phase.

The finite element method (FEM) is well appreciated for its versatility [32–37]. However, the micro-coil turn dimensions are characterized by their low thickness compared to the other dimensions of the modeled system; also the minimization of the lift-off thickness is necessary to obtain the best control performance in the ECNDT. The mesh of fine media can lead with the FEM to convergence problems and possibly a poor solution.

The originality of this paper lies in the implementation of an FEM approach that yields an efficiency to model the 3D microsensor, taking into account the presence of thin geometrical domains (the micro-coil and the lift-off) without degrading the mesh quality. Moreover, the coil displacement in the 3D plane can be taken into account without remeshing all the domains in each displacement. For this purpose, the moving band method is used. This method leads to optimal storage and ensures fast convergence of the system.

The paper is organized as follows. In Section I, the design of the sensor's elements as well as the simplified geometry are introduced. In Section II, the sensor is characterized and optimized. Section III reviews the geometry of the problem and the motion band method. Section IV describes the dual formulation implemented for the EC microsensor. The results for impedance variations calculated by the FEM model are presented in Section V, where three applications are studied and discussed. The first test case is an ECT configuration where the probe consists of a micro-coil. The results for impedance variations calculated by the FEM model are compared to the reference model (experimental results) to show the applicability of the modeled sensor. The second test case shows the influence of lift-off on the coil impedance variations. The third test case study the crack size effect on the EC signal which enables us to identify the sensitivity of the ECNDT device.

II. CONCEPTION

The proposed sensor consists, in fact, of a square flat coil, distributed over a total thickness of 1.25 mm. The length of the side is c = 2.6 mm, the width of tracks ℓ_p = 100 μm, and the thickness e_p = 25 μm. The coil features five turns distributed over its entire surface with a spacing of e = 100 μm. Figure 1 shows a schematic view of the coil used in our application. This geometry gives the coil the highest inductance value and it is favorable in several points (Section III).

III. SENSOR CHARACTERIZATION

A. Geometrical characterization

It is interesting for the characterization to calculate the two geometrical quantities, which are the developed length of the wire and the effective total surface. The developed length or the total wire length l_{tot} can be calculated by the following formula:

$$l_{\text{tot}} = \sum_{i=0}^{n-1} 4\,(c - (e + l_p)i). \tag{1}$$

The total effective surface S_{tot}, which is the equivalent surface of all the turns, is given by

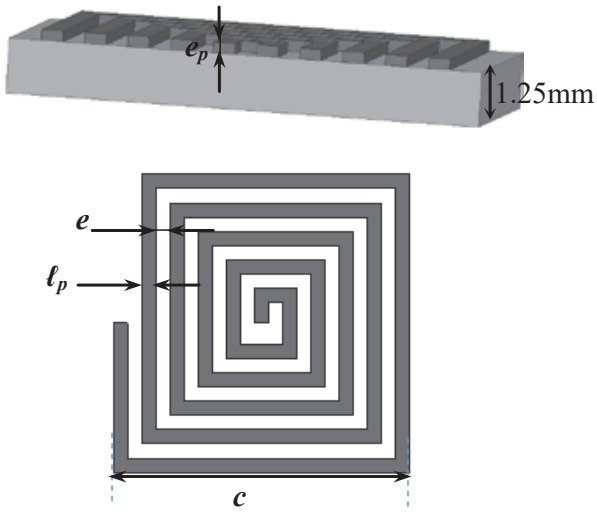

Fig. 1. Schematic view of the sensor.

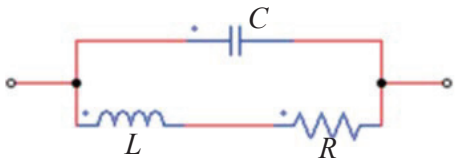

Fig. 2. Electrical model of the coil.

$$S_{\text{tot}} = \sum_{i=0}^{n-1} (c - 2(e + l_p)\, i)^2, \tag{2}$$

where c is the external rib of the coil, e is the inter-line distance,l_p is the line width, and n is the number of turns (see Figure 1).

B. Electrical characterization

The theoretical model of a coil (Figure 2) is an *RLC* dipole whose impedance is written as

$$Z = \frac{R + jL\omega}{1 + jRC\omega - LC\omega^2}, \tag{3}$$

with ω being the current/voltage pulsation, L, R, and C are, respectively, the inductance, the resistance, and the capacity of the induction coil. In standardized form, the impedance can be explained as

$$Z = R \frac{1 + j\frac{Q\,\omega}{\omega_0}}{1 + j\frac{\omega}{Q\,\omega_0} - (\frac{\omega}{\omega_0})^2}, \tag{4}$$

with $Q = \frac{1}{R}\sqrt{\frac{L}{C}}$ being the quality factor and $\omega_0 = \frac{1}{\sqrt{LC}}$ the resonant pulsation of the sensor.

The probe impedance with an excited current I at a frequency f which is our parameter of interest can be computed by using the FE modeling developed in Section IV.

The inductance of the probe is obtained by the following expression:

$$L = \frac{2\,W_m}{I^2}, \tag{5}$$

where I is the coil excitation current and W_m is the average magnetic energy stored throughout the space defined by the following relation:

$$W_m = R_e\,(\frac{1}{2}\int_{\Omega} \boldsymbol{b}.\boldsymbol{h}^*\, d\Omega)\,, \tag{6}$$

where $\boldsymbol{b}$ is the magnetic flux density and $\boldsymbol{h}$ is the magnetic field.

The resistance of the coil can be calculated from the power losses in the conductive medium

$$R = \frac{P_j}{I^2}\,, \tag{7}$$

with

$$P_j = \int_{\Omega_c} \frac{1}{\sigma} \|\boldsymbol{j}\|^2\, d\Omega\,, \tag{8}$$

where $\boldsymbol{j}$ is the EC density and σ is the material conductivity.

The total capacitance is expressed as a function of the electrical energy W_e stored in the simulated space and the total voltage V_{tot}

$$C = \frac{2\,W_e}{V_{tot}^2}\,, \tag{9}$$

with

$$W_e = \frac{\varepsilon}{2}\int_{\Omega} \|\boldsymbol{e}\|^2\, d\Omega\,, \tag{10}$$

where ε is the electric permittivity, $\boldsymbol{e}$ is the electric field, and Ω is the whole computation area (sensor and air box).

C. Sensitive element characterization

The sensitivity of a sensor is the ratio of the respective variations of the output quantity of the sensor and the measurand. In the case of a coil used as an EC sensor, a magnetic field b is transformed into a voltage V. The sensitivity at a frequency f is written as

$$S = \left|\frac{dV}{db}\right| = 2\pi f\, S_{\text{tot}}\,. \tag{11}$$

The effective noise voltage of a coil when it is not traversed by a current is written as

$$v_b = \sqrt{4kTR\Delta f}\,, \tag{12}$$

where T is the temperature, Δf is the measuring frequency range, and k is Boltzmann's constant.

The effective value of the equivalent magnetic noise is the ratio of the effective noise voltage v_b and the sensitivity

$$B_b = \frac{v_b}{S}\,. \tag{13}$$

The emissive ability is the ratio of the emitted field b and the current I required for its emission. Its expression is obtained using that of the magnetic flux produced by an inductance element L crossed by a current I, which is written with b assumed to be uniform over the entire effective area of the coil

$$\Phi = LI = b\,S_{\text{tot}}.$$

The emissive ability P_e is given by

$$P_e = \frac{b}{I} = \frac{L}{S_{\text{tot}}}\,. \tag{14}$$

D. Optimization of the coil

The values of the geometrical, electrical, and physical characteristics are summarized in Table 1. The miniaturization of the coils in the printed circuit board is favorable on several points: the sensitivity is very high and the noise is very low. In all cases, the level noise is lower than the noise generally provided by the instrumentation and is, therefore, not very disturbing. Also,

Table 1 Numerical values of the coil characteristics calculated at 800 kHz

	Parameter	Value
Geometrical characterization	Number of turns	5
	External length	2.6 μm
	Line width	100 μm
	Inter-line width	100 μm
	Developed length	36 mm
	Total surface	17.8 mm^2
Electrical characterization	Capacity C	79.65 f F
	Resistance R	0.028 Ω
	Inductance L	0.023 μm
	Resonant frequency f_0	1.98 MHz
Sensitive element	Sensitivity S	89.42 V/T
	Noise voltage v_b	0.214 μV
	Equivalent noise field B_b	2.39 ηT
	Emissive ability P_e	1.29 mT/A

the thermal noise calculation is carried out over a wide range of frequencies, and, therefore, it is very strongly overestimated. In addition, the resolution is significantly improved by the printed coils: indeed, it is roughly proportional to the footprint, which is very small for this technology. The emitting power is inversely proportional to the total effective area, which means that a solenoid coil will emit a weaker field at an equal current.

IV. MODELING

The test case is related to Eddy current nondestructive testing (ECT). It consists of a printed coil placed above a conductive plate. The inspected specimen is a nickel-based alloy affected by a rectangular defect (flaw). The parameters of the configuration are given in Table 2. The following figure shows the geometry of the considered problem. It is composed of two domains where the first one, D_1, contains a coil, Ω_{t_0}, where a uniform current density $\boldsymbol{j_0}$ is imposed, and the second one, D_2, contains a nickel alloy plate noted by Ω_c which includes the flaw Ω_d. These domains are separated by a meshed region D_0 called the lift-off.

The FEM program was written using the developed ANSYS program with conjunction with Matlab. The calculation is carried out in the context of harmonic quasi-stationary regime.

The displacement of the sensor along the conductive plate is formed using the motion band method defined from the extension of the 2D FEM. Figures 4 and 5 show the scheme illustrating this technique. It consists of two steps.

Create a geometrical band, during which the moving zone is subdivided into elementary regions of the identical lengthΔx. Then the geometry is all meshed.

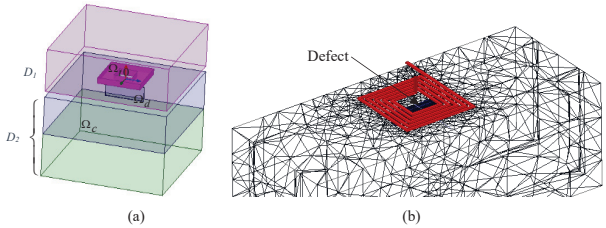

Fig. 3. (a) Description of the studied problem. (b) 3D mesh of the geometry.

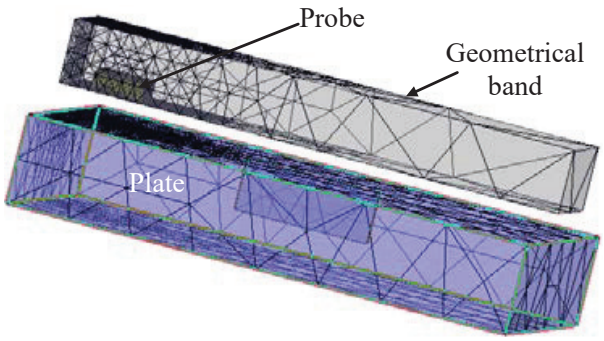

Fig. 4. Moving band technique for sensor displacement: before probe displacement.

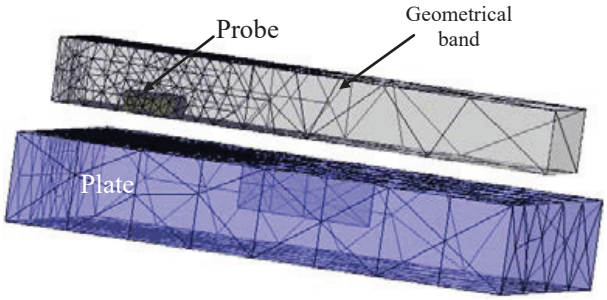

Fig. 5. Moving band technique for sensor displacement: after probe displacement.

Locate in the geometrical band (moving zone) the regions corresponding to the sensor and the air, and then the physical properties of the sensor and the air are assigned at each step displacement.

V. DUAL FORMULATIONS FOR EDDY CURRENT PROBLEMS

Most three-dimensional finite element formulations of EC problems can be classified into two dual formulations. One works with the variables of the Ampere's law system, and the other uses the variables of the Faraday's law system. We will be interested in the two electric and magnetic formulations in combined potentials.

A. Magnetic formulation

The magnetic field $\boldsymbol{h}$ is then expressed by the sum of electric potential vectors $\boldsymbol{t}$ and $\boldsymbol{t}_0$, and the gradient of the magnetic scalar potential φ

$$\begin{aligned} &\boldsymbol{h} = \boldsymbol{t} + \boldsymbol{t}_0 - \boldsymbol{grad}\varphi \quad , \\ &\text{with} \quad \boldsymbol{n} \times \boldsymbol{t}|_{\Gamma_h} = 0 \text{ and } \varphi|_{\Gamma_h} = 0, \end{aligned} \tag{15}$$

such as $\boldsymbol{curl}\,(\boldsymbol{t}) = \boldsymbol{j}$ and $\boldsymbol{curl}\,(\boldsymbol{t}_0) = \boldsymbol{j}_0$, with $\boldsymbol{j}$ and $\boldsymbol{j}_0$ being the density of ECs and the density of current source. By introducing these equalities into the Faraday law and the flow conservation law, the system to solve is written as

$$\begin{cases} \operatorname{div}(\mu\,(\boldsymbol{t} + \boldsymbol{t}_0 - \boldsymbol{grad}\varphi)) = 0 \text{ in } \Omega \\ \boldsymbol{curl}\,(\frac{1}{\sigma}\,\boldsymbol{curl}\,\boldsymbol{t}) + j\omega\mu\,(\boldsymbol{t} - \boldsymbol{grad}\varphi) = 0 \text{ in } \Omega_c \end{cases}, \tag{16}$$

with ω being the current/voltage pulsation, $\mu = \mu_0.\mu_r\,(\mu_0 = 4\pi 10^{-7} H/m)$ and μ_r the relative permeability of the material used as inductor. The electric vector potential $\boldsymbol{t}$ and the magnetic scalar potential in an element are then expressed by

$$\varphi = \sum_{n=1}^{N_n} w_n \overline{\varphi_n} \tag{17}$$

$$\boldsymbol{t} = \sum_{a=1}^{N_a} \boldsymbol{w}_a \overline{t_a} \tag{18}$$

where w_n is the vector of nodal shape functions, $\overline{\varphi_n}$ is the value of φ at the n$^{\text{th}}$ node, $\boldsymbol{w}_a$ is the vector of edge shape functions, and $\overline{t_a}$ is the circulation of $\boldsymbol{t}$ along the a^{th} edge. The matrix form of the system of equation is written as follows:

$$\begin{pmatrix} R_N & C_{AN} \\ C_{AN}^t & M_A + R_A \end{pmatrix} \begin{pmatrix} \Phi \\ T \end{pmatrix} = \begin{pmatrix} S \\ 0 \end{pmatrix},$$
$$\text{with } \Phi = \begin{pmatrix} \overline{\varphi}_1 \\ . \\ . \\ \overline{\varphi}_{N_n} \end{pmatrix} \quad T = \begin{pmatrix} \overline{t}_1 \\ . \\ . \\ \overline{t}_{N_a} \end{pmatrix} \tag{19}$$

The system thus obtained is symmetrical and the matrix terms are

$$\begin{cases} R_{N_{nm}} = j\omega \int_\Omega \mu\ \boldsymbol{grad} w_n \cdot \boldsymbol{grad} w_m\, d\Omega \\ C_{AN_{an}} = -j\omega \int_{\Omega_c} \mu\ \boldsymbol{grad} w_n \cdot \boldsymbol{w}_a\, d\Omega \\ M_{A_{ab}} = j\omega \int_{\Omega_c} \mu\ \boldsymbol{w}_a \cdot \boldsymbol{w}_b\, d\Omega \\ R_{A_{ab}} = \int_{\Omega_c} \frac{1}{\sigma}\ \boldsymbol{curl}\,(\boldsymbol{w}_a) \cdot \boldsymbol{curl}\,(\boldsymbol{w}_b)\, d\Omega \\ S_m = j\omega \int_{\Omega_t} \mu\ \boldsymbol{grad}(w_m) \cdot \boldsymbol{t}_0 d\Omega \end{cases} \tag{20}$$

where R_N is the stiffness matrix of the nodes, R_A is the stiffness matrix of the edges,M_A is the mass matrix of the edges,C_{AN} is the node-edge coupling matrix, and S is the source term.

The vectors Φ and T contain the unknowns of the system which are, respectively, the values of the magnetic scalar potential at the nodes and the circulations of the electric vector potential along the edges of the mesh.

B. Electric formulation

The electric field $\boldsymbol{e}$ can be expressed by the combination of the magnetic vector potential $\boldsymbol{a}$ and electric scalar potential ψ

$$\begin{cases} \boldsymbol{e} = -j\omega(\,\boldsymbol{a} + \boldsymbol{grad}\psi) \text{ with} \\ \boldsymbol{b} = \boldsymbol{curl}\ \boldsymbol{a} \end{cases}. \tag{21}$$

The conduction current density $\boldsymbol{j}$ is thus calculated as

$$\begin{aligned} \boldsymbol{j} &= \boldsymbol{j}_i + \boldsymbol{j}_0 \\ &= -\sigma j\omega(\boldsymbol{a} + \boldsymbol{grad}\psi) + \boldsymbol{curl}\,\boldsymbol{t}_0. \end{aligned} \tag{22}$$

Following the same procedure as for $\boldsymbol{t} - \varphi$ formulation: The magnetic vector potential $\boldsymbol{a}$ and the electric scalar potential ψ are then expressed by

$$\psi = \sum_{n=1}^{N_n} w_n \overline{\psi_n} \tag{23}$$

$$\boldsymbol{a} = \sum_{a=1}^{N_a} \boldsymbol{w}_a \overline{a_a}. \tag{24}$$

In the same way as the $\boldsymbol{t} - \varphi$ formulation, the magnetic vector potential $\boldsymbol{a}$ is discretized by edge elements, while the electric scalar potential ψ is discretized by nodal elements. The system of equations is written within the matrix form

$$\begin{pmatrix} R_N & C_{AN} \\ C_{AN}^t & M_A + R_A \end{pmatrix} \begin{pmatrix} \Psi \\ A \end{pmatrix} = \begin{pmatrix} 0 \\ S \end{pmatrix}$$
$$\text{and } \Psi = \begin{pmatrix} \overline{\psi}_1 \\ . \\ . \\ \overline{\psi}_{N_n} \end{pmatrix} \quad A = \begin{pmatrix} \overline{a}_1 \\ . \\ . \\ \overline{a}_{N_a} \end{pmatrix}. \tag{25}$$

The system thus obtained is symmetrical and the matrix terms are

$$\begin{cases} R_{N_{nm}} = j\omega \int_{\Omega_c} \sigma\ \boldsymbol{grad} w_n \cdot \boldsymbol{grad} w_m\, d\Omega \\ C_{AN_{an}} = j\omega \int_{\Omega_c} \sigma\ \boldsymbol{w}_a \cdot \boldsymbol{grad}\, w_m\, d\Omega \\ M_{A_{ab}} = j\omega \int_\Omega \sigma\ \boldsymbol{w}_a \cdot \boldsymbol{w}_b\, d\Omega \\ R_{A_{ab}} = \int_\Omega \frac{1}{\mu}\ \boldsymbol{curl}\,(\boldsymbol{w}_a) \cdot \boldsymbol{curl}\,(\boldsymbol{w}_b)\, d\Omega \\ S_b = \int_{\Omega_t} \boldsymbol{curl}(w_b) \cdot \boldsymbol{t}_0 d\Omega \end{cases} \tag{26}$$

The vectors Ψ and A are the unknowns of the system, respectively, the values of the electric scalar potential at the nodes and the circulations of the magnetic vector potential at the edges of the mesh.

VI. APPLICATIONS

Our study relies on analyzing the data of scans, allotted by little displacements of the detector, parallel to the crack on the conductive plate. The change of the real and imaginary parts of the coil impedance reflects the change in the physical parameters of a test specimen in the presence of defects. The real part of the coil impedance is

Table 2 Dimensions of the problem

Turn width	100 μm
Turn thickness	25 μm
Gap between turns	100 μm
Plate thickness	3 mm
Plate conductivity	0,76 MS/m
Relative permeability of the plate	1
Lift-off thickness	50 μm
Excitation frequency	800 kHz
Length of the flaw	800 μm
Width of the flaw	100 μm
Depth of the flaw	400 μm

determined by calculating the Joule losses in the conductive media. The imaginary part of this impedance is determined from the magnetic energy stored in the entire meshed space.

For both dual formulations, the variations of the real part and the variation of the imaginary part of the impedance due to the flaw are calculated by subtracting for each of them the values with and without flaw. $\Delta X_n = (X - X_0)/X_0$ and $\Delta R_n = (R - R_0)/X_0$ with X, R being the reactance and resistance of the coil in presence of the conducting domain. X_0, R_0 are the reactance and resistance of the empty coil (absence of the plate).

A. Application I

The parameters of the configuration are given in Table 2.

Figure 6 illustrates the distribution of ECs produced by the coil. As can be seen in Figure 6(a), a circular-shaped EC loop is produced beneath the surface of the material. The current density is null in the defect zone because the conductivity is zero ($\boldsymbol{j} = \sigma \boldsymbol{e}$), and it is also very significant in the surface and it decreases gradually as we head to the bottom because of the skin effect as shown in Figure 6(b).

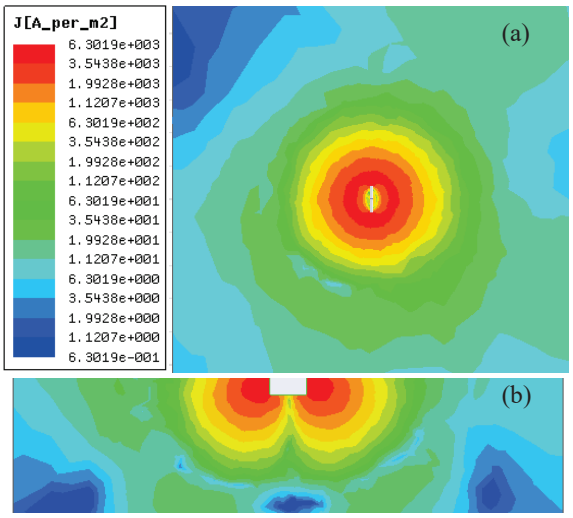

Fig. 6. Eddy current distribution. (a) Top view. (b) Front view.

Figure 7(a) and (b) presents the variation of resistance and reactance as a function of the position of the symmetry axis of the coil relatively to the center of the flaw. The impedance real part (resistance) presents a trough curve and the imaginary part (reactance) presents a crest curve. As seen from the defect response curve of the impedance imaginary part [Figure 7(b)], the defect response begins to rise when the crack is near to the bottom edge of the coil, and it reaches a climax when the sensor coincides with the first edge of the defect and starts to decrease as the sensor leaves the other edge of the defect. It can be observed from the next figures that there is a good agreement between the FEM results

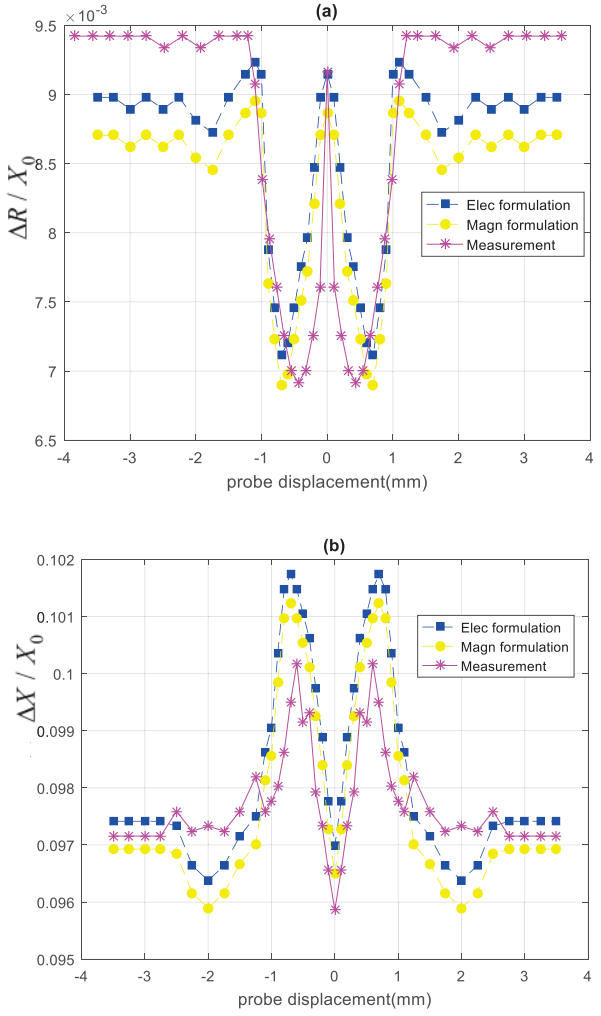

Fig. 7. The variation of normalized impedance of the system as a function of displacement of the sensor. (a) Impedance real part. (b) Impedance imaginary part.

issued from the magnetic and the electric formulation and the experimental results. These signals represent the signatures of the crack.

B. Application II

As the lift-off is a predominant factor in the EC detection performance, the modeling must take into account the physical phenomena associated with its values. The geometrical and physical parameters of the problem are summarized in Table 2. The lift-off varies within a range of $0.1-11$ mm. the resistance and reactance of the coil were calculated with both the electrical and magnetic formulations and shown in Figure 8(a) and (b). The results presented in these figures show that the influence on the coil impedance of a lift-off less than 1 mm is negligible. Indeed, for a lift-off of less than 1 mm, the reactance and the resistance of the coil are almost constant. On the other hand, beyond this value, the lift-off has a strong influence on the impedance, and it is essential to take this into account in the modeling. The results also show that the two curves obtained by the two electric and magnetic formulations are in good agreement. This value (1 mm) depends on the coil used. In a general way, an increase in the size of the coil will lead to an increase in these values.

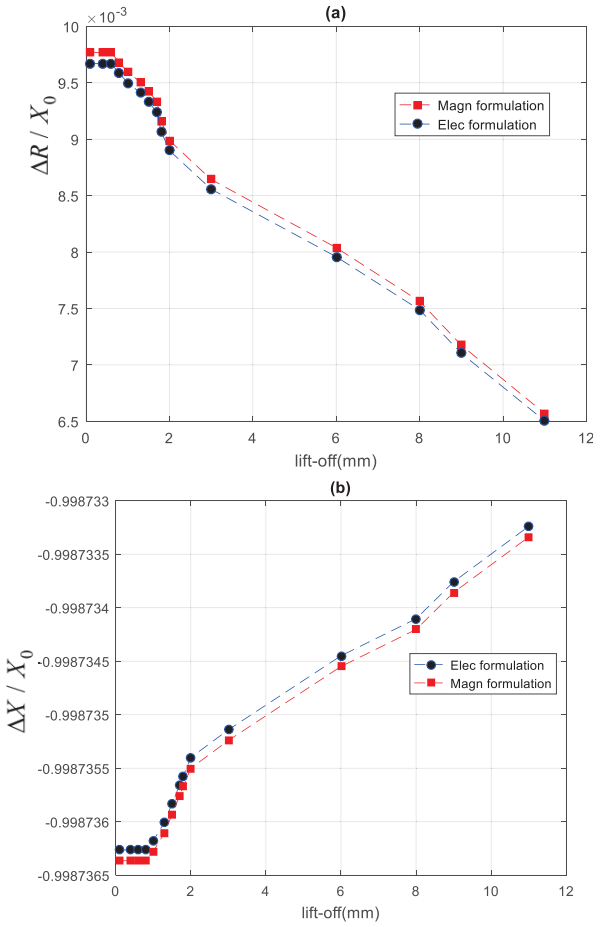

Fig. 8. (a) Normalized resistance. (b) Normalized reactance variation as a function of the lift-off.

C. Application III

The study of the crack size effect on the EC signal will enable us to identify the ECNDT device sensitivity.

Effect analysis of crack width:

In the previous works, the authors were more interested in studying the effect of the length and depth of the crack on the EC signal, while only a few of them were interested in studying the width effect.

The model used is the same one used for application I by changing the geometric parameters of the defect. The frequency of the sensor is fixed at 0.8 MHz and the

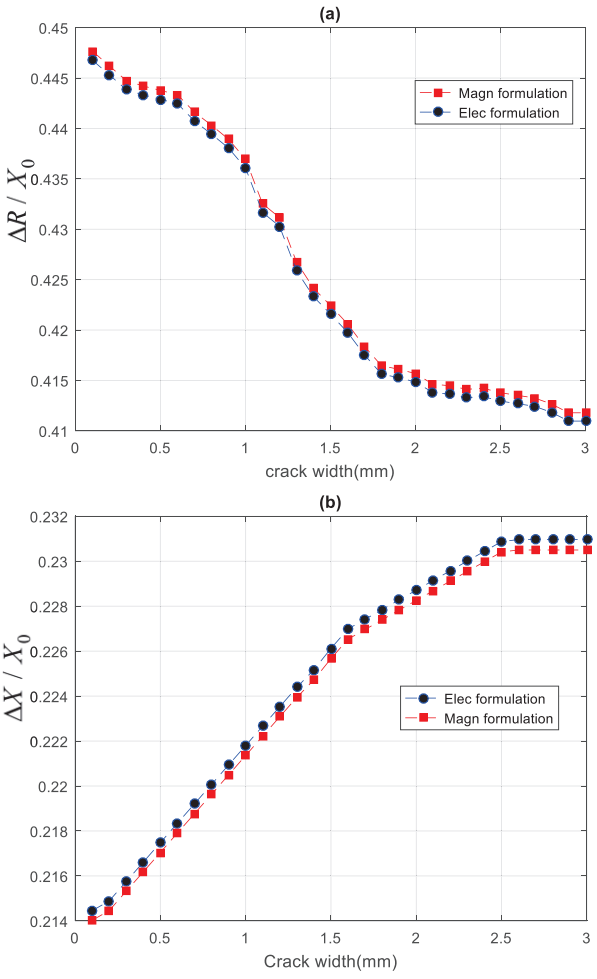

Fig. 9. (a) Normalized impedance real part. (b) Normalized impedance imaginary part variation as a function of the crack width.

lift-off at 0.0625 mm (application II), and the length of the plate is much greater than that of the crack, the crack length and depth are fixed at 0.8 and 0.4 mm, respectively, while the width is varying between 0.1 and 3 mm for a step of 0.1 mm. In this case, we fix the crack beneath the center of the sensor where its output is in the maximum. The graphs of the impedance real part and imaginary part versus crack width are shown in Figure 9(a) and (b), respectively.

Effect analysis of crack length:

Next the influence of crack length on the sensor response is studied. The lift-off is set to be 0.0625 mm, and cracks of identical width (0.1 mm) and depth (0.4 mm) having different lengths are altered. Data of scans are carried out by small displacements of the sensor with a step of 0.1 mm, parallel to the crack on the surface of the material. Figure 10(a) and (b) presents EC signatures of the resistance and reactance variations with respect to the sensor displacement produced by cracks having different lengths. Based on the curves of impedance real part and imaginary part, the shapes of the curves for all the defects are similar; however, the defect length influences the width and the peak value of the response curve. As the crack length grows, the width of the curve grows and the peak value increases.

Effect analysis of crack depth:

Defects with depths of 0.1, 0.2, and 0.4 mm are studied. All the defects are 0.8 mm in length and 0.1 mm in width. Figure 11(a) and (b) shows EC signatures of the impedance real part and imaginary part variations with respect to the sensor displacement produced by defects having different depths. As can be seen, the waveforms are similar; however, the crack depth influences the peak

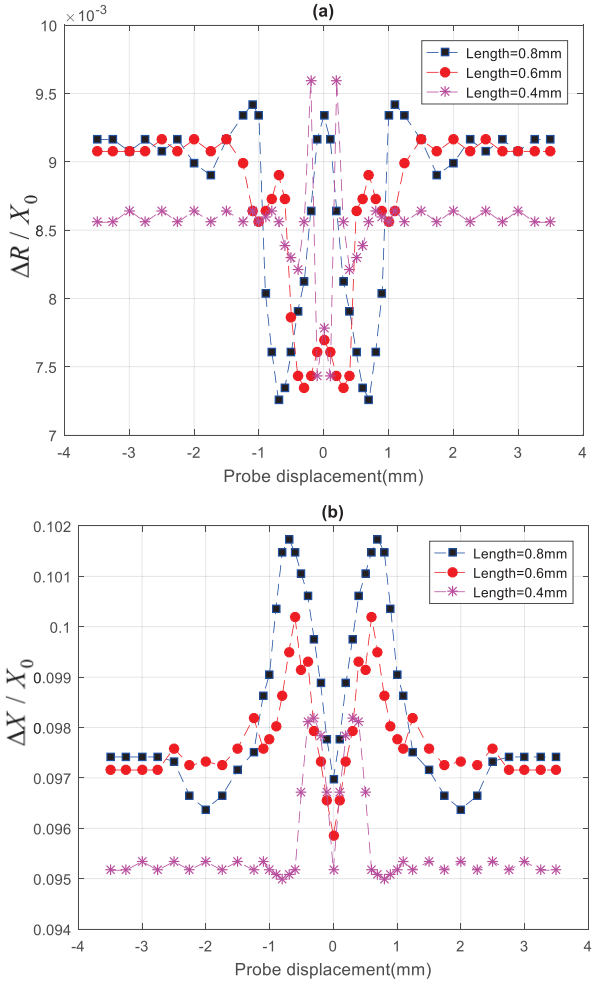

Fig. 10. (a) Normalized impedance real part. (b) Normalized impedance imaginary part variation of cracks having different lengths.

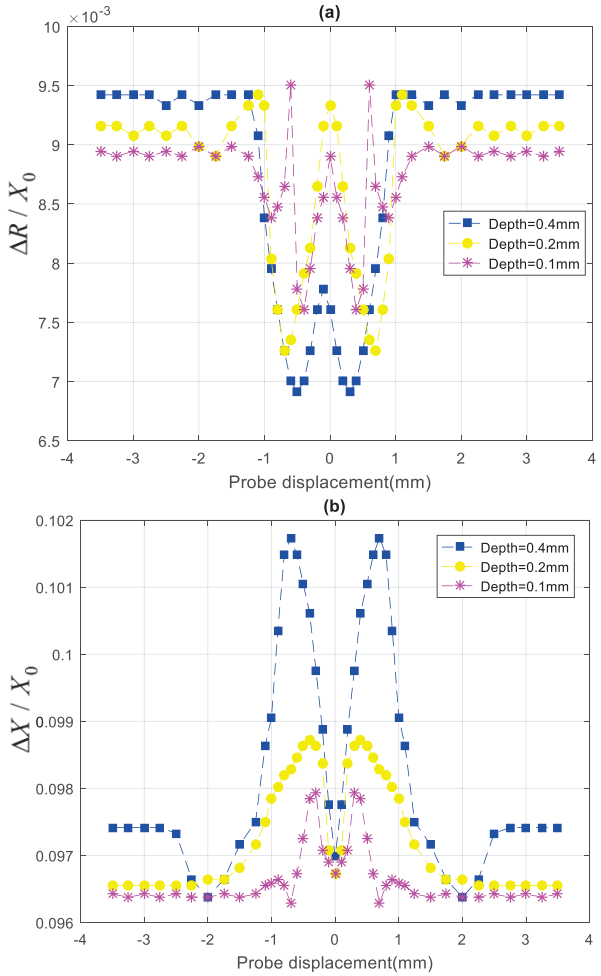

Fig. 11. (a) Normalized impedance real part. (b) Normalized impedance imaginary part variation of cracks having different depths.

value of the response curves. The deeper the crack is, the greater the peak will be.

EC signal and the depth limit:

Next, the depth limit is studied; the crack length and width are fixed at 0.8 and 0.1 mm, respectively, while the depth is varying between 0.1 and 3 mm for a step of 0.1 mm. In this case, we fix the crack beneath the center of the sensor where its output is in the maximum. The graph of the impedance real part and imaginary part versus crack depth are shown in Figure 12(a) and (b), respectively.

As can be seen, at the beginning, the resistance values decrease rapidly, then slow down gradually with increasing crack depth, and then stabilize when the crack depth reaches 2.5 mm. On the other hand, the reactance values increase rapidly at the beginning and slow down gradually, while the crack depth increases and then stabilizes when the crack depth reaches 2 mm. The reason is that when we use a high frequency excitation, the EC will be spread out much more on the surface of the material so that the sensor will not be very sensitive to deep defects as it is with the shallow defects. Both Figures 12(a) and (b) show that the depth limit is not the same for the impedance real part and imaginary part. The real part is more sensitive to the crack depth than the imaginary part.

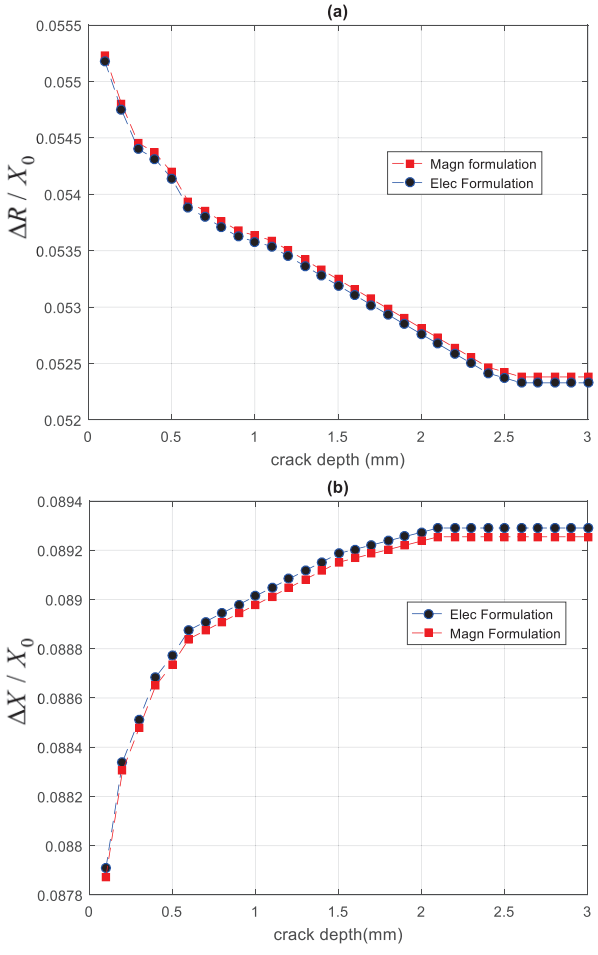

Fig. 12. (a) Normalized impedance real part. (b) Normalized impedance imaginary part variation as a function of the crack depth.

VII. CONCLUSION

A microsensor dedicated to the ECNDT application is proposed in this paper. An FEM approach that yields an efficiency to model the 3D microsensor, taking into account the presence of thin geometrical domains and the sensor displacement in the 3D plane without remeshing all the domains in each displacement, has been proposed. The real and imaginary parts of the impedance at every position of the sensor computed by experiments and simulations were consistent with each other for the first application. The optimal lift-off, which is less than 1 mm, is determined by FEM simulation in the second application and taken into account in all the applications (I and III). The principle of the sensor and the response of cracks with different sizes are demonstrated by simulation, and the results are very close because both the proposed differential formulations (in terms of the magnetic formulation and the electric formulation) can deal with currents flowing in conductors and are well fitted for computing fields within the current regions with accuracy. The difference between the impedance values obtained using the magnetic formulation and the electric formulation did not exceed, in any case, 0.1%. The novel sensor has the following advantages:

1. The design of the sensor conforms it to the small geometry.
2. It provides high spatial resolution and high detection efficiency.
3. The sensor was capable of detecting micro-defects with a size starting from 0.1 mm under the optimal excitation frequency of 0.8 MHz.
4. The sensor can distinguish the different crack sizes (length, width, and depth).

Future research will be required to extend the proposed sensor for solving problems with complex geometry and arbitrary defect.

REFERENCES

[1] Q. Yu, O. Obeidat, and X. Han, "Ultrasound wave excitation in thermal NDE for defect detection," *NDT E Int.*, vol. 100, pp. 153-165, Sept. 2018.

[2] O. Obeidat, Q. Yu, L. Favro, and X. Han, "The effect of heating duration on the quantitative

estimation of defect depth using sonic infrared imaging," *J. Nondestruct. Eval. Diagn. Progn. Eng. Syst.*, vol. 4, no. 4, pp. 302-307, Nov. 2021.

[3] D. Velicheti, P. B. Nagy, and W. Hassan, "Residual stress and cold work assessment in shot-peened IN718 using a dual-mode electromagnetic technique," *NDT E Int.*, vol. 121, May 2021.

[4] D. Velicheti, P. B. Nagy, and W. Hassan, "Inversion procedure for dual-mode electromagnetic nondestructive characterization of shot-peened IN718," *NDT E Int.*, vol. 101, pp. 17-28, Oct. 2019.

[5] K. Li and al., "A fast and non-destructive method to evaluate yield strength of cold-rolled steel via incremental permeability," *J. Magn. Magn. Mater.*, vol. 498, Nov. 2020.

[6] A. Goti, A. Oyarbide-Zubillaga, A. Sanchez, T. Akyazi, and E. Alberdi, "Multi equipment condition based maintenance optimization using multi-objective evolutionary algorithms," *Appl. Sci. Switz.*, vol. 9, no. 22, Nov. 2019.

[7] M. Alsharqawi, T. Zayed, and S. Abu Dabous, "Integrated condition-based rating model for sustainable bridge management," *J. Perform. Constr. Facil.*, vol. 34, no. 5, Jun. 2020.

[8] R. M. Ayo-Imoru and A. C. Cilliers, "A survey of the state of condition-based maintenance (CBM) in the nuclear power industry," *Ann. Nucl. Energy*, vol. 112, pp. 177-188, Feb. 2018.

[9] M. M. Derriso, C. D. McCurry, and C. M. Schubert Kabban, "2 - A novel approach for implementing structural health monitoring systems for aerospace structures," in Structural Health Monitoring (SHM) in Aerospace Structures, F.-G. Yuan, Éd. Woodhead Publishing, pp. 33-56, Oct. 2016.

[10] M. Lu, X. Meng, L. Chen, R. Huang, W. Yin, and A. Peyton, "Measurement of ferromagnetic slabs permeability based on a novel planar triple-coil sensor," *IEEE Sens. J.*, vol. 20, no. 6, pp. 2904-2910, March 2020.

[11] Y. Long, S. Huang, Y. Zheng, S. Wang, and W. Zhao, "A method using magnetic eddy current testing for distinguishing ID and OD defects of pipelines under saturation magnetization," *Applied Computational Electromagnetic Society (ACES) Journal*, pp. 1089-1098, Sept. 2020.

[12] X. Chen and Y. Lei,"Electrical conductivity measurement of ferromagnetic metallic materials using pulsed eddy current method," *NDT E Int.*, vol. 75, pp. 33-38, Oct. 2015.

[13] B. Helifa, M. Feliachi, I. K. Lefkaier, F. Boubenider, A. Zaoui, and N. Lagraa, "Characterization of surface cracks using eddy current NDT simulation by 3D-FEM and inversion by neural network," *Applied Computational Electromagnetic Society (ACES) Journal*, pp. 187-194, Feb. 2016.

[14] F. Jiang, S. Liu, and L. Tao, "Quantitative research on cracks in pipe based on magnetic field response method of eddy current testing," *Applied Computational Electromagnetic Society (ACES) Journal*, pp. 99-107, Jan. 2021.

[15] J. O. Fava, L. Lanzani, and M. C. Ruch, "Multilayer planar rectangular coils for eddy current testing: Design considerations," *NDT E Int.*, vol. 42, no. 8, pp. 713-720, Dec. 2009.

[16] M. A. Machado, K.-N. Antin, L. S. Rosado, P. Vilaça, and T. G. Santos, "Contactless high-speed eddy current inspection of unidirectional carbon fiber reinforced polymer," *Compos. Part B Eng.*, vol. 168, pp. 226-235, July 2019.

[17] H. Zhang, L. Ma, and F. Xie, "A method of steel ball surface quality inspection based on flexible arrayed eddy current sensor," *Measurement*, vol. 144, pp. 192-202, Oct. 2019.

[18] N. Zhang, C. Ye, L. Peng, and Y. Tao, "Eddy current probe with three-phase excitation and integrated array tunnel magnetoresistance sensors," *IEEE Trans. Ind. Electron.*, vol. 68, no. 6, pp. 5325-5336, April 2021.

[19] Z. Sun, D. Cai, C. Zou, W. Zhang, and Q. Chen, "Design and optimization of a flexible arrayed eddy current sensor," *Meas. Sci. Technol.*, vol. 28, no. 4, Feb. 2017.

[20] W. Zhang, C. Wang, F. Xie, and H. Zhang, "Defect imaging curved surface based on flexible eddy current array sensor," *Measurement*, vol. 151, Feb. 2020.

[21] J. Ge, B. Hu, and C. Yang, "Bobbin pulsed eddy current array probe for detection and classification of defects in nonferromagnetic tubes," *Sens. Actuators Phys.*, vol. 317, Jan. 2021.

[22] S. Xie, Z. Duan, J. Li, Z. Tong, M. Tian, and Z. Chen, "A novel magnetic force transmission eddy current array probe and its application for nondestructive testing of defects in pipeline structures," *Sens. Actuators Phys.*, vol. 309, July. 2020.

[23] M. Lu, X. Meng, R. Huang, L. Chen, A. Peyton, and W. Yin, "Lift-off invariant inductance of steels in multi-frequency eddy-current testing," *NDT E Int.*, vol. 121, April 2021.

[24] Z. A. Ansari, B. A. Abu-Nabah, M. Alkhader, and A. Muhammed, "Experimental evaluation of nonmagnetic metal clad thicknesses over nonmagnetic metals using apparent eddy current conductivity spectroscopy," *Meas. J. Int. Meas. Confed.*, vol. 164, June 2020.

[25] N. M. Rodrigues, L. S. Rosado, and P. M. Ramos, "A portable embedded contactless system for the measurement of metallic material conductivity and lift-off," *Measurement*, vol. 111, pp. 441-450, Dec. 2017.
[26] S. Zhang, "An analytical model of a new T-cored coil used for Eddy current nondestructive evaluation," *Applied Computational Electromagnetic Society (ACES) Journal*, pp. 1099-1104, Sept. 2020.
[27] S. da Silva, "Data-driven model identification of guided wave propagation in composite structures," *J. Braz. Soc. Mech. Sci. Eng.*, vol. 40, no. 11, Oct. 2018.
[28] F. Jiang and S. Liu, "Calculation and analysis of an analytical model for magnetic field monitoring based on TREE in Eddy current testing," *Applied Computational Electromagnetic Society (ACES) Journal*, pp. 1489-1497, Dec. 2018.
[29] O. Obeidat, Q. Yu, and X. Han, "Developing algorithms to improve defect extraction and suppressing undesired heat patterns in sonic IR images," *Sens. Imaging*, vol. 17, no. 1, Oct. 2016.
[30] G. Tytko and L. Dziczkowski, "Fast calculation of the filamentary coil impedance using the truncated region eigenfunction expansion method," *Applied Computational Electromagnetic Society (ACES) Journal,* pp. 1461-1466, Dec. 2018.
[31] M. Haywood-Alexander, N. Dervilis, K. Worden, E. J. Cross, R. S. Mills, and T. J. Rogers, "Structured machine learning tools for modelling characteristics of guided waves," *Mech. Syst. Signal Process.*, vol. 156, July 2021.
[32] K. Mizukami and Y. Watanabe, "A simple inverse analysis method for eddy current-based measurement of through-thickness conductivity of carbon fiber composites," *Polym. Test.*, vol. 69, pp. 320-324, Aug. 2018.
[33] M. Mirzaei, P. Ripka, A. Chirtsov, and V. Grim, "Eddy current speed sensor with magnetic shielding," *J. Magn. Magn. Mater.*, vol. 502, May 2020.
[34] K. Mizukami et al., "Enhancement of sensitivity to delamination in eddy current testing of carbon fiber composites by varying probe geometry," *Compos. Struct.*, vol. 226, Oct. 2019.
[35] C. Ye, Y. Wang, M. Wang, L. Udpa, and S. S. Udpa, "Frequency domain analysis of magnetic field images obtained using TMR array sensors for subsurface defect detection and quantification," *NDT E Int.*, vol. 116, Dec. 2020.
[36] Y. Kuang et al., "Magnetic field energy harvesting from the traction return current in rail tracks," *Appl. Energy*, vol. 292, June 2021.
[37] S. She, Y. Chen, Y. He, Z. zhou, and X. Zou, "Optimal design of remote field eddy current testing probe for ferromagnetic pipeline inspection," *Measurement*, vol. 168, Jan. 2021.

Chifaa Aber received the magister degree in applied optics from the University of Ferhat Abbas Setif, Sétif, Algeria, in 2010. She is currently working toward the Ph.D. degree with the University of Sciences and Technologies of Oran USTO-MB.

She is a member of Applied Power Electronics Laboratory LEPA and temporary teacher with Larbi Ben M'hidi OEB University. Her research interests include Eddy current, microelectronics, neural network, FEM, and optical sensors.

Azzedine Hamid was born in Algies, Algeria, in 1961. He received the magister degree in electrical engineering from the Mohamed Boudiaf University of Oran in 1994 and the Ph.D. degree from the Mohamed Boudiaf University of Sciences and Technology of Oran in 2005.

He is a head member of LEPA laboratory research team.

Mokhtar Elchikh received the Ph.D. degree in nuclear and particle physics from the University of Grenoble I, Grenoble, France, in 1992.

His is currently a Professor of Physics with the University of Sciences and Technology of Oran, Algeria. He has been interested in nuclear physics, spin physics, ion-surface interactions, condensed matter physics, ab initio calculations, and, recently, in power electronic.

Thierry Lebey received the M.Sc. degree in solid state physics in 1984 and in microelectronics in 1985, and the Ph.D. degree in electrical engineering in 1989. He was a CNRS Research Scientist for 30 years. His fields of interest concern the characterization, modeling, and aging of solid dielectrics and insulating materials used in electrical engineering applications. From 2016 to 2019, he was the Director of LAPLACE, the French largest electrical engineering laboratory located in Toulouse, France. Since then, he joined SafranTech, the corporate research center of Safran, one of the first world aerospace companies, as the head of research on high voltage engineering for aviation applications. He is the author of around 90 papers in international journals AND more than 160 conference papers (mainly in IEEE conferences) and holds 18 international patents. https://www.safran-group.com/

The Comparison of EMF Monitoring Campaigns in Vicinity of Power Distribution Facilities

Goran S. Nedic[1], Nikola M. Djuric[2], and Dragan R. Kljajic[2]

[1]Public Enterprise Electric Power Industry of Serbia
Novi Sad, 21000, Serbia
goran.nedic@eps.rs

[2]Faculty of Technical Sciences, University of Novi Sad
Novi Sad, 21000, Serbia
ndjuric@uns.ac.rs, dkljajic@uns.ac.rs

***Abstract* –** Monitoring of electromagnetic field (EMF) near power distribution facilities, both in the low- and the high-frequency ranges, has become highly demanded in recent years. The reason lies in the accumulated concerns on public health, which is mostly caused by the evolution of electric power and communication infrastructure, in and around the power substations, as well as their closeness to residential areas. In this paper, the initial comparative analysis of the EMF monitoring results of three one-day campaigns, in 2015, 2018 and 2020, performed in the vicinity of the Serbian high-power distribution substation "Novi Sad 7", is presented. The overall EMF levels in all campaigns comply with the reference levels prescribed by the Serbian legislation, including some new EMF sources which were detected in 2018 and 2020. Likewise, the used continuous monitoring has demonstrated suitability to systematically address EMF fluctuation on daily basis, as well as corresponding concerns on EMF exposure.

***Keywords* –** electromagnetic field, power system, power substation, radiation monitoring, RF signals.

I. INTRODUCTION

Constantly growing number of industrial and residential consumers resulted in a greater demand for electric energy, particularly in recent decade. The first action and an accepted response to such demand is to boost existing power substations, followed by the installation of new ones. Also, the interconnection is accomplished between substations, strengthening the power distribution network, while enabling its remote management.

The power distribution facilities are well known as sources of the low-frequency magnetic fields [1]. However, their remote-control by using radio links, as well as different wireless equipment, promote them as sources of the high-frequency electric field. Consequently, their usual presence in residential and industrial areas has increased the public concerns on adverse health effects, demanding the electromagnetic field (EMF) level monitoring in their vicinity [1].

The worldwide efforts are invested in measurements and simulations of both the low-frequency magnetic and the high-frequency electric fields. In a number of recent studies, measurements were oriented towards the short-term methods and estimation of the exposure. Results are used in a computational prediction of the low-frequency magnetic field strength within the power substation [2] or for the high-frequency electric field investigation produced by the cellular network base stations over sensitive locations [3]. The obtained results were mandatory compared with the proposed reference levels [4].

Additionally, the short-term measurements of magnetic and electric fields were conducted inside the power substation in order to determine EMF distribution [5], as well as indoor and outdoor substation evaluation [6–8], elaborating safety levels of the human exposure to those fields. Also, the measurements of magnetic field inside the substations of various voltage levels were presented, as well as measurements related to near feeder lines, such as the overhead power lines and underground cables [9].

Similarly, wide range of the magnetic field measurements were performed in surrounding areas of the power substations in [10]. Consequently, occupational EMF exposure were also in focus [11], particularly during working tasks within the power substations, such as switching and transforming 110 kV and 20 kV, analyzing whether the occupational reference levels were exceeded [4].

A common attribute in the mentioned studies is that measurements were short-term oriented, no longer than a few minutes. Unfortunately, in utmost cases, such approach cannot provide a full insight in EMFs fluctuation and their long-term behavior. In order to provide a comprehensive insight, the modern long-term EMF

Submitted On: February 12, 2021
Accepted On: November 4, 2021

https://doi.org/10.13052/2022.ACES.J.370115

monitoring systems have been developed and utilized [12, 13]. They are intended to perform continuous EMF monitoring in numerous sensitive zones, such as schools, kindergartens, hospitals and other public institutions [13].

In this study, the approach of broadband continuous EMF monitoring was used. It is implemented in the Serbian Electromagnetic Field Monitoring Network – SEMONT [14], counting the contribution of all active EMF sources in the frequency range of interest. Furthermore, such long-term monitoring is followed by continuous exposure assessment, using SEMONT boundary exposure assessment approach [15, 16].

This paper presents a comparative analysis of measurement results of three different one-day EMF monitoring campaigns, performed in 2015, 2018 and 2020, in the vicinity of the high-power distribution substation "Novi Sad 7". Those campaigns are first systematic monitoring campaigns in the Serbian power distribution system.

This paper is established on Serbian national legislation, where appropriate field reference levels have been prescribed [17]. The reference levels ensure the protection of people against all established health hazards when they are exposed to EMFs. In that sense, this paper is intended to only check compliance with the prescribed reference limits and has no intention of further investigation on basic effects of EMF interaction with human tissues.

II. SUBSTATION EQUIPMENT

The distribution substation "Novi Sad 7", with nominal rates of 110/35/20 kV, is a high-power outdoor air-insulated electric power substation. With outer dimensions of 85 m by 85 m, it is situated in a residential area of the Serbian city of Novi Sad, at the corner of Heroja Pinkija and Ohridska streets, as shown in Figure 1.

The substation is equipped for remote control and supervision of power distribution and its other processes.

Fig. 1. Position of the substation "Novi Sad 7".

Table 1: Technical characteristics of radios

-	**Radio #1 (Narrowband)**	**Radio #2 (Broadband)**
Frequency range	438 – 470 MHz	5.725 – 5.850 GHz
Radiated power	25.35 W	31.52 W
Directional Antenna, Elevation/ Azimuth	No	Yes, 8°/8°
Position/Height	AN1/11 m	AN2/12 m

The control is done via dedicated radio links, from dispatch center of "EPS Distribucija", which is the national electricity Distribution System Operator (DSO) [18].

A. Installed high-frequency equipment

Regarding the sources of the high-frequency electric field, the communication between the substation technicians and dispatchers is realized via a narrowband radio link – radio #1, described in Table 1.

Furthermore, the broadband radio link, named radio #2, is intended for the control and supervision of the following substation processes: SCADA (Supervisory Control and Data Acquisition) application, then the continuous video surveillance and facility access control, as well as the internal IP telephony system.

The antenna systems for the narrowband radio are installed at the AN1 place, while for the broadband radio at the AN2, as depicted in Figure 1, avoiding the existing obstacles in the line of sight between the antenna and dispatch center. The main beam of directed antenna from radio link #2 (dashed white lines) is oriented towards the DSO dispatch center.

It should be stated that additional narrow-band radio link on AN1 site, with directional antenna (dashed white lines), was used for SCADA in 2015 [19], while during 2018 it was used as the redundant one [20]. In the 2020 campaign, this radio link was out of order. Considering antenna radiation patterns, the half-power beam width of directional antennas is shown in Figure 1 (dotted red and blue lines), while the radiation pattern of the omnidirectional antenna (radio #1), positioned on AN1, is omitted.

B. Installed low-frequency equipment

The substation high-voltage (HV) and medium-voltage (MV) electric power equipment is a dominant source of the low-frequency magnetic field. These includes the three-phase HV (110 kV) overhead line, which enter the substation from the south side, shown by red lines in Figure 1, while in the central part of the substation, there are 110 kV circuit breakers, lighting protection and bus bar systems. Two high-power transformers have nominal voltage rates of 110/20 kV (nominal power of 31.5 MVA), whereas the third one has a nominal rate of 110/35 kV (with the nominal power of 20 MVA).

Also, the MV compartments with MV bus bars and circuit breakers are located inside the substation building. There are twenty-one MV 20 kV lines, from which eighteen were present in the 2015 monitoring campaign, and three MV 35 kV lines connected to the substation on the north side, as depicted by dashed orange lines in Figure 1. All of them are installed as underground cables.

The MV 35 kV lines are used for the interconnection with neighboring 35/10 kV power substations, while MV 20 kV lines supply consumers with electricity via 20/0.4 kV distribution substations.

III. MONITORING CAMPAIGNS

The initial one-day EMF monitoring campaign was performed in 2015, followed by additional one-day campaigns in 2018 and 2020, shown in Table 2.

The opening step of each campaign was the visual inspection of the substation surroundings in order to discover the present EMF sources – antenna systems of radio communication links and mobile telephony base station sites for the high-frequency electric field, as well as overhead power lines and power transformers for the low-frequency magnetic field.

During visual inspection in 2015, the two substation locations, labeled as L1 and L2 in Figure 1, were identified as locations with potentially increased field levels.

Location L1 presents an area on the south of the substation, in Ohridska street, whose driveway is also a pedestrian pathway, passing below the HV power line, as shown in Figure 2a.

This location was selected considering the fact that a few residential houses, parking lots and business buildings are present in the vicinity of HV power lines. Therefore, there is a significant probability that residents could be exposed to the EMF radiation, passing beneath those lines. Besides, in line of sight on L1 location, the antennas of AN1 site are visible, where the distance between L1 and AN1 is about 80 m.

Location L2 is situated in the public access area, on the north side of the substation facility, on the frequently used sidewalk of Heroj Pinki street, as shown in Figure 2b. The L2 is close to the residential houses, as well as to the antenna AN2, which is a dominant source of the high-frequency electric field, positioned at a distance of about 15 m from L2. Moreover, L2 location is above the intersected underground MV power line corridors.

Both locations are of high importance, since they are frequently passed by local residents, as well as by employees of local companies.

In 2018 and 2020 campaigns, the visual inspections were repeated, observing the presence of some new the low- and the high-frequency sources in and around the substation, as well in L1-L2 vicinity.

Table 2: Details of one-day EMF monitoring campaigns

Year	Date	Time	Label
2015	06/15/2015	9:00 – 13:00	2015
2018	07/24/2018	9:00 – 13:00	2018
2020	05/22/2020	9:00 – 13:00	May_r 2020
2020	05/29/2020	9:00 – 13:00	May 2020
2020	09/17/2020	9:00 – 13:00	Sep 2020

A. The high-frequency campaign

During the first visual inspection in 2015, two sites with antennas were detected, labeled as AN1 and AN2. Substation internal radio systems appeared to be dominant source of the high-frequency field [19, 20].

Since no changes were detected in 2020 campaign, it was decided to perform the high-frequency monitoring only at location L2. Insignificant difference between the high-frequency electric field strengths over locations L1 and L2, in 2015 and 2018 campaigns, was additional reason for such decision [19–21].

During the 2015 campaign, only at location L2, the appropriate spectral components of the internal DSO radio communication links were detected [19]. However, the spectral component of the broadband radio #2 on L1 location was not noticed, since that location was influenced only by low-power side-lobes of the directed antenna [19], while it has a considerable distance of 115 m from AN2.

B. The low-frequency campaign

Regarding the low-frequency part, besides one HV line and three HV power transformers, there was no presence of newly installed low-frequency sources in 2020. Hence, it was decided to conduct the new measurements only at location L1, which is in vicinity of the HV power line [16]. There was almost certain presence of people, since L1 site has only one traffic lane and all vehicles/pedestrians have to pass through that lane.

Another reason was that magnetic field attenuation from underground MV cables, present on location L2, was higher than field attenuation from HV power lines. It turned out that L1 has higher field levels, thus it is better suited for population EMF exposure assessment.

IV. PROCEDURE AND EQUIPMENT

The same measuring procedure was used in all three monitoring campaigns. The low-frequency magnetic and high-frequency electric field monitoring were conducted over L1 and L2, applying the broadband monitoring approach and accompanying frequency selective measurement. The broadband monitoring was done according to the SEMONT measuring procedure [14, 15], followed by the frequency spectrum analysis [22].

Regarding monitoring campaigns, all measurements were conducted in the hot-spot position of the measuring

a) L1 location b) L2 location

Fig. 2. Monitoring locations near the substation "Novi Sad 7".

network [14, 15], at L1 for the low-frequency and at L2 for the high-frequency field.

Monitoring started at 9:00 A.M. and lasted for four hours, as presented in Table 2. Such monitoring period was selected regarding assumption that maximum daily activities of the general population and substation's employees occur during that period of the day, causing an increase of usual telecommunication traffic and electric power consumption.

A. Measuring equipment

The high-frequency broadband monitoring was performed using Narda NBM-550 measurement equipment, covering the frequency range of 100 kHz to 6 GHz [19] and using sampling rate of 6 minutes, as recommended in [23]. The frequency selective analysis was performed using Narda SRM 3006 measurement equipment, covering the frequency range from 420 MHz to 6 GHz [19].

Observing the low-frequency magnetic field, Narda EFA 300 instrument, with the magnetic field probe, was used, covering the frequency range from 5 Hz to 32 kHz [16] and employing the sampling rate of 6 minutes [23]. This equipment was used for field measurements, as well as for its spectral analysis.

V. MEASUREMENT RESULTS

Results of the broadband continuous EMF monitoring and the frequency selective analysis, in the substation vicinity, are presented in this chapter.

A. The broadband EMF monitoring approach

The broadband monitoring approach is able to provide information on cumulative EMF level, which originates from all active sources on location, in the observed frequency range. Unfortunately, the broadband approach cannot provide field level per each frequency, nor the individual contribution of specific EMF sources.

A.1. The high-frequency electric field monitoring

Regarding the high-frequency electric field strength monitoring, at location L2, the comparative overview of obtained average values in 2015, 2018 and 2020 is depicted in Figure 3.

Once more, it should be pointed out that those campaigns are one-day campaigns, as described in Table 2.

Even though there was slight fluctuation, the presented high-frequency electric field strengths were significantly below the minimal reference level of 11 V/m, prescribed by legislation of the Republic of Serbia [17], for the NBM-550 field probe's frequency range.

Average field strength values in 2018 and 2020 were lower than 0.2 V/m, while in 2015 they ranged up to 0.27 V/m. This could be explained by the fact that one of the dominant sources, the narrowband radio intended for the SCADA system [19], was in a full operational mode in 2015, while in 2018 it was put by DSO to hot stand-by mode. That was done because the SCADA traffic needed to be diverted to the radio #2 link in order to accommodate more efficient management of the processes in the substation, by providing faster links with

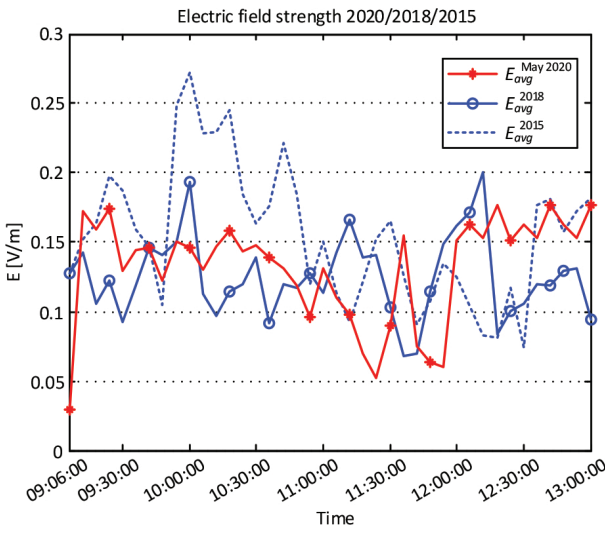

Fig. 3. Comparative view of L2 location monitoring.

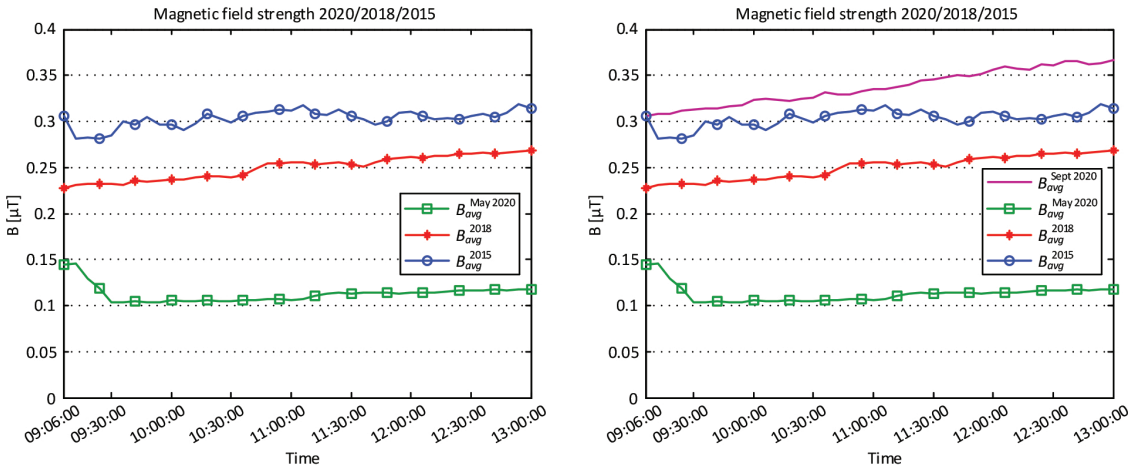

a) Initial monitoring in May 2020 b) Repeated monitoring in September 2020

Fig. 4. Comparative view on the low-frequency magnetic field continuous monitoring.

higher throughputs. In a stand-by mode, the inspection of radio-communication was performed at least few times a day, increasing the high-frequency EMF level in substation vicinity. In the year 2020, this radio was put out of order.

A.2. The low-frequency magnetic field monitoring

A comparative overview of the average values of the L1 low-frequency magnetic field strength, acquired during 2015, 2018 and 2020 campaigns, is shown in Figure 4a.

An increase could be noticed in field strength levels approaching 13:00 P.M. It is the period of the day when electric energy consumption regularly grows. However, observing the campaigns, the maximum average value was around 0.32 μT, which was about eight times lower than the maximum one, allowed by reference level of 2.5 μT, prescribed by the Republic of Serbia national legislation [17].

The obtained results demonstrated that the average magnetic field strength values were around 0.25 μT in 2018, slightly lower than those from 2015. However, the average field strength values from 2020, close to 0.1 μT, were noticeably lower than in previous campaigns.

Unfortunately, while the original May 2020 measurement campaign was in progress, the DSO informed the public on the malfunction of the city distribution system. They needed to make certain reconfiguration and reconstruction in core distribution network, changing the power loads between the HV power substations. As a result, some of the city consumers were supplied from the neighboring substations instead of "Novi Sad 7". Therefore, its current intensity was decreased, compared with regular day – May_r 2020, as presented in Table 3a.

The current intensity of the HV power line, as a very important parameter for the management of the substation, for the entire monitoring period of all campaigns, was registered by the internal SCADA system [18] and at the end of each campaign was provided to the research team by DSO. The simple statistical analysis of those data is offered in Table 3.

The reduction of the current intensity for sure would affect the magnetic field strength, as it is directly proportional to the current intensity [4]. Since the state of the distribution system was not regular, it was decided to finish the ongoing May 2020 campaign and to perform an additional monitoring of the magnetic field after the establishment of the system's steady state condition.

Comparison of the averaged magnetic field strength values, including the repeated monitoring campaign in September 2020, is provided in Figure 4b. The maximum average value for magnetic field was 0.37 μT, which was also the highest measured value in all campaigns. Additionally, the average magnetic field strengths from September 2020 were higher than in previous campaigns, as it is noticeable in Figure 4b. However, it was expected, having in mind increased number of industrial and residential consumers with a greater demand for electric energy.

The significant differences in current intensity were found for the incident May 2020 monitoring, where current consumption was lowered more than twice, comparing it with 2015 and 2108 campaigns. However, regarding regular day in May – May_r 2020, the substation current was on the expected level, as shown in Table 3.

Finally, the consumption was the highest in all campaigns during September 2020, as presented in Table 3b.

Table 3: The HV power line current intensity

Campaign	I_{min} (A)	I_{max} (A)	$I_{average}$ (A)
May 2020	55.00	80.10	61.96
May_r 2020 (regular day)	148.20	171.00	162.20
2018	123.81	148.28	139.78
2015	137.14	165.57	155.61

a) Current intensity in May 2020

Campaign	I_{min} (A)	I_{max} (A)	$I_{average}$ (A)
Sept 2020	157.20	190.70	175.25
May 2020	55.00	80.10	61.96
May_r 2020 (regular day)	148.20	171.00	162.20
2018	123.81	148.28	139.78
2015	137.14	165.57	155.61

b) Current intensity in September 2020

That can be explained with the increased number of connections to the power supply network for newly built residential objects, malls and enterprise buildings of Novi Sad, in the nearby area of the power substations.

Such conclusion is supported by energy consumption diagrams of the high-power substation "Novi Sad 7" [18], presented in Figure 5. We can clearly notice the difference in the shape of the curve for May 2020 in period of the power system failure, which occurs between 07:00 A.M. and 17:00 P.M., compared to other curves.

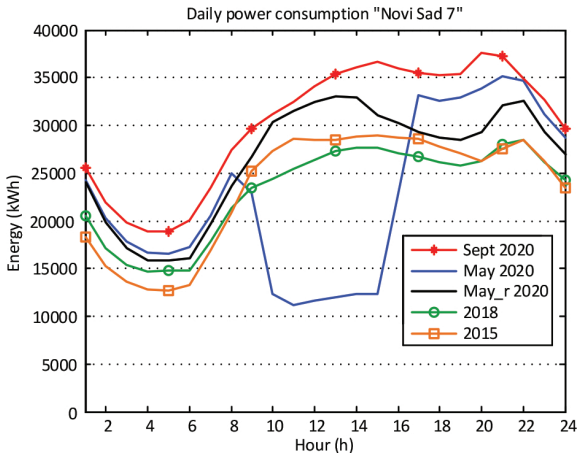

Fig. 5. Energy consumption of substation "Novi Sad 7".

According to the DSO, the overall energy consumption of the substation "Novi Sad 7" up to the year 2020, compared to 2015, increased from about 2.8% to about 3.5%, in the region under the DSO dispatch center [24].

B. Frequency selective measurement

The frequency selective analysis, as an important part of the monitoring process, was intended for the spectral evaluation of monitored locations, providing valuable information on neighboring EMF sources.

B.1. The high-frequency spectrum

The analyses of the high-frequency spectrum were performed at position of L2 hot-spot. This spectral measurement was performed once, assuming that the present EMF sources regularly emitted at detected frequencies. The analyses of spectral content were made for all three campaigns, and the results for 2015 and 2020 campaigns are displayed in Figure 6.

Spectral components were detected in several sub-bands, which are produced by well-known telecommunications services: the TV broadcasting, GSM 900, GSM 1800 and UMTS 2100. The highest strength of the electric field in 2020 campaign was observed in sub-bands near 1800 MHz, while in the 2015 campaign that was the case with UHF sub-band near 450 MHz.

The decreased activity of the UHF sub-band sources (near 450 MHz) can be noticed in 2020, since, according to national "Decree on determining the allocation plan of radio frequency bands" [25], this sub-band is intended for DSO internal communication systems, such as the voice communication system presented in Table 1.

Furthermore, more RF carriers were logged in 2020, in the sub-band intended for the emission of the digital broadcasting DBV-T2 signal. This telecommunications service was not in full operational usage in the Republic of Serbia during the 2015 campaign [19].

Similarly, the increased activity in the sub-band near 800 MHz was present in 2020, which is intended for LTE service, a technology that was extensively deployed during 2018 by the Serbian mobile telephony operators [20]. Also, the GSM 900, GSM 1800 and UMTS 2100 sub-bands had more radio-frequency carriers in 2020 than in the 2015 campaign, due to the increased number of residential subscribers and increased traffic needs.

Furthermore, spectral components in 2.4 GHz sub-band could be observed in both campaigns, since it was likely that local residents extensively used Wi-Fi equipment. Finally, the origin of the spectral components in 5.8 GHz sub-band was an internal DSO point-to-point broadband radio link, described in Table 1.

B.2. The low-frequency spectrum

The results of the low-frequency selective analysis, during the 2020 campaign, in the hot-spot of location L1, are presented in Figure 7.

In the low-frequency spectrum, there was no difference between three campaigns [16], since no new low-frequency magnetic field sources were detected.

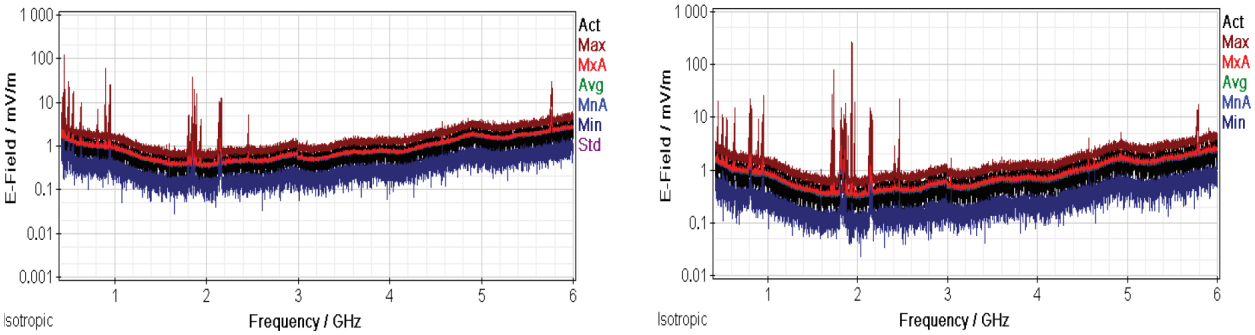

a) 2015 campaign b) 2020 campaign

Fig. 6. The high-frequency spectrum at location L2 per campaigns.

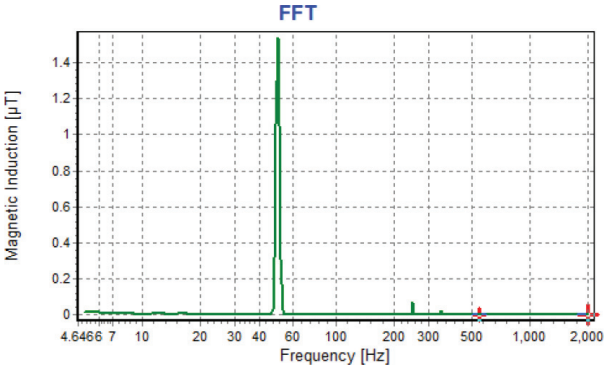

Fig. 7. The low-frequency spectrum at location L1.

Regarding this spectral content, the highest strength of the magnetic field was at the dominant spectral component of 50 Hz, as expected, while the last detected harmonic was at 450 Hz. The field strength of higher components was below the threshold of Narda EFA 300 analyzer and thus they could be neglected.

VI. EXPOSURE ASSESSMENT ANALYSIS

The exposure assessment was carried out by applying the SEMONT approach, based on the calculation of daily boundaries of Global Exposure Ratio (*GER*), thus determining the range where actual exposure lied [15].

The assessment of exposure, regarding the high-frequency electric field, was performed using the following equations [15]:

$$GER_{lower} = \left(\frac{E_m}{E_{ref\,\max}}\right)^2 \quad and \quad GER_{uppper} = \left(\frac{E_m}{E_{ref\,\min}}\right)^2. \tag{1}$$

The E_m is the average measured value of the electric field strength, while E_{refmin} and E_{refmax} are the minimum and maximum reference levels prescribed by the Serbian legislation for the general population [17], in the observed frequency range.

The assessment of lower and upper exposure boundaries, for the low-frequency magnetic field, was calculated using the following equations [16]:

$$GER_{lower} = \frac{B_m}{B_{ref\,\max}} \quad and \quad GER_{uppper} = \frac{B_m}{B_{ref\,\min}}, \tag{2}$$

where B_m is average measured strength of magnetic field, while B_{refmin} and B_{refmax} are the minimum and maximum Serbian prescribed reference levels [17], in the observed frequency range.

The exposure boundaries were calculated continuously, day by day, illustrating the campaigns' exposure range, while the real exposure was located between those boundaries [15].

A. The high-frequency electric field GER analysis

The high-frequency *GER* boundaries for location L2 were calculated for the frequency range of 100 kHz–6 GHz, and are presented in Figure 8.

There is a visible decrease of the upper *GER* boundary in 2018 campaign, compared to the data from 2015, which occur due to the change in the operational regime of radio #2, described in Table 1 [20]. This source was turned into a redundant link, intended only for the DSO SCADA application.

Common to all campaigns is that the maximal activity of communication services occurred near 10:00 A.M., whereas an additional slight increase of the activities can be noticed after 11:30 A.M.

Statistical analysis of the high-frequency *GER* values for all three monitoring campaigns is presented in Table 4.

In 2020, the maximum values of *GER* boundaries were $2.581 \cdot 10^{-4}$ and $2.579 \cdot 10^{-5}$, which were considerably below the maximum allowed limit of $GER_{allowed} = 1$, prescribed by Serbian legislation [17].

Likewise, comparing the *GER* boundary values, it can be observed that the average value of GER_{upper} boundary of $1.360 \cdot 10^{-4}$ in 2018 was almost two times lower than $2.196 \cdot 10^{-4}$ obtained in 2015. Also, in the

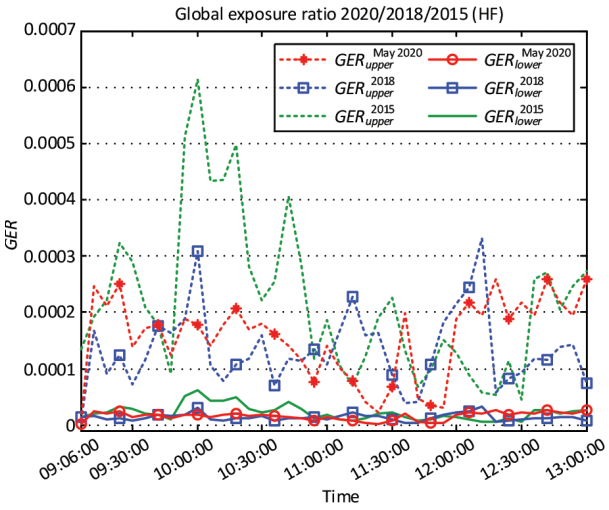

Fig. 8. The high-frequency *GER* boundaries.

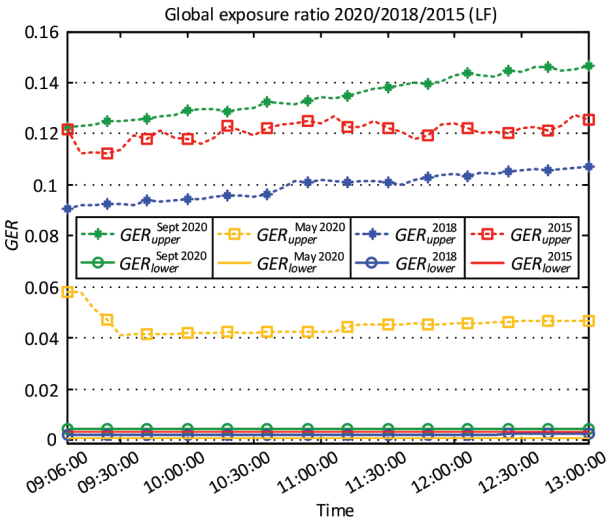

Fig. 9. The low-frequency *GER* boundaries.

Table 4: Statistical analysis of the high-frequency *GER*

Frequency range (100 kHz–6 GHz)		**Min**	**Max**	**Avg**
GER_{upper}	2020	$7.054{\cdot}10^{-6}$	$2.581{\cdot}10^{-4}$	$1.552{\cdot}10^{-4}$
	2018	$3.832{\cdot}10^{-5}$	$3.306{\cdot}10^{-4}$	$1.360{\cdot}10^{-4}$
	2015	$4.567{\cdot}10^{-5}$	$6.140{\cdot}10^{-4}$	$2.196{\cdot}10^{-4}$
GER_{lower}	2020	$7.048{\cdot}10^{-7}$	$2.579{\cdot}10^{-5}$	$1.551{\cdot}10^{-5}$
	2018	$3.829{\cdot}10^{-6}$	$3.304{\cdot}10^{-5}$	$1.359{\cdot}10^{-5}$
	2015	$4.563{\cdot}10^{-6}$	$6.134{\cdot}10^{-5}$	$2.194{\cdot}10^{-5}$

2020 campaign, this value was $1.552 \cdot 10^{-4}$, a slightly higher than in the 2018 campaign.

However, the *GER* data confirms that the high-frequency electric field exposure at L2 location is very low.

B. The low-frequency magnetic field GER analysis

Measurements of the low-frequency magnetic field, at location L1, were conducted in the frequency range of 5 Hz to 32 kHz. Regarding the exposure assessment, the comparative overview of the low-frequency *GER* boundaries is provided in Figure 9.

Analyzing this figure, the trend of the moderate increase of the upper *GER* boundaries can be noticed, as we approach the end of all campaigns. That could be explained by the increased consumption of electric power, at that period of the day, as shown in Figure 5 [18].

Statistical analysis of the low-frequency *GER* values is displayed in Table 5.

It can be observed that the maximum values of *GER* in September 2020 campaign are between $1.473 \cdot 10^{-1}$ and $5.755 \cdot 10^{-4}$, which is clearly lower than $GER_{allowed} = 1$, the maximum level allowed by the legislation of the Republic of Serbia [17].

Table 5: Statistical analysis of the low-frequency *GER*

Frequency range (5 Hz–32 kHz)		**Min**	**Max**	**Avg**
GER_{upper}	Sept 2020	$1.223 \cdot 10^{-1}$	$1.473 \cdot 10^{-1}$	$1.352 \cdot 10^{-1}$
	May 2020	$4.135 \cdot 10^{-2}$	$5.813 \cdot 10^{-2}$	$4.513 \cdot 10^{-2}$
	2018	$9.096 \cdot 10^{-2}$	$1.074 \cdot 10^{-1}$	$1.000 \cdot 10^{-1}$
	2015	$1.126 \cdot 10^{-1}$	$1.276 \cdot 10^{-1}$	$1.214 \cdot 10^{-1}$
GER_{lower}	Sept 2020	$4.470 \cdot 10^{-4}$	$5.755 \cdot 10^{-4}$	$5.280 \cdot 10^{-4}$
	May 2020	$1.615 \cdot 10^{-4}$	$2.271 \cdot 10^{-4}$	$1.763 \cdot 10^{-4}$
	2018	$3.553 \cdot 10^{-4}$	$4.195 \cdot 10^{-4}$	$3.907 \cdot 10^{-4}$
	2015	$4.399 \cdot 10^{-4}$	$4.983 \cdot 10^{-4}$	$4.470 \cdot 10^{-4}$

Furthermore, comparing the obtained *GER* boundaries, it can be observed that the average value of GER_{upper} in 2018 campaign was less than in 2015 by nearly 20%. In May 2020 campaign it was more than 2.5 times lower than in 2015, while in September 2020 it was about 10% higher than in the 2015 campaign.

Conclusively, all those *GER* values imply that the L1 location is a continuously low exposed location to the low-frequency magnetic field.

VII. CONCLUSION

The power distribution facilities cause public concerns related to the EMF exposure and potential health effects, especially in circumstances of their presence in residential areas. The high-power substation "Novi Sad 7" is a typical example of a distribution substation that is surrounded by a moderately populated area.

Thus, EMF monitoring campaigns were conducted in 2015, 2018 and 2020, in the close vicinity of this substation. The focus of these campaigns was the determination of the existing EMF levels, both in the low- and the high-frequency ranges, as well as general population exposure. The positions close to substation, where people had access, such as frequently used pedestrian paths outside the substation area, were of special interest.

Regarding the high-frequency electric field, a comparative analysis of EMF exposure has showed that *GER* boundaries in 2018 were almost two times lower than in 2015. The reason was the fact that the internal radio for the SCADA application, as one of the dominant sources, was changed due to the operational regime, transferring data only in the case of malfunction of the primary link.

Exposure boundaries in 2020 campaign had somewhat higher values than in 2018, possibly due to the increased mobile communication traffic. The maximal detected electric field level, in all performed campaigns, was 0.27 V/m, which is well below the Serbian minimal prescribed reference level of 11 V/m.

With regard to the low-frequency magnetic field, the analysis revealed that there was an increase in the current consumption and also an increase in the maximum value of upper exposure boundaries, for about 10%, comparing the first 2015 campaign and the last one in September 2020. A significant decrease of the exposure level during May 2020 campaign was noticed, which was caused by the power distribution system failure. However, the maximum exposure level, detected in September 2020 campaign, was about 6.8 times lower than the maximum allowed level prescribed by the Serbian legislation.

According to the obtained measurement results and performed analysis, it can be concluded that monitored locations at the vicinity of "Novi Sad 7" substation are low exposed locations, both to the low-frequency magnetic and the high-frequency electric fields.

However, the construction of the second HV line, as an underground cable, interconnecting the "Novi Sad 7" to some other neighboring high-power substations is under work. Additionally, due to further improvement and construction of Smart Grid, the expansion of the internal radio communication systems is under consideration. Finally, the power distribution facilities have a commercial potential for service providers and mobile operators. In that sense, in due time, they will become an even more important radio communication nodes, besides their already crucial role in electric power system.

All these circumstances will lead to a potential increase of EMF radiation, imposing the necessity for future periodic monitoring campaigns. The goal is and will be to obtain a detailed insight into the EMF field changes and exposure levels in the substation's vicinity.

ACKNOWLEDGMENT

This paper has been supported by the Provincial Secretariat for Science and Technological Development of Autonomous Province of Vojvodina, through grant for project 142-451-2603/2021-01/02.

REFERENCES

[1] Special Eurobarometer 347, "Electromagnetic Fields," https://data.europa.eu/euodp/en/data/dataset/S843_73_3_EBS347, 2014, last accessed September 2021.

[2] A. I. Tarmizi, M. D. Rotaru, and J. K. Sykulski, "Magnetic field calculations within substation environment for EMC studies," 2016 IEEE 16th International Conference on Environment and Electrical Engineering (EEEIC), Florence, Italy, pp. 1-6, Jun. 2016, doi: 10.1109/EEEIC.2016.7555613.

[3] A. Orłowski, R. Pawlak, A. Kalinowski, and A. Wójcik, "Assessment of human exposure to cellular networks electromagnetic fields," 2018 Baltic URSI Symposium (URSI), Poznan, Poland, pp. 257-260, May 2018, doi: 10.23919/URSI.2018.8406750.

[4] ICNIRP, "Guidelines for Limiting Exposure to Time-Varying Electric, Magnetic and Electromagnetic Fields (up to 300 GHz)," Health Physics, vol. 75, no.4, pp. 494-522, Apr. 1998.

[5] C. D. Abreu Silveira, C. A. Da Costa, R. D. Costa E Silva, L. R. Soares, and J. C. Pugliese Guimaraes, "Electromagnetic Environment Measurement under Steady-State Conditions in Utility Substations," 2006 IEEE/PES Transmission & Distribution Conference and Exposition: Latin America, Venezuela, pp. 1-6, Aug. 2006, doi: 10.1109/TDCLA.2006.311511.

[6] A. S. Safigianni and C. G. Tsompanidou, "Measurements of electric and magnetic fields due to the operation of indoor power distribution substations," in *IEEE Transactions on Power Delivery*, vol. 20, no. 3, pp. 1800-1805, Jul. 2005, doi: 10.1109/TPWRD.2005.848659.

[7] A. S. Safigianni and C. G. Tsompanidou, "Electric and magnetic field measurements in an outdoor electric power substation," in *IEEE Transactions on Power Delivery*, vol. 24, no. 1, pp. 38-42, Jan. 2009, doi: 10.1109/TPWRD.2008.917690.

[8] A. S. Safigianni, C. G. Tsompanidou, and V. L. Kanas, "Electric and magnetic field measurements in a high voltage venter," *The Annals of Occupational Hygiene*, vol. 56, no. 1, pp. 18–24, Jan. 2012, doi: 10.1093/annhyg/mer076.

[9] K. Ellithy, A. Al Shafai, F. Al Assiry, "Measuring human exposure to magnetic fields in substations and power lines located in Qatar,"

Study Committee C3 – System Environmental Performance, CIGRE, Paris, Aug. 2012.

[10] W. Joseph, L. Verloock, and L. Martens, "General public exposure by ELF fields of 150–36/11 kV substations in urban environment," in *IEEE Transactions on Power Delivery*, vol. 24, no. 2, pp. 642-649, Apr. 2009, doi: 10.1109/TPWRD.2008.2002686.

[11] L. Korpinen, H. Kuisti, R. Paakkonen, and J. Elovaara, "Occupational exposure to electric and magnetic fields while working at switching and transforming stations of 110 kV," Annals of Occupational Hygiene, vol. 55, no. 5, pp. 526-536, Jun. 2011, doi: 10.1093/annhyg/mer013.

[12] C. Oliveira, D. Sebastiao, G. Carpinteiro, L. Correia, C. Fernandes, A. Serralha, and N. Marques, "The moniT project: electromagnetic radiation exposure assessment in mobile communications," *IEEE Antennas and Propagation Magazine*, vol. 49, no. 1, pp. 44-53, Feb. 2007, doi: 10.1109/MAP.2007.370981.

[13] E. Lunca, A. Salceanu, "An overview of RF-EMF monitoring systems and associated monitoring data," 2016 International Conference and Exposition on Electrical and Power Engineering (EPE 2016), Lasi, Romania, pp. 418-421, Oct. 2016, doi: 10.1109/ICEPE.2016.7781374.

[14] N. Djuric, D. Kljajic, K. Kasas-Lazetic, and V. Bajovic, "The measurement procedure in the SEMONT monitoring system," *Environmental Monitoring and Assessment*, vol. 186, no. 3, pp. 1865-1874, Mar. 2014, doi: 10.1007/s10661-013-3500-0.

[15] N. Djuric and D. Kljajic, "Assessment of daily exposure in the broadband continuous monitoring system – SEMONT," 11th IEEE AFRICON Conference, Mauritius, pp. 903-907, Sep. 2013, doi: 10.1109/AFRCON.2013.6757844.

[16] N. Djuric, J. Bjelica, D. Kljajic, M. Milutinov, K. Kasas-Lazetic, and D. Antic, "The SEMONT continuous monitoring and exposure assessment for the low-frequency EMF," 2016 IEEE on Emerging Technologies and Innovative Business Practices for the Transformation of Societies (EmergiTech), Mauritius, pp. 50-55, Aug. 2016, doi: 10.1109/EmergiTech.2016.7737309.

[17] "Rulebook on non-ionizing radiation exposure limits," Official gazette of the Republic of Serbia, no. 104/09, http://www.sepa.gov.rs/download/strano/pravilnik5.pdf, last accessed September 2021.

[18] Distribution System Operator "EPS Distribucija," Internet portal, http://www.epsdistribucija.rs, last accessed September 2021.

[19] G. Nedic, N. Djuric, D. Kljajic, M. Milutinov, and S. Josic, "The exposure assessment to communication equipment of high-power substation," IEEE 24th Telecommunications Forum TELFOR 2016, Section 6 – Applied Electromagnetics, Belgrade, Serbia, pp. 609-612, Nov. 2016, doi: 10.1109/TELFOR.2016.7818857.

[20] G. Nedic, N. Djuric, D. Kljajic, K. Kasas-Lazetic, and M. Pascan, "Comparative analysis of the exposure assessment to communication equipment of high-power substation," IEEE 26th Telecommunications Forum TELFOR 2018, Section 6 – Applied Electromagnetics, Belgrade, Serbia, pp. 450-453, Nov. 2018, doi: 10.1109/TELFOR.2018.8612018.

[21] G. Nedic, D. Antic, D. Kljajic, and N. Djuric, "The SEMONT system utilization for high-frequency EMF monitoring in vicinity of 110/x kV "Novi Sad 7" power substation," Study Committee EC 2 – Power Quality and Electromagnetic Compatibility, 10. CIRED Conference, Vrnjacka Banja, Serbia, pp. 1-9, Sep. 2016.

[22] D. Kljajic and N. Djuric, "The adaptive boundary approach for exposure assessment in a broadband EMF monitoring," *Measurement*, vol. 93, pp. 515-523, Nov. 2016, doi: 10.1016/j.measurement.2016.07.055.

[23] SRPS EN 50413:2020, 2020: "Basic standard on measurement and calculation procedures for human exposure to electric, magnetic and electromagnetic fields (0 Hz–300 GHz)".

[24] Distribution System Operator "EPS Distribucija," "Energy data 2020" newsletter, http://epsdistribucija.rs/pdf/GI_2020.pdf, last accessed September 2021.

[25] "Decree on determining the allocation plan of radio frequency bands," Official gazette of the Republic of Serbia, no. 89, 2020, http://www.srv.org.rs/pages/dok/plan_namene_rf_opsega.pdf, last time accessed September 2021.

Goran Nedic graduated in 1992 at the Faculty of Technical Sciences, University of Novi Sad, while he was awarded M. Sc. in Electrical Engineering from the University of Belgrade, Republic of Serbia, in 2008. He is an Information and Communication Technology (ICT) engineer with significant experience in wireless and fixed communications and various monitoring and control systems for large enterprises. His interests include an issue about the reliability of ICT and SCADA equipment in specific working environment, such as electric power distribution system.

Nikola Djuric was born in Novi Sad, Serbia, in 1973. He received M.Sc. and Ph.D. degrees in Telecommunication and Signal Processing from the Faculty of Technical Sciences, University of Novi Sad, in 2003 and 2009, respectively. From 1997 to 2010 he was a Teaching Assistant; from 2010 to 2015 Assistant Professor; from 2015 to 2020 Associate Professor; while since 2020 he has been a Full Professor at FTN-UNS. He is the author or co-author of more than 100 journal and conference articles. His research interests include the computational and applied electromagnetics, with environmental EMF measurement and monitoring for EMF compliance testing, estimation, and simulation of EMF whole-body exposure. He is a member of IEEE society.

Dragan Kljajic was born on April 29, 1987 in Novi Sad, Republic of Serbia. He obtained his Ph.D. in Electrical and Computer Engineering from the Faculty of Technical Sciences, Novi Sad, from the Department of Power, Electronic and Telecommunication Engineering. He works as an Assistant Professor. His scientific area is theoretical electrotechnics, while his research interests are in the field of theoretical electrical engineering, theoretical and applied electromagnetics and microelectronics. He is the author or co-author of more than 50 scientific papers, published in Proceedings of international conferences and high impact factor journals. He is a member of IEEE society.